

## JRC SCIENCE AND POLICY REPORTS

# Titanium Dioxide, NM-100, NM-101, NM-102, NM-103, NM-104, NM-105: Characterisation and Physico- Chemical Properties

### *JRC Repository: NM-series of Representative Manufactured Nanomaterials*

Kirsten Rasmussen, Jan Mast, Pieter-Jan De Temmerman, Eveline Verleysen, Nadia Waegeneers, Frederic Van Steen, Jean Christophe Pizzolon, Ludwig De Temmerman, Elke Van Doren, Keld Alstrup Jensen, Renie Birkedal, Marcus Levin, Signe Hjortkjær Nielsen, Ismo Kalevi Koponen, Per Axel Clausen, Vivi Kofoed-Sørensen, Yahia Kembouche, Nathalie Thieriet, Olivier Spalla, Camille Guiot, Davy Rousset, Olivier Witschger, Sebastian Bau, Bernard Bianchi, Charles Motzkus, Boris Shivachev, Louiza Dimowa, Rositsa Nikolova, Diana Nihtianova, Mihail Tarassov, Ognyan Petrov, Snejana Bakardjieva, Douglas Gilliland, Francesca Pianella, Giacomo Ceccone, Valentina Spampinato, Giulio Cotogno, Neil Gibson, Claire Gaillard and Agnieszka Mech



Co-funded by  
the Health Programme  
of the European Union  
Grant Agreement n°2009 21 01

2014



Report EUR 26637 EN

**European Commission**

Joint Research Centre  
Institute for Health and Consumer Protection

**Contact information**

IHCP Communication Office  
Address: Joint Research Centre, Via Enrico Fermi 2749, 21027 Ispra (VA), Italy  
E-mail: [jrc-ihcp-communication@ec.europa.eu](mailto:jrc-ihcp-communication@ec.europa.eu)  
Tel.: +39 0332 78 9618  
Fax: +39 0332 78 5388

<http://ihcp.jrc.ec.europa.eu/>  
<https://ec.europa.eu/jrc>

This publication is a Science and Policy Report by the Joint Research Centre of the European Commission.

**Legal Notice**

This publication is a Science and Policy Report by the Joint Research Centre, the European Commission's in-house science service. It aims to provide evidence-based scientific support to the European policy-making process. The scientific output expressed does not imply a policy position of the European Commission. Neither the European Commission nor any person acting on behalf of the Commission is responsible for the use which might be made of this publication.

JRC 86291

EUR 26637 EN

ISBN 978-92-79-38188-1 (pdf)  
ISBN 978-92-79-38189-8 (print)

ISSN 1018-5593 (print)  
ISSN 1831-9424 (online)

doi: 10.2788/79554 (online)

Luxembourg: Publications Office of the European Union, 2014

© European Union, 2014

Reproduction is authorised provided the source is acknowledged.

Printed in Italy

# **Titanium Dioxide, NM-100, NM-101, NM-102, NM-103, NM-104, NM-105: Characterisation and Physico-Chemical Properties**

## **JRC Repository: NM-Series of Representative Manufactured Nanomaterials**

**Kirsten Rasmussen, Douglas Gilliland, Francesca Pianella,  
Giacomo Ceccone, Valentina Spampinato, Giulio Cotogno, Neil Gibson,  
Claire Gaillard, Agnieszka Mech**

European Commission, Joint Research Centre, Institute for Health and Consumer Protection, Italy

**Jan Mast, Pieter-Jan De Temmerman, Eveline Verleysen, Nadia Waegeneers,  
Frederic Van Steen, Jean Christophe Pizzolon, Ludwig De Temmerman,  
Elke Van Doren**

Veterinary and Agrochemical Research Centre (CODA-CERVA), Belgium

**Keld Alstrup Jensen, Renie Birkedal, Marcus Levin, Signe Hjortkjær Nielsen,  
Ismo Kalevi Koponen, Per Axel Clausen, Vivi Kofoed-Sørensen, Yahia Kembouche**  
National Research Centre for the Working Environment (NRCWE), Denmark

**Nathalie Thieriet**

L'Agence nationale de sécurité sanitaire de l'alimentation, de l'environnement et du travail  
(ANSES), France

**Olivier Spalla, Camille Guiot**

Commissariat à l'énergie atomique et aux énergies alternatives (CEA), France

**Davy Rousset, Olivier Witschger, Sébastien Bau, Bernard Bianchi**

Institut National de Recherche et de Sécurité (INRS), France

**Charles Motzkus**

Laboratoire National de métrologie et d'essais (LNE), France

**Boris Shivachev Louiza Dimowa, Rositsa Nikolova, Diana Nihtianova,  
Mihail Tarassov, Ognyan Petrov, Snejana Bakardjieva**  
Institute of Mineralogy and Crystallography (IMC-BAS), Bulgaria

## Abstract

The European Commission's Joint Research Centre (JRC) provides scientific support to European Union policy including nanotechnology. Within this context, the JRC launched, in February 2011, a repository for Representative Test Materials (RTMs), based on preparatory work started in 2008. It supports both EU and international research projects, and especially the OECD Working Party on Manufactured Nanomaterials (WPMN). The WPMN leads an exploratory testing programme "Testing a Representative set of Manufactured Nanomaterials" for the development and collection of data on characterisation, toxicological and ecotoxicological properties, as well as risk assessment and safety evaluation of nanomaterials. The purpose is to understand the applicability of the OECD Test Guidelines for the testing of nanomaterials as well as end-points relevant for such materials.

The Repository responds to a need for nanosafety research purposes: availability of nanomaterial from a single production batch to enhance the comparability of results between different research laboratories and projects. The availability of representative nanomaterials to the international scientific community furthermore enhances and enables development of safe materials and products.

The present report presents the physico-chemical characterisation of the Titanium dioxide series from the JRC repository: NM-100, NM-101, NM-102, NM-103, NM-104 and NM-105. NM-105 was selected as principal material for the OECD test programme "Testing a representative set of manufactured nanomaterials". NM-100 is included in the series as a bulk comparator.

Each of these NMs originates from one batch of commercially manufactured TiO<sub>2</sub>. The TiO<sub>2</sub> NMs may be used as representative material in the measurement and testing with regard to hazard identification, risk and exposure assessment studies.

The results for more than 15 endpoints are addressed in the present report, including physico-chemical properties, such as size and size distribution, crystallite size and electron microscopy images. Sample and test item preparation procedures are addressed. The results are based on studies by several European laboratories participating to the NANOGENOTOX Joint Action, as well as by the JRC.

## **Table of contents**

<b>Abstract</b> .....	<b>iv</b>
<b>List of abbreviations</b> .....	<b>vii</b>
<b>1. Introduction</b> .....	<b>1</b>
1.1.Production of TiO <sub>2</sub> .....	2
1.2.About this report.....	2
<b>2. Overview of the JRC NM-Series of Representative Test Materials</b> .....	<b>4</b>
2.1.Representativeness of the materials in the NM-series.....	5
2.2.The OECD WPMN and Testing the NM-Series.....	7
2.3.Characterisation of the NM-series .....	9
<b>3. Materials, Methods and End-points</b> .....	<b>11</b>
<b>4. Homogeneity within and between vials. Sample preparation reproducibility among laboratories</b> .....	<b>16</b>
4.1.Procedure and sample preparation .....	16
4.2.Homogeneity Results for NM-102.....	17
4.3.Homogeneity Results for NM-103.....	18
4.4.Homogeneity Results for NM-104.....	19
4.5.Homogeneity Results for NM-105.....	20
<b>5. Chemical composition</b> .....	<b>21</b>
5.1.Elemental Composition by EDS and ICP-OES.....	21
5.2.Presence of associated organic matter by TGA and DTA.....	23
5.2.1 Analysis of associated organic matter .....	28
5.2.2. Results .....	29
5.3.Surface composition by XPS .....	30
5.3.1. Measurements .....	30
5.3.2. Results .....	31
5.4.Observations and conclusions for chemical composition.....	36
<b>6. Hydrochemical reactivity, solubility and biodurability</b> .....	<b>38</b>
6.1.Results, Hydrochemical pH reactivity .....	39
6.2.Hydrochemical O <sub>2</sub> Activity.....	46
6.3.In vitro dissolution and solubility .....	53
6.4.Estimation of biodurability .....	56
6.5.Conclusions.....	56
<b>7. Dynamic Light Scattering measurements for size distributions, mean aggregate size and structure</b> .....	<b>57</b>
7.1.DLS measurements and data treatment.....	57
7.1.1. Sample preparation .....	57
7.1.2. Suspension Stability over time followed by DLS .....	58
7.1.3. DLS results: size distribution and intensity averaged mean size of aggregates.....	59
7.2.JRC DLS measurements and data treatment.....	60
7.2.1. Sample preparation .....	60
7.2.2. Measurement results .....	60
7.3.Conclusions on DLS measurements .....	62
<b>8. Zeta potential</b> .....	<b>65</b>
<b>9. SAXS and USAXS measurements and data treatment</b> .....	<b>67</b>
9.1.Stability of the samples .....	69
9.2.Size and structure of fractal aggregates by SAXS .....	69
<b>10. Brunauer, Emmett and Teller (BET) measurements</b> .....	<b>74</b>
10.1.BET results.....	75
10.2.Comparison between BET data from research laboratories and producers .....	77

10.3.Comparison of SAXS and BET data .....	78
<b>11. XRD measurements .....</b>	<b>80</b>
11.1.XRD analysis.....	80
11.2.XRD results .....	82
<b>12. Transmission Electron Microscopy (TEM) .....</b>	<b>90</b>
12.1.Sample preparation and analytical methods .....	90
12.1.1.Sample preparation .....	90
12.1.2.Recording of the electron micrographs .....	91
12.1.3.Qualitative TEM characterisation and measurement of primary particles .....	92
12.1.4.Quantitative analysis of aggregated/agglomerated NM based on TEM micrographs ..	95
12.2.Results for transmission electron microscopy .....	97
12.2.1.Sample preparation and image analysis .....	97
12.2.2.Results for NM-100.....	99
12.2.3.Results for NM-101 .....	102
12.2.4.Results for NM-102.....	107
12.2.5.Results for NM-103.....	108
12.2.6.Results for NM-104.....	113
12.2.7.Results for NM-105.....	120
12.3.Combination of the results of quantitative AFM and TEM analyses.....	123
12.4.Discussion of TEM results .....	125
<b>13. Dustiness .....</b>	<b>128</b>
13.1.Description and measurement.....	129
13.2.Experimental Setup and Results.....	129
13.2.1.Small rotating drum method .....	129
13.2.2.Vortex shaker method.....	133
13.2.3.Results for the Vortex Shaker Method .....	138
13.2.4.Comparison of the SD and VS methods .....	139
<b>14. Discussion and Conclusions .....</b>	<b>141</b>
14.1.Materials and dispersion .....	141
14.2.Characterisation .....	141
14.1.1.Overview tables of characterisation data .....	143
14.1.2.Characterisation data, description and conclusion.....	163
<b>15. References .....</b>	<b>167</b>
<b>A. Appendix. SOP: Dynamic Light Scattering Measurements and Data Treatment.....</b>	<b>171</b>
<b>B. Appendix. The Sensor Dish Reader System .....</b>	<b>182</b>
<b>C. Appendix. SOP for surface charge and isoelectrical point by zetametry.....</b>	<b>185</b>
<b>D. Appendix. SOP for Small Angle X-ray Scattering.....</b>	<b>191</b>
<b>E. Comparative overview of the TiO<sub>2</sub> NMs .....</b>	<b>205</b>

## List of abbreviations

2D	Two Dimensional
3D	Three Dimensional
ANOVA	Analysis of Variance
APS	Aerodynamic Particle Sizer
ASASP	Association of Synthetic Amorphous Silica Producers
at%	Atomic percent
BET	Brunauer, Emmet and Teller
BSA	Bovine Serum Albumin
CEA	Commissariat à l'énergie atomique et aux énergies alternatives
CEN	Comité Européen de Normalisation
CLS	Centrifugal Liquid Sedimentation
CODA-CERVA	Veterinary and Agrochemical Research Centre (Belgium)
CPC	Condensation Particle Counter
DLS	Dynamic Light Scattering
ELPI	Electrical Low Pressure Impactor
EM	Electron microscopy
EDX	Energy-Dispersive X-ray spectroscopy
FMPS	Fast Mobility Particle Sizer
FWHM	Full-Width Half-Maximum
GLP	Good Laboratory Practice
h	hours
HEPA filter	High-Efficiency Particulate Air filter
ICP-OES	Inductively Coupled Plasma – Optical Emission Spectrometry
IEP	Iso-Electric Point
IHCP	Institute for Health and Consumer Protection (JRC)
IMC-BAS	Institute of Mineralogy and Crystallography, Bulgaria
INRS	Institut National de Recherche et de Sécurité
ISO	International Organisation for Standardization
ISO/TC 229	ISO/Technical Committee on Nanotechnologies
IUPAC	International Union of Pure and Applied Chemistry
JRC	Joint Research Centre, European Commission
L or l	Litre
LNE	Laboratoire national de métrologie et d'essais, France
lpm	Litre per minute
mL	Milli litre
MWCNT	Multi Walled Carbon Nanotube
NIST	USA, National Institute of Standards and Technology

NM	Nanomaterial
NRCWE	National Research Centre for the Working Environment
OECD	Organisation for Economic Co-operation and Development
PSD	Particle Size Distribution
PBS	Phosphate Buffered Saline
PCS	Photon Correlation Spectroscopy
PdI	Poly Dispersion Index
pH	Acidity value
REACH	Registration, Evaluation, Authorisation and restriction of Chemicals
RH	Relative Humidity
RMN	Representative Manufactured Nanomaterial
rpm	Rounds Per Minute
RSD	Relative Standard Deviation
RTM	Representative Test Material
s	second
SAXS	Small Angle X-ray Scattering
SD	Standard Deviation
SD (chapter 13)	Small Rotating Drum
SDR	Sensor Disk Reader
SEM	Scanning Electron Microscopy
SEM-EDS	Scanning Electron Microscopy-Energy Dispersive Spectroscopy
SIRT	Simultaneous Iterative Reconstruction Technique
SOP	Standard Operating Procedure
SCENIHR	Scientific Committee for Emerging and Newly Identified Health Risks
TEM	Transmission Electron Microscopy
USA	United States of America
USA-EPA	USA Environmental Protection Agency
USAXS	Ultra Small Angle X-ray Scattering
VS	Vortex Shaker
WPMN	Working Party on Manufactured Nanomaterials
wt%	weight percent
XPS	X-ray Photoelectron Spectrometry
XRD	X-ray Diffraction



# 1. Introduction

Over the past decade, nanomaterials have gained increasing attention and they are subject to numerous international research projects aiming at both evaluating their potential for technological innovation and understanding possible adverse effects (Morris et al., 2011). It is of special interest to identify if the nanoform induces adverse effects (e.g. other effects, or different potency) different to non-nano forms of the same material.

For nanosafety research purposes, availability of nanomaterial from a single batch is desirable to enhance the comparability of results between different laboratories and research projects. Such availability would overcome questions related to whether a nanomaterial tested in one project is the same or just similar to a nanomaterial tested in other project(s) and how results compare. In response to this need as well as supporting the OECD Working Party on Manufactured Nanomaterials (WPMN) programme for "Testing a Representative set of Manufactured Nanomaterials", the European Commission's Joint Research Centre (JRC) established a repository with Representative Test Materials (RTMs) consisting of different types of particulate nanomaterials. The role of Representative Test Materials is described in a recent publication (Roebben et al., 2013).

One of the nanomaterials tested by the OECD WPMN is titanium dioxide, which is widely used as an additive in a broad variety of final products, e.g. as a pigment in paints, varnishes and plastics, as an additive to food (colorant E171), or as UV-filter in cosmetic products. Due to the recognised photo catalytic properties of some of the crystal phases of titanium dioxide, it is widely used as a photo-catalyser of various chemical reactions and active ingredient of coatings (self-cleaning surfaces). As the final products are available in very large quantities even a minor product content of TiO<sub>2</sub> will add up to a large total volume. According to ECHA's REACH Registered Substance data base, titanium dioxide in Europe is registered at the 1000 000 - 10 000 000 tonnes/year level.<sup>1</sup>

A substantial part of the information in this report come from a Joint Action, NANOGENOTOX, see <http://www.nanogenotox.eu>, which was co-financed by the Executive Agency of the Directorate General for Health and Consumers of the European Commission and 11 EU member states. In NANOGENOTOX, characterisation and testing of TiO<sub>2</sub> was an important task. In addition, results and data from the JRC laboratories are included. Other examples of EU projects testing the materials from the Repository are MARINA (<http://www.marina-fp7.eu/>) and NANoREG (<http://www.nanoreg.eu/>).

---

<sup>1</sup> <http://echa.europa.eu/it/information-on-chemicals/registered-substances>

## 1.1 Production of TiO<sub>2</sub>

TiO<sub>2</sub> is produced from ilmenite ore that has the chemical composition FeTiO<sub>3</sub>; furthermore TiO<sub>2</sub> exists in nature as the well-known minerals rutile, anatase and brookite. Additional TiO<sub>2</sub> containing minerals are found, but they are rarer.

For pigment grade TiO<sub>2</sub> manufacturing, two processes exist using titanium-containing ores or slags as the starting material:

- The sulphate process, applied to ilmenite. By mixing ilmenite with sulphuric acid the iron can be removed as iron sulphate. This process leads to the rutile form of TiO<sub>2</sub>.
- The chloride process, where the crude TiO<sub>2</sub> is converted to TiCl<sub>4</sub> and re-oxidized to TiO<sub>2</sub>. Aluminium chloride is often added to the process as a rutile promotor, and when not added the TiO<sub>2</sub> product is mostly anatase.

For the ultrafine TiO<sub>2</sub> grade manufacturing, several processes exist for crystal formation using either titanium tetrachloride or titanyl sulphate as starting material:

- Precipitation
- Thermal hydrolysis
- Flame hydrolysis.

For the ultrafine TiO<sub>2</sub> grade, the crystal may be further processed by milling, then coating and milling again. Depending on the medium relevant to final use, a possible last dispersion step (with water / cosmetic oils) can be applied.

## 1.2 About this report

This report presents the characterisation methods and data for TiO<sub>2</sub> from the JRC Nanomaterials Repository: NM-100, NM-101, NM-102, NM-103, NM-104 and NM-105.

Chapter 2 introduces the JRC Repository for representative nanomaterials and its link to the OECD Working Party on Manufactured Nanomaterials (WPMN). Chapter 3 describes the materials, methods and end-points and presents an overview of the end-points tested and the methods applied for each end-point. Table 4 gives an overview of the end-points investigated, methods applied and the institutions involved. Then homogeneity within and between vials is addressed in chapter 4.

Chapters 5 to 13 describe in detail the physico-chemical characterisation together with the applied methodology. The characterisation includes properties such as hydrodynamic size, size distribution and zeta potential in aqueous suspensions and includes techniques such as dynamic light scattering (DLS), small-angle X-ray scattering (SAXS) and Ultra Small Angle X-

ray Scattering (USAXS). The zeta potential as a function of pH was analysed to determine stability properties of the aqueous suspensions over a pH range, and subsequently the isoelectric point (IEP, i.e. the pH at which the surface charge is globally neutral) was identified. In addition, the size distribution was analysed through Transmission Electron Microscopy (TEM) micrographs, and the specific surface area was measured by BET<sup>2</sup> and SAXS. Atomic Force Microscopy (AFM) was also applied to obtain information on particle size. The crystallinity was investigated by SAXS and X-ray Diffraction (XRD). For the dustiness testing, NRCWE modified an ISO method, ISO EN 15051, and INRS used the vortex shaker method. The conclusions are presented in chapter 14, and include a summary of results for each of the titanium dioxide NMs.

A list of abbreviations has been included before the introduction. Furthermore, further details of some of the methods applied are given in appendices A to D.

---

<sup>2</sup> Stephen Brunauer, Paul Hugh Emmett, and Edward Teller developed a theory that aims to explain the physical adsorption of gas molecules on a solid surface and serves as the basis for an important analysis technique, named after them by the initials of their last names, BET, for the measurement of the specific surface area of a material.

## 2. Overview of the JRC NM-Series of Representative Test Materials

The European Commission's Joint Research Centre (JRC) established the JRC Nanomaterials Repository for the NM-series of Representative Test Materials. The JRC Repository is hosted at the Institute for Health and Consumer Protection in Italy.

**Table 1. List of representative Nanomaterials in the JRC NM Repository (2013).**

NM code	Type of material*	Label name	Other information
<b>NM-100</b>	<b>Titanium Dioxide</b>	Titanium Dioxide	
NM-101	Titanium Dioxide	Titanium Dioxide	anatase
NM-102	Titanium Dioxide	Titanium Dioxide, anatase	anatase
NM-103	Titanium Dioxide	Titanium Dioxide thermal, hydrophobic	rutile
NM-104	Titanium Dioxide	Titanium Dioxide thermal, hydrophilic	rutile
NM-105	Titanium Dioxide	Titanium Dioxide rutile-anatase	anatase-rutile
<b>NM-110</b>	<b>Zinc Oxide, uncoated</b>	Zinc Oxide	
NM-111	Zinc Oxide, coated	Zinc Oxide coated triethoxycaprylsilane	
<b>NM-200</b>	<b>Silicon Dioxide</b>	Synthetic Amorphous Silica PR-A-02	precipitated
NM-201	Silicon Dioxide	Synthetic Amorphous Silica PR-B-01	precipitated
NM-202	Silicon Dioxide	Synthetic Amorphous Silica PY-AB-03	thermal
NM-203	Silicon Dioxide	Synthetic Amorphous Silica PY-A-04	thermal
NM-204	Silicon Dioxide	Synthetic Amorphous Silica PR-A-05	precipitated
<b>NM-211</b>	<b>Cerium Dioxide</b>	Cerium (IV) Oxide precipitated, uncoated, cubic	
NM-212	Cerium Dioxide	Cerium (IV) Oxide precipitated, uncoated	
<b>NM-300K</b>	<b>Silver</b>	Silver<20 nm	
NM-300K DIS	Silver - dispersant	Ag - dispersant	
<b>NM-330</b>	<b>Gold</b>		
NM-330 DIS	Gold - dispersant	Gold - dispersant	
<b>NM-400</b>	<b>MWCNT</b>	Multi-walled Carbon Nanotubes	
NM-401	MWCNT	Multi-walled Carbon Nanotubes	
NM-402	MWCNT	Multi-walled Carbon Nanotubes	
NM-403	MWCNT	Multi-walled Carbon Nanotubes	
<b>NM-600</b>	<b>Nanoclay</b>	Bentonite	

\*Nanomaterials, even of the same chemical composition, may be available e.g. in various sizes and/or shapes, which may influence their chemical and physical properties

The Repository contains 24 representative nanomaterials of 8 different chemistries of the following chemical composition: titanium dioxide, zinc oxide, silicon dioxide, cerium dioxide, silver, gold, multi-walled carbon nanotubes and bentonite (a nanoclay), see Table 1. Furthermore, the dispersants for silver and gold are also available from the repository. The sub-sampling was done in collaboration with the Fraunhofer Institute for Molecular Biology and Applied Ecology. Each individual nanomaterial in the NM-series originates from one batch and was allocated an identifying code with the following format: the letters "NM" followed by a dash and three digits (NM-XXX), therefore it is also called the NM-series; in

2014 where the code format was changed to JRCNM<5 digit number><letter><6 digit number>.

The NM-series are studied in national, European and global scientific projects. They are also used for testing models, and as performance standards and comparators. More than 10 000 individual samples have been distributed to research institutions, national authorities, industrial research laboratories and other scientific stakeholders in the EU, Switzerland, USA, Canada, Australia, China, Russia, Japan, and Korea. Several research projects have been undertaken to investigate properties of nanomaterials using the representative nanomaterials from the JRC repository.

Study results are collated in a JRC database, JRC NANOhub, and are made available to the OECD through dedicated data submissions to the JRC NANOhub. The combination of availability of representative test nanomaterials and JRC NANOhub reference data support innovation and competitiveness in Europe's growing nanotechnology industries by building foundations for research and product development.

## **2.1. Representativeness of the materials in the NM-series**

To reliably address the scientific questions of nanomaterial induced effects for toxicity, ecotoxicity and environmental fate and behaviour, it is important to study representative test nanomaterials that are relevant for industrial application and commercial use, and for which a critical mass of study results are available. Representative test materials allow enhanced comparison of test results, robust assessment of data, and pave the way for appropriate test method optimisation, harmonisation and validation and may finally serve as performance standards for testing.

In the following, the concept of Representative Test Material (RTM) is briefly outlined, clarifying the difference to reference materials. Reference Material (RM) is the generic name for materials that have a proven and sufficient homogeneity and stability in terms of a defined intended use, and for certified reference materials, there is a certified value for the property of interest. Reference Materials and Certified Reference Materials need to be produced and used applying the conditions and terms standardised and described in ISO Guides 30 to 35 relating to reference material production. Currently, only a small number of certified reference materials exist in the field of manufactured nanomaterials, for example gold nanoparticles (certified size) and single-wall carbon nanotube soot (certified composition) from the USA National Institute of Standards and Technology (NIST) and colloid silica (certified size) from the European Commission (JRC-IRMM).

The nanomaterials in the JRC repository are representative test materials. For RTMs the following definition was proposed by Roebben et al. (2013):

*A **representative test material (RTM)** is a material from a single batch, which is sufficiently homogeneous and stable with respect to one or more specified properties, and which implicitly is assumed to be fit for its intended use in the development of test methods which target properties other than the properties for which homogeneity and stability have been demonstrated.*

An RTM is not a reference material for the tests for which it is intended to be used, because homogeneity and stability are not demonstrated for the corresponding measurand. However, an RTM is more valuable than an ordinary test material, since it has been checked for homogeneity and stability in terms of one or more specified properties. RTMs are extremely useful tools in intra- or interlaboratory development of methods for which reference materials are not (yet) available. Thus, the NM-series of representative test materials are complementary to (certified) Reference Materials as illustrated in Table 2.

**Table 2. Essential characteristics of the concept 'representative test material' compared to the existing concepts of reference material and certified reference material.**

	Representative Test Material	Reference Material	
		Not certified	Certified
<b>Parent material</b>	Representative for a class of materials to be investigated with the target method(s)		
<b>Homogeneity / stability</b>	Assumed for the measurands of interest, demonstrated for other measurands	Demonstrated for the measurands of interest	Demonstrated for the measurands of interest
<b>Assigned property value</b>	None	None, or indicative only.	Certified for the measurand of interest

The OECD WPMN uses the term “Representative Manufactured Nanomaterial” for the nanomaterials selected for testing, which are assumed to be representative for a large fraction of nanomaterials on the market. The nanomaterials in the NM-series are a (random) sample from one industrial production batch, produced within industrial specifications. The NM-series ensures that the particular sample has been homogenised, and is sub-sampled into vials under reproducible (GLP) conditions, and the stability of the sub-samples is monitored. Thus, to the extent feasible for industrial materials, all sub-samples from one material should be identical and differences in test results between laboratories for the same end-point should not be attributed to differences in the material tested.

## 2.2. The OECD WPMN and Testing the NM-Series

In 2006 international recognition of the need of a deeper understanding of nanomaterials, including relevant characterisation information as well as hazard profiles of nanomaterials led to the establishment of the WPMN under the Chemicals Committee of the OECD. The WPMN leads one of the most comprehensive nanomaterial research programmes "Safety Testing of a Set of Representative Manufactured Nanomaterials", established in 2007.

The WPMN agreed on a list of Representative Manufactured Nanomaterials to be tested and relevant end-points to test for exploratory purposes. The nanomaterials listed in the testing programme are (2012): fullerenes, single-wall and multi-wall carbonnanotubes, cerium dioxide, zinc oxide, iron, gold, silver, titanium dioxide, silicon dioxide, nanoclay and dendrimers. Some of these materials are hosted in the JRC Repository.

For TiO<sub>2</sub> in the OECD testing programme, NM-105 was selected as the principal material, i.e. a full data set, as listed in Table 3, should be provided to the WPMN for this material.

Data in the OECD testing programme regarding characterisation, toxicological and ecotoxicological effects are generated in Phase 1 to understand the hazard profiles of the nanomaterials. A Phase 2 is planned and will start by evaluating the data received in Phase 1, and especially the test guidelines applied to identify their applicability and necessary modifications (if any). It may be considered if further testing is needed.

The endpoints addressed within Phase 1 are presented in Table 3. The Guidance Manual for the Testing of Manufactured Nanomaterials (OECD 2010) describes in detail the information expectations for each end-point and all end-points have to be addressed.

In addition to the listed endpoints in the Guidance Manual for Sponsors (GMS), the GMS advises (p. 25): *"To aid in assuring the identical nature of the sponsored MN, the material used in different tests should be obtained preferably in a single lot, and stored and manipulated in comparable, if not identical procedures."* and further *"Sponsors will identify the source of test nanomaterials, including all known aspects of material production, the manufacturer, facility location, lot number, and any other pertinent information as noted in Annex I "Nanomaterial Information/Identification"."* Thus, the GMS recommends ensuring that, as far as possible, the testing of all endpoints is performed with a nanomaterial from one batch, and the JRC repository assists the WPMN in doing this.

The provision of the JRC NM-Series to the OECD WPMN test programme enables the development of the comprehensive data set on characterisation nanomaterial properties and toxicological and ecotoxicological behaviour, as described above. In June 2012, the OECD

WPMN recommended the development of a risk assessment/safety evaluation methodology for nanomaterials, based on, among others, this data set.

**Table 3. Endpoints agreed by the OECD WPMN for the Representative Manufactured Nanomaterials.**

Nanomaterial Information / Identification		Environmental fate	
1	Nano material name	27	Dispersion stability in water
2	CAS number	28	Biotic degradability
3	Structural formula / molecular structure	29	- Ready biodegradability
4	Composition of NM being tested (incl. degree of purity, known impurities or additives)	30	- Simulation testing on ultimate degradation in surface water
5	Basic Morphology	31	- Soil simulation testing
6	Description of surface chemistry (e.g. coating or modification)	32	- Sediment simulation testing
7	Major commercial uses	33	- Sewage treatment simulation testing
8	Known catalytic activity	34	Identification of degradation product(s)
9	Method of production (e.g. precipitation, gas phase)	35	Further testing of degradation product(s) as required
<b>Physical-chemical Properties and Material Characterization</b>		36	Abiotic degradability and fate
10	Agglomeration / aggregation	37	- Hydrolysis, for surface modified nanomaterials
11	Water solubility	38	Adsorption - desorption
12	Crystalline phase	39	Adsorption to soil or sediment
13	Dustiness	40	Bioaccumulation potential
14	Crystallite size	41	Bioaccumulation in sediment
15	Representative TEM picture(s)	<b>Environmental toxicology</b>	
16	Particle size distribution	42	Effects on pelagic species (short/ long term)
17	Specific surface area	43	Effects on sediment species (short/ long term)
18	Zeta potential (surface charge)	44	Effects on soil species (short/ long term)
19	Surface chemistry (where appropriate)	45	Effect on terrestrial species
20	Photo-catalytic activity	46	Effect on micro-organisms
21	Pour density (must be completed)	47	Other relevant information
22	Porosity	<b>Mammalian toxicology</b>	
23	Octanol-water partition coefficient, where relevant	48	Pharmacokinetics (ADME)
24	Redox potential	49	Acute Toxicity
25	Radical formation	50	Repeated dose toxicity
26	Other relevant information (where available)	IF AVAILABLE	
		51	Chronic toxicity
<b>Material safety</b>		52	Reproductive toxicity
57	Flammability	53	Developmental toxicity
58	Explosivity	54	Genetic toxicity
59	Incompatibility	55	Experience with human exposure
		56	Other relevant test data



### 2.3. Characterisation of the NM-series

For nanomaterials, it is known that their properties, including any hazardous properties, can be affected by for example shape, size and surface area, because these parameters affect the transport properties of the particles (absorption, distribution, and excretion).

In addition, for nanomaterials, one of the issues raised consistently in the discussions under the OECD WPMN is the “test item” preparations and dispersion protocols. A “test item” is simply (the actual fraction of) the sample tested. This discussion is linked to the characterisation of the nanomaterials for which a number of relevant scenarios have been identified, and among these are:

Characterisation

- I. as received
- II. as dispersed
- III. during testing

These scenarios reflect that many of the nanomaterials tested are insoluble (in water and other media) or only slightly soluble nanoparticles, and their physico-chemical properties as well as their (eco)toxicological effects are closely linked also to their physical surroundings. Thus, to acquire an in-depth understanding of the nanomaterials, material characterisation should be performed for a number of the different stages of the nanomaterials' use cycle. Table 3, sections "nanomaterial information" and "physico-chemical properties", list the characterisation end-points. Most of these may be measured both for the dry material and in dispersion; however, obviously some belong to a specific preparation form for the measurement: dustiness is a dry measurement whereas the water/octanol coefficient can be measured only in solution. Additional issues could be relevant, e.g. if the physical state and preparation of the material tested are representative for production and use, taking into account the chain of actors and life cycle.

Below are described a number of issues to consider for the characterisation.

**I. “as received”** is the characterisation of the properties of a RTM as received, and typical preparations are dry or aqueous.

**II and III. “as dispersed”** and **"during testing"** are for the nanomaterials undergoing further sample preparation steps, which should be assessed with regard to influence on measurement results, such as particle size determinations for the different scenarios: dry material, in aqueous or physiological media.

In addition to the physico-chemical characterisation also data relating to (eco)toxicological effects are requested in the OECD Test Programme. For this kind of testing, the test item

preparation needs to be carefully considered. The characterisation of matrix-dependent properties of the prepared test item is an important issue for nanomaterials. Results are dependent on the matrix composition and protocols used.

For the testing, RTMs can best be used and brought into a matrix under defined conditions and applying defined procedures, and availability of protocols also for the matrices should minimise sources of uncertainties and methodological errors. Thus, dispersion protocols have been developed for test item preparation for use in test systems for (eco)toxicological testing or environmental fate analysis, comprising conditioning and choice of matrix components. Hence, the prepared test item should fulfil the requirements of the test method under GLP conditions and be representative for the selected exposure route. Test items are prepared for environmental testing in the compartments soil, water, sediment, sewage treatment plants as well as for oral, dermal, (intravenous) and inhalation toxicity testing, in the form it is assumed to reach the biological entity in the test system.

Depending on the various protocols used, different results may be obtained for the same parameter measured. Also the effect of a particle's 'corona', the molecules surrounding it in a given medium has recently been acknowledged (Cedervall et al., 2007), emphasising that the constituents of the corona depend on the medium. Biophysical characterisation, such as corona composition, kinetics/exchange rates, corona structure and depletion effects/changes in matrix kinetics, is therefore required in support of understanding the test items properties.

The determination of a property should be addressed by the selection of the appropriate measurand and the corresponding measurement method. For nanomaterials the "appropriate measurand" is not yet fully understood for all endpoints, and extensive discussion and guidance development take place in several international fora: the Scientific Committee on Emerging and Newly Identified Health Risks (SCENIHR 2010), the OECD WPMN, the Comité Européen de Normalisation Technical Committee 352 Nanotechnologies (CEN/TC 352), and the International Standardisation Organisation (ISO) under Technical Committee 229 Nanotechnologies (ISO/TC 229). In addition, for the measurements, an uncertainty estimate should be described based on the Guide for Uncertainty in Measurements.

### 3. Materials, Methods and End-points

The titanium dioxides NM-100, NM-101, NM-102, NM-103, NM-104 and NM-105 are available as white powders in amber coloured vials containing up to 2000 mg under argon atmosphere. Each individual vial has a unique sample identification number.

This chapter gives an overview of the physico-chemical end-points tested and associated method(s), as well as the equipment used to characterise the titanium dioxide NMs.

The testing was performed by several European research institutes (alphabetical order):

CEA	Commissariat à l'énergie atomique et aux énergies alternatives, France
CODA-CERVA	Veterinary and Agrochemical Research Centre, Belgium
IMC-BAS	Institute of Mineralogy and Crystallography, Bulgaria
INRS	Institut National de Recherche et de Sécurité, France
JRC	Joint Research Centre, European Commission
LNE	Laboratoire national de métrologie et d'essais, France
NRCWE	National Research Centre for the Working Environment, Denmark

The data was generated in the context of several European projects, for example the Joint Action NANOGENOTOX, which was co-financed by DG SANCO and participating of EU member states, and research at the JRC. The NANOGENOTOX Joint Action was coordinated by l'Agence Nationale de Sécurité Sanitaire de l'alimentation, de l'environnement et du travail (ANSES), France.

Table 4 lists the physico-chemical characterisation end-points suggested by the OECD WPMN and gives an overview for each TiO<sub>2</sub> NM of the characterisation performed, methods used, and institution(s) involved. The experimental undertakings and results are described in chapter 4 and onwards. As seen from Table 4, the following testing and measurements were performed: surface charge, hydrodynamic particle size and particle size distribution in aqueous suspensions by dynamic light scattering (DLS), small-angle X-ray scattering (SAXS) and Ultra Small Angle X-ray Scattering (USAXS). The surface charge as a function of pH was analysed to assess the stability properties of the aqueous suspensions over the pH range, and subsequently the iso-electric point (IEP), which is the pH value at which the surface charge is globally neutral, was determined. The particle size distribution was analysed through TEM micrographs, and the specific surface area was measured by BET, and SAXS and USAXS. For the dustiness testing, NRCWE developed a dedicated method; the crystallinity was investigated by SAXS and XRD. The solubility was tested in Gambles solution, Caco2 medium and the NANOGENOTOX diluted BSA-water dispersion.

**Table 4. TiO<sub>2</sub> NMs: physico-chemical characterisation performed, and institutions involved.**

Physico-chemical Properties and Material Characterization (from OECD list)	NM characterised						Method	Institution(s)	Chapter
	100	101	102	103	104	105			
Homogeneity			x	x	x	x	DLS	NRCWE, INRS, CEA	4
Agglomeration / aggregation	x		x	x	x	x	DLS	CEA, NRCWE, INRS, JRC	7
			x	x	x	x	SAXS/USAXS	CEA	9
	x	x		x	x		TEM	CODA-CERVA, IMC-BAS	12
Water solubility *)	x	x	x	x	x	x	SDR	NRCWE	6.3, 6.4
Crystalline phase	x	x	x	x	x	x	XRD	IMC-BAS, JRC, NRCWE	11
Dustiness		x	x	x	x	x	Small rotating drum	NRCWE	13.1.1
	x	x	x	x	x	x	Vortex shaker method	INRS	13.1.2
Crystallite size		x	x	x	x	x	SAXS/USAXS	CEA, NRCWE	9
	x	x	x	x	x	x	XRD	JRC, NRCWE, IMC-BAS	11
Representative TEM picture(s)	x	x	x	x	x	x	TEM	CODA-CERVA IMC-BAS	12
Particle size distribution	x	x	x	x	x	x	TEM	CODA-CERVA IMC-BAS	12
	x		x	x	x	x	DLS	CEA, NRCWE, INRS, JRC	7
				x	x		AFM	CEA	12.3
Specific surface area (SSA)		x	x	x	x	x	SAXS	CEA	9
	x	x	x	x	x	x	BET	IMC-BAS, JRC	10
Zeta potential			x	x	x	x	Zeta-metry	CEA	8
Surface chemistry (where appropriate).	x	x	x	x	x	x	TGA	NRCWE	5.2
				x	x	x	DTA	IMC-BAS	5.2
	x	x	x	x	x	x	XPS	JRC	5.4
Presence of organic coating	x	x	x	x	x	x	TGA and GC-MS on SOXHLET extracted compounds	NRCWE	5.2
Photo-catalytic activity	End-point not tested								
Porosity	x	x	x	x	x	x	BET	IMC-BAS	10
Octanol-water partition coefficient, where relevant	End-point not relevant								
Loss in ignition	x	x	x	x	x	x	TGA	NRCWE	5.2
OH radical formation, acellular	x		x	x	x	x	Benzoic acid probe to form hydroxyl-benzoic acid analysed by HPLC-UV	NRCWE	
Respirable dustiness		x	x	x	x	x	Miniaturized EN 15051 rotating drum (Schneider T. and Jensen K.A. (2008))	NRCWE	13.1

Physico-chemical Properties and Material Characterization (from OECD list)	NM characterised						Method	Institution(s)	Chapter
	100	101	102	103	104	105			
Other relevant information (where available)									
Elemental analysis/impurities	x	x	x	x	x	x	Semi-quantitative ICP-OES	CODA-CERVA	5.1
Elemental analysis/impurities	x	x	x	x	x	x	Semi-quantitative EDS	IMC-BAS	5.1
24-hour solubility*	x	x	x	x	x	x	24-h incubation in different cell media at 37 °C and 5 % RH	NRCWE	6.3

\* the solubility was investigated in Gambles solution, Caco2 medium, and the NANOGENOTOX dispersion medium

The institutes participating to the characterisation of the titanium dioxides used a number of different apparatus and equipment when performing the measurements. Table 5 gives an overview of equipment and conditions.

**Table 5. Overview of apparatus used by the institutes for the testing.**

Method	
Institution	Apparatus and methodology and descriptive text
<b>AFM</b>	
CEA	Atomic Force Microscope VEECO, Dimension V, in tapping mode, with standard silicon probe tip having Al backside coating [Mikromasch NSC15, 300kHz, 40 N/m, typical probe radius 10 nm. Nanoscope software v7.0. for image analysis.
<b>BET</b>	
IMC-BAS	High-speed surface area and pore size analyser NOVA 4200e (Quantachrome)
<b>DLS and Zeta potential</b>	
CEA/LIONS	Zetasizer Nano ZS (Malvern Instruments), equipped with laser 633 nm, computer controlled by Malvern software (DTS 5.03 or higher), samples inserted in DLS cuvettes of clear disposable polymer (optical path length 1 cm) or glass cells or folded capillary zeta cells (Malvern Instruments) volume 0.75 to 1 mL, DTS1061, with gold electrodes
INRS	VASCO™ particle size analyzer (VASCO-2 Cordouan Technologies, France) with a 65 mW fiber semiconductor laser at the wave length 635 nm. Data collection and analysis is provided by the proprietary software nanoQ™ 1.2.0.4. The sample is dropped directly with a pipette (volume ≈ 2 µl) in the center of the cell. The cell bottom formed by the upper surface of the glass prism guiding the laser beam.
JRC	Zetasizer NanoZS (Malvern Instruments), equipped with laser 633 nm, computer controlled by Malvern software (DTS 6.12), samples inserted in DLS cuvettes of clear disposable polymer (optical path length 1 cm) or glass cells or folded capillary zeta cells.
NRCWE	Zetasizer NanoZS (Malvern Instruments), equipped with laser 633 nm, computer controlled by Malvern software (DTS 5.03 or higher), samples inserted in DLS cuvettes of clear disposable polymer (optical path length 1 cm) or glass cells or folded capillary zeta cells.
<b>DTA</b>	
IMC-BAS	A STA781 and DTA 675 from Stanton Redcroft was used for the differential thermal analysis (DTA). The heating rate was 10 °C /Min.
<b>EDS</b>	
IMC-BAS	Philips TEM420 at 120 kV acceleration voltage

<b>Method</b>	
Institution	Apparatus and methodology and descriptive text
<b>GC-MS</b>	
NRCWE	On-column GC-MS equipped with FactorFour™ 30 m VF-5ms capillary column with a diameter of 0.25 mm and 0.25 µm stationary phase containing 5 % phenyl poly dimethylsiloxane (Varian). The MS was run in positive mode using EI (electron ionisation).
<b>ICP-OES</b>	
CODA-CERVA	Inductively coupled plasma-optical emission spectrometry using a Varian 720-ES, Agilent Technologies
<b>SAXS and USAXS</b>	
CEA/LIONS	<p>The main set up components used for SAXS and USAXS experiments are:</p> <ul style="list-style-type: none"> <li>▪ X-ray generator : Rigaku generator RUH3000 with copper rotating anode (<math>\lambda = 1.54 \text{ \AA}</math>), 3kW</li> <li>▪ Home made optic pathways and sample holders (with two channel-cut Ge (111) crystals in Bonse/Hart geometry for USAXS set up, cf Lambard (1992).</li> <li>▪ Flux measurement for SAXS set up : pico amperemeter Keithley 615</li> <li>▪ Flux measurement for USAXS set up : DonPhysik ionisation chamber</li> <li>▪ Detector for SAXS set up : 2D image plate detector MAR300</li> <li>▪ Detector for USAXS set up: 1D high count rate CyberStar X200 associated to a scintillator/ photomultiplier detector.</li> </ul> <p>All experimental parameters are monitored by computer by a centralized control-command system based on TANGO, and interfaced by Python programming. 2D images are treated using the software <i>ImageJ</i> supplemented with specific plug-ins developed at CEA/LIONS, see O. Taché, 2006.</p>
<b>SDR</b>	
NRCWE	24-well SensorDish Reader (SDR) system from PreSens Precision Sensing GmbH, Germany
<b>Small rotating drum</b>	
NRCWE	Small (5.9 L) rotating drum system modified and optimized by NRCWE with online measurement of size-distribution using Fast Mobility Particle Sizer, Aerodynamic Particles Sizer, particle number concentration using Condensation Particle Sizer and filter sampling of either respirable or inhalable dust for calm air.
<b>Sonication</b>	
CEA	Ultrasonic probe equipped with a standard 13 mm disruptor horn: Sonics & Materials, VCX500-220V, 500 W, 20 kHz
CODA-CERVA	Vibracell™ 75041 ultrasonifier (750 W, 20 kHz, Fisher Bioblock Scientific, Aalst, Belgium). 13 mm horn (CV33)
INRS	Ultrasonic probe equipped with a 14 mm Ti disruptor horn: Heilscher UP200H (200W)
JRC	Tweeter sonicator from Hielscher, Ultrasound technology, vial tweeter UIS250v, 250 watt; 24 kHz. The tweeter sonicator does not have a horn.
NRCWE	Ultrasonic probe equipped with standard 13 mm disruptor horn: Branson Branson 400W
<b>TEM</b>	
CODA-CERVA	Tecnai™ G2 Spirit microscope (FEI, Eindhoven, The Netherlands) with biotwin lens configuration operating at 120 kV
IMC-BAS	Philips TEM420 at 120 kV acceleration voltage
<b>TGA</b>	
NRCWE	A Mettler Toledo TGA/SDTA 851e was used with oxygen atmosphere. The heating rate was 10 K/min and the temperature range was from 25 to 1000 °C. The sample holders used for the TGA measurements were made of alumina with a volume of 70 µL or 150 µL.

Method	
Institution	Apparatus and methodology and descriptive text
Vortex Shaker Method	
INRS	Vortex dustiness test system modified and optimised at INRS. CPC: Model 3785 Water-based Condensation Particle Counter (TSI, USA)
XPS	
JRC	AXIS ULTRA Spectrometer (KRATOS Analytical, UK). Monochromatic Al Ka source X-rays ( $h\nu=1486.6\text{eV}$ ) using X-ray spot size of $400\times 700\text{mm}^2$ and a take off angle (TOA) of $90^\circ$ with respect to the sample surface. Surface charging was compensated by means of a filament ( $I=1.9\text{A}$ , $3.6\text{V}$ ) inserted in a magnetic lens system and all spectra were corrected by setting the C1s hydrocarbon component to $285.00\text{eV}$
XRD	
IMC-BAS	Bruker D2 Phaser diffractometer in reflection mode with $\Theta - \Theta$ geometry. Cu X-rays were generated by a sealed Cu X-ray tube run at 30 kV and 10 mA and focused using a Ni filter and a fixed $0.2^\circ$ divergence slit. Data generated with a step size of 0.02 degree $2\Theta$ and with a step time of 10 s and collected scintillation detector with opening angle $0.2^\circ$ . Since the instrument does not use a monochromator, the raw data contains reflections from both $K\alpha_1$ and $K\alpha_2$ rays. For data comparison, the $K\alpha_2$ contribution was therefore stripped from the data using the EVA software (Bruker).
JRC	In-house constructed glancing-angle X-ray diffractometer. Variable incident angle and incident beam slit width, with laser sample alignment system. Ka radiation, with tube operating at 1kW. Germanium solid state detector for background reduction and elimination of Kb radiation. Instrumental resolution with diffracted beam Soller slit approximately $0.15^\circ - 0.2^\circ$ , depending on incident beam slit width. Additional measurements with broker D8 DISCOVER instrument both in Bragg-Brentano and glancing angle modes.
NRCWE	Bruker D8 Advanced diffractometer in reflection mode with Bragg-Brentano geometry. The analysis were made using $\text{CuK}\alpha_1$ X-rays ( $1.5406 \text{ \AA}$ ) generated using a sealed Cu X-ray tube run at 40 kV and 40 mA. The x-ray beam was filtered for $\text{CuK}\alpha_2$ and focused using a primary beam Ge monochromator and fixed divergence slit $0.2^\circ$ . The analyses were made in the stepping mode stepping 0.02 degree $2\Theta$ per second and data were collected using a linear PSD detector (Lynx-eye) with opening angle $3.3^\circ$ .

The NANOGENOTOX sample preparation protocol was developed by CEA, INRS and NRCWE and the final dispersion protocol is published on the project's web page at

<http://www.nanogenotox.eu/files/PDF/web%20nanogenotox%20dispersion%20protocol.pdf>

Briefly, the final dispersion following the protocol has a concentration of 2.56 mg/mL and sterile-filtered 0.05 % w/v BSA-ultrapure water. The samples are sonicated (probe sonicator) for 16 minutes, placed in an ice bath, at 400 W and 10 % amplitude while controlling that the sonication probe does not touch the walls of the scintillation vial. Use of different sonication conditions (power and amplitude) may require different sonication times. The energy input should be calibrated to be in the order of  $3,136 \text{ MJ/m}^3$ .

## 4. Homogeneity within and between vials. Sample preparation reproducibility among laboratories

### 4.1. Procedure and sample preparation

Samples are provided in vials. The homogeneity both within vials and between vials was assessed by DLS measurements of aqueous suspensions in the best-dispersed state after probe sonication. The DLS technique is further detailed in chapter 7 and in Appendix A. It should be noted that this type of analysis gives information on the spherical equivalent hydrodynamic aggregate size.

The main technical difference, which could lead to interlaboratory variability in the analytical results from the suspended particles may be the different sonicators used in the different laboratories as well as differences due to the different DLS equipment used. The comparison of measurements and data treatment procedures between the different DLS apparatus, i.e. Zetasizer NanoZS from Malvern Instrument for CEA and NRCWE, and Vasco Cordouan for INRS are discussed in Appendix C. Homogeneity data is available for NM-102, NM-103, NM-104 and NM-105.

Three laboratories each assessed the **homogeneity within (intra) a vial** by DLS measurements; NM-102, NM-103, NM-104 and NM-105 were evaluated. Each laboratory performed measurements of a series of independent samples from one vial particular to the laboratory. Within a laboratory, the samples were prepared by the same operator, under the same conditions and from the same vial, and thus illustrate both the homogeneity within one vial and the reproducibility of the sample preparation by a given operator.

The **homogeneity between (inter) vials** was evaluated by measuring a series of samples from different vials of a given NM, prepared by the different laboratories; NM-104 and NM-105 were evaluated. The results from the "homogeneity within a vial" were included in this analysis, thus quantifying both the variability between vials of the given NM, and between sample preparations from the different laboratories.

The main results are reported below in sections 4.2 to 4.5 for NM-102 to NM-105. When several samples from one vial were tested, mean values with standard deviations are reported. The data reported are Z-average particle diameter (Nobbmann et al., 2007) and polydispersity index (Pdl), calculated using the cumulant method both for Malvern and Vasco Cordouan apparatus. The position of the main peak of the intensity size distribution was modelled with a multimodal analysis. For the Malvern apparatus, the CONTIN method was used and the width of the main intensity peak (FWHM) is also reported. For the



measurements with the Cordouan apparatus, this peak corresponds to the position of the main mode obtained with the Padé-Laplace method (see Appendix A).

## 4.2. Homogeneity Results for NM-102

Results from one laboratory for repeated DLS measurements of NM-102 (intra-vial study) are reported in Table 6 and DLS results for NM-102 obtained from different vials are shown in Table 7. The suspensions of NM-102 contained large micron-sized aggregates, prone to sedimentation. Thus, it is no surprise that the results reported below show a wide variation in size and a high polydispersivity as well as a poor reproducibility within vials (tested on one vial).

**Table 6. DLS main size parameters (Z-average, polydispersity index, width and position of main peak in intensity distribution) obtained from independent suspensions of NM-102 prepared from the same vial under the same conditions.**

NM	Lab.	vial n°	repetition /date	Z-Average	Pdl	Intensity distribution main peak	FWHM peak width
NM-102	CEA	34	20111006	478.8	0.455	633.6	264.7
			20110719	533.3	0.486	964.5	769.3
			20110729	380.3	0.352	622.5	362.8
			20110802	377.9	0.419	587.4	417.3
<b>intra vial</b>				<b>442.6 ± 76.6</b>	<b>0.428 ± 0.058</b>	<b>702.0 ± 176.1</b>	<b>460.3 ± 232.7</b>

**Table 7. DLS main size parameters (Z-average, polydispersity index, width and position of the main peak in intensity distribution) obtained from independent suspensions of NM-102 prepared from different vials.**

NM	Lab.	vial n°	Z-Average	Pdl	Intensity distribution main peak	FWHM peak width
NM-102	CEA	34 (4)	442.6 ± 76.6	0.428 ± 0.058	702.0 ± 176.1	460.3 ± 232.7
NM-102	CEA	35	403.1	0.411	695.8	373.9
NM-102	CEA	24	400.4	0.441	654.8	493.2
NM-102	CEA	31	389.5	0.426	685.4	572.4
<b>Average over the 4 vials</b>			<b>408.9 ± 23.2</b>	<b>0.427 ± 0.012</b>	<b>684 ± 21.0</b>	<b>474.9 ± 82.2</b>

Given the difficulties related to keeping NM-102 in suspension, the variability observed is more likely due to difficulties in obtaining a suspension of NM-102 for DLS measurements than related to (lack of) homogeneity of sub-sampling. Furthermore, the intra-vial variability is actually higher than the one observed between different vials, so no conclusion can be

drawn. The TEM analysis of NM-102 (see section 12.2.4) reports similar problems of producing a stable dispersion.

### 4.3. Homogeneity Results for NM-103

Results from repeated DLS measurements of NM-103 dispersions made by two laboratories are reported in Table 8. Each laboratory used independent samples from one vial particular to the laboratory for the measurements.

**Table 8. DLS main size parameters (Z-average, polydispersity index, width and position of main peak in intensity distribution) obtained from independent suspensions of NM-103 prepared from the same vial under the same conditions.**

NM	Lab.	vial n°	repetition /date	Z-Average	Pdl	Intensity distribution main peak	FWHM peak width
NM-103	CEA	47	20100927	112.1	0.244	139.2	72.3
			20110718	115.7	0.253	137.9	69.3
			20110722	113.6	0.258	139.5	80.3
<b>intra vial</b>				<b>113.8 ± 1.8</b>	<b>0.252 ± 0.007</b>	<b>138.9 ± 0.9</b>	<b>74.0 ± 5.7</b>
NM-103	CEA	557	20110729	117.3	0.212	148	78.1
			20110915	112.6	0.255	141.4	86.5
			20110930	108	0.229	124.5	54.8
<b>intra vial</b>				<b>112.6 ± 4.7</b>	<b>0.232 ± 0.022</b>	<b>138.0 ± 12.1</b>	<b>73.1 ± 16.4</b>
NM-103	INRS	576	N1	138.7	0.244	123.1	
			N2	133.7	0.202	117.5	
			N3	124.4	0.115	117.5	
<b>intra vial</b>				<b>132.3 ± 7.3</b>	<b>0.187 ± 0.066</b>	<b>119.4 ± 3.2</b>	
<b>Average over the 3 vials</b>				<b>119.6 ± 11.0</b>	<b>0.244 ± 0.33</b>	<b>132.1 ± 11.0</b>	

The reproducibility inter vial for the 2 vials tested at CEA is of a few percent. However, a systematic variation (15 %) from one laboratory to the other is observed, which is greater than the intravial reproducibility. This variability is thought to originate from systematic differences between laboratories, especially the different types of sonicator used for dispersion, and handling including time-lapse from preparation to measurement, and not from inhomogeneities between the vials.

#### 4.4. Homogeneity Results for NM-104

Results from repeated DLS measurements of NM-104 by two laboratories are reported in Table 9 and Table 10. For the measurements, each laboratory used independent samples from one vial particular to the laboratory.

**Table 9. DLS main size parameters (Z-average, polydispersity index, width and position of main peak in intensity distribution) obtained from independent suspensions of NM-104 prepared from the same vial under the same conditions.**

NM	Lab.	vial n°	repetition /date	Z-Average	Pdl	Intensity distribution main peak	FWHM peak width
NM-104	CEA	465	20110722	130.6	0.226	169	91.0
			20110907	127.1	0.218	164.8	87.5
			20110929	129	0.216	156.7	74.7
<b>intra vial</b>				<b>128.9 ± 1.8</b>	<b>0.220 ± 0.005</b>	<b>163.5 ± 6.3</b>	<b>84.4 ± 8.6</b>
NM-104	NRCWE	1157	1	125.9	0.220	161.8	85.4
			2	125.4	0.201	159.4	81.1
			3	123.5	0.196	155.0	74.6
			4	127.9	0.220	167.2	89.4
			5	124.0	0.211	158.7	83.0
<b>intra vial</b>				<b>125.3 ± 1.7</b>	<b>0.210 ± 0.011</b>	<b>160.4 ± 4.5</b>	<b>82.7 ± 5.5</b>

**Table 10. DLS main size parameters (Z-average, polydispersity index, width and position of main peak in intensity distribution) obtained from independent suspensions of NM-104 prepared from different vials.**

NM	Lab.	vial n°	Z-Average	Pdl	Intensity distribution main peak	FWHM peak width
NM-104	CEA	39 (2)	128.3 ± 0.8	0.222 ± 0.003	169.2 ± 4.5	95.8 ± 10.9
NM-104	CEA	465 (3)	128.9 ± 1.8	0.220 ± 0.005	163.5 ± 6.3	84.4 ± 8.6
NM-104	NRCWE	1157 (5)	125.3 ± 1.7	0.210 ± 0.011	160.4 ± 4.5	82.7 ± 5.5
NM-104	NRCWE	803	124.6	0.204	160.0	80.1
NM-104	NRCWE	885	129.6	0.229	166.9	91.2
<b>Average 3 vials NRCWE</b>			<b>126.5 ± 2.7</b>	<b>0.214 ± 0.013</b>	<b>162.4 ± 3.9</b>	<b>84.7 ± 5.8</b>
<b>Average over 5 vials</b>			<b>127.3 ± 2.2</b>	<b>0.217 ± 0.010</b>	<b>162.0 ± 4.0</b>	<b>86.9 ± 6.5</b>

The intra and inter vial measurements are reproducible, within a few percent within and between laboratories, which demonstrates a very good homogeneity of NM-104.

## 4.5. Homogeneity Results for NM-105

Results from repeated DLS measurements of NM-105 dispersions prepared by two laboratories are reported in Table 11 and Table 12. Each laboratory used independent samples from one vial particular to the laboratory for the measurements.

**Table 11. DLS main size parameters (Z-average, polydispersity index, width and position of main peak in intensity distribution) obtained from independent suspensions of NM-105 prepared from the same vial under the same conditions.**

NM	Lab.	vial n°	repetition /date	Z-Average	Pdl	Intensity distribution main peak	FWHM peak width
NM-105	CEA	305	20100209	128	0.162	15.1	69.7
			20101006	120.7	0.192	152.4	74.7
			20101011	121.6	0.189	153.3	73.7
			20110705	122.7	0.143	143.1	58.4
			20110928	129.3	0.172	156.2	69.6
<b>intra vial</b>				<b>124.5 ± 3.9</b>	<b>0.172 ± 0.020</b>	<b>152.0 ± 5.2</b>	<b>69.2 ± 6.5</b>

**Table 12. DLS main size parameters (Z-average, polydispersity index, width and position of main peak in intensity distribution) obtained from independent suspensions of NM-105 prepared from the different vial number.**

NM	Lab.	vial n°	Z-Average	Pdl	Intensity distribution main peak	FWHM peak width
NM-105	CEA	305(5)	124.5 ± 3.9	0.172 ± 0.020	152.0 ± 5.2	69.2 ± 6.5
		2194(2)	130.1	0.170	158.1	72.3
NM-105	NRCWE	2758	135.6	0.134	156.5	61.8
		2749	127.9	0.145	151.4	63.9
		2701	127.8	0.143	150.7	61.9
NM-105	INRS	2194(2)	132.9 ± 1.6	0.057 ± 0.006	138.1 ± 4.5	
<b>Intra vial</b>			<b>132.3 ± 7.3</b>	<b>0.187 ± 0.066</b>	<b>119.4 ± 3.2</b>	<b>69.2 ± 6.5</b>
<b>Average over the 3 vials NRCWE</b>			<b>130.4 ± 4.5</b>	<b>0.141 ± 0.006</b>	<b>152.9 ± 3.2</b>	<b>62.5 ± 1.2</b>

The reproducibility of results from the intra-vial measurements performed at both at CEA NRCWE is very good with a deviation of only a few percent, which demonstrates a rather good homogeneity within vials with NM-105, and a good reproducibility of the sample preparation.

Regarding the inter-vial measurements, the results from the six vials by the three laboratories are comparable with a few percent; only the value of the polydispersity index is found to be much lower by INRS. Hence, the homogeneity intra-vial and inter-vial for NM-105 are both of the same order and good. Based on the data obtained by all laboratories, the polydispersity of NM-105 is the lowest of the TiO<sub>2</sub> NMs tested.

## 5. Chemical composition

### 5.1. Elemental Composition by EDS and ICP-OES

The elemental composition of any nanomaterial is an essential information for its chemical categorisation; the observed toxicity of a nanomaterial may also be linked to the presence of coatings, catalysts and impurities. The elemental composition may be analysed using a range of different techniques. Depending on the technique used, the elemental analysis will provide results that range from qualitative to fully quantitative.

The composition of the TiO<sub>2</sub> NMs was analysed using semi-quantitative energy dispersive X-ray spectroscopy (EDS or EDX) on powder tablets by IMC-BAS. Additional analyses were performed using semi-quantitative inductive coupled plasma (ICP) with optical emission spectrometry (OES) for detection and semi-quantitative determination on extracted elements. Whereas EDS is suitable for major and minor elements, ICP techniques are generally most suitable for detecting and quantification of trace elements in the ppt to ppm levels. The applied techniques are described below.

#### Energy dispersive X-ray spectroscopy

EDS is short for Energy-dispersive X-ray spectroscopy and is available as an analytical tool in some electron microscopes.

In the present analysis, elements from Na and up were analysed using semi-quantitative analyses, which is an analysis based on factory-defined calibration curves with theoretical corrections for matrix effects etc. Oxygen was calculated by difference (assumed to be the residual un-quantified part of the sample). Therefore the sum of all elements adds up to 100 wt%. Due to current quality of detectors and instrument stability, semi-quantitative analyses are relatively reliable for major and minor elements if the samples are of sufficient thickness and have low roughness.

Samples were prepared by pelletizing a known amount of powder. The results are given as wt% and mass-based parts per million (ppm) depending on the absolute concentrations in the sample.

Table 13 lists the elemental composition determined on the TiO<sub>2</sub> NMs. NM-102 and NM-105 are relatively pure with presence of less than 1000 ppm Si and 500 ppm Al. NM-100 contains from 600 ppm to 4900 ppm Fe, as well as more than 2000 ppm Si, K and P as well as Al, and a trace of Cr. NM-101 contains comparable amounts of Si, Al and P as found in NM-100, but in addition also 2500 ppm S was identified. NM-103 and NM-104 contains 3.4 and 3.2 wt% (34 000 – 32 000 ppm) Al; 6800 and 1800 ppm Si; and 2600 and 3200 ppm S

respectively. Based on the weight percent Ti, the purity was also calculated assuming the ideal stoichiometric composition TiO<sub>2</sub>.

**Table 13. Elemental concentrations by EDS measurements of the TiO<sub>2</sub> NMs performed at IMC-BAS.**

Material	Ti (wt%)	Al* (ppm)	Si (ppm)	S* (ppm)	P* (ppm)	K (ppm)	Cr (ppm)	Fe (ppm)	O calculated <sup>#</sup> (wt%)	Calculated <sup>@</sup> indicative content of TiO <sub>2</sub> (wt%)
NM-100	58.57	900	2800	-	2100	2500	300	4900	40.08	97.7
NM-101	58.79	900	2900	2200	2700				40.35	98.1
NM-102	59.73	500	800	-				700	40.07	99.6
NM-103	54.74	34 300	6800	2600				600	40.82	91.3
NM-104	55.60	32 200	1800	3200					40.68	92.7
NM-105	59.81	400	700	-					40.07	99.8

\* ppm by weight <sup>#</sup> calculated by difference

<sup>@</sup> formula used: wt% TiO<sub>2</sub> = wt% Ti x (1 + {molar weight O<sub>2</sub>/molar weight Ti})

### Inductively coupled plasma-optical emission spectrometry (ICP-OES)

All ICP-OES measurements were carried out by CODA-CERVA using a Varian 720-ES (Agilent Technologies). The analyses were performed using the SemiQuant feature, which is designed to provide a fast estimate of the concentration of non-calibrated compounds in samples. The samples were screened for 68 elements: Ag, Al, As, Au, B, Ba, Be, Bi, Ca, Cd, Ce, Co, Cr, Cu, Dy, Er, Eu, Fe, Ga, Gd, Ge, Hf, Hg, Ho, In, Ir, K, La, Li, Lu, Mg, Mn, Mo, Na, Nb, Nd, Ni, P, Pb, Pd, Pr, Pt, Rb, Re, Rh, Ru, S, Sb, Sc, Se, Si, Sm, Sn, Sr, Ta, Tb, Te, Th, Ti, Tl, Tm, U, V, W, Y, Yb, Zn and Zr.

Samples were prepared for analysis by dissolving the TiO<sub>2</sub> NMs in hydrofluoric acid. 0.1 g was weighed in a 50 mL DigiPREP HT tube (SCP SCIENCE) for each sample and 2 mL of concentrated hydrofluoric acid was added. The mixture was heated overnight at 80°C in a DigiPREP MS (SCP SCIENCE). After cooling double distilled water was added until the volume was 10 mL.

Table 14 presents the elemental concentration ranges found after screening the TiO<sub>2</sub> NMs by ICP-OES. No impurities/elements in NM-102 and NM-105 were found to be present in concentrations above 0.1 wt%. Only K was found in concentrations between 0.1 and 1 wt% in NM-100. Na, P, Ca, and Zr were found in trace amounts in the NMs, except NM-105. The most abundant impurities (> 1 wt%) were found to be Al in NM-103 and NM-104. Na and K (both 0.1–1 wt%) were the most abundant impurities in NM-102 and NM-100, respectively.

**Table 14. Overview of impurities detected in TiO<sub>2</sub> by semi-quantitative ICP-OES.**

Material	Vial no.	Impurities > 0.01%	Impurities 0.005 – 0.01%	Impurities 0.001 – 0.005%
NM-100	0047	K (>0.1%),P	Zr	Ca, Na
NM-101	1252	Al , Na (>0.1%), P, S, Zr	-	K, Ca
	1265	Al , Na (>0.1%), P, S,	K, Zr	Ca
NM-102	0054 & 0060	S	Ca, Zr	K, Na, P, W
NM-103	0584 & 0585	Al (>0.1%),Na, S,	Ca	Fe, K, Mg, Zr
NM-104	0502 & 0505	Al (>0.1%), Ca, Na, S	-	K, Mg, Zr
NM-105	2209 & 2217	-	-	Na

The TiO<sub>2</sub> NMs contained trace to minor amounts (0.01 to 0.1 wt% in NM-101) of Na according to ICP-OES results. Na was not detected in the EDS analyses of TiO<sub>2</sub>. Zr (from 10-50 ppm to > 0.1 wt%) was found in all TiO<sub>2</sub> NMs except NM-105 by ICP-OES, but not identified by EDS. The EDS analysis found Fe in NM-100 (0.5 wt%), NM-102 (700 ppm) and NM-103 (600 ppm), but only detected in trace amounts in NM-103 (10-50 ppm) by ICP-OES. Both EDS and ICP-OES identified Al and S among the most abundant impurities in NM-101, NM-103 and NM-104, but the relatively abundant Si impurity found by EDS was not reported in the ICP-OES analysis for these NMs; Si was not detected in TiO<sub>2</sub> by ICP-OES.

EDS and ICP-OES were used to perform a semi-quantitative screening of contaminant elements in NM-10x. Several impurities were found in the TiO<sub>2</sub> NMs, but between the two analytical techniques there was not always a good agreement of the elements reported and their concentrations. This may in part, but not always, be explained by the much lower detection limit of ICP-OES and interference between specific energies in the EDS spectra obtained, which are not easily resolved in semi-quantitative analysis. Overall from the elemental analyses, it must be concluded that further work remains to be done in development of elemental analysis of TiO<sub>2</sub> NMs. For ICP analyses, extraction procedures should be further evaluated. Additionally, analytical methods such as XRF and INAA should be considered to avoid the challenges in digestion of complex materials with great variation in elemental concentrations.

## **5.2. Presence of associated organic matter by TGA and DTA**

Identification of potential presence of organic coating was assessed by sample mass-loss during heating using thermogravimetric analysis (TGA) at NRCWE and differential thermal analysis (DTA) at IMC-BAS. Nanomaterials with more than 1 wt% mass-losses above the dehydration temperatures were subject to extraction thermally or with organic solvents and analyses by gas chromatography and mass spectrometry (GC-MS).

In a TGA measurement, a sample is heated in a gas (usually air, O<sub>2</sub> or N<sub>2</sub>) and the weight of the sample is measured as a function of the temperature. The decomposition temperature and loss of mass may give information about the sample, e.g. water adsorbed to the surface of particles will evaporate around 100 °C, whereas most other added organic matter will evaporate or combust at higher temperature.

In DTA, the reference and the sample undergo identical thermal cycles; they are either heated or cooled with the same rate. The temperature is measured both for the sample and reference, and the difference is calculated. Most transformations such as phase transitions, melting, crystallisation, decomposition etc. are either endothermic or exothermic; that is they either require or release energy. Thus, when such a transformation takes place, the temperature of the material will deviate from a reference, which is what is seen by DTA. Figure 1 to Figure 9 show the results from thermogravimetric analyses of the TiO<sub>2</sub> NMs. Table 15 summarises the results of the evaluation of presence/absence of coating and estimated amount. TGA measurements of the TiO<sub>2</sub> NMs were performed once only.

**Table 15. Estimation of presence/absence of coating and estimated quantity based on TGA data.**

Material	Coating	Weight of coating (wt%)
NM-100	N	-
NM-101	Y	8
NM-102	N	-
NM-103	Y	2
NM-104	Y	2
NM-105	N	-

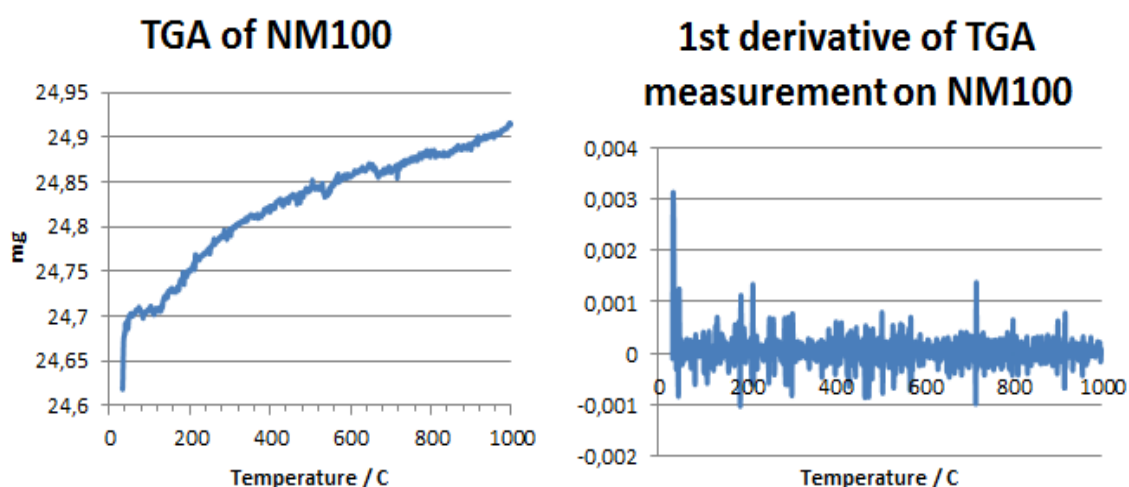


**Figure 1. Results from TGA measurement of NM-100. The change in weight is due to buoyancy.**



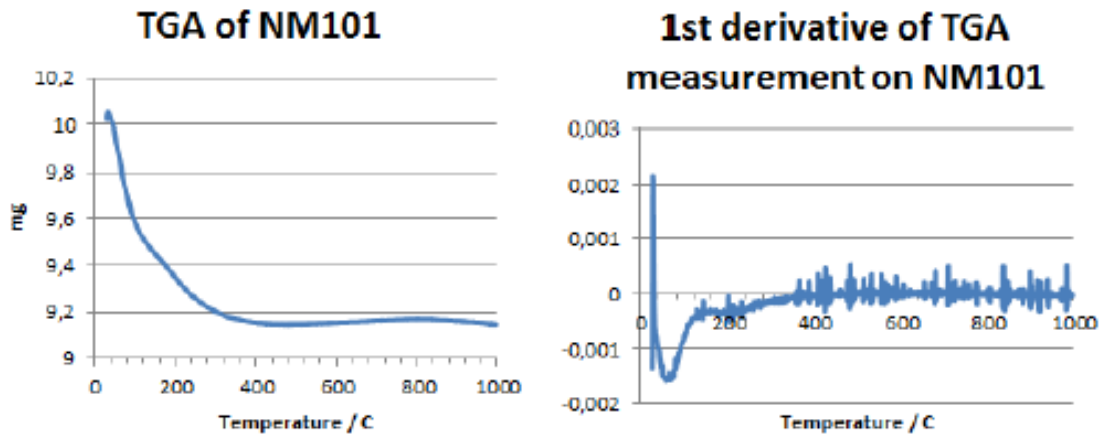


Figure 2. Results from TGA measurements of NM-101. There are two weight losses. The first and largest is below 100 °C, most likely water. The second is around 200 °C and is most likely coating.

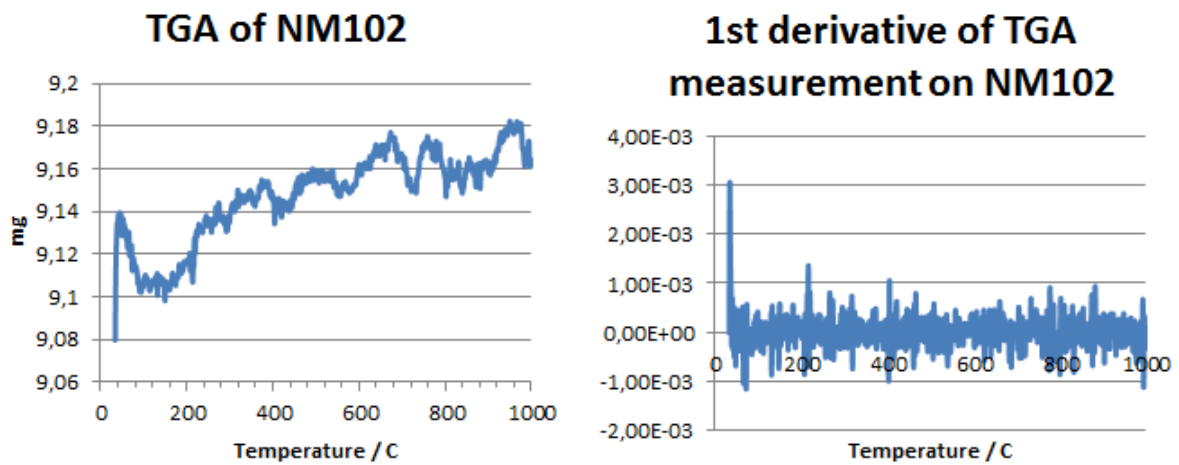


Figure 3. Results from TGA measurement of NM-102. The change in weight is due to buoyancy. Due to problems with the instrument the signal obtained is very noisy.

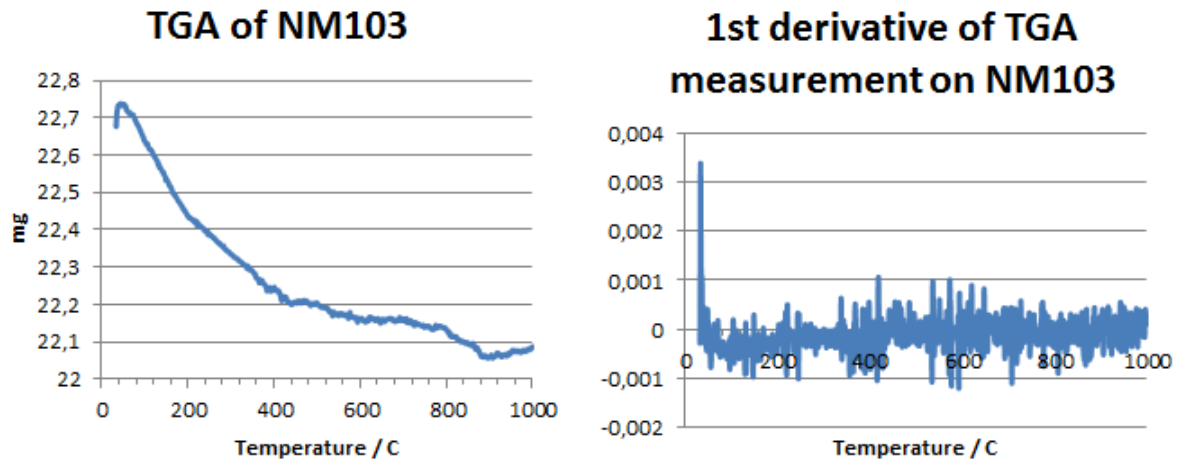


Figure 4. Results from TGA measurement of NM-103. There is a small but gradual weight loss, which may be due to evaporation/combustion in several steps. There appears to be a change in the slope around 200 °C, but the significant noise in the signal means that the interpretation is uncertain. However, the weight loss is above 100 °C and is most likely due to a coating.

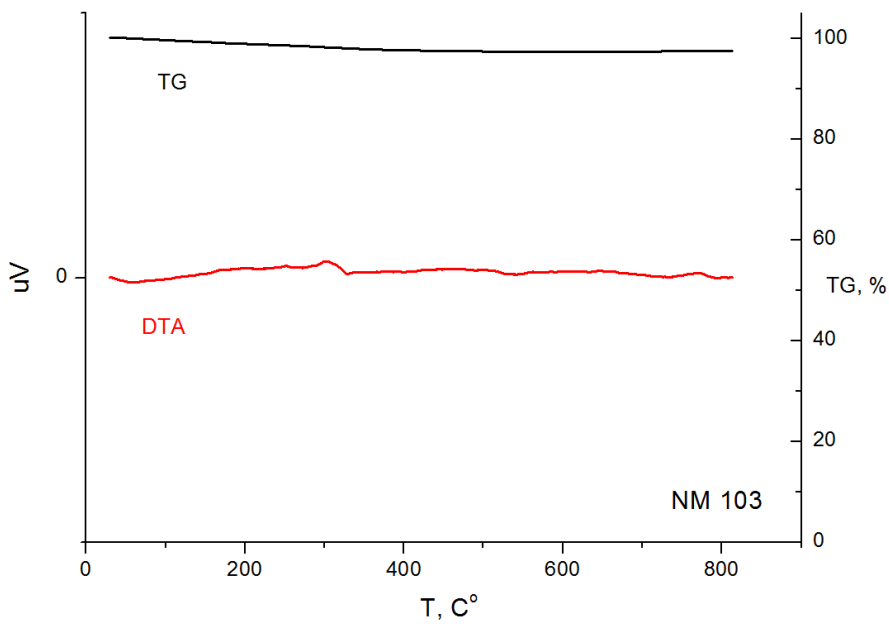


Figure 5. DTA/TG results for NM-103. There are no indications of any significant phase transformation.

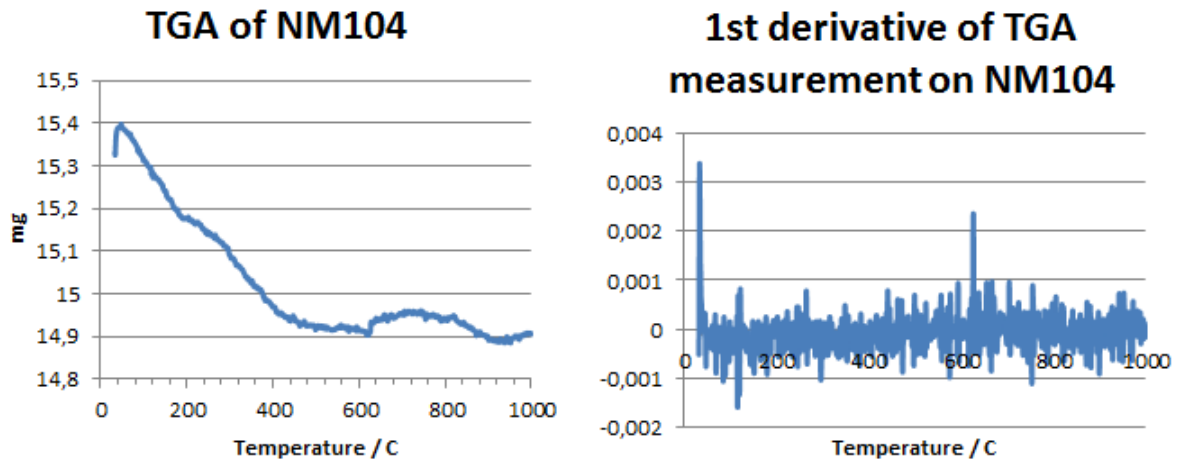


Figure 6. Results from TGA measurement of NM-104. There is a small gradual weight loss that most likely occurs in two steps, as there appears to be a change in the slope around 200 °C. The second weight loss is above 100 °C and is most likely due to a coating.

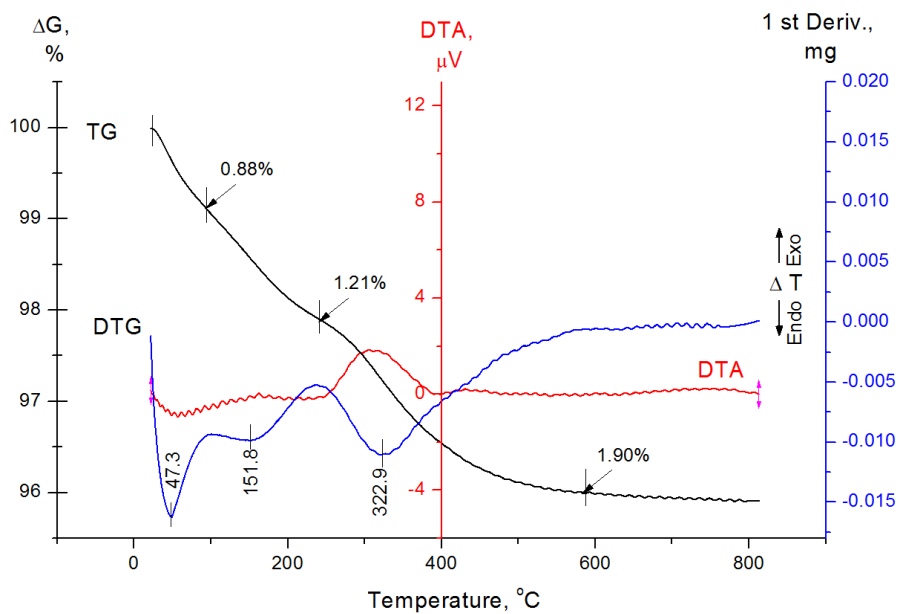


Figure 7. DTA/TG results for NM-104. For the final weight loss around 320 °C a peak is seen at the DTA curve (red curve) indicating a phase transformation.

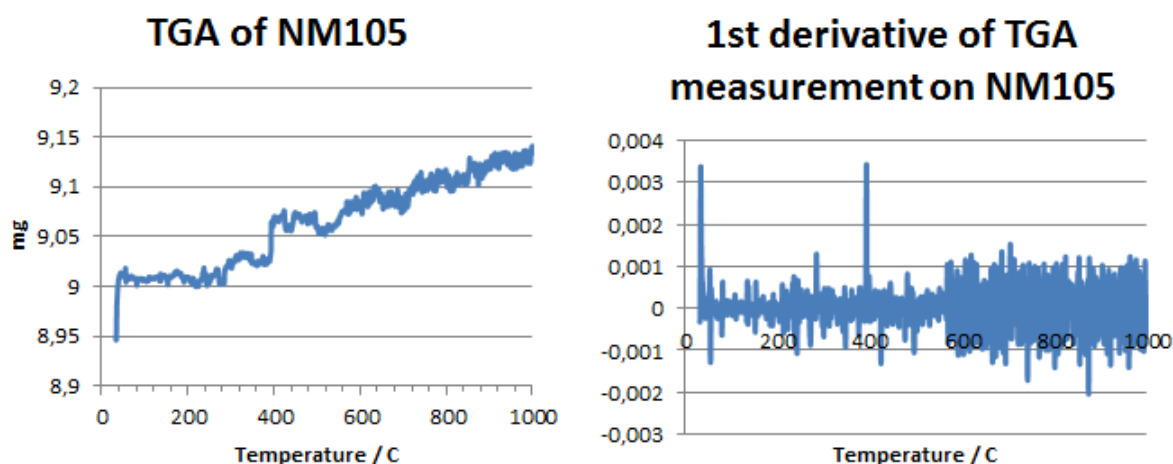


Figure 8. Results from TGA measurement of NM-105. The change in weight is due to buoyancy.

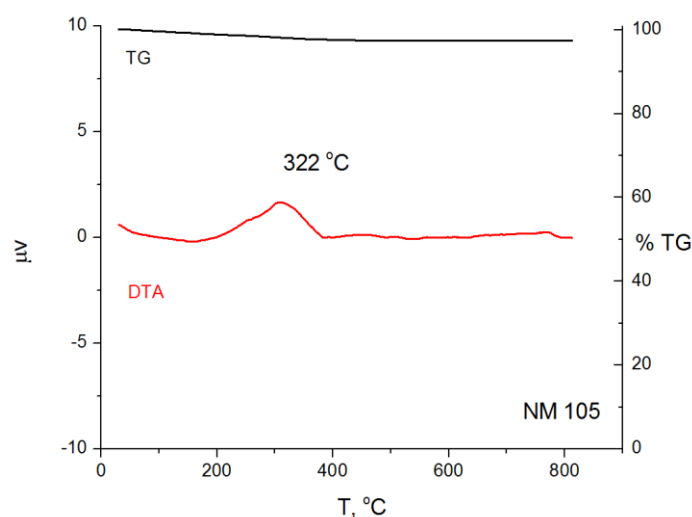


Figure 9. DTA/TG results for NM-105. A phase transformation is seen at the 322 °C.

### 5.2.1. Analysis of associated organic matter

Analysis of the chemical composition of the organic matter coating or associated with the TiO<sub>2</sub> NMs was made at NRCWE. Samples that above 110°C had a weight-loss of 1 wt% or more were analysed, and these were NM-101, NM-103 and NM-104. In the general analysis, organic compounds were either extracted using ASE (Accelerated Solvent Extraction) or desorbed by TD (Thermal Desorption). The solvent extraction can be used for several chromatographic and mass spectrometric techniques and enable quantitative determination, but it has been found that TD combined with gas chromatography – mass spectrometry (GC-MS) generally is suitable for screening of the samples for up to medium molecular weights of the organic coatings.

For the TiO<sub>2</sub> samples, approximately 300 mg of each NM was extracted in methanol using ASE and analysed using on-column GC-MS. The extract was injected directly (1 µl) into the on-column-GC-MS (Perkin Elmer Turbomass) which was equipped with a FactorFour™ 30 m VF-5ms capillary column with a diameter of 0.25 mm and 0.25 µm stationary phase containing 5 % phenyl poly dimethylsiloxane (Varian). The column flow was 1 mL/min helium and the injector temperature at 50 °C was held for 2 min and then heated to 250 °C at a rate of 50°C/min. The GC oven program was 50 °C for 4 min increased by 4 °/min to 120 °C and 8 °/min to 250° and held for 10 min. The transfer-line temperature was 275 °C. The MS was run in positive mode using EI (electron ionisation). Scanning mass range was from 50 to 500 m/z. Identification of the organic compounds was performed by AMDIS version 2.65 June 26, 2008 and NIST/EPA/NIH Mass Spectral Library Version 2.0f, 23 June 25, 2008 (NIST, USA). Compounds for which authentic standards were used and matched both retention time and spectrum were considered as clearly identified. The following GC-MS properties of the authentic standards were used for identification: Retention time (t<sub>R</sub>), mass spectrum (MS spectrum), fragmentation pattern and peak shape.

### 5.2.2. Results

The identification of coating was expected for both NM-103 and NM-104, which are expected to have 2% of dimethicone as an external organic coating. Such coating was, however, not expected for NM-101 despite the reported of weight-loss 9% wt for NM-101 upon calcination.

The results from the GC-MS analysis at NRCWE are listed in Table 16 and as seen, ten organic compounds were identified: dimethoxydimethylsilane, silane, glycerol, tetramethyl silicate; hexadecanoic acid methyl ester; hexadecanoic acid and octadecanoic acid.

The content of tetramethyl silicate in the extracts was surprising due to its relative high chemical reactivity (hydrolysis). However, indirect proof of the presence in the extracts was the observation that the peaks of tetramethyl silicate disappeared few days after extraction. This was also the case for the authentic tetramethyl silicate standards. Water vapour from the laboratory air will undoubtedly be taken up by the extracts and standard solutions and degrade tetramethyl silicate by hydrolysis. Tetramethyl silicate may have been produced during the extraction process, which uses relatively harsh extraction conditions (150 °C and 140 bar) and methanol, either directly through reaction between Si and methanol or from tetraalkoxy silanes with other chain lengths in the samples, which in excess alcohol and basic conditions, may produce tetramethyl silicate. It was not possible to confirm or reject these hypotheses at this point in time.

**Table 16. NM-101, NM-103 and NM-104. Results of the GC-MS measurements performed at NRCWE.**

Organic Compounds in the order of retention time On-Column-GC-MS	Retention time (min)	Relative amount in NM-101*	Relative amount in NM-103*	Relative amount in NM-104*
Dimethoxydimethylsilane	2.4		xxx	
Silane?	3.3		x	
Tetramethyl silicate?	4.9			xxx
Silane?	7		xx	
Glycerol	13			xx
Silane?	31.6	x		x
Silane?	32.9	x		x
Hexadecanoic acid methyl ester	33.4	xx		xx
Hexadecanoic acid	33.9	x		x
Octadecanoic acid	35.8	xx		xx

\*x= minor; xxx=major

### 5.3. Surface composition by XPS

#### 5.3.1. Measurements

JRC performed XPS analysis of the surface composition. In these measurements TiO<sub>2</sub> NMs were compressed into pellets and mounted on the sample holder with double-sided Ultra High Vacuum (UHV) compatible Cu tape.

XPS measurements were performed with an AXIS ULTRA Spectrometer (KRATOS Analytical, UK). Instrument calibration was performed using a clean pure Au/Cu sample and pure Ag sample (99.99 %). Measured values for electron binding energies (BE) were 84.00 ± 0.02 eV, and 932.00 ± 0.05 eV.

The samples were irradiated with monochromatic AlK $\alpha$  X-rays ( $h\nu=1486.6$  eV) using X-ray spot size of 400x700  $\mu\text{m}^2$  and a take-off angle (TOA) of 90 ° with respect to the sample surface. The base pressure of the instrument was better than 1x10<sup>-8</sup> Torr and the operating pressure better than 3x10<sup>-8</sup> Torr. A filament (I=1.9 A) was used to compensate for surface charging and all spectra were corrected by setting hydrocarbon 285.00 eV.

For each TiO<sub>2</sub> NM, a survey spectrum (0-1110 eV), from which the surface chemical compositions (at%) were determined, was recorded at pass energy of 160 eV. In addition one set of high-resolution spectra (PE=20 eV) was also recorded on each sample.

Selected samples were also etched using an Ar<sup>+</sup> gun (3 keV, I<sub>s</sub>= 1.3  $\mu\text{A}$ ) and then analysed using a 100  $\mu\text{m}$  spot size.

The data were processed using the Vision2 software (Kratos, UK) and CasaXPS v16R1 (Casa Software, UK). Sample compositions were obtained from the survey spectra after linear background subtraction and using the RSF (Relative Sensitivity Factors) included in the software derived from Scofield cross-sections. This method is estimated to give an accuracy of 10 % in the measurement of elemental compositions. Curve fitting of C1s peaks was carried out using the same initial parameters and inter-peak constraints to reduce scattering. The C1s envelope was fitted with Gaussian-Lorentzian function (G/L=30) and variable full width half maximum.

ToF-SIMS analyses were performed with a ToF-SIMS spectra were acquired with a reflector-type TOFSIMS IV spectrometer (ION-TOF GmbH, Münster, Germany) using 25 KeV Bi primary ions. Spectra were acquired in static mode (Bi<sup>+</sup> primary ion fluence < 10<sup>12</sup> ions·cm<sup>-2</sup>) in order to preserve the molecular information. Spectra interpretation was carried out using IonSpec software V6 (ION-TOF).

### 5.3.2. Results

In Table 17 the surface compositions of the different TiO<sub>2</sub> NMs are reported. In Figure 10 (a to e) examples of survey spectra of different samples are reported.

**Table 17. Surface composition of the NMs obtained from the survey spectra.**

<b>Material</b>	<b>C (at%)</b>	<b>O</b>	<b>Ti</b>	<b>Al</b>	<b>K</b>	<b>Other (Fe, Ca)</b>
<b>NM-100</b>	27.7(0.7)*	53.8(0.7)	17.3(0.5)		1.2 (0.3)	--
<b>NM-101</b>	23.4(0.5)	55.9(0.7)	20.5(0.1)	--	--	1.2(0.3)
<b>NM-102</b>	30.7(2.4)	50.7(1.5)	18.6(0.9)	--	--	
<b>NM-103</b>	25.9(1.4)	56.0(1.2)	10.7(0.4)	4.9(0.4)		2.5(1.0)
<b>NM-104</b>	16.3(0.3)	63.5(0.8)	13.1(0.3)	7.1(1.0)	--	--
<b>NM-105</b>	24.5(0.6)	54.0(0.3)	21.5(0.4)	--	--	--

\* standard deviation in brackets

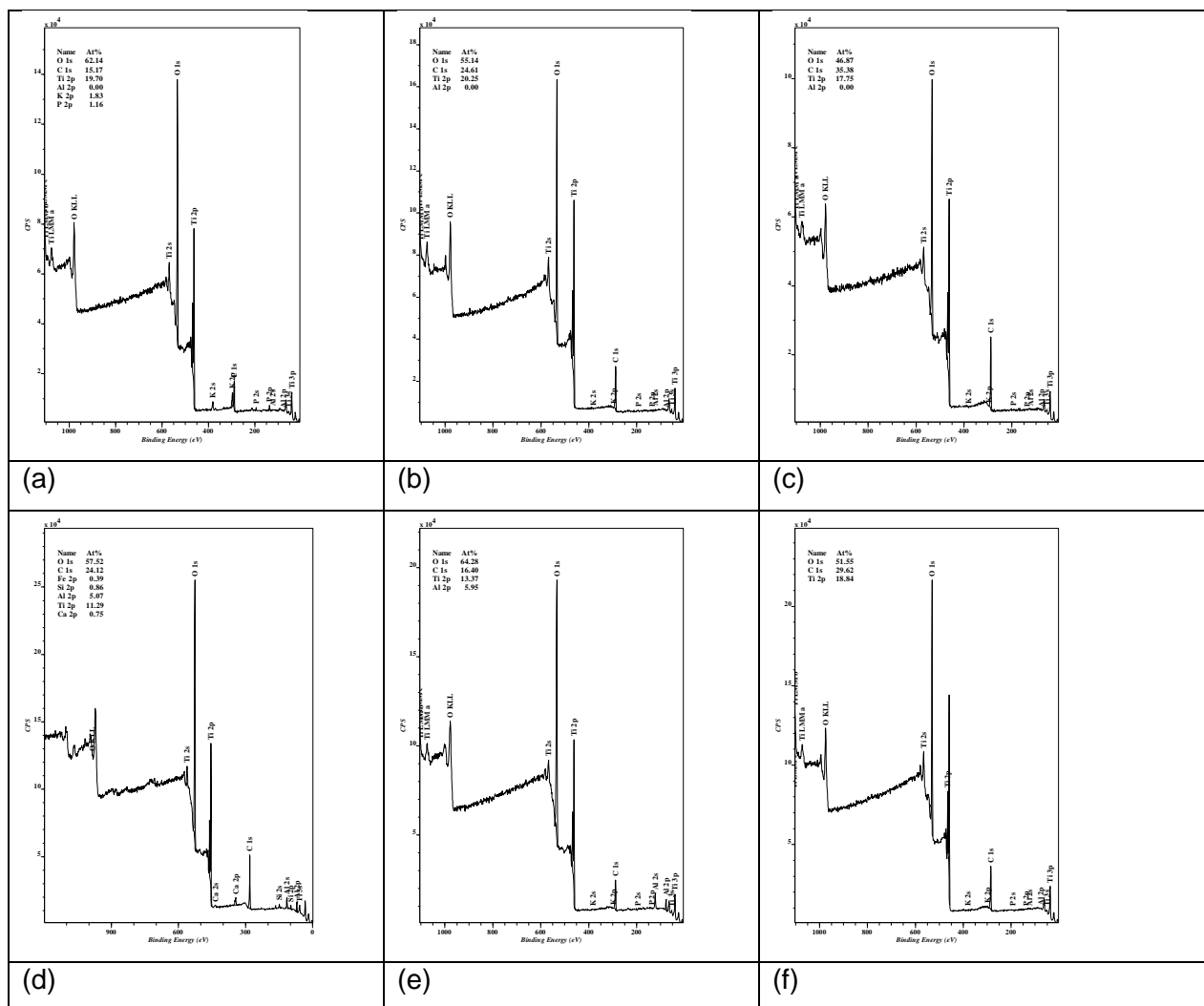


**Figure 10. Survey spectra of: (a) NM-100, (b) NM-101, (c) NM-102, (d) NM-103, (e) NM-104 and (f) NM-105.**

Besides the Ti, O and C, other elements were detected on the TiO<sub>2</sub> NM surfaces. In particular, NM-100 and NM-101 showed the presence of K and Ca, whilst on NM-103 and NM-104, a quite high Al content was detected. NM-105 resulted to be the most pure with the only surface contaminant detected being hydrocarbon.

The Ti2p core level spectra of the TiO<sub>2</sub> NMs are presented in Figure 11. The spectra can be fitted with two peaks representing the spin orbit splitting 2p<sub>3/2</sub> at about 458.7 eV and 2p<sub>1/2</sub> at ~464.3 eV, respectively. The positions of these peaks correspond to Ti<sup>4+</sup> oxidation state (i.e. Ti atom bonded to two oxygen atoms) and are well in agreement with published data (Chen et al. 2006, Yang et al 2006). Since no other components (doublets) are observed, it can be concluded that no Titanium suboxides are present on the TiO<sub>2</sub> NM surfaces.



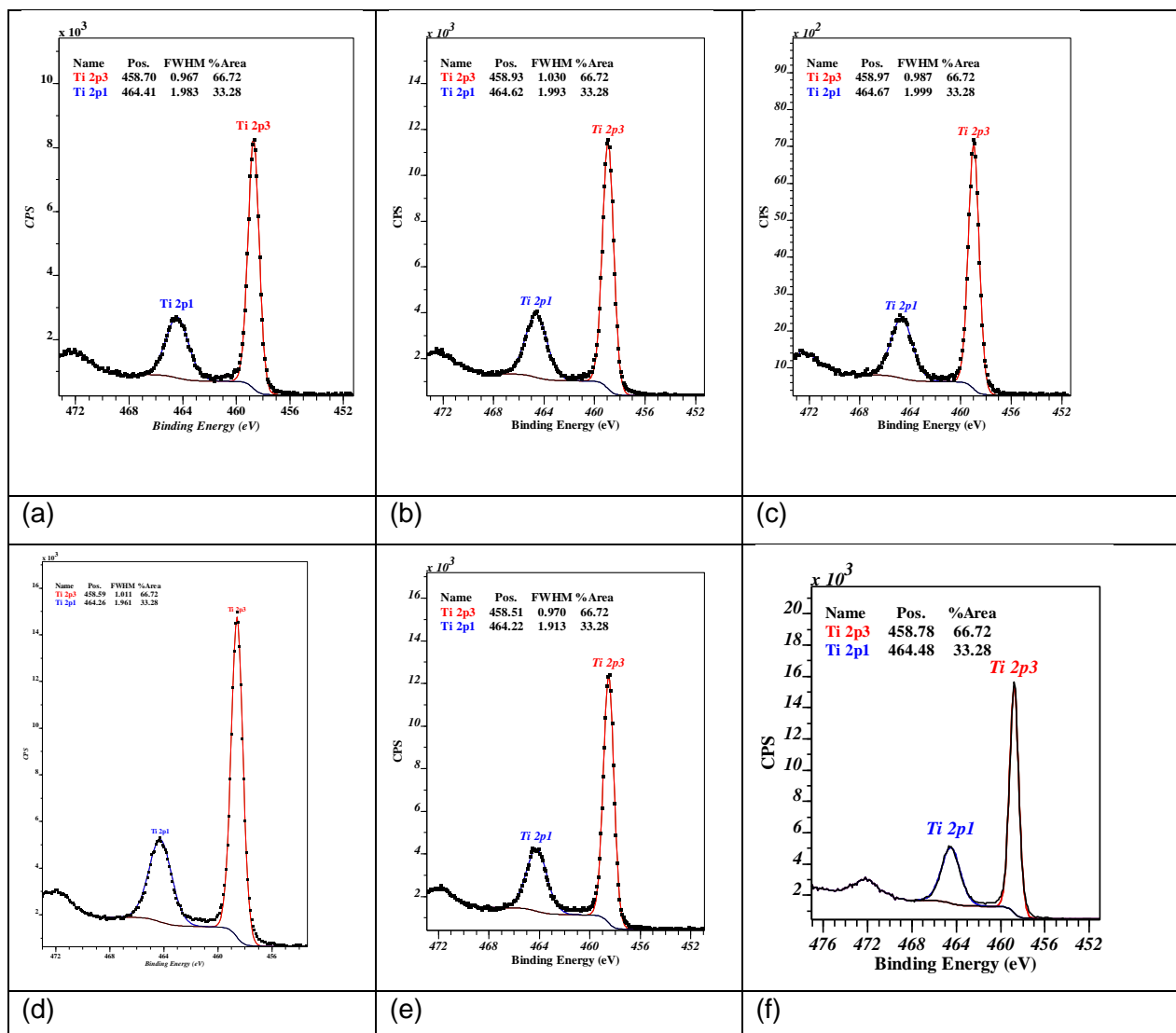


**Figure 11. Ti2p core level spectra of different TiO<sub>2</sub> powders: (a) NM-100, (b) NM-101, (c) NM-102, (d) NM-103, (e) NM-104 and (f) NM-105.**

ToF-SIMS data support the XPS results as illustrated in Figure 12, where a portion of Positive spectra of different TiO<sub>2</sub> NMs are reported. As can be seen, beside the expected Ti peak at 47.95 m/z, NM-100 presents the peak at 38.97 m/z related to potassium, whilst NM-104 presents peaks at 26.98 m/z and 27.99 m/z attributable to Al<sup>+</sup> and AlH<sup>+</sup> ions, respectively.

The presence of Al at the surface of NM-103 and NM-104 is explained by the surface finishing of these nanoparticles that show a hydrophilic and hydrophobic surface, respectively. Both nanoparticles are coated with a layer of Al<sub>2</sub>O<sub>3</sub>, but in the case of NM-103 a polysiloxane polymer layer is also included and this explains the presence of Si (Table 17).

On the other hand the potassium observed in NM-100 is probably due to contamination such as the Ca, Si, and Fe observed in NM-101 and NM-103.

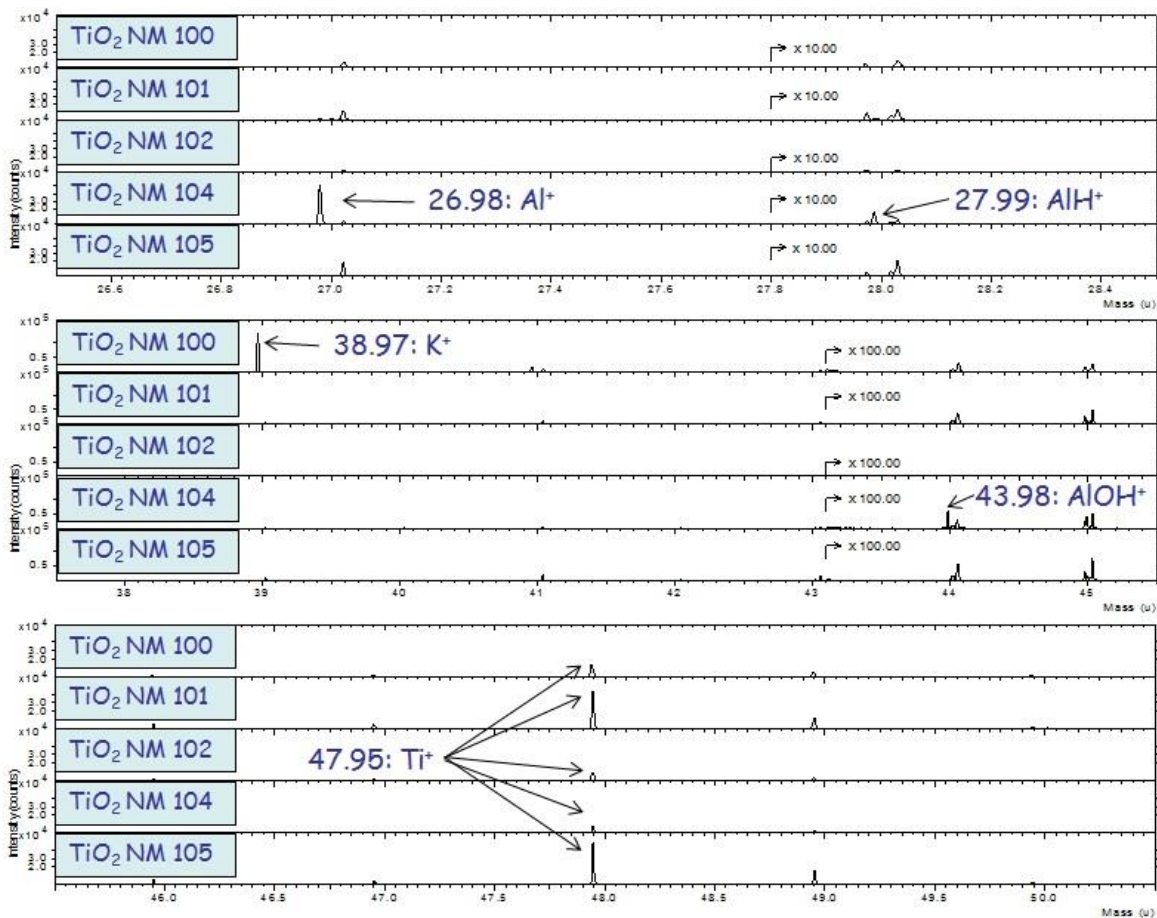


Figure 12. Positive ToF-SIMS spectra of the TiO<sub>2</sub> NM powders.

In order to better understand the presence of the contaminants, an etching with Ar<sup>+</sup> ions (3 keV) gun was also carried out. In Table 18, the surface compositions after 2 min etching are reported.

Table 18. Surface compositions obtained from the survey spectra after Ar ion etching for 2 min at 3 keV.

Material	C (at%)	O	Ti	Al	K	Other (Fe, Ca)
NM-100	4.73	67.42	25.96		1.9	--
NM-101	12.69	62	25.28			--
NM-102	34.71	47.12	18.27			--
NM-103	7.1	66.6	20.6	4.0		1.5
NM-104	7.32	19.63	19.63	9.22		--
NM-105	11.93	62.98	25.1			--

As can be seen, the carbon content is decreasing strongly in all TiO<sub>2</sub> NMs except NM-102. Correspondingly there is an increase of Ti and O content. Moreover, in the case of NM-104 there is an increase of the Al content, whilst a slightly decrease is observed for NM-103. Furthermore, after etching, Si is not observed on the surface of NM-103; the other contaminants (Ca, Fe) are also reduced. These results indicate the Al is present on the NM-103 and NM-104 nanoparticles, most likely as Al<sub>y</sub>O<sub>x</sub>; this conclusion is also supported by the Al2p high resolution peak at about 74.9 eV (data not shown) and also by the component at high binding energy present in the O1s core level spectra Figure 13.

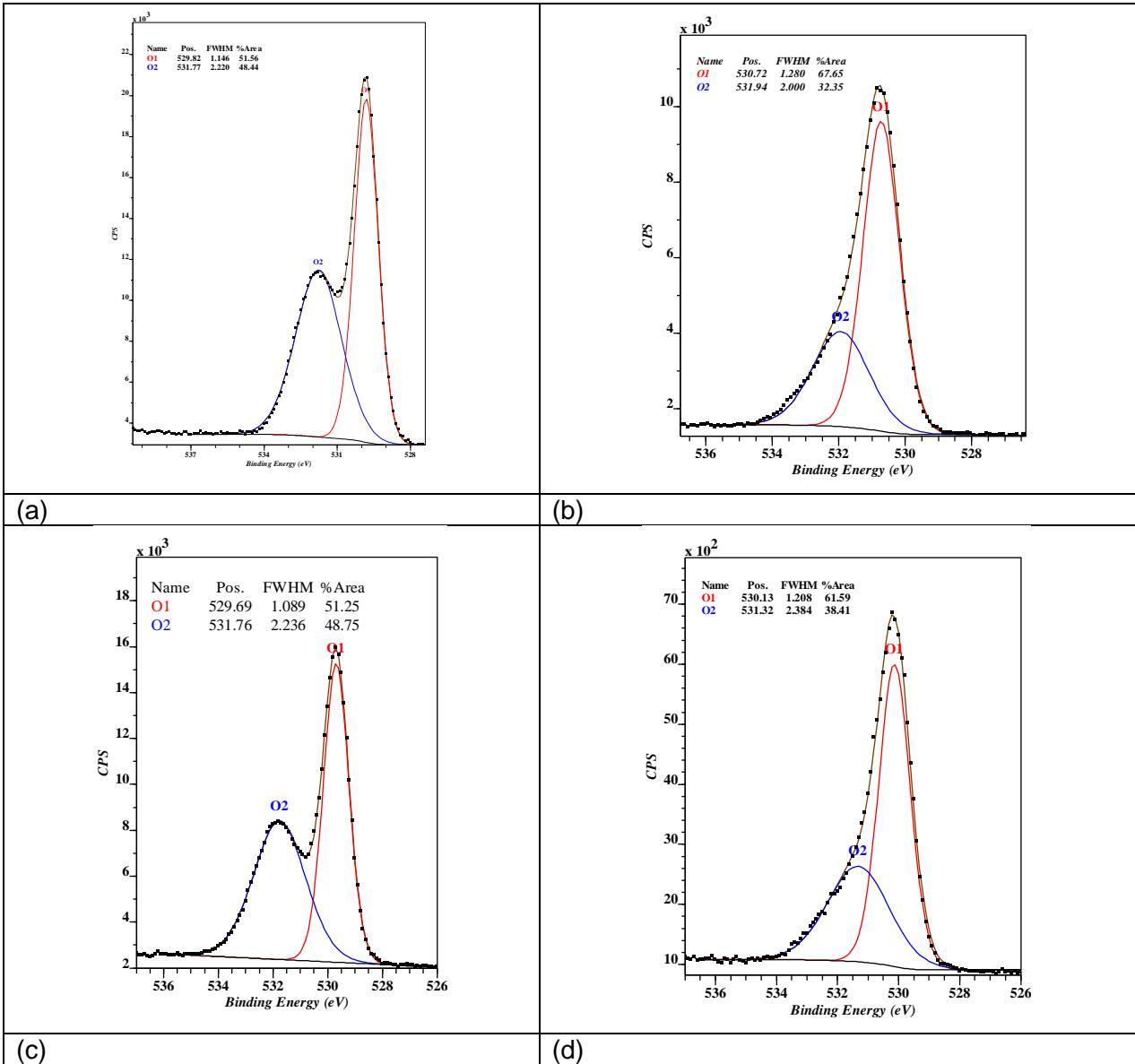


Figure 13. O1s core level spectrum of NM-103 and NM-104: (a) NM-103 as received and (b) after 2 min Ar etching at 3 keV; (c) NM-104 as received and (d) NM-104 after 2 min etching. The O<sub>2</sub> component can be attributed to the Al<sub>y</sub>O<sub>x</sub> coating present on the nanoparticles surfaces.

NM-102 is the only one for which the Ar ion etching show almost no effect after 2 min, and thus further etching was carried out for other 8 min (total time etching 10 min). However, for NM-102 this did not result in a reduction of the Carbon content. On the contrary, a slight decrease in Oxygen content was observed. This result indicates that NM-102 could be porous and able to entrap carbon. This is also supported by the fact that etching for long time resulted in the appearance of a second doublet at lower binding energy (Ti2p<sub>3/2</sub> ~ 456.5 eV) in the Ti2p core level spectrum resulting from the TiO<sub>2</sub> reduction upon ion bombardment.

For NM-104, further ion etching produces a reduction in the Al content to about 5 at%. Furthermore, also in this case, the Ar ion etching resulted in the formation of TiO<sub>x</sub> (x<2) suboxides species. The reduction of transition metal oxides upon ion etching is well documented in literature and the present results show that high caution should be taken in using this procedure to remove hydrocarbon and contaminants from inorganic nanoparticles.

#### 5.4. Observations and conclusions for chemical composition

As expected all the analytical methods applied indicate that the TiO<sub>2</sub> NMs mainly consist of the elements Ti and O, and impurities are only a minor part. Depending on the analytical technique used and the TiO<sub>2</sub> NMs analysed, several additional elements and compounds were identified, see Table 19 that reports only the impurities. The ICP-OES analysis identified a number of impurities below 0.01 % for the TiO<sub>2</sub> NMs and these are reported in Table 14. Also the results from the biodurability study (chapter 6.4) are reported as Al was detected in the TiO<sub>2</sub> NMs. Furthermore, the TGA analysis indicated that NM-103 and NM-104 had an organic coating above 1 wt% (see chapter 5.2).

**Table 19. Elements (impurities) detected in the TiO<sub>2</sub> NMs according to analytical method.**

Material	EDS*	ICP-OES* (above 0.01 %)	XPS (surface analysis technique)	XRD <sup>§</sup>	Biodurability information <sup>&amp;</sup>
NM-100	Al, Si, P, K, Fe, Cr	K, P	C, K	No crystalline impurities detected	Al
NM-101	Al, Si, P, S, K, Fe, Cr	Al, Na, P, S, Zr	C	No crystalline impurities detected	Al
NM-102	Al, Si, Fe	S	C	No crystalline impurities detected	-
NM-103	Al, Si, S, Fe,	Al, S, Na	C, Al	No crystalline impurities detected	Al, Fe
NM-104	Al, Si, S	Al, Ca, Na, S	C, Al	No crystalline impurities detected	Al
NM-105	Al, Si	-	C	No crystalline impurities detected	-

\* Semi-quantitative

<sup>&</sup> Determined by ICP-MS

<sup>§</sup> The XRD analysis was performed by three laboratories.

As seen from Table 19, the different techniques applied for analysis of the materials composition indicate that different impurities are present in the TiO<sub>2</sub> NMs. The results of these analyses agree to a certain degree (between laboratories and between methods), however the different methods applied have different detection limits, resolution and detection abilities. Thus, the exact nature and amount of the impurities is not fully understood. Thus, the precise composition of the different TiO<sub>2</sub> NMs, impurities and surface chemistry still deserve further investigation. More detailed quantitative bulk elemental, organic and surface chemical analyses are required for full assessment of the chemical composition.

## 6. Hydrochemical reactivity, solubility and biodurability

The 24-hour hydrochemical reactivity, solubility and inferred biodurability of the TiO<sub>2</sub> NMs were investigated by NRCWE. The tests were completed in the NANOGENOTOX batch dispersion medium (sterile filtered 0.05 % w/v BSA water with 0.5% v/v ethanol prewetting) and two synthetic biological media relevant for assessing the NM behaviour in the lung-lining fluid (low-Ca Gambles solution) and intestinal system (Caco2 cell medium).

Data on the hydrochemical reactivity of NMs and their biodurability may be important to better understand the biochemical reactivity of nanoparticles and dissolution in contact with specific biofluids. When particles come in contact with biofluids, reactions may take place that cause e.g. changes in pH, adsorption of ions or biomolecules, dissolution, and electron loss or gain, which can result in formation of reactive oxygen species (ROS). ROS are often considered as being one of the most important parameters of hydrochemical reactivity (e.g. Dick et al., 2003; Xia et al., 2006).

Biodurability is another classical test, originally established to analyse the degradation (dissolution) rate of asbestos, minerals and man-made fibres in synthetic lung-fluids (e.g. Forster and Tiesler, 1993; Christensen et al., 1994; Sebastian et al., 2002). Recently, the development of biodurability testing has gained new interest (Wiecinski et al., 2009; Xinyuan et al., 2010; Osmond-McLeod et al., 2011; Cho et al., 2011). Quantification of biodurability is usually done by weighing residual particles on a filter sample and/or measurement of specific constituent elements. However, representative retrieval of NMs from a small volume may pose some difficulty.

In this analysis, we performed a batch dissolution test of the hydrochemical reactivity and solubility under external environmental control mimicking *in vitro* toxicological test conditions. For the experiments, we used a commercial 24-well pH and O<sub>2</sub> SensorDish Reader (SDR) system (PreSens GmbH; Germany). Dispersions were prepared as described in the generic NANOGENOTOX dispersion protocol to mimic the treatment used for toxicological studies.

The SDR system enables simultaneous measurement in 24 wells at one second resolution and therefore, it has the ability to establish a variety of data as function of dose and time. The test conditions using the SDR system are maintained by a cell-incubator and consequently directly corresponds to the conditions of a given *in vitro* exposure event (here 37 °C and 5 % CO<sub>2</sub> for lung conditions), but the measurable pH-range is limited to pH 5 to 9. The range in O<sub>2</sub> concentrations varies from 0 to 250 % O<sub>2</sub> saturation (0 to 707.6 µmol/l). Due to the principle link between electron activity and oxygen fugacity (e.g. Nordstöm and Munoz,

1994), the variation in  $O_2$  may correspond to values obtained by direct redox potential measurement.

As a final output from the SDR studies, the measured amount of soluble NM (concentrations of dissolved elements) after the 24-hour incubation in each of the three incubation media is reported. For this, liquid samples were carefully extracted, filtered and centrifuged to remove dispersed NM in the liquid sample. Quantification of the elemental concentrations in the solute was done by ICP-OES (Si) and ICP-MS (Al, Ti, and Fe) without further acid treatment other than stabilisation. The NMs were analysed for Si, Al, Ti, and Fe as these elements were identified in some of the  $TiO_2$  NMs analysed. The concentrations of dissolved elements give indication on the durable fraction (total – the dissolved amount) in the three media. However, the values are still indicative as high-precision analysis was not performed on the starting materials.

## **6.1. Results, Hydrochemical pH reactivity**

As explained in Appendix B, four concentrations and six dose response measurements are made in one test round.

Figure 14 to 19 show the temporal pH evolution for each tested NM incubation, considering the highest dose experiments compared to the reference (zero-dose). The results show that most of the NMs have negligible to minor influence on the pH-evolution in the three test media, and a pH reaction, if any, normally occurs within the first few hours. It is especially noteworthy that pH-evolution paths are mostly controlled by the test media.

The pH in the the NANOGENOTOX batch dispersion medium typically increases from near or below pH 5 (lower detection limit of the SDR) to between pH 5 and 6 within the first hour. Addition of nanomaterial to BSA-water appears generally to cause a small increase of pH compared to the reference medium.

The Gambles solution medium has slightly basic pH values, typically starting between pH 8 and 9. In a few cases, the pH even exceeds the pH 9 upper detection limit of the SDR (e.g. Figure 14 centre). This demonstrates clearly that there may be a need to perform accurate online pH control to avoid episodes with unrealistic biological simulation or test conditions. Moreover, the protocol should ensure that in this type of static experiment without online pH control, proper pH adjustment is made in the initial step of the test. By deviation from the protocol, this was not done in these tests.

The Caco2 cell medium normally has an initial pH around 7.5 to 8 and the pH usually drops slightly during the 24-hour experiment. The known presence of organic coatings in NM-103 and NM-104 did not appear to affect the temporal pH evolution notably.

As a general conclusion, it is found that the selected incubation media and the incubator atmosphere are the primary controllers of the temporal pH evolution for the nanomaterials.

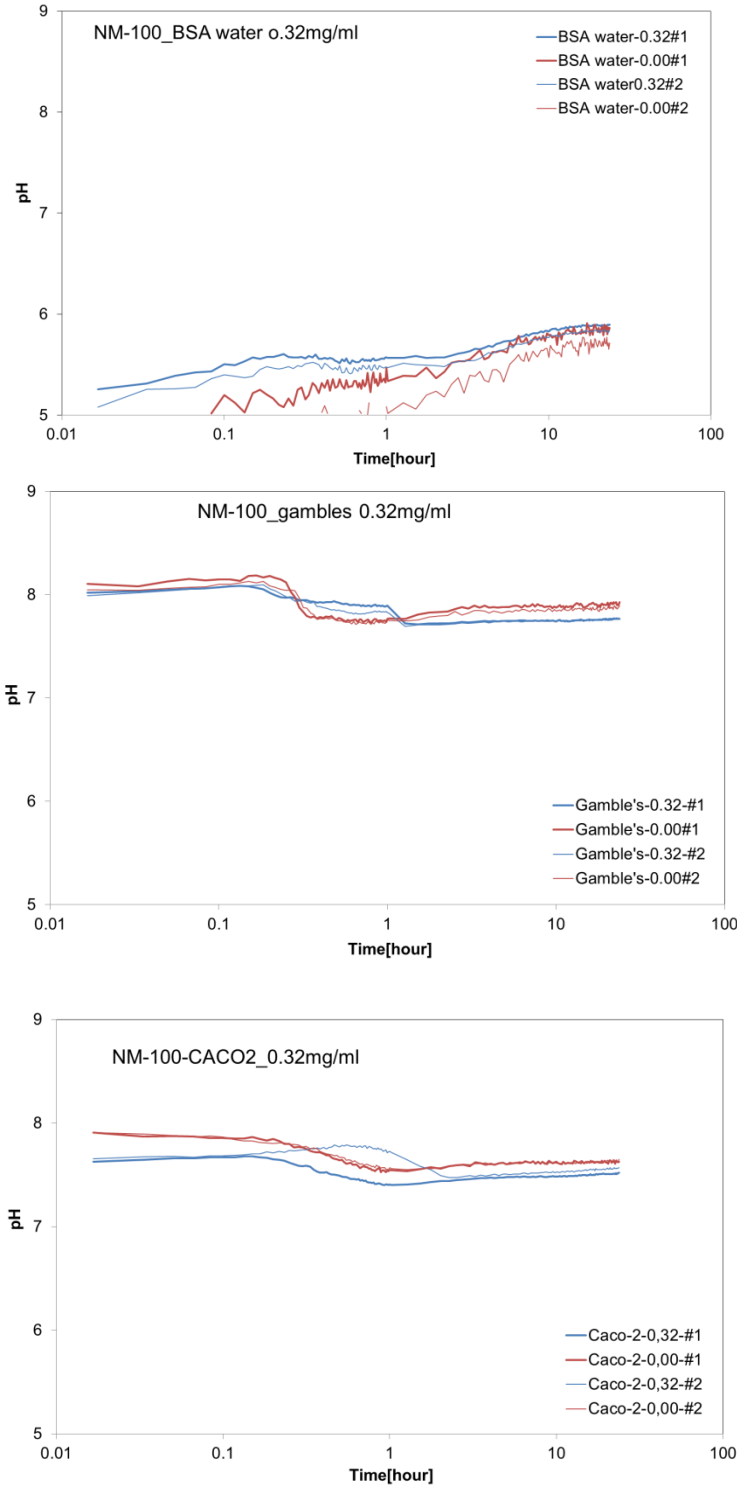


Figure 14. pH-evolution during 24-hour incubation of NM-100 in a) 0.05 % BSA water NANOGENOTOX batch dispersion medium; b) Gambles solution; and c) Caco2 cell medium. The particle concentrations in the Gambles solution and Caco2 cell medium were dosed from the batch dispersion tested in a).



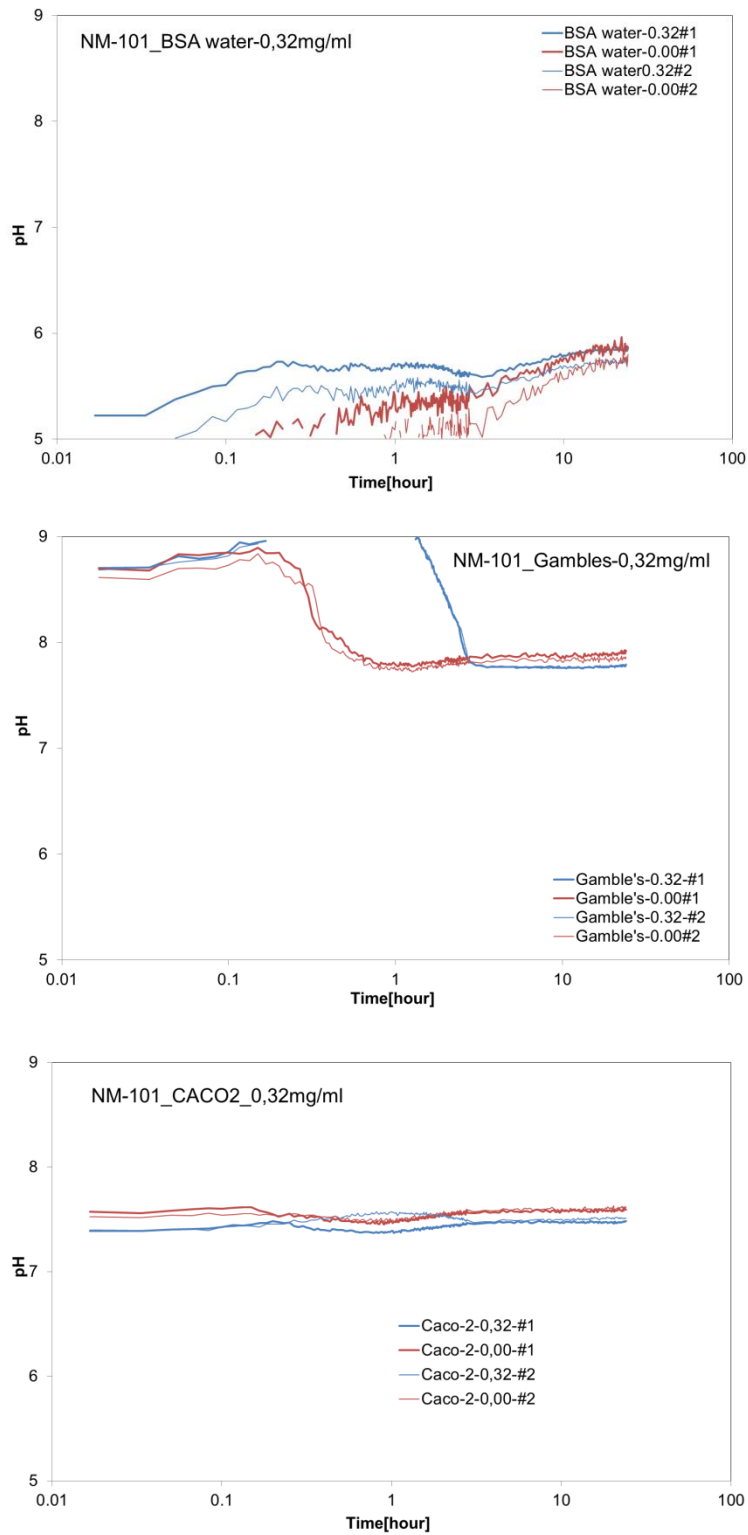


Figure 15. pH-evolution during 24-hour incubation of NM-101 in a) 0.05 % BSA water NANOGENOTOX batch dispersion; b) Gambles solution; and c) Caco2 cell medium. The particle concentrations in the Gambles solution and Caco2 cell medium were dosed from the batch dispersion tested in a).

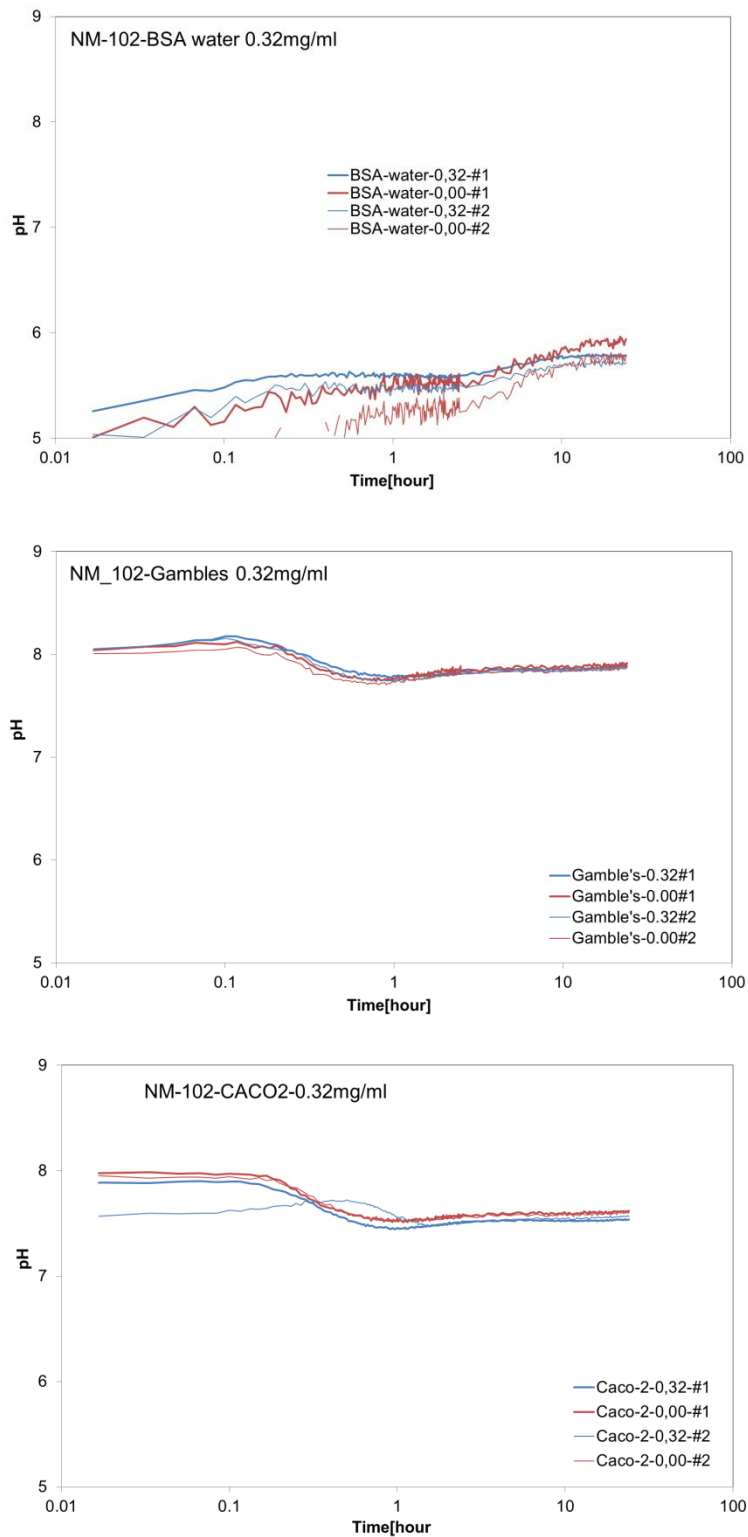


Figure 16. pH-evolution during 24-hour incubation of NM-102 in a) 0.05 % BSA water NANOGENOTOX batch dispersion; b) Gambles solution; and c) Caco2 cell medium. The particle concentrations in the Gambles solution and Caco2 cell medium were dosed from the batch dispersion tested in a).

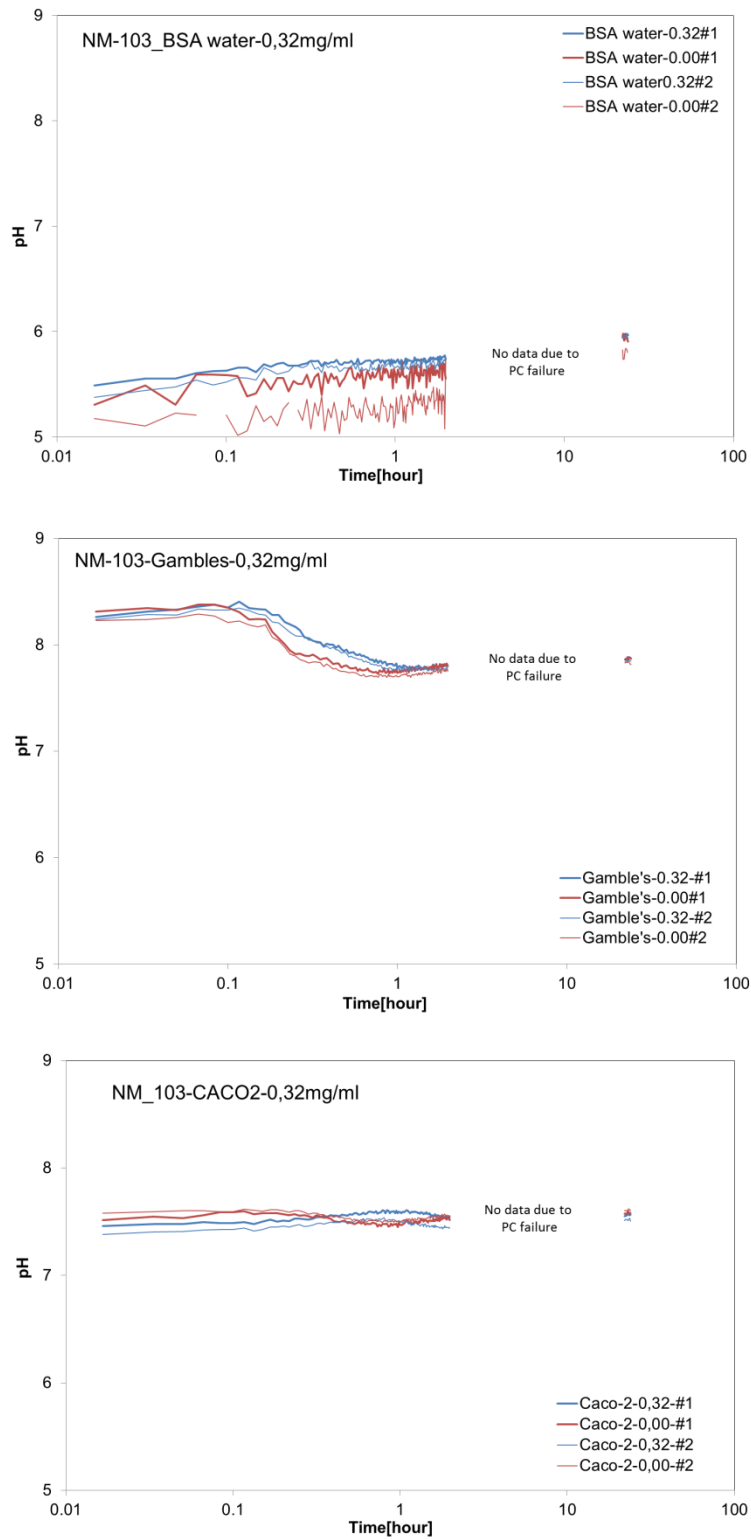


Figure 17. pH-evolution during 24-hour incubation of NM-103 in a) 0.05 % BSA water NANOGENOTOX batch dispersion; b) Gambles solution; and c) Caco2 cell medium. The particle concentrations in the Gambles solution and Caco2 cell medium were dosed from the batch dispersion tested in a).

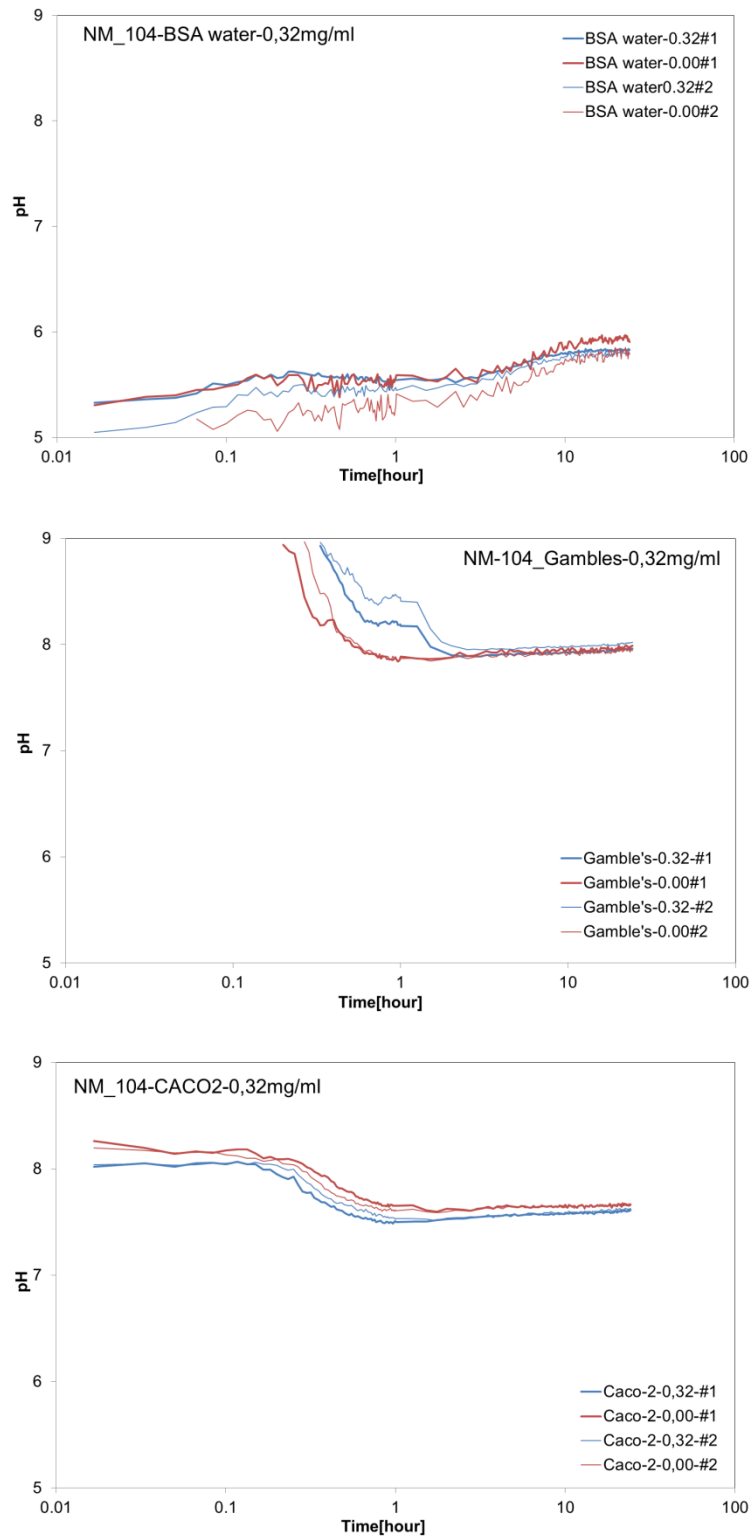


Figure 18. pH-evolution during 24-hour incubation of NM-104 in a) 0.05 % BSA water NANOGENOTOX batch dispersion; b) Gambles solution; and c) Caco2 cell medium. The particle concentrations in the Gambles solution and Caco2 cell medium were dosed from the batch dispersion tested in a).

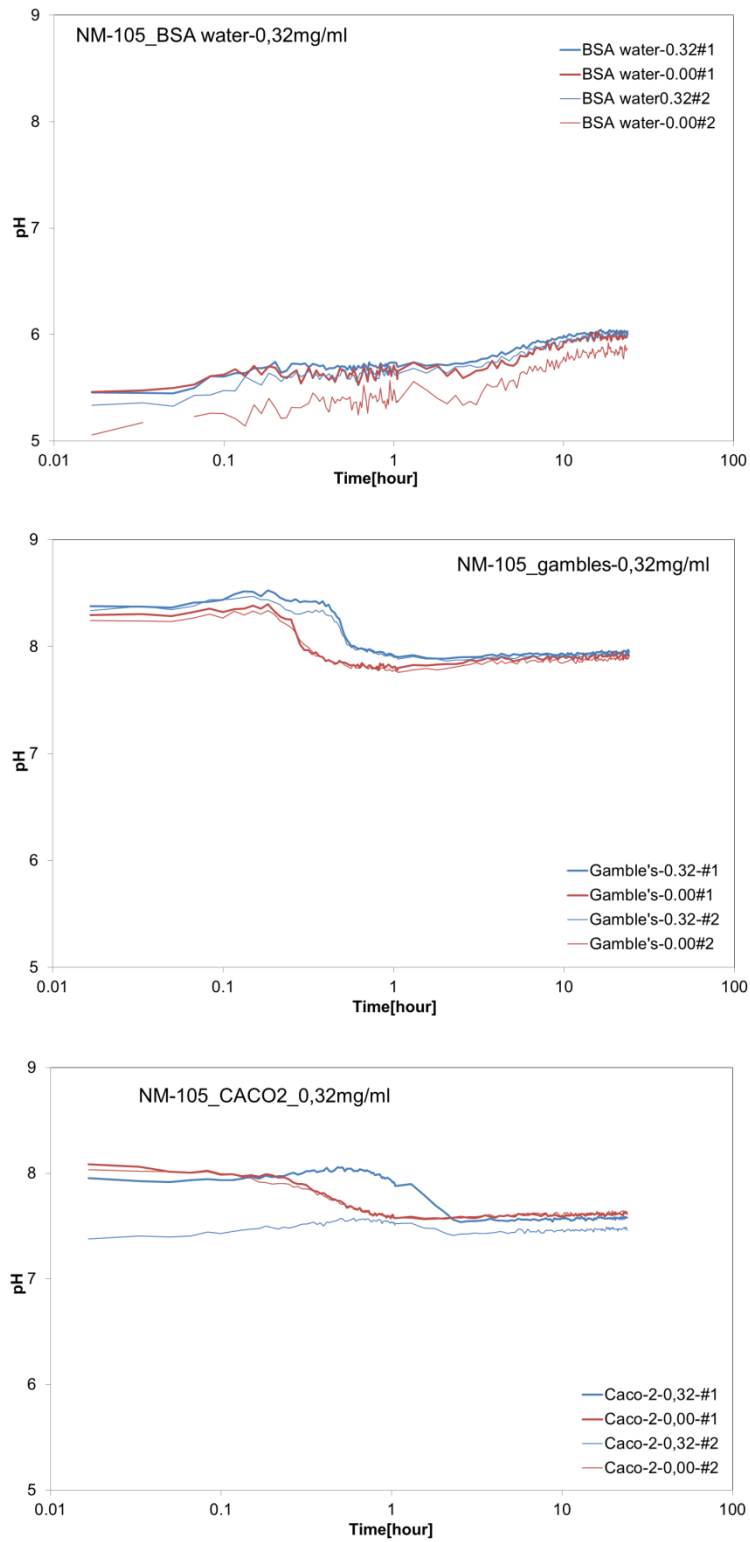


Figure 19. pH-evolution during 24-hour incubation of NM-105 in a) 0.05 % BSA water NANOGENOTOX batch dispersion; b) Gambles solution; and c) Caco2 cell medium. The particle concentrations in the Gambles solution and Caco2 cell medium were dosed from the batch dispersion tested in a).

## 6.2. Hydrochemical O<sub>2</sub> Activity

In the O<sub>2</sub> analyses the temporal evolution of O<sub>2</sub> was expressed as  $dO_2 = O_{2, \text{dose}} - O_{2, \text{medium control}}$ , where  $O_{2, \text{medium control}}$  is the O<sub>2</sub> from the control, i.e. medium without any NM added, and  $O_{2, \text{dose}}$  is the O<sub>2</sub> from the dispersed sample. Figure 20 to Figure 25 show the temporal variation in  $dO_2$  (average of two experiments) and show that the TiO<sub>2</sub> NMs have a wide range of reactivity. Interestingly, the reactivity may not be exerted to similar degree in the different media. It appears as though the reactivity for the TiO<sub>2</sub> NMs often is less pronounced in BSA medium than in Gambles solution and Caco2 media.

For TiO<sub>2</sub> NMs, no notable reactivity was observed in BSA medium for NM-103, NM-104 and NM-105. In addition NM-104 and NM-105 also showed low reactivity by slightly increased  $dO_2$  in the other two test media. In Gambles solution and Caco2 media, both NM-100 and NM-103 acted as reducer by lowering the  $dO_2$  value. NM-102 caused increased  $dO_2$  in these two media, whereas the  $dO_2$  was only increased for NM-101 in Caco2. Considering the applied doses, this suggests that the particle reactivity easily can exceed 1  $\mu\text{mol O}_2/\text{mg}$ .

This type of analysis is still in development and a clear data interpretation is not possible at this point in time. It is, however, evident that the TiO<sub>2</sub> NMs do react and have influence on the O<sub>2</sub> concentrations in the dispersions. Currently, the interpretation of the  $dO_2$  variations is that the TiO<sub>2</sub> NMs are redox-active. This activity may be due to direct electron transfer processes or caused by changes in the O<sub>2</sub> concentration due to dissolution-related reactions.

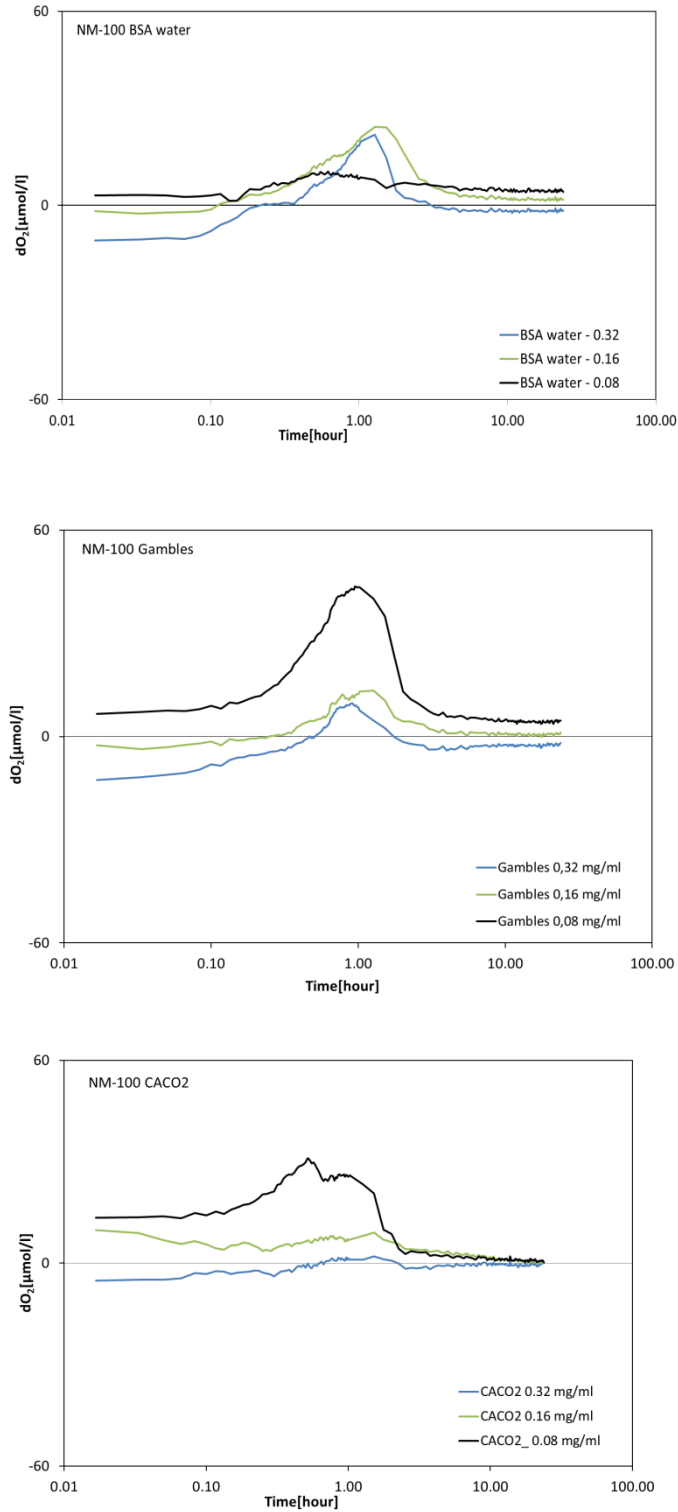
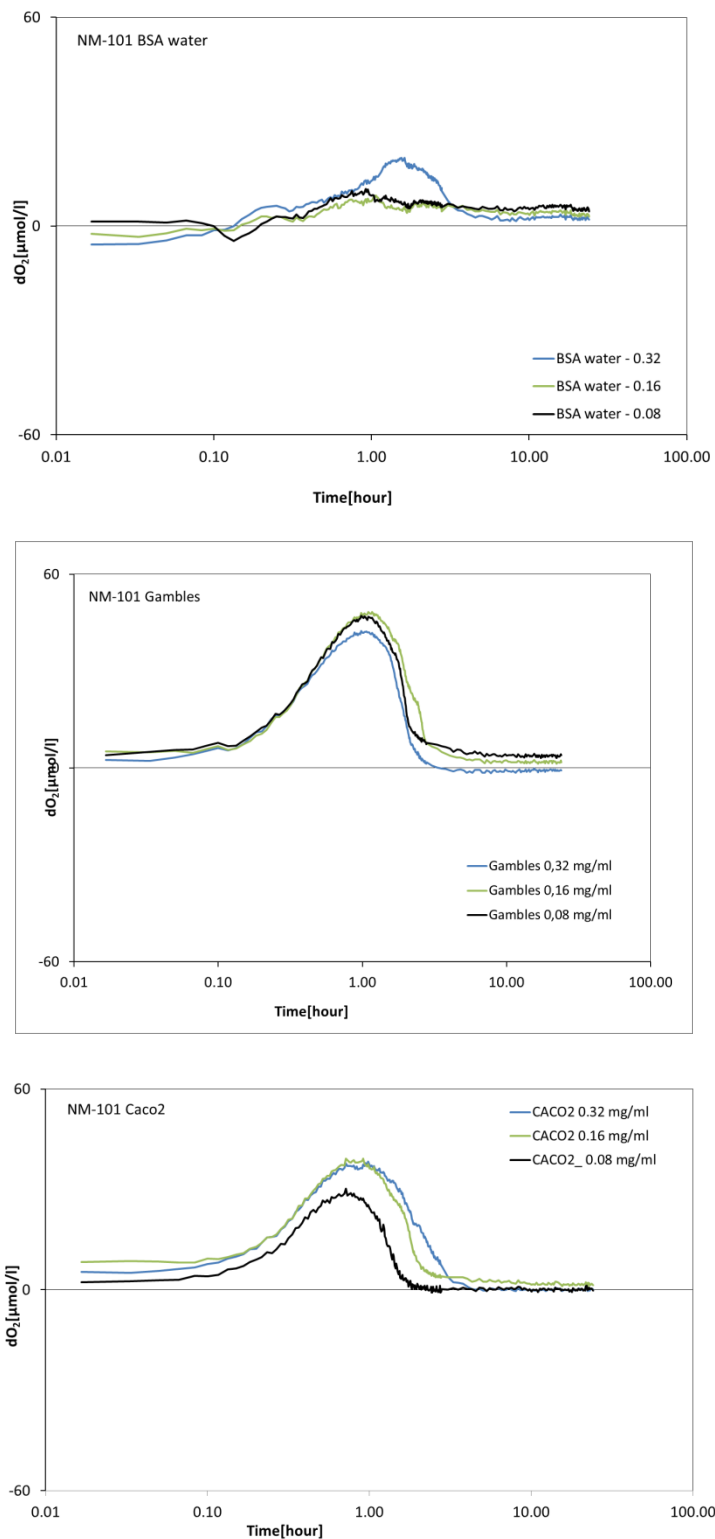
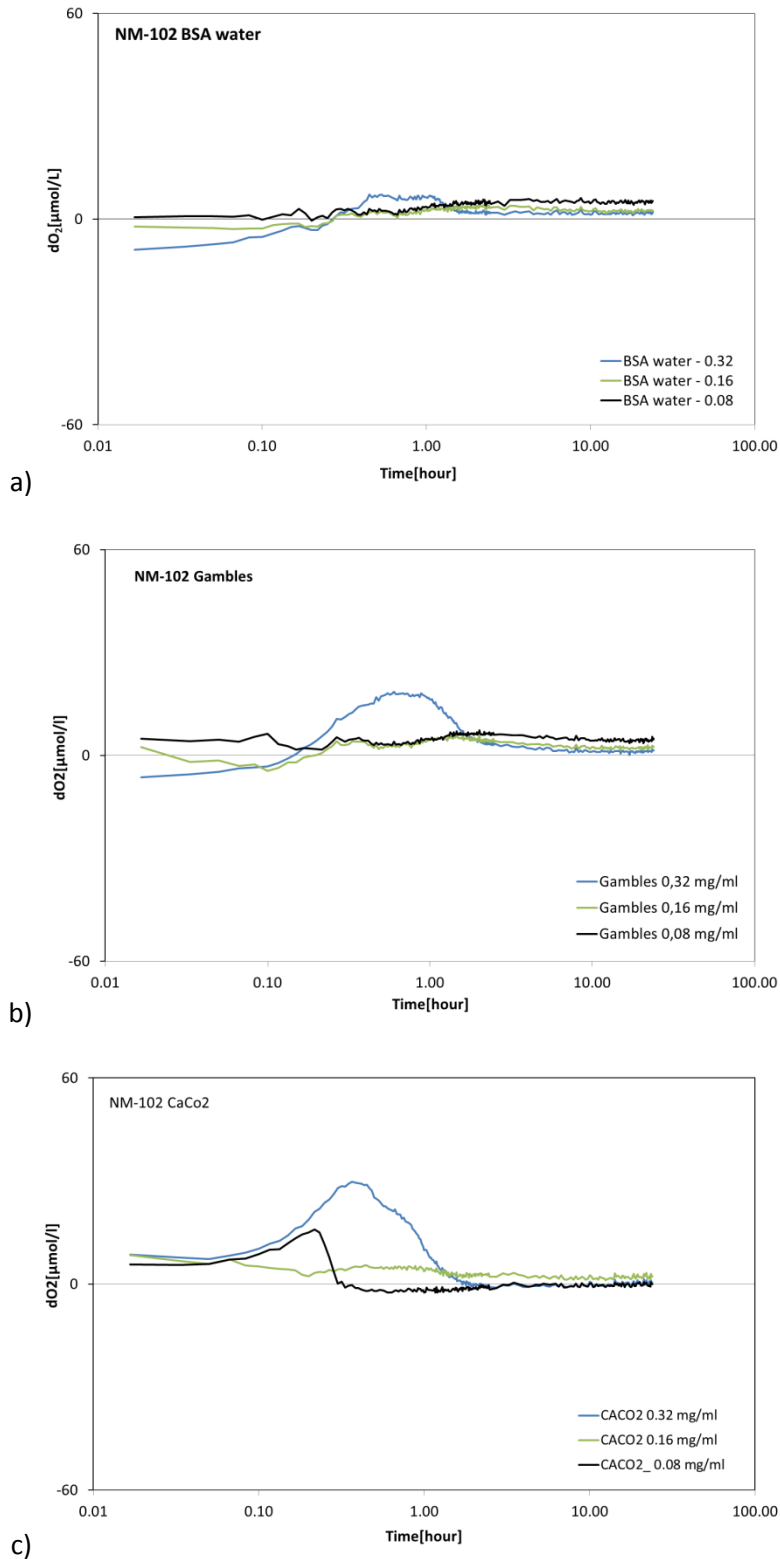


Figure 20.  $O_2$ -evolution during 24-hour incubation of NM-100 in 0.05 % BSA water NANOGENOTOX batch dispersion (top); Gambles solution (centre); and Caco2 cell medium (bottom). The particle concentrations in the Gambles solution and Caco2 cell medium were dosed from the batch dispersion tested in (top).



**Figure 21.**  $O_2$ -evolution during 24-hour incubation of NM-101 in 0.05 % BSA water NANOGENOTOX batch dispersion (top); Gambles solution (centre); and Caco2 cell medium (bottom). The particle concentrations in the Gambles solution and Caco2 cell medium were dosed from the batch dispersion tested in (top).





**Figure 22.**  $O_2$ -evolution during 24-hour incubation of NM-102 in 0.05 % BSA water NANOGENOTOX batch dispersion (top); Gambles solution (centre); and Caco2 cell medium (bottom). The particle concentrations in the Gambles solution and Caco2 cell medium were dosed from the batch dispersion tested in (top).

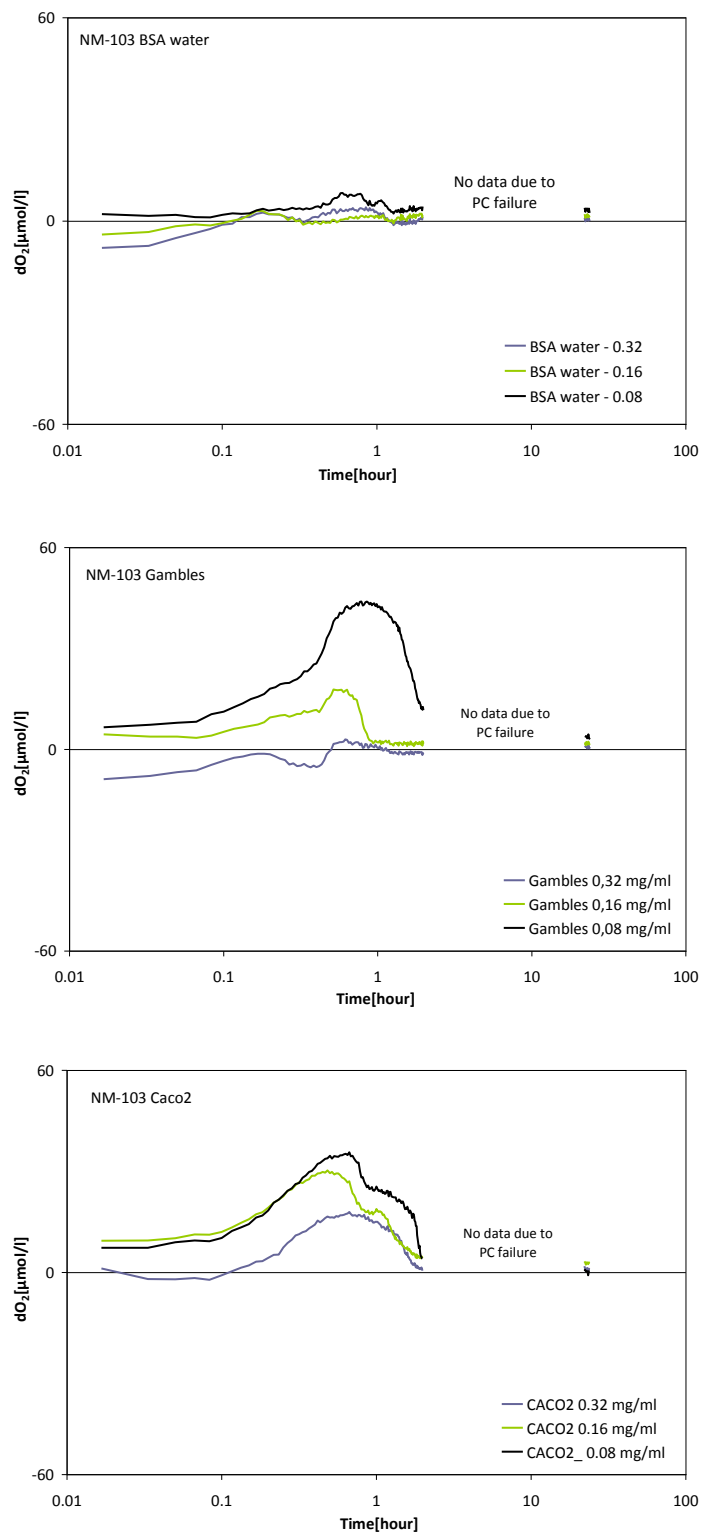


**Figure 23.**  $O_2$ -evolution during 24-hour incubation of NM-103 in 0.05 % BSA water NANOGENTOX batch dispersion (top); Gambles solution (centre); and Caco2 cell medium (bottom). The particle concentrations in the Gambles solution and Caco2 cell medium were dosed from the batch dispersion tested in (top).

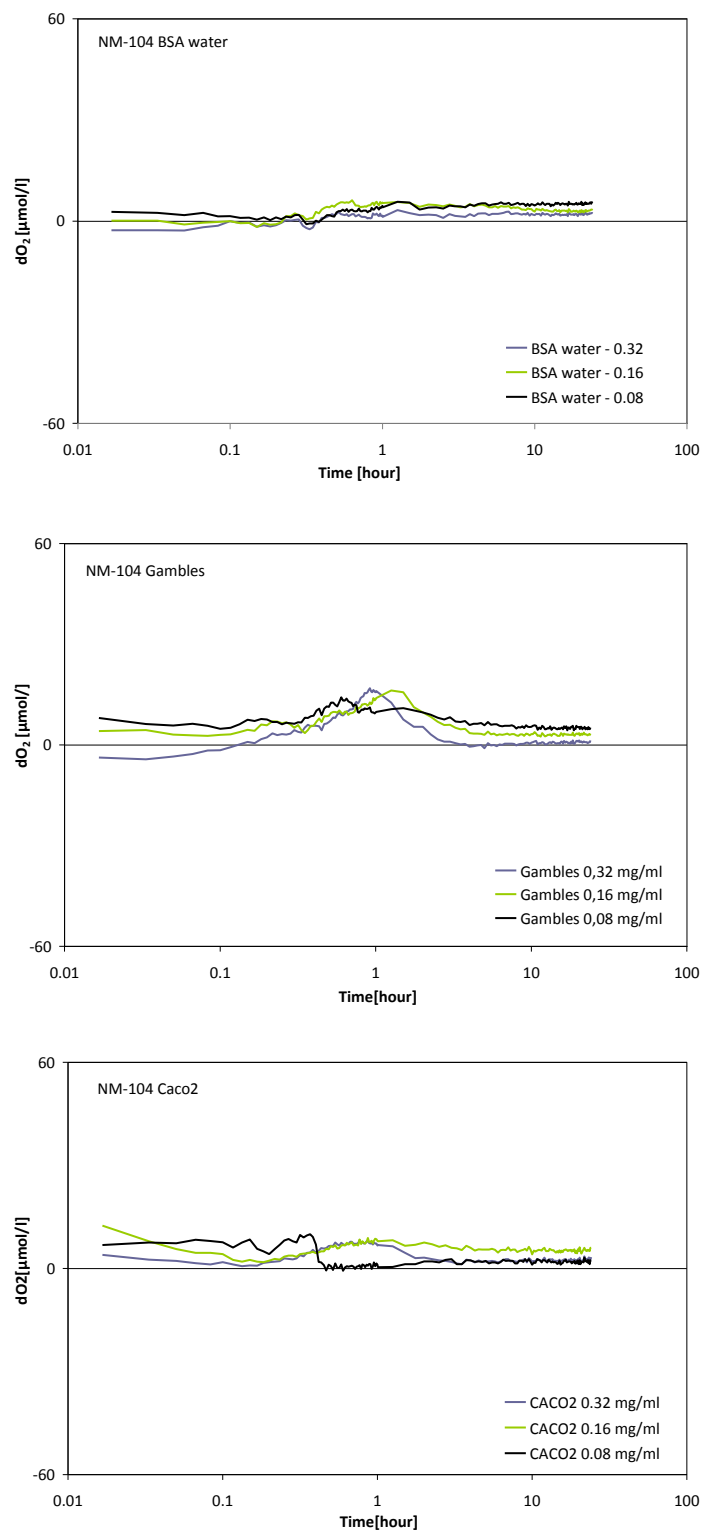


**Figure 24.**  $O_2$ -evolution during 24-hour incubation of NM-104 in 0.05 % BSA water NANOGENTOX batch dispersion (top); Gambles solution (centre); and Caco2 cell medium (bottom). The particle concentrations in the Gambles solution and Caco2 cell medium were dosed from the batch dispersion tested in (top).

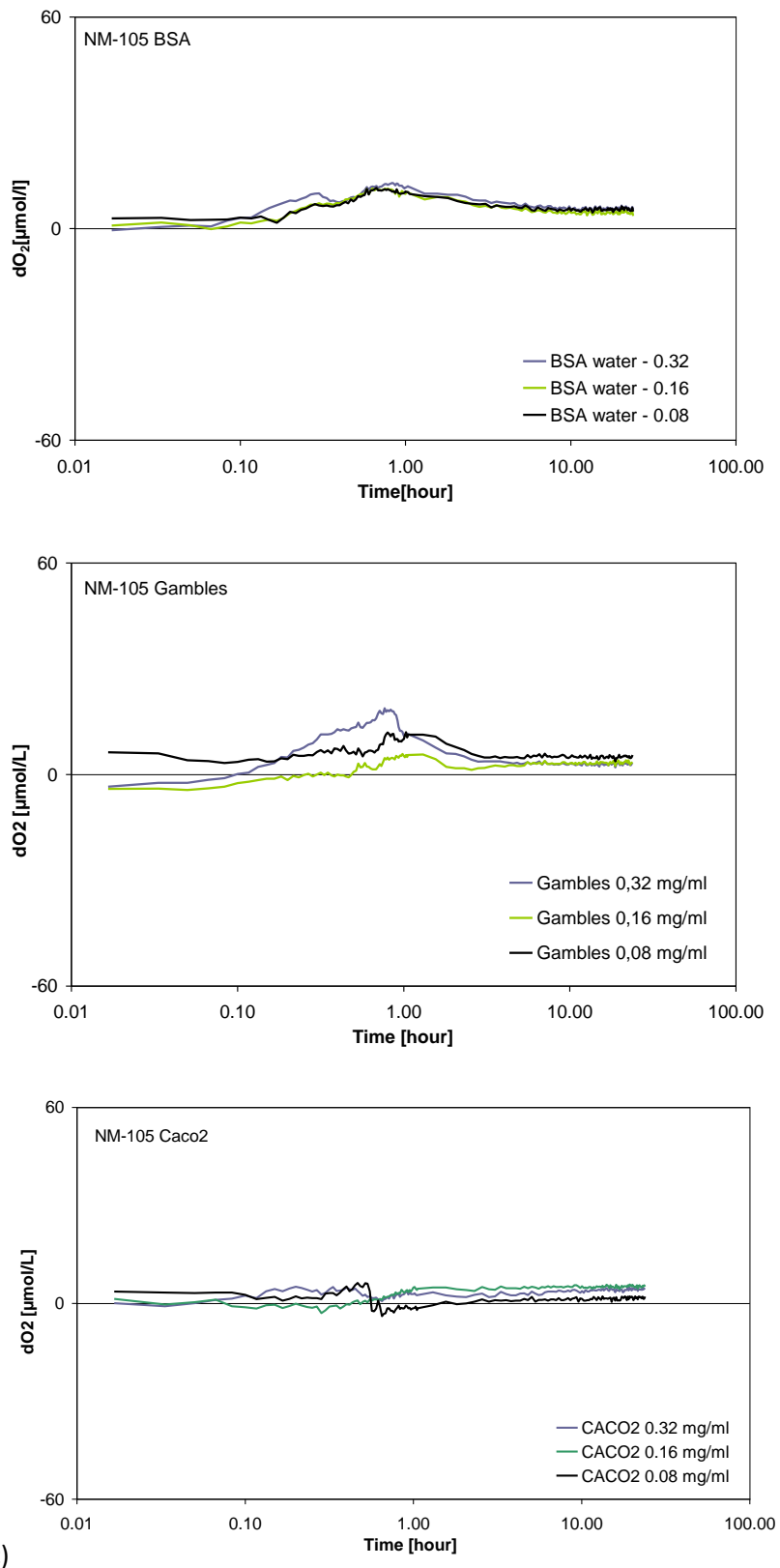


Figure 25.  $O_2$ -evolution during 24-hour incubation of NM-105 in 0.05 % BSA water NANOGENOTOX batch dispersion (top); Gambles solution (centre); and Caco2 cell medium (bottom). The particle concentrations in the Gambles solution and Caco2 cell medium were dosed from the batch dispersion tested in (top).

### 6.3. In vitro dissolution and solubility

The NM dissolution and biodurability was assessed from elemental analyses of the solute adjusted for background concentrations in the three test media. It was assumed that maximum dissolution would be observed at the 0.32 mg/mL dose and that equilibrium was reached in 24 hours. Thus, if the elemental composition of the test materials is given, the results enable calculation of the solubility limit as well as the durability (the un-dissolved residual) of the specific NM in the batch dispersion, the lung lining fluid and the Caco2 media. In this study, we have only semi-quantitative elemental composition data on the TiO<sub>2</sub>.

Ti, Al, Fe, Co, and Ni were determined by ICP Mass-spectrometry (by Eurofins, DK-6600 Vejen, Denmark). The elemental background concentrations in the three test media were determined on three doublet samples for each media. The elemental concentrations after dissolution were determined in two sub-samples for each NM.

Table 20 presents the elemental analysis of the media after careful centrifugation and filtration but before addition of nanomaterial. As seen the three media give only minor background concentrations of Ti, Si, Al, and Fe, which were the target elements for assessing the 24-hour NM dissolution of the TiO<sub>2</sub> NMs (see also Table 21).

**Table 20. Elemental concentrations in the investigated incubation media (n=6).**

MDL <sup>€</sup>	Element	unit	BSA	σ	Gambles	σ	Caco2	σ
1	K	mg/l	<	<	<	<	160	<
1	Si		<	<	<	<	<	
0.05	Fe		<	<	<	<	0.31	0.36
30	Al	µg/l	<	<	<	<	<	<
5	Ti		7.6	1.0	10.2	1.4	11.5	1.3
1	Cr		0.9	0.7	1.3	0.4	1.8	0.6
5	Co		<	<	<	<	<	<
1	Ni		1.8	0.8	1.97	0.33	2.4	1.5
5	Zn		22.3	11.5	11.0	3.8	88	7

<sup>€</sup> MDL = Minimum detection limit; < = not detected or below MDL.

Table 21 lists the elemental concentrations used for the assessment of NMs' solubility and biodurability. As mentioned in Chapter 5, only semi-quantitative analyses were made on the TiO<sub>2</sub> NMs. Therefore, the assessment of 24-hour solubility limits and biodurable fraction must be considered approximate. The TiO<sub>2</sub> NMs have relevant high concentrations of Si, Al, Fe (NM-100, NM-102, and NM-103), and of course Ti as the major element. The concentration of Al is quite significant in the two surface treated materials NM-103 and NM-104.

**Table 21. Elemental concentrations ( $\mu\text{g/g}$ ) in the  $\text{TiO}_2$  NMs used for assessment of dissolved fraction and particle biodurability.**

Material	Ti*	Al*	Si*	Fe*	Co*	Ni*
NM-100	585 700	900	2 800	4 900	<	<
NM-101	587 900	900	2 900		<	<
NM-102	597 300	500	800	700	<	<
NM-103	547 400	34 300	6 800	600	<	<
NM-104	556 000	32 200	1 800	<	<	<
NM-105	598 100	400	700	<	<	<

\*From EDS measurements in Chapter 5

Table 22 lists the elemental compositions in the three incubation media corrected for the background concentrations in the incubation media. It is clear that most elements are present in relatively low concentrations. However, for assessment of the dissolved fraction of the MN, the applied elemental dose in the experiments must be taken into consideration.

**Table 22. Background-corrected\* elemental concentration in the test mediums after 24-hour dissolution tests with  $\text{TiO}_2$  NM (n=2).**

MDL			NM-100	$\sigma$	NM-101	$\sigma$	NM-102	$\sigma$	NM-103	$\sigma$	NM-104	$\sigma$	NM-105	$\sigma$
0.05 % BSA														
1	mg/l	Si	-	-	-	-	-	-	0.9	1.3	-	-	-	-
30	$\mu\text{g/l}$	Al			175	49			198	116	137	25	-	-
5	$\mu\text{g/l}$	Ti	5.2	3.5	-	-	<	6.8	-	-	-	-	-	-
Gambles solution														
1	mg/l	Si	-	-	-	-	-	-	2.0	0.2	-	-	-	-
30	$\mu\text{g/l}$	Al	-	-	177	185	-	-	868	59	413	327	-	-
5	$\mu\text{g/l}$	Ti	-	-	-	-	3388	3900	-	-	-	-	-	-
Caco2														
1	mg/l	Si	-	-	-	-	-	-	1.7	<	-	-	-	-
30	$\mu\text{g/l}$	Al	24	34	252	277	-	-	182	<	413	327	-	-
5	$\mu\text{g/l}$	Ti	796	2	3414	1683	1741	683	222	337	3386	3900	2724	3846

MDL: Minimum detection limit in the raw analysis; - denotes not detected; < denotes background corrected concentration lower than  $0.1 \times \text{MDL}$ . Measurements were performed twice, i.e. n=2

\* the background correction combined with a small number of repeated measurements mean that the  $\sigma$  value may be larger than the corrected measurement value

In this analysis, 0.32 mg/ml NM powder was dosed into each incubation media. Therefore, the elemental dose of the NM concentration was determined by simple multiplication of the element concentration (Table 21) in  $\mu\text{g/mg}$  with the applied dose 0.32 mg sample/ml medium. These concentration data were used to calculate the weight percent of dissolved element using the background-corrected elemental concentrations in the three incubation media after 24-hour incubation (as indicated in Table 22). The results from these calculations are shown in Figure 26, which shows the elemental dose and the percent dissolved Si, Ti, Al, and Fe in the three incubation media. The results from the dissolution studies with  $\text{TiO}_2$  NMs

show that TiO<sub>2</sub> is almost insoluble in the three media. When detected, values are in the order of 1 wt% of the 0.32 mg/mL dose used in the experiments. In contrast to Ti, the key element of the NMs, Si, Al, and Fe present as impurities or coatings generally appear more soluble.

Al was indicated as coating material (EDS results indicated in the order of 3.2 - 3.4 wt%) for NM-103 and NM-104, and found as a trace element (0.04 to 0.09 wt%) in all semi-quantitative EDS-analyses of the TiO<sub>2</sub> NMs (Table 21). In the dissolution experiments, Al was observed in all three media incubated with NM-101, NM-103, and NM-104, as well as NM-100 incubated in Caco2 cell medium. At the tested dose, the amount of dissolved Al was in the order of 1 to 8 wt% for NM-103 and NM-104 with the highest Al contents. In the low-Al TiO<sub>2</sub> NMs, the fraction of dissolved Al was up to 60 to 80 wt% (Figure 26).

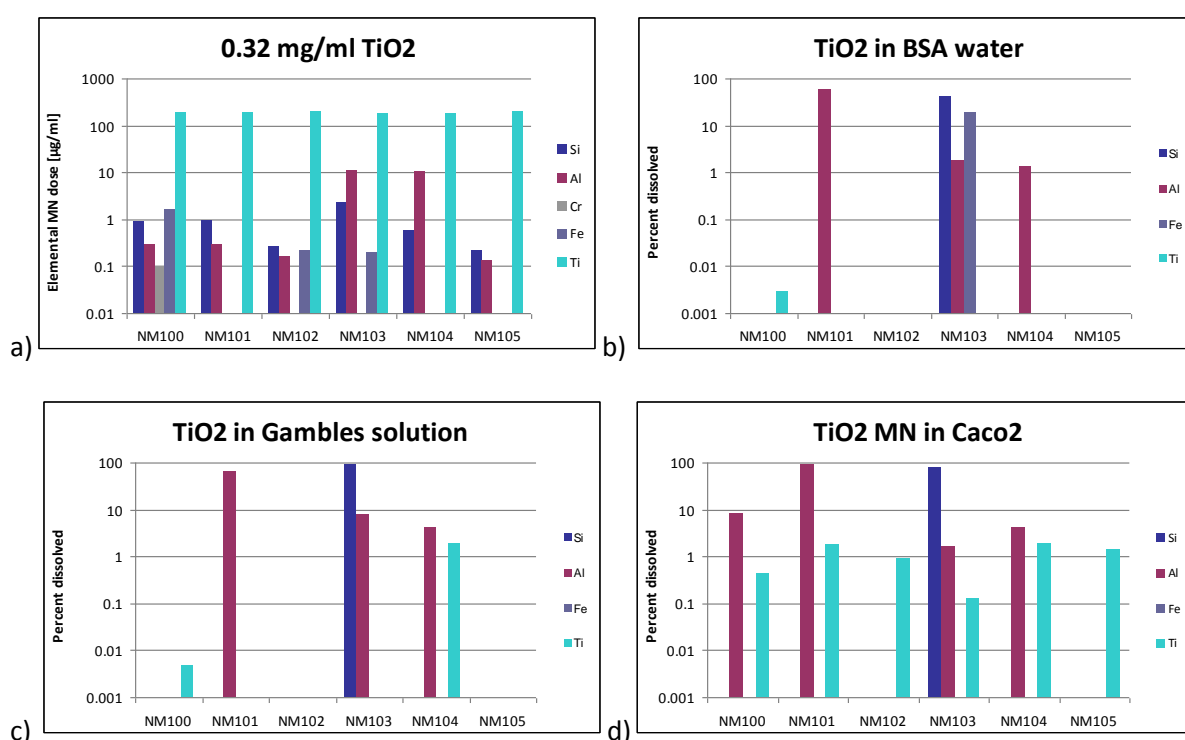


**Figure 26.** a) Relative elemental composition of the TiO<sub>2</sub> NMs (please note that the scale on the y-axis is logarithmic). Percent dissolved element in b) BSA water; c) Gambles solution; and d) Caco2 cell medium.

EDS analysis indicated the presence of Si (0.07 to 0.68 wt%) in all TiO<sub>2</sub> NMs (Table 22). The highest concentrations were observed in NM-103, followed by NM-100, NM-101, and NM-104 (0.18-0.29 wt%). The Si concentration in NM-102 and NM-105 was in the order of 0.07-0.08. From the industry data, silicone (dimethicone coating) was reported for NM-103 and NM-104. GC-MS analysis indicated presence of compounds tentatively identified as silanes in NM-101, NM-103, and NM-104, as well as possibly tetramethyl silicate in NM-104. From dissolution studies of NM-103, the elemental analyses consistently revealed presence of Si

in all three incubation media. The fraction of the Si available at the 0.32 mg/ml dose varied between 42 wt% (BSA-water) and 90 wt% (Gambles solution).

Fe was identified in three TiO<sub>2</sub> NMs (NM-100, NM-102 and NM-103) by EDS (Table 16). The highest concentration was found in NM-100 (0.49 wt%), and ca. 0.06 to 0.07 wt% was observed in NM-102 and NM-103. In the dissolution experiments, Fe was only detected in NM-103 incubated in BSA water. The fraction of dissolved Fe appeared to be in the order of 18 wt% at the 0.32 mg/ml dose.

Overall, the dissolution experiments with TiO<sub>2</sub> suggest, as would be expected, that only a very minor fraction of TiO<sub>2</sub> is dissolved if any. However, the Al and organic Si coatings, or otherwise associated Al, Si, and Fe may at least partly dissolve during the 24-hour incubation experiment. Si is present as a constituent in associated silane and silicone, which probably explains part of the dissolved fraction in NM-103 and NM-104.

#### **6.4. Estimation of biodurability**

The results from the 24-hour reactivity and dissolution tests can give some indication on the biodurability of the nanomaterials. It is interesting to note that the elemental analysis of the three media after incubation with the TiO<sub>2</sub> NMs has demonstrated different behaviour of the elements in the TiO<sub>2</sub> NMs including their coatings and impurities. From the analyses, we can conclude that the TiO<sub>2</sub> NMs are categorised as highly durable nanomaterials with regard to the TiO<sub>2</sub> core. However, the coatings may degrade rapidly over the first 24-hours and this varies with the incubation media used; it was most pronounced in the Caco2 cell medium.

#### **6.5. Conclusions**

Under in vitro test conditions, pH reactivity tests revealed negligible to moderate effects on pH of the tested NMs in 0.05 % w/v BSA-water, Gambles solution, and Caco2 cell medium. However, during the course of experiments relatively large variations could occur, which are tentatively assumed to be due to small fluctuations in CO<sub>2</sub> concentrations delivered from external pressure tanks.

O<sub>2</sub> reactivity tests showed some material and media-dependent effects on dO<sub>2</sub>. Increased dO<sub>2</sub> values were observed for NM-102 in Gambles solution and Caco2 cell medium. In these two media NM-100 and NM-103 decreased the dO<sub>2</sub> value. Almost no reactivity was observed for the TiO<sub>2</sub> NMs in BSA-water solution. For NM-104 very low reactivity was detected in Gambles solution and Caco2 cell media. Evaluation of NM dissolution and biodurability revealed element dependent behaviour as TiO<sub>2</sub> has very low solubility, and the Al and Si coatings appear to be partly or completely released to the media in the 24-hour experiment, thus indicating that the TiO<sub>2</sub> NMs are durable, but the coatings may not be.



## **7. Dynamic Light Scattering measurements for size distributions, mean aggregate size and structure**

Dynamic Light Scattering (DLS) is a technique to characterise colloidal systems based on the scattering of visible light resulting from the difference in refractive index between the dispersed colloids and the dispersion medium. DLS may be applied for sizing particles in the range from ca. 0.6 nm to ca. 6  $\mu\text{m}$  depending on the optical properties of the material and medium. In DLS, the transmitted or back-scattered light from a laser diode is measured as function of time. A photo-detector collects the signal, which will fluctuate with time depending on the level of Brownian motion of the suspended nm- to  $\mu\text{m}$ -size objects in liquid suspension. The Brownian motion is caused by collision between the particle and the molecules of the medium and varies as a function of particle size and causes variation in the intensity of transmitted or scattered light as function of time. A correlator compares the signal measured at a time  $t_0$  with different, very short time delays  $dt$  (autocorrelation). As the particles move, the correlation between  $t_0$  and subsequent  $dt$  signals decreases with time, from a perfect correlation at  $t_0$ , to a complete decorrelation at infinite time (in practice order of milliseconds). For big particles, the signal changes slowly and the correlation persists for a longer time, whereas small particles have high Brownian movement causing rapid decorrelation. Details are given in Appendix A, which also describes the equipment used, measurements performed and algorithms used for data analysis.

For DLS measurement results, care should be taken regarding their interpretation, as the performance of the DLS method and instrumentation may be limited for measurements of mixtures of particles of different sizes. DLS measurements of the single components of one well defined size gave results corresponding to the findings obtained by using TEM, however the measurement results regarding the size distribution of mixtures of such components showed significant limitations, e.g. the smaller particles were not identified by the measured distribution (Calzolari et al., 2011, Linsinger et al. 2012).

DLS characterisation was performed by CEA, NRCWE, INRS and JRC, and the results from these institutes are described in the following. The apparatus used are listed in Table 5.

### **7.1. DLS measurements and data treatment**

#### **7.1.1. Sample preparation**

For the characterisation of the  $\text{TiO}_2$ -NMs, CEA developed a dispersion protocol to achieve conditions giving the best dispersion state of the NM in order to assess the size of the smallest aggregates, which was in acidic media. The dispersion medium must be filtrated before use to avoid any dust contamination. Suspensions were sonicated under conditions

where the TiO<sub>2</sub> NMs have a high surface charge to prevent subsequent agglomeration, i.e. sonication of 3.41 mg/mL TiO<sub>2</sub> NM suspension was performed at 40 % amplitude for 20 min in ice-water cooling bath. The dispersion prepared for these DLS measurements were also used for SAXS measurements performed by CEA. The measurements and data analysis are explained in Appendix A.

### 7.1.2. Suspension Stability over time followed by DLS

The stability of such suspensions is assessed by following in DLS the evolution of Z-average and mean count rate of resting sample over 17 h. Results for TiO<sub>2</sub> NM suspensions dispersed by sonication in HNO<sub>3</sub> 10<sup>-2</sup> M are reported in Figure 27.

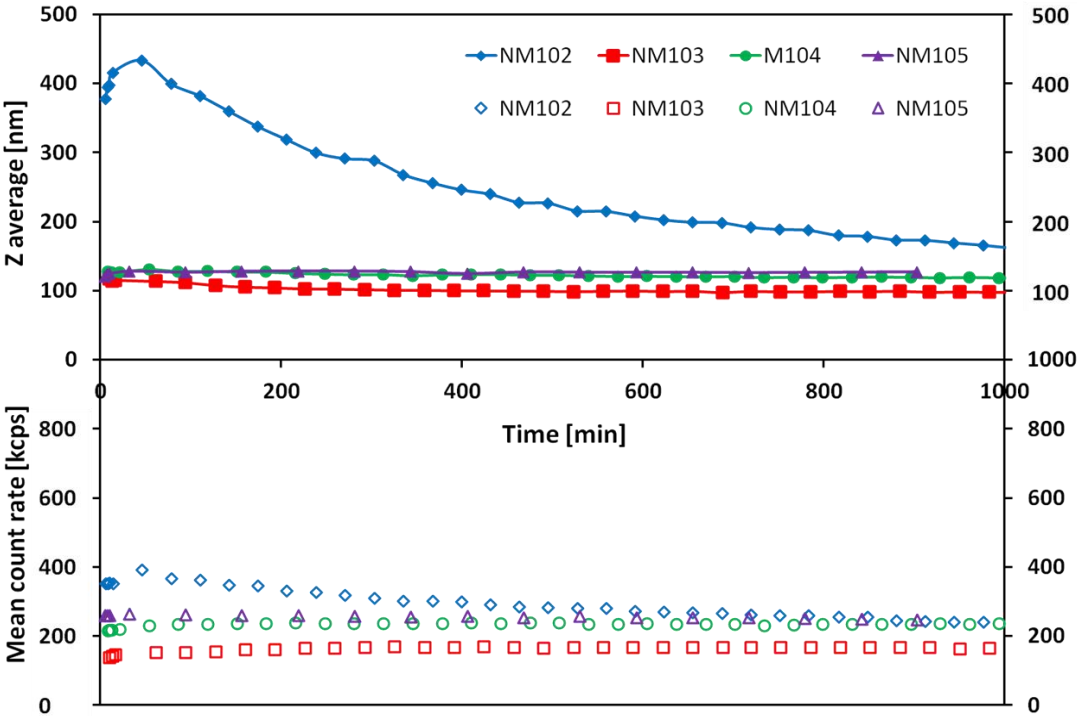


**Figure 27. Evolution of DLS representative quantities (Top: Z-average mean size. Bottom: mean count rate) with residence time over 17 hours for TiO<sub>2</sub> suspensions ultrasonicated (20 min at 40 % amplitude) in pure water.**

For NM-103, NM-104 and NM-105, the mean count rate (mainly proportional to the concentration at the position of the laser beam) and Z-average remained unchanged during the observation period, indicating that almost no sedimentation occurred and the suspensions were very stable.

On the other hand, a sedimentation trend was observed for NM-102. Indeed, even under the best dispersion conditions the aggregates in suspension are much bigger (400 – 600 nm) than for NM-103, NM-104 and NM-105. This is also seen on the top part of Figure 27 where

the curve for NM-102 shows a decrease of Z-average over time. The slow sedimentation of the biggest aggregates, induced by gravity, gave rise to a regular decrease of Z-average mean size measured at the position of the laser beam, while the mean count rate was less affected.

### 7.1.3. DLS results: size distribution and intensity averaged mean size of aggregates

Intensity size distributions for NM-102, NM-103, NM-104 and NM-105 studied by CEA are shown in Figure 28 left (average of 3 measurements).

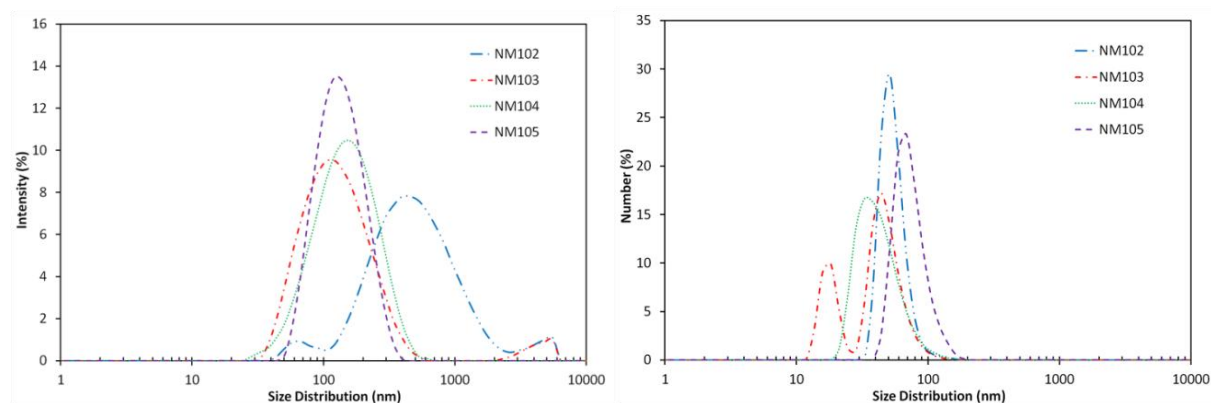


**Figure 28. DLS intensity size distributions (left) and number size distributions (right) for suspensions of TiO<sub>2</sub> nanomaterials dispersed by ultrasonication (20 min at 40 % amplitude) in in HNO<sub>3</sub> 10<sup>-2</sup>M.**

The corresponding number size distributions are also displayed, (see Figure 28 right), to illustrate the size range and proportions in number. The high polydispersity and the presence of large particle aggregates of several  $\mu\text{m}$  size result in an intensity signal weighing towards the bigger aggregates. Conversion to the number distribution weighs the intensity distribution with the size-intensity relationship. The dispersions analysed by number distribution have a high frequency of occurrence of small-size particles. Due to the wide size-distribution and presence of large aggregates, the smallest particles may not be resolved well and the true sizes may be smaller than derived from these DLS measurements

The distribution curves of NM-103, NM-104 and NM-105 are well centred at 100-150 nm with visibly narrower distribution for NM-105. The size distribution of NM-102 is much wider than for other NM materials indicating the presence of big aggregates of more than 500 nm.

For NM-103 the Z-average values were found to be considerably smaller than for NM-104 although these two materials are supposed to be similar in terms of the pristine structure and size of nanoparticles. These differences most probably originate from the different coatings of NM-103 and NM-104, which were claimed to be hydrophobic and hydrophilic respectively.

The hydrophilic moiety present on the surface of NM-104 could induce bigger hydrodynamic radii influencing the Z-average value.

DLS measurements were repeated with dispersions prepared with different samples from the same vial and with samples from different vials to obtain mean values and standard deviation of size parameters. An overview of the results of Z-average, polydispersity index, position and width (FWHM) of the main peak in intensity size distribution is given for NM-102, NM-103, NM-104 and NM-105 in Table 23.

The previous observations are confirmed. However, the polydispersity indices for NM-102 are all above 0.25 indicating that the DLS data should not be analysed using the model for multimodal analysis. The values of Table 23 can be used for comparative purposes, e.g. for the homogeneity analysis, see section 5.1.

**Table 23. Size parameters and standard deviations from DLS measurements by CEA averaged on a given number of TiO<sub>2</sub> samples prepared by ultrasonication ((20 min at 40 % amplitude) in HNO<sub>3</sub> 10<sup>-2</sup>M. Z-average, polydispersity index, position and width (FWHM) of the main peak in intensity size distribution.**

Material (number of samples)	Size parameters from DLS (intensity averaged)			
	Z-Average (nm)	Pdl	Intensity distribution main peak (nm)	FWHM peak with (nm)
<b>NM-102</b> (7)	423.3 ± 59.4	0.427 ± 0.042	686.6 ± 40.6	414.1 ± 107.6
<b>NM-103</b> (6)	113.2 ± 3.2	0.242 ± 0.018	138.4 ± 7.7	73.6 ± 11.0
<b>NM-104</b> (5)	128.6 ± 1.3	0.221 ± 0.004	165.8 ± 5.9	89.0 ± 10.3
<b>NM-105</b> (6)	125.4 ± 4.2	0.171 ± 0.018	153.0 ± 5.3	69.7 ± 5.9

Also JRC, NRCWE and INRS performed DLS measurements to confirm the protocol and to perform an interlaboratory comparison of results that are shown in Table 25.

## 7.2. JRC DLS measurements and data treatment

### 7.2.1. Sample preparation

JRC used a dispersion protocol for dispersion in water in which 50-100 mg of TiO<sub>2</sub> NM was diluted to obtain the 0.1 mg/mL solution. This was then sonicated for 15 minutes in the ultrasonic tweeter sonicator. For comparison, additional dispersion of each TiO<sub>2</sub> NM sample was prepared and then sonicated for 5 minutes with ultrasonic bath. DLS measurement was performed immediately after sonication.

### 7.2.2. Measurement results

When sonicated with the ultrasonic bath, NM-105 presented some large sediments of size > 1 µm, which were impossible to disperse and did not disappear even after prolonged sonication. DLS measurements are highly affected by the presence of large particles (here

particles > 1 μm) whose scattering of the light covers the signal of smaller particles. NM-105 had a Pdl > 0.6 clearly indicating a high poly-dispersivity.

When sonicated with ultrasonic tweeter, the Pdl of NM-105 dropped drastically to the value of 0.163 which underlines the importance of the choice of ultrasonicator for the final results of the DLS measurements. Table 24 gives an overview of the Particle Size Distribution (PSD) range observed from the measurements and the DLS intensity distributions are presented in Figure 29 and Figure 30.

**Table 24. Size parameters (Z-average, polydispersity index) from DLS measurements by JRC averaged on a given number of TiO<sub>2</sub> samples.**

Size parameters from DLS (intensity averaged)		
Material	Z-Average (nm)	Pdl
NM-100	228.6	0.145
NM-105*	155.6	0.163
NM-105**	554.9	0.679

\* Dispersed ultrasonic tweeter

\*\* Dispersed with ultrasonic bath

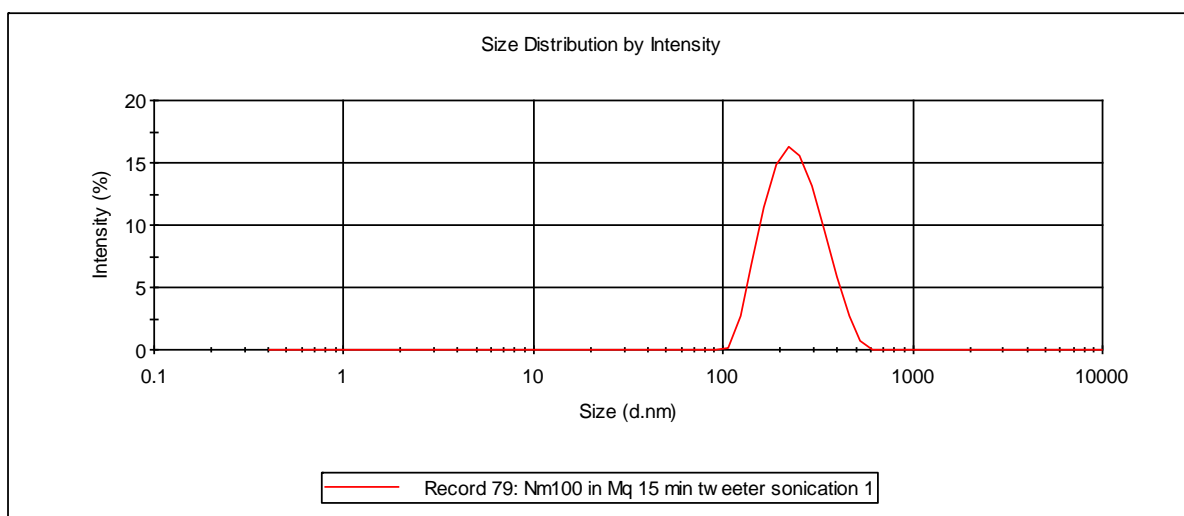


**Figure29. DLS size distribution by intensity for NM-100 dispersed in Milli-Q® water.**

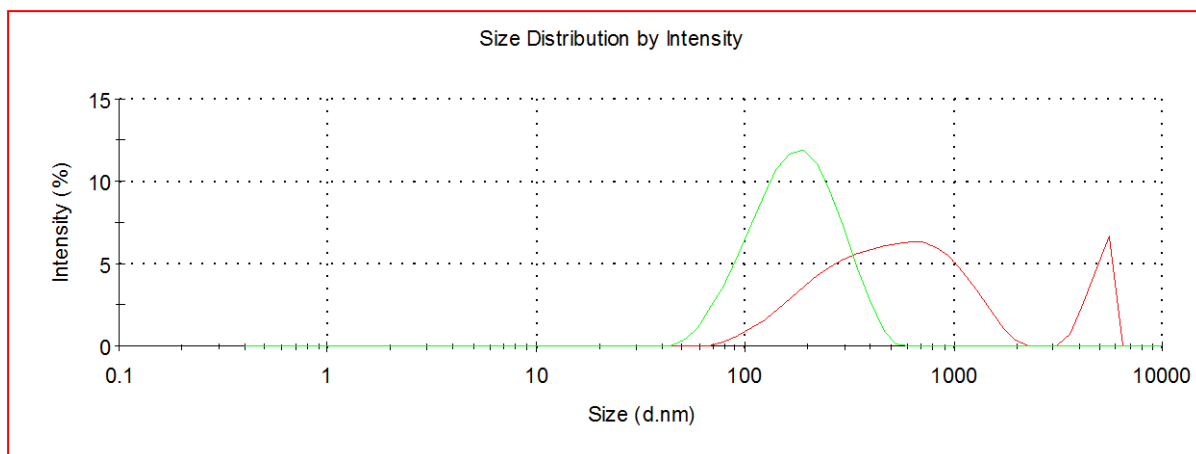


**Figure 30. Comparison of DLS size distribution by intensity for NM-105 dispersed in MilliQ-water by using ultrasonic bath (red) and ultrasonic tweeter (green).**

### 7.3. Conclusions on DLS measurements

Table 25 gives an overview of the DLS measurement results of particle size distribution in ultra-pure water. The DLS results all indicate that the TiO<sub>2</sub> NMs are polydisperse.

Measurements performed applying the same dispersion protocol by different institutions give similar results.

The JRC results displayed in Table 24 are DLS measurements for NM-100 and NM-105 using different dispersion protocols. The JRC measurements also indicate that the NMs are polydisperse, however the peaks are at different positions depending on the protocol used. This observation is not surprising, due to the use of a procedure at JRC that was not harmonised with respect to sonication power and media as used in NANOGENOTOX.

**Table 25. Size parameters and SD of DLS measurements of TiO<sub>2</sub> NMs prepared by ultrasonication (20 min at 40 % amplitude) in HNO<sub>3</sub> 10<sup>-2</sup>M. Z-average, polydispersity index, position and width of the main peak in intensity size distribution are shown.**

Institution	Vial no.	Repetition / date	Z-average	(SD)	PdI	(SD)	Intensity distribution main peak	(SD)	FWHM peak width	(SD)
<b>RESULTS for NM-102</b>										
CEA	34	20110719	533.3		0.486		964.5		796.3	
CEA	34	20110802	377.9		0.419		587.4		417.3	
CEA	34	20110729	380.3		0.352		622.5		362.8	
CEA	34	20111006	478.8		0.455		633.6		264.7	
<b>Intra vial</b>			<b>442.6</b>	<b>76.6</b>	<b>0.428</b>	<b>0.058</b>	<b>702.0</b>	<b>176.1</b>	<b>460.3</b>	<b>232.7</b>
CEA	35	20110328	403.1		0.411		695.8		373.9	
CEA	24	20111123	400.4		0.441		654.8		493.2	
CEA	31	20111207	389.5		0.426		685.4		572.4	
<b>Inter vial (4 CEA)</b>			<b>408.9</b>	<b>23.2</b>	<b>0.427</b>	<b>0.012</b>	<b>684.5</b>	<b>21.0</b>	<b>474.9</b>	<b>82.2</b>
<b>all</b>			<b>423.3</b>	<b>59.4</b>	<b>0.427</b>	<b>0.042</b>	<b>692.0</b>	<b>125.8</b>	<b>468.7</b>	<b>174.7</b>
<b>RESULTS for NM-103</b>										
CEA	47	20100927	112.1		0.244		139.2		72.34	
CEA	47	20110718	115.7		0.253		137.9		69.33	
CEA	47	20110722	113.6		0.258		139.5		80.34	
<b>Intra vial</b>			<b>113.8</b>	<b>1.8</b>	<b>0.252</b>	<b>0.007</b>	<b>138.9</b>	<b>0.9</b>	<b>74.0</b>	<b>5.7</b>
CEA	557	20110729	117.3		0.212		148		78.1	
CEA	557	20110915	112.6		0.255		141.4		86.51	
CEA	557	20110930	108		0.229		124.5		54.81	
<b>Intra vial</b>			<b>112.6</b>	<b>4.7</b>	<b>0.232</b>	<b>0.022</b>	<b>138.0</b>	<b>12.1</b>	<b>73.1</b>	<b>16.4</b>
INRS	576	N1	138.7		0.244		123.06			
INRS	576	N2	133.7		0.202		117.52			
INRS	576	N3	124.4		0.115		117.52			
<b>intra vial</b>			<b>132.3</b>	<b>7.3</b>	<b>0.187</b>	<b>0.066</b>	<b>119.4</b>	<b>3.2</b>		
<b>inter vial all (3)</b>			<b>119.6</b>	<b>11.0</b>	<b>0.224</b>	<b>0.033</b>	<b>132.1</b>	<b>11.0</b>	<b>73.6</b>	<b>0.6</b>
<b>all</b>			<b>119.6</b>	<b>10.5</b>	<b>0.224</b>	<b>0.045</b>	<b>132.1</b>	<b>11.4</b>	<b>73.6</b>	<b>11.0</b>
<b>RESULTS for NM-104</b>										
CEA	39	20110119	127.7		0.220		166		88.14	
CEA	39	20110214	128.8		0.224		172.4		103.6	
<b>intra vial</b>			<b>128.3</b>	<b>0.8</b>	<b>0.222</b>	<b>0.003</b>	<b>169.2</b>	<b>4.5</b>	<b>95.9</b>	<b>10.9</b>
CEA	465	20110072 2	130.6		0.226		169		90.98	
CEA	465	20110907	127.1		0.218		164.8		87.49	
CEA	465	20110929	129		0.216		156.7		74.69	
<b>intra vial</b>			<b>128.9</b>	<b>1.8</b>	<b>0.220</b>	<b>0.005</b>	<b>163.5</b>	<b>6.3</b>	<b>84.4</b>	<b>8.6</b>
NRCWE	1157	-1	125.9		0.220		161.8		85.44	
NRCWE	1157	-2	125.4		0.201		159.4		81.09	
NRCWE	1157	-3	123.5		0.196		155		74.55	
NRCWE	1157	-4	127.9		0.220		167.2		89.37	
NRCWE	1157	-5	124		0.211		158.7		82.98	
<b>intra vial</b>			<b>125.3</b>	<b>1.7</b>	<b>0.210</b>	<b>0.011</b>	<b>160.4</b>	<b>4.5</b>	<b>82.7</b>	<b>5.5</b>
NRCWE	803		124.6		0.204		160		80.14	
NRCWE	885		129.6		0.229		166.9		91.18	
<b>inter vial all (3 NRCWE)</b>			<b>126.5</b>	<b>2.7</b>	<b>0.214</b>	<b>0.013</b>	<b>162.4</b>	<b>3.9</b>	<b>84.7</b>	<b>5.8</b>
<b>inter vial all (5)</b>			<b>127.3</b>	<b>2.2</b>	<b>0.217</b>	<b>0.010</b>	<b>164.0</b>	<b>4.0</b>	<b>86.9</b>	<b>6.5</b>
<b>all</b>			<b>127.0</b>	<b>2.3</b>	<b>0.215</b>	<b>0.010</b>	<b>163.2</b>	<b>5.3</b>	<b>85.8</b>	<b>8.0</b>

Institution	Vial no.	Repetition / date	Z-average	(SD)	PdI	(SD)	Intensity distribution main peak	(SD)	FWHM peak width	(SD)
<b>RESULTS for NM-105</b>										
CEA	305	20100209	128		0.162		155.1		69.71	
CEA	305	20101006	120.7		0.192		152.4		74.72	
CEA	305	20101011	121.6		0.189		153.3		73.72	
CEA	305	20110705	122.7		0.143		143.1		58.42	
CEA	305	20110928	129.3		0.172		156.2		69.59	
<b>intra vial</b>			<b>124.5</b>	<b>3.9</b>	<b>0.172</b>	<b>0.020</b>	<b>152.0</b>	<b>5.2</b>	<b>69.2</b>	<b>6.5</b>
INRS	2194	N1	313.7		0.061		141.29			
INRS	2194	N2	134.0		0.052		134.93			
<b>intra vial</b>			<b>132.9</b>	<b>1.6</b>	<b>0.057</b>	<b>0.006</b>	<b>138.1</b>	<b>4.5</b>		
NRCWE	2758		135.6		0.134		156.5		61.83	
NRCWE	2749		127.9		0.145		151.4		63.85	
NRCWE	2701		127.8		0.143		150.7		61.86	
NRCWE	2176	20111123	130.1		0.170		158.1		72.26	
<b>inter vial (3-NRCWE)</b>			<b>130.4</b>	<b>4.5</b>	<b>0.141</b>	<b>0.006</b>	<b>152.9</b>	<b>3.2</b>	<b>62.5</b>	<b>1.2</b>
<b>inter vial all (6)</b>			<b>129.8</b>	<b>4.0</b>	<b>0.137</b>	<b>0.042</b>	<b>151.1</b>	<b>7.0</b>	<b>65.8</b>	<b>4.7</b>
<b>all</b>			<b>128</b>	<b>4.7</b>	<b>0.142</b>	<b>0.044</b>	<b>150.3</b>	<b>7.1</b>	<b>67.3</b>	<b>5.8</b>



## 8. Zeta potential

Appendix B gives the detailed procedures for the measurements performed. Samples for zeta potential measurements were prepared by CEA as aqueous suspensions of 0.5 g/L TiO<sub>2</sub> NMs with a constant ionic strength of 0.036 mol/L (monovalent salt) and controlled pH. Concentrated sonicated stock suspensions of 10 g/L in pure water was diluted into pH and ionic strength controlled “buffers” prepared by addition of HNO<sub>3</sub>, NaOH and NaNO<sub>3</sub> in various proportions. For each suspension of known pH, fixed ionic strength and fixed NM concentration, a "general purpose mode" was used for the zeta potential measurements with automatic determination of measurement parameters (position of the laser focus, attenuator, number and duration of runs). For each data point three measurements were performed and the average value was reported. Zeta potentials were then plotted against pH to determine the stability domains and isoelectric point (IEP).

Figure 31 shows the zeta potential vs. pH for NM-102 to NM-105 while the corresponding IEP values are shown in the inserted table (right, top corner of the figure). Results obtained for unstable sample preparations, which are strongly aggregated and sediment, are marked with the half-filled dots. For these sample preparations, zeta potential was measured on supernatants. In Figure 32, a photograph is presented of NM-103 dispersion in constant ionic strength aqueous solution.

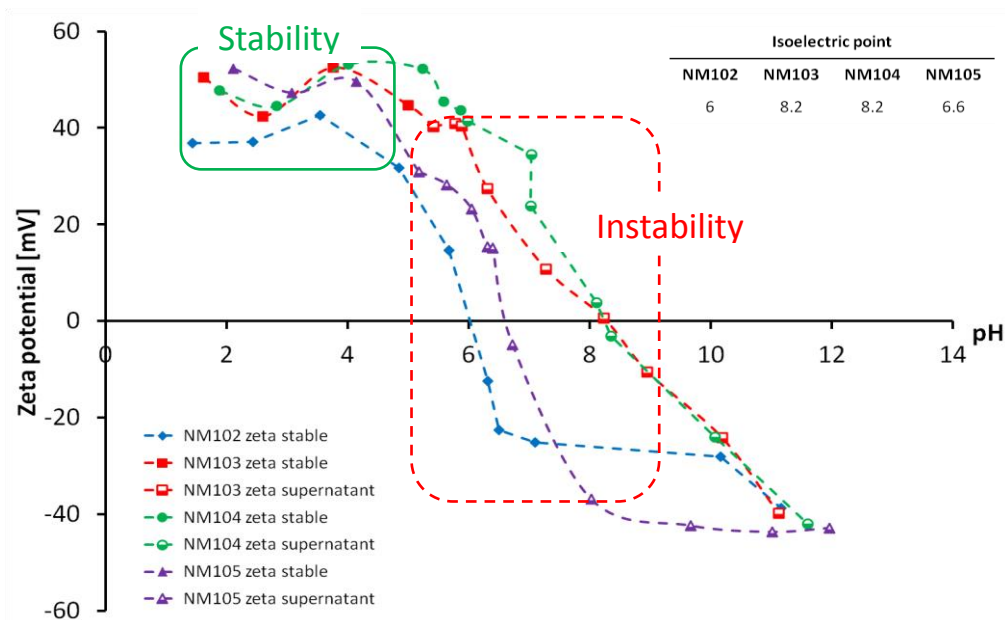


**Figure 31. Zeta potential as a function of pH for TiO<sub>2</sub> NM suspensions (0.5 g/L) in constant ionic strength aqueous media (0.036 mol/L HNO<sub>3</sub>/NaOH), highlighting the domain of higher stability for pH lower than 5; the IEP values are also reported in the figure.**

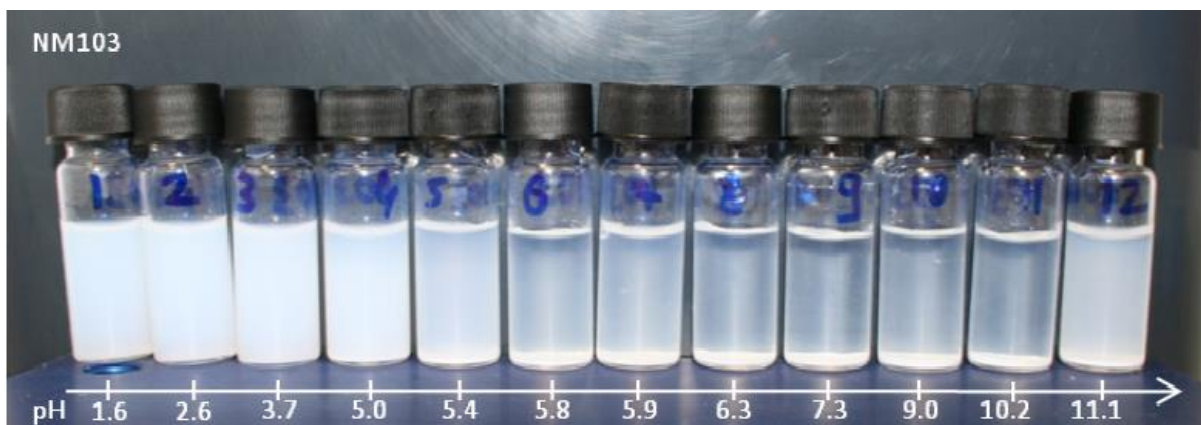


**Figure 32. Photograph of NM-103 series of sample preparations, 0.5 g/L NM-103 in constant ionic strength aqueous media ( $\text{HNO}_3/\text{NaOH}$  0.036 mol/L).**

NM-102 to NM-105 were tested and they form stable suspensions at acidic pH (below pH 4) where the NMs have high positive charge, exceeding 30 mV. Negative zeta potentials, lower than -30 mV, were observed at high pH values (from 2 pH units above the IEP). The IEP obtained for NM-102 and NM-105 (pH 6 to 7), are in accordance with expected values for  $\text{TiO}_2$  nanomaterials (Marek K., 2009)). The higher IEP of pH 8.2 observed for NM-103 and NM-104 can be explained by the presence of an  $\text{Al}_2\text{O}_3$  coating on the surface of these nanoparticles, similarly to other observations from the literature regarding alumina particles (Singh et al. 2005). In addition, NM-103 and NM-104 were unstable at pH-levels around 6 despite measuring a zeta-potential of app. +40 mV on their supernatant. This may be due to surface heterogeneities of these NM leading to populations of NP with different Zpot and stability properties.

The average aggregate sizes measured by DLS (not presented here) increase when increasing pH from the acidic stability domain toward the isoelectric points. This is consistent with theory where agglomeration and hence average size will increase with decreasing surface charge. For higher pH, suspensions were not stable and sediment rapidly. Stability should, however, be regained at high pH values, where the negative zeta potentials become smaller than -40 mV.

## 9. SAXS and USAXS measurements and data treatment

Small-angle X-ray scattering (SAXS) is a technique based on the interaction between X-rays and matter to probe the structure of materials. The processed data are the intensity,  $I$ , of X-ray scattered by a sample as a function of angular position of a detector, see Figure 33.

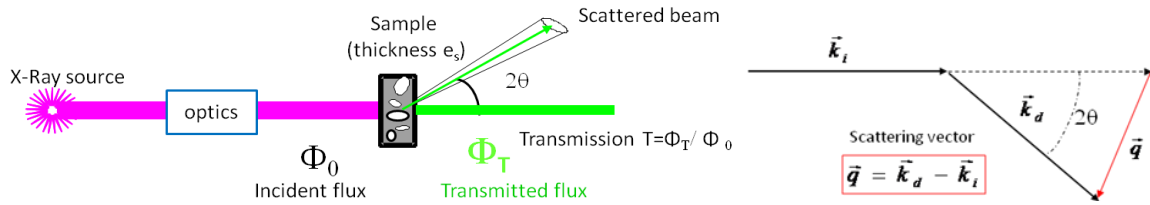


**Figure 33. Schematic set up for SAXS and physical quantities.**

The intensity is expressed in absolute scale,  $cm^{-1}$ , independent from test parameters such as X-ray wavelength, experimental background, time of acquisition and sample thickness. 2D raw data images are converted into diffractograms displaying the scattered intensity  $I$  as a function of scattering vector  $q$  defined by:

$$q = \frac{4\pi \sin \theta}{\lambda}$$

$\lambda$ : X-ray wavelength

Ultra small angle X-ray scattering (USAXS) measurements give access to X-ray scattering data for a smaller range of  $q$  and then complement the SAXS diffractograms. It requires a specific and very precise set-up, usually different from the one used for SAXS. General theorems of experimental physics have been developed for the interpretation of the diffractograms to extract different properties of nanostructured materials, such as shape of nanoparticles, surface area, interactions occurring, etc.

In the high  $q$  range, diffractograms display an intensity decrease in a  $q^{-4}$  trend, called the “Porod region”, corresponding to the “real space” to the scale of the interfaces (for smooth interfaces). Therefore, for a sample with two phases, the asymptotic limit of the “Porod’s plateau”, when data are represented as  $Iq^4=f(q)$ , is related to the total quantity of interface  $\Sigma$  (in  $m^2/m^3$ ) between the two phases, as follows (Porod’s law):

$$\Sigma [m^{-1}] = \frac{\lim_{plateau} (I \cdot q^4)}{2\pi(\Delta\rho)^2}$$

$\Delta\rho$  is the difference in scattering length density between the two phases.

To treat raw SAXS data and obtain absolute intensities, the intensity related to the thickness of the scattering material need to be normalised. For powder samples where sample thickness has no real meaning, a model system is used, in which the effective thickness of material crossed by X-rays,  $e_B$ , is considered and it corresponds to a thickness equivalent to the material arranged in a fully dense (no inner or outer porosity) and uniform layer. The sample transmission is related to this equivalent thickness by the following equation:

$$e_B = -\frac{1}{\mu} \ln(T_{\text{exp}})$$

where  $\mu$ : material absorption coefficient for X-rays ( $\mu_{\text{SiO}_2} = 470\text{cm}^{-1}$ ) and  $T_{\text{exp}}$  is the experimental transmission (transmitted flux  $\Phi_T$ /incident flux  $\Phi_0$ ), i.e. transmission of the sample plus cell with regard to the transmission of the empty cell (kapton alone, empty capillary, etc.).

The intensity scaled by this thickness  $e_B$  is called  $I_1$ . Porod's law can then be applied for  $I_1$  to calculate the specific surface area of the powder. The optimum parameters for measurements are given in Table 26.

**Table 26. Material properties considered and corresponding calculated optimum thickness of dense material for a sample transmission of 0.3.**

Material	Density	Scattering length density	Absorption coefficient ( $\mu$ )	Optimum thickness ( $e_B$ )
TiO <sub>2</sub>	4.23 g/cm <sup>3</sup>	$3.418 \cdot 10^{11} \text{ cm}^{-2}$	470 cm <sup>-1</sup>	25 $\mu\text{m}$

Firstly, the TiO<sub>2</sub> powder samples were prepared between two sticky kapton® films pressed on a 0.4 mm brass cell (typical thickness of dense material around 30  $\mu\text{m}$ ). However, it was inferred that the presence of glue may affect the calculation of the specific surface area of powders. Therefore, in a subsequent step, the TiO<sub>2</sub> powder samples were measured in a flattened polyimide capillary, mounted on a circular sample holder. The typical equivalent thickness of dense material obtained was 30  $\mu\text{m}$ .

SAXS measurements were performed by CEA using kapton capillaries of internal thickness 1.425 mm and run for 3600s. USAXS measurements were performed in 1 mm or 1.5 mm non-sticky double kapton cells. A measurement is considered optimal for a transmission around 0.3 and the optimum thicknesses  $e_B$  for the TiO<sub>2</sub> NMs are gathered in Table 27.

For each TiO<sub>2</sub> NM, two SAXS measurements were performed, one with a short acquisition time to prevent saturation of the detector, typically 200 s or 150 s, and one with a long-time acquisition of 1800 s to lower the signal/noise ratio at high  $q$ .

**Table 27. Experimental parameters for the TiO<sub>2</sub> NMs.**

Material	Cell	$e_B$	$T_{exp}$
NM-101	Flattened kapton capillary	25 $\mu\text{m}$	0.31
NM-102		27 $\mu\text{m}$	0.28
NM-103		23 $\mu\text{m}$	0.33
NM-104		36 $\mu\text{m}$	0.18
NM-105		31 $\mu\text{m}$	0.23

Image treatment and calculations on radial averaged data are described in Appendix D for SAXS and USAXS data. It includes normalisation of the intensity by the parameters of the experiments, e.g. acquisition time, sample thickness, calibration constants determined using reference samples and background subtraction. SAXS data obtained for short time and long-time and USAXS data are merged to get continuous diffractograms for the whole  $q$  range.

All specific surface area results, together with their uncertainty calculations are presented below. Errors on the Porod's plateaus have been determined manually for each diffractogram, and the uncertainty on the material density is considered to be about 5 %.

The specific surface areas of powders are determined on the Porod plateau, see Appendix D. More details regarding the general principles of measurement and the measurement technique as well as the data treatment are described in Appendix D.

### 9.1. Stability of the samples

The stability of suspensions prepared for the SAXS measurements was followed by DLS and the DLS measurements are shown in Figure 27 for NM-102, NM-103, NM-104 and NM-105.

### 9.2. Size and structure of fractal aggregates by SAXS

All SAXS diffractograms and the corresponding representations in  $I(q)q^4$  for TiO<sub>2</sub> powders are displayed in Figure 34 to Figure 37.

The SAXS diffractograms and the corresponding fitting size and morphology parameters for different NMs vary. In particular, the NM-102 SAXS diffractogram differs from the other NMs. NM-103, NM-104 and NM-105 have similar size of particles ( $2 R_{g1}^3 = 26 \text{ nm}$ ) and display very loose aggregates of fractal dimension close to 2.3 whereas NM-102 is characterised by much smaller particles ( $2 R_{g1} = 12.8 \text{ nm}$ ) but actually assembled into very dense and compact 3D aggregates which reflected in a fractal dimension of 3. These findings were also confirmed by TEM micrographs.

---

<sup>3</sup>  $R_{g1}$  = radius of gyration of primary particles

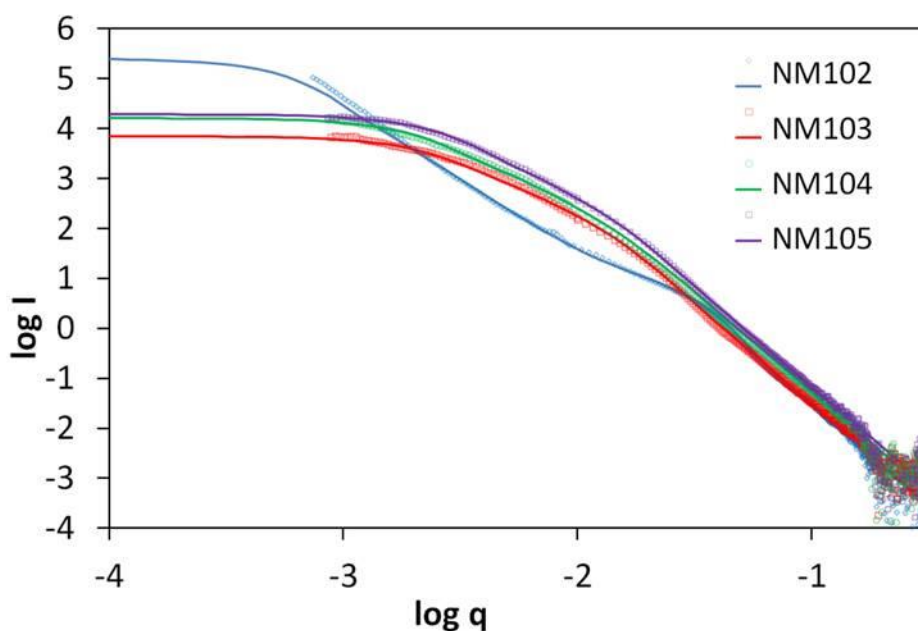


**Figure 34. SAXS diffractograms fitted by the unified model for TiO<sub>2</sub> suspensions ultrasonicated (20 min - 40 %) in HNO<sub>3</sub> 10<sup>-2</sup> M.\*NM-102 cannot be perfectly fitted at low q with D<sub>f</sub> <3.**

The structure and main size parameters determined by the model, i.e. radius of gyration of primary particles ( $R_{g1}$ ), radius of gyration of aggregates ( $R_{g2}$ ) fractal dimension ( $D_f$ ) and average number of primaries per aggregates ( $N_{part/agg}$ ) are reported in Appendix D. The full sets of parameters used for the fit of experimental curves with the unified model are gathered in Appendix D. Table 28 gives an overview of the size parameters obtained. The increase of intensity observed at low  $q$  for NM-102 cannot be fitted by the model, and parameters extracted from such a poor fit are unreliable and thus not reported here.

**Table 28. Structure and size parameters extracted from SAXS data fitting by the unified model from TiO<sub>2</sub> suspensions ultrasonicated (20 min at 40 % amplitude) in HNO<sub>3</sub> 10<sup>-2</sup>M. Gyration diameter of primary particles (2  $R_{g1}$ ) and aggregates (2  $R_{g2}$ ), fractal dimension  $D_f$  and number  $N_{part/agg}$  of particles per aggregate.**

Main size and structure parameters from SAXS unified fit model				
	2 $R_{g1}$ (nm)	2 $R_{g2}$ (nm)	$D_f$	$N_{part/agg}$
NM-102*	12.8	560	3	20000
NM-103	26	140	2.2	113
NM-104	26	160	2.3	171
NM-105	26	130	2.45	117

\*NM-102 measurements cannot be fitted to the model at low  $q$  at  $D_f < 3$ , and very different values of the parameters would lead to the same (bad) fit. Therefore, no parameters are reported.

The calculation results for specific surface area of TiO<sub>2</sub> powders, expressed in m<sup>-1</sup> and in m<sup>2</sup>/g, together with uncertainty estimations, are reported in Table 29. The diameter

calculated in the last column corresponds to the size of dense, perfectly monodisperse and spherical TiO<sub>2</sub> nanoparticles that would exhibit the same mean surface area.

**Table 29. Specific surface area measured by SAXS for the TiO<sub>2</sub> NMs.**

Material	$\text{Lim } Iq^4$ ( $10^{-3} \text{ cm}^{-1} \text{ \AA}^{-4}$ )	$\Sigma$ ( $\text{m}^{-1}$ )	Specific surface area ( $\text{m}^2/\text{g}$ )	Error on plateau ( $\text{m}^2/\text{g}$ )	+ 5% error on density ( $\text{m}^2/\text{g}$ )	Equivalent diameter for spheres (nm)
<b>NM-101</b>	52.7	7.17E+08	169.5	$\pm 8.5$	$\pm 25.4$	8
<b>NM-102</b>	20.4	2.78E+08	65.6	$\pm 3.3$	$\pm 9.8$	22
<b>NM-103</b>	15.9	2.16E+08	51.1	$\pm 1.8$	$\pm 6.9$	28
<b>NM-104</b>	16.3	2.22E+08	52.4	$\pm 2.1$	$\pm 7.3$	27
<b>NM-105</b>	14.6	1.99E+08	47.0	$\pm 2.3$	$\pm 7.0$	30

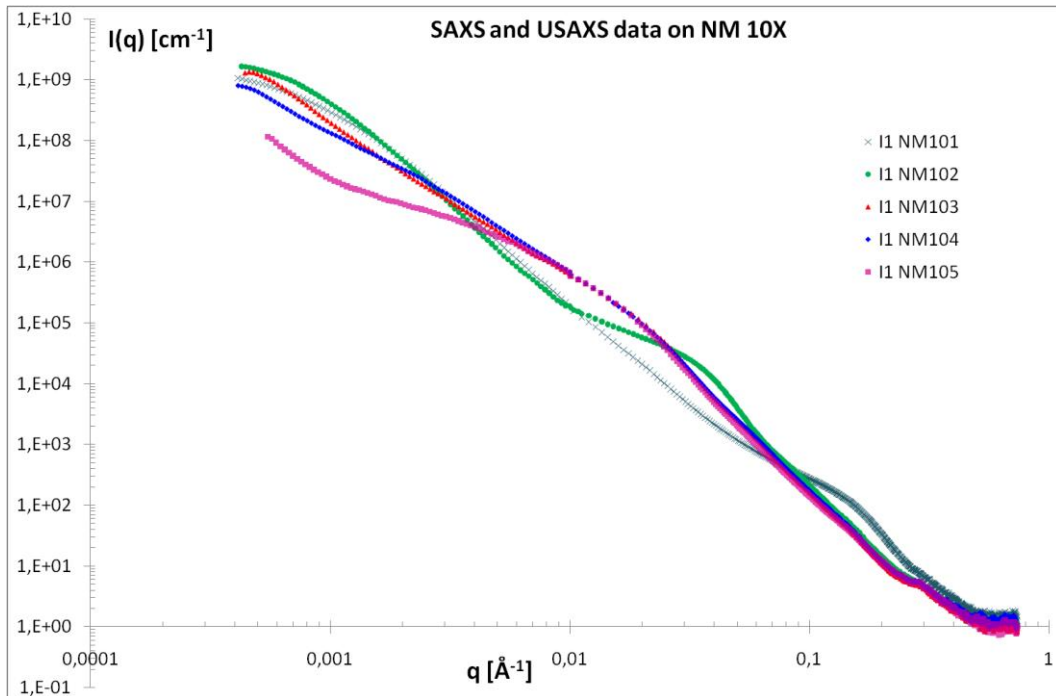


**Figure 35. SAXS and USAXS results for TiO<sub>2</sub> raw powders NM-101 (blue crosses), NM-102 (green circles), NM-103 (red triangles), NM-104 (blue diamonds) and NM-105 (pink squares).**

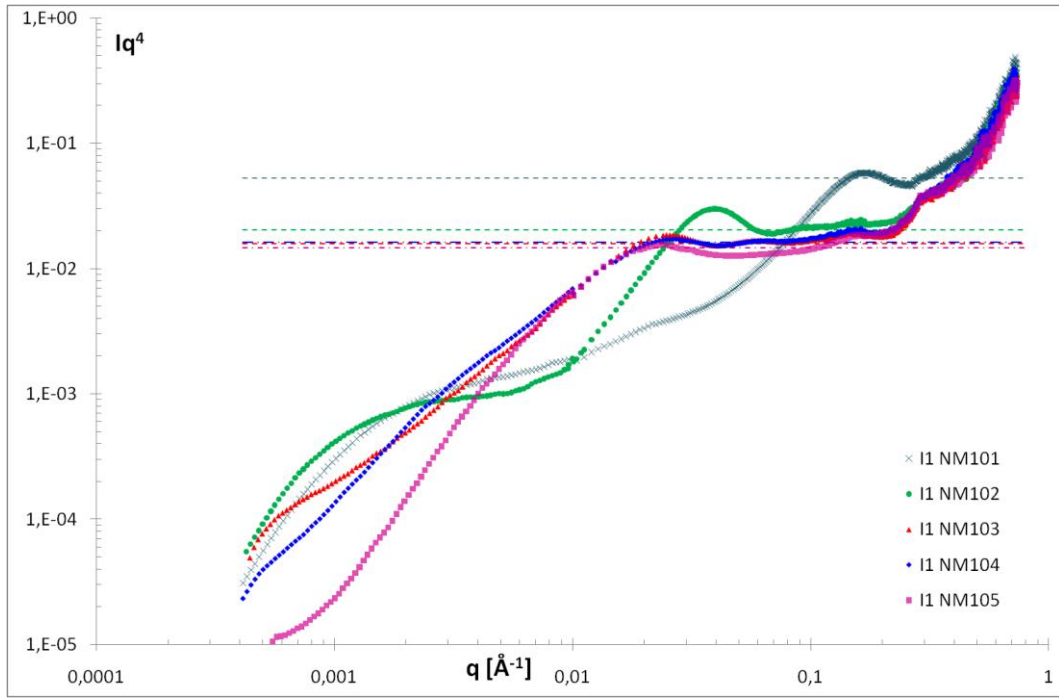
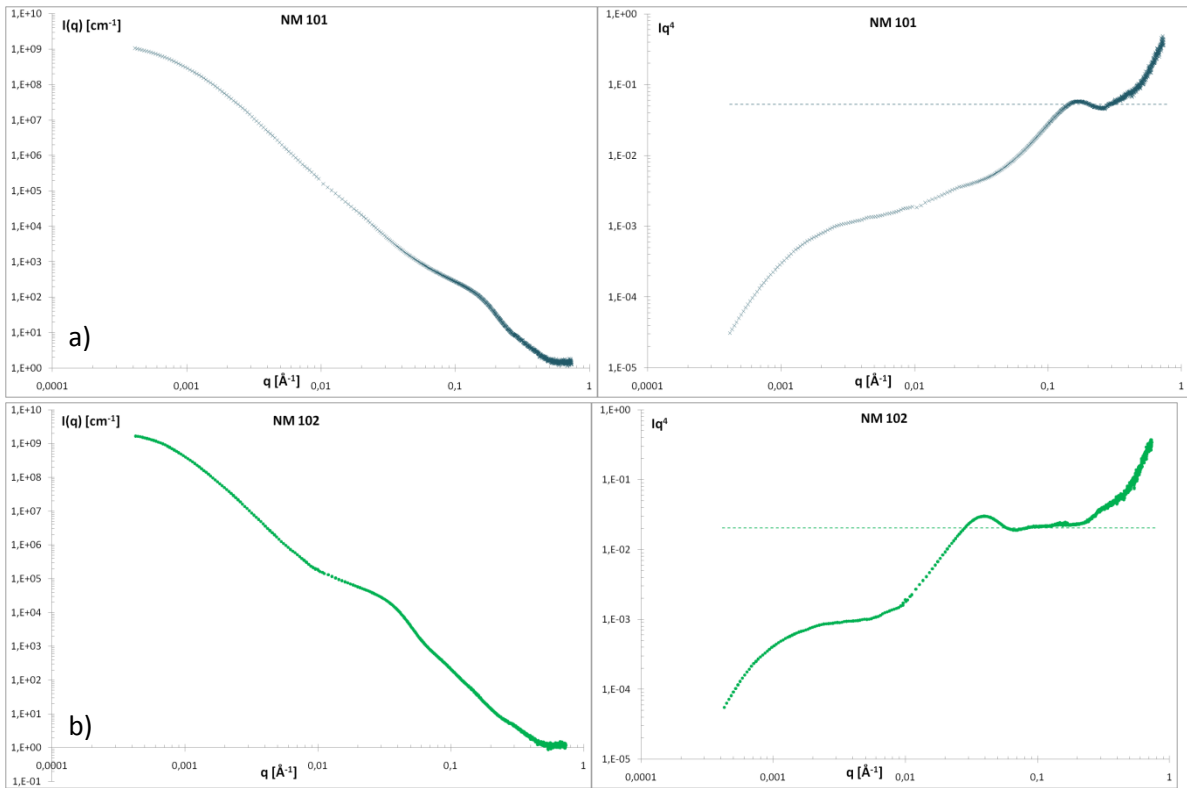


Figure 36. Representation in  $Iq^4$  of SAXS and USAXS results of **NM-101 (blue crosses)**, **NM-102 (green circles)**, **NM-103 (red triangles)**, **NM-104 (blue diamonds)** and **NM-105 (pink squares)**. The dotted lines are the corresponding Porod's plateaus.





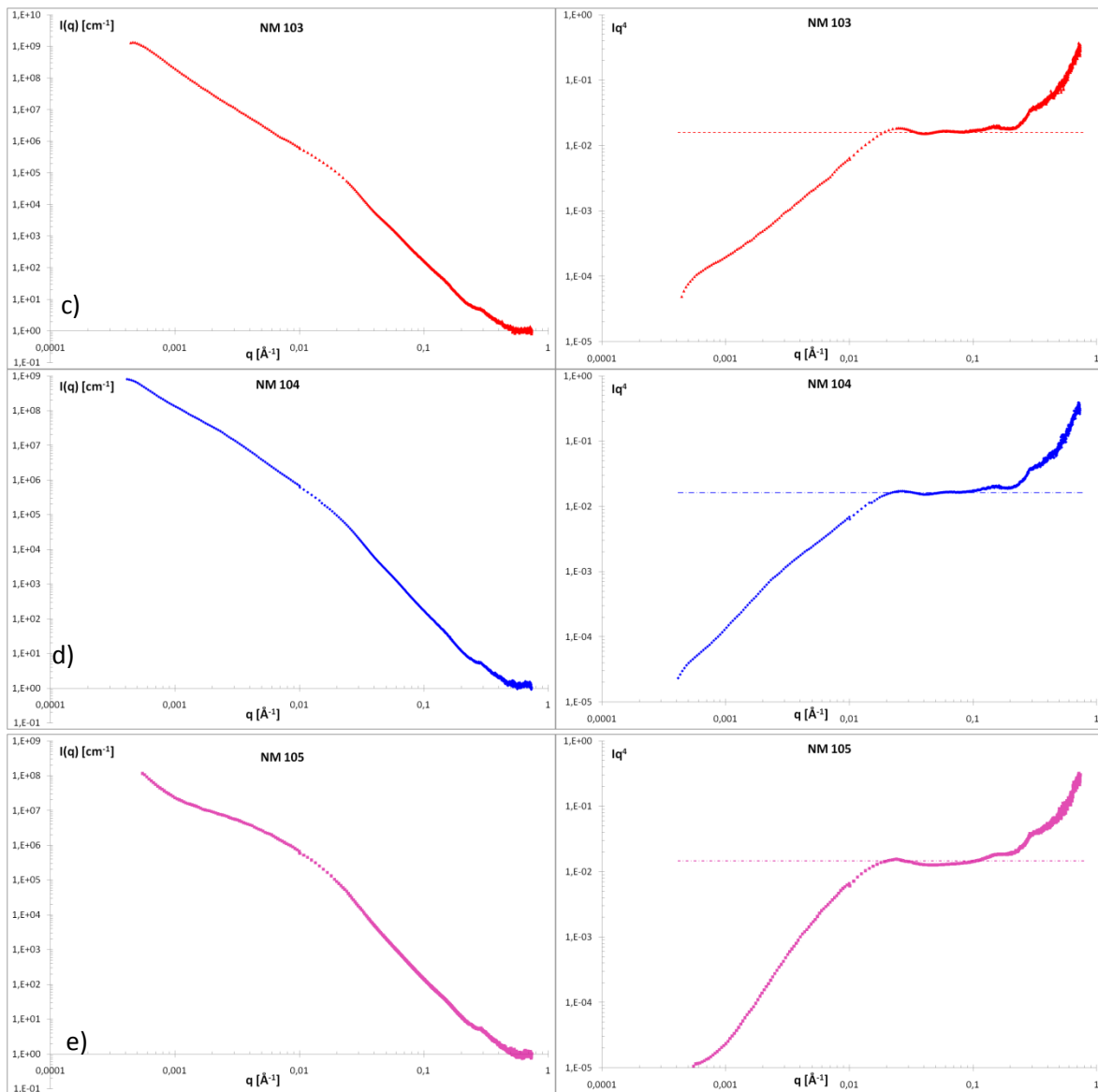


Figure 37. SAXS and USAXS results for  $\text{TiO}_2$  raw powders of a) NM-101, b) NM-102, c) NM-103, d) NM-104 and e) NM-105.  $I(q)$  representations on the left;  $I(q)q^4$  representation revealing Porod's plateaus on the right.

## 10. Brunauer, Emmett and Teller (BET) measurements

The most widely used technique for estimating surface area and porosity is the BET method (Brunauer, Emmett and Teller, 1938). The concept of the theory is an extension of the Langmuir theory for monolayer molecular adsorption to multilayer adsorption with the following hypotheses: (a) gas molecules physically adsorb on a solid in layers infinitely; (b) there is no interaction between each adsorption layer; and (c) the Langmuir theory can be applied to each layer. The BET equation is

$$\frac{1}{v[(p_0/p) - 1]} = \frac{c - 1}{v_m c} \left( \frac{p}{p_0} \right) + \frac{1}{v_m c}$$

where  $p$  and  $p_0$  are the equilibrium and the saturation pressure of adsorbates at the temperature of adsorption,  $v$  is the adsorbed gas quantity (for example, in volume units), and  $v_m$  is the monolayer adsorbed gas quantity,  $c$  is the BET constant.

$$c = \exp\left(\frac{E_1 - E_L}{RT}\right)$$

where  $E_1$  is the heat of adsorption for the first layer, and  $E_L$  is that for the second and higher layers and is equal to the heat of liquefaction.

The equation is an adsorption isotherm and can be plotted as a straight line with the y-axis showing  $1/v[(P_0/P)-1]$  and  $\phi = P/P_0$  on the x-axis according to experimental results (BET plot).  $P$  is the equilibrium pressure and  $P_0$  is the saturation pressure. The value of the slope,  $A$ , and the y-intercept,  $I$ , of the line are used to calculate the monolayer adsorbed gas quantity  $V_m$  and the BET constant  $c$ . The following equations are used:

$$v_m = \frac{1}{A + I} \quad \text{and} \quad c = 1 + \frac{A}{I}$$

A total surface area  $S_{BET, total}$  and a specific surface area  $S_{BET}$  are estimated by the following equations:

$$S_{BET, Total} = \frac{v_m N S}{V} \quad \text{and} \quad S_{BET} = \frac{S_{Total}}{a}$$

where  $v_m$  is in units of volume which are also the units of the molar volume of the adsorbate gas,  $N$  is Avogadro's number,  $S$  is the adsorption cross section of the adsorbing species,  $V$  is the molar volume of adsorbate gas,  $a$  is the mass of adsorbent (in g).

## 10.1. BET results

The results for the specific surface area, pore volume and microporosity of the TiO<sub>2</sub> NMs obtained by IMC-BAS are summarised in Table 30.

The nitrogen adsorption isotherms for the TiO<sub>2</sub> NMs are shown in Figure 38 and the curves (except for NM-102) are very similar in shape suggesting that the TiO<sub>2</sub> NMs (except NM-102) have very similar behaviour. For the TiO<sub>2</sub> NMs (except for NM-102) BET results were straightforward and after data treatment produced very good correlation coefficients. NM-102 is photocatalytic anatase and thus the initial desorption may lead to some changes. Nevertheless, surface area of NM-102 stated by the producers and the one measured here are quite similar (90 vs 78 m<sup>2</sup>/g).

**Table 30. Results of the IMC-BAS BET measurements of the TiO<sub>2</sub> NMs.**

	<b>BET surface</b> m <sup>2</sup> /g	<b>Total pore volume</b> mL/g	<b>Micro surface area</b> m <sup>2</sup> /g	<b>Micropore volume</b> mL/g
<b>NM-100</b>	9.230	0.0324	0.0	0.0
<b>NM-101</b>	316.07	0.3190	13.625	0.00179
<b>NM-102</b>	77.992	0.2996	1.108	0.00034
<b>NM-103</b>	50.835	0.2616	0.0	0.0
<b>NM-104</b>	56.261	0.1935	0.0	0.0
<b>NM-105</b>	46.175	0.1937	0.0	0.0

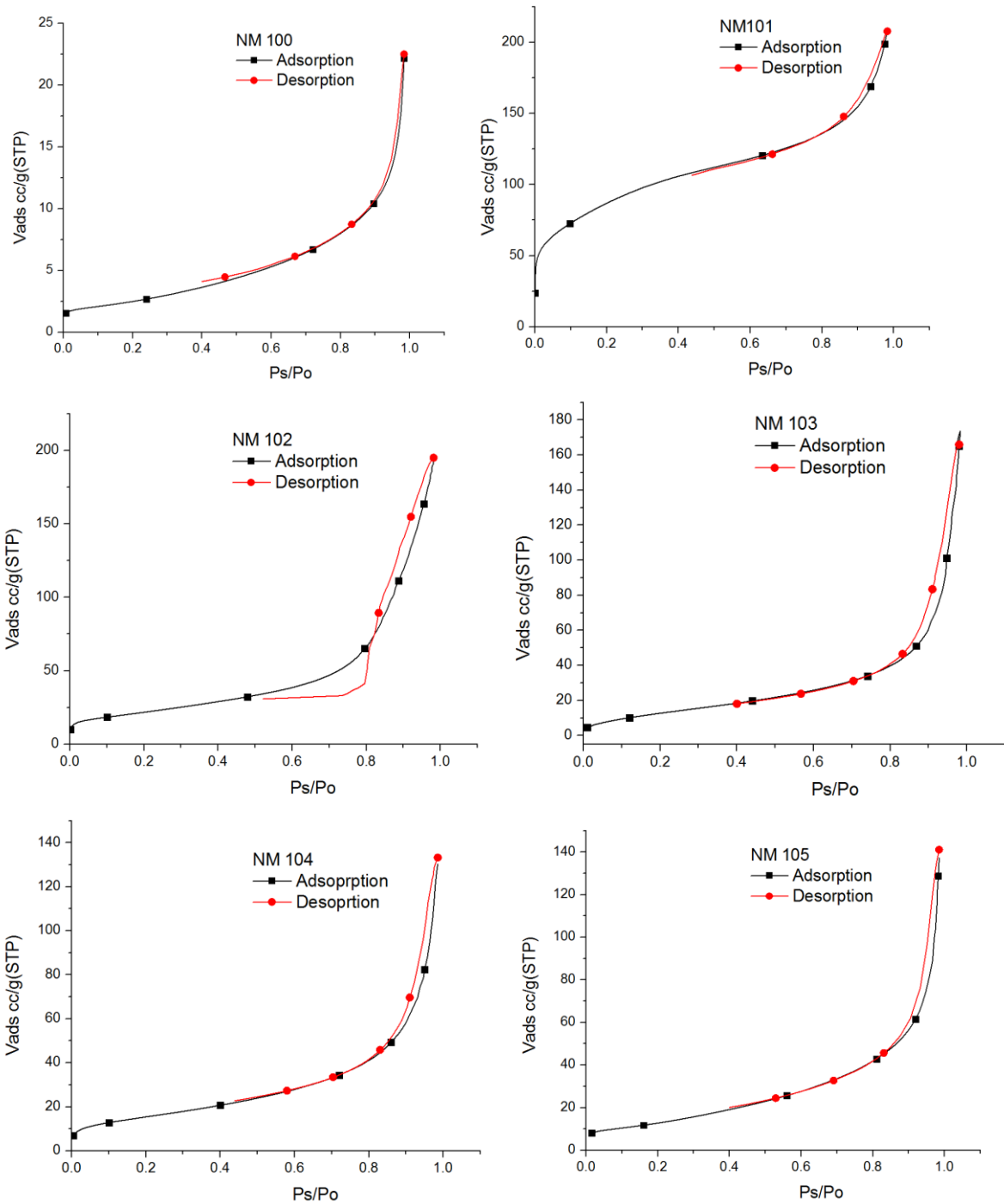


**Figure 38. Isotherms of nitrogen sorption experiments by IMC-BAS at 77K for TiO<sub>2</sub> NMs giving the adsorbed volume ( $V_{ads}$ ) in  $\text{cm}^3$  per gram ( $\text{cc/g}$ ) [y-axis] and  $P/P_0$  on the x-axis. The NM-numbers are mentioned in the title of each plot.**

The results for the specific surface area of TiO<sub>2</sub> NMs obtained by JRC are summarised in Table 31. The JRC measurements were multipoint BET measurements and were performed on NMs samples stored at two different temperatures: -80 °C and room temperature.

**Table 31. Results of the JRC BET measurements of TiO<sub>2</sub> NMs.**

Material	Vial No.	Storage temperature for the sample	BET surface. m <sup>2</sup> /g	Δ% (40 °C vs -80 °C)
NM-100	00682	40 °C	10.03	3.08 %
	03358	-80 °C	10.35	
NM-101	0344	40 °C	234.47	2.33 %
	1443	-80 °C	229.00	
NM-102	0222	40 °C	78.97	4.71 %
	1130	-80 °C	82.88	
NM-103	1067	40 °C	51.69	1.60 %
	1137	-80 °C	50.86	
NM-104	04560	40 °C	57.07	0.19 %
	02243	-80 °C	57.18	
NM-105	04924	40 °C	52.81	1.58 %
	03245	-80 °C	53.66	
	2293	40 °C	53.37	3.82 %
	06542	-80 °C	55.49	

## 10.2. Comparison between BET data from research laboratories and producers

In Table 32, the results from the BET analyses made here are compared with data provided by manufacturers of the industrial materials. Despite clear differences in absolute numbers, it is evident that there is an overall quite good comparability between the three data sets. The results suggest reasonable material homogeneity and/or that both the NANOGENOTOX and producer instrumental capacity and the SOPs for BET analysis are of similar quality. However, a final conclusion cannot be made on comparability as the results were not produced using traceable standards for calibration or benchmarking.

**Table 32. Comparison of BET data by the manufacturers and measured in the NANOGENOTOX project, and SAXS data.**

Material	BET surface Producer (m <sup>2</sup> /g)	BET surface IMC-BAS (m <sup>2</sup> /g)	BET surface JRC (range)* (m <sup>2</sup> /g)	SAXS surface CEA (m <sup>2</sup> /g)
NM-100	-	9.230	10.03-10.35	-
NM-101	>250	316.07	234.47-229.00	169.5(± 8.5)
NM-102	90	77.992	78.97-82.88	65.6(± 3.3)
NM-103	60	50.835	51.69-50.86	51.1(± 1.8)
NM-104	60	56.261	57.07-57.18	52.4(± 2.1)
NM-105	50(± 15)	46.175	52.81-55.49	47.0(± 2.3)

\*the JRC measurements reflect samples stored at two different temperatures and two different BET measurements, see Table 31.

### 10.3. Comparison of SAXS and BET data

The TiO<sub>2</sub> NMs were analysed with regard to specific surface area using both BET and SAXS and there is good agreement between the results obtained by these two techniques, see Table 32. As shown in Figure 38, an almost linear relationship between SAXS and BET specific surface area was observed for NM-102 to NM-105. Only for one material, NM-101, a relatively large difference was observed and the value of SSA obtained from the BET model was twice as big as the one from SAXS measurements.

In the Specific Surface Area assessment, differences and limitations of the BET and SAXS methods also need to be considered. For SAXS, most of the differences in the obtained results may be explained by the combined errors in density and placement of plateau. For BET an explanation is the difference in thermal treatment and outgassing of the powders before BET analysis. Indeed, thermogravimetric analysis showed a major weight loss in the analysis of NM-101, which could come from adsorbed water “wrapping” the nanoparticles and therefore the reason for a decrease of the X-ray contrast and subsequently of the specific surface area seen by SAXS.

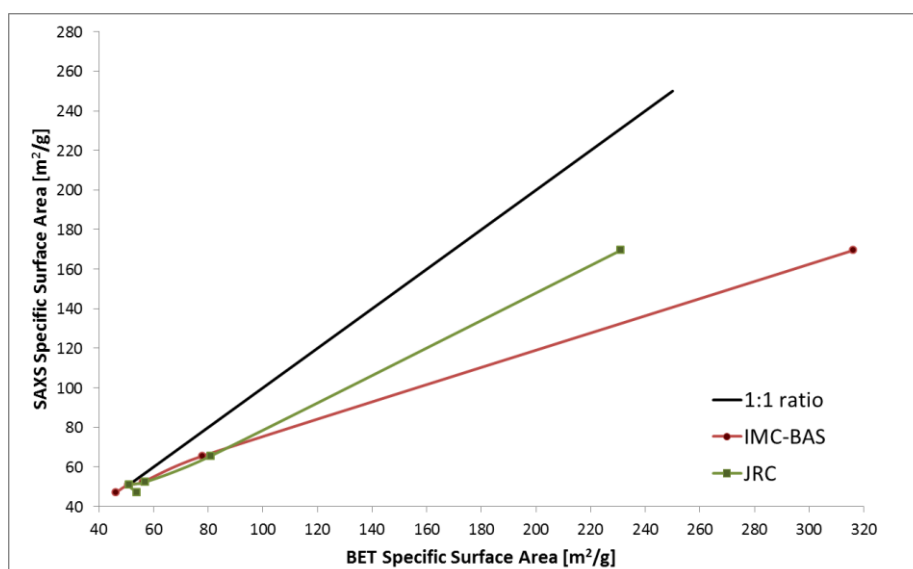
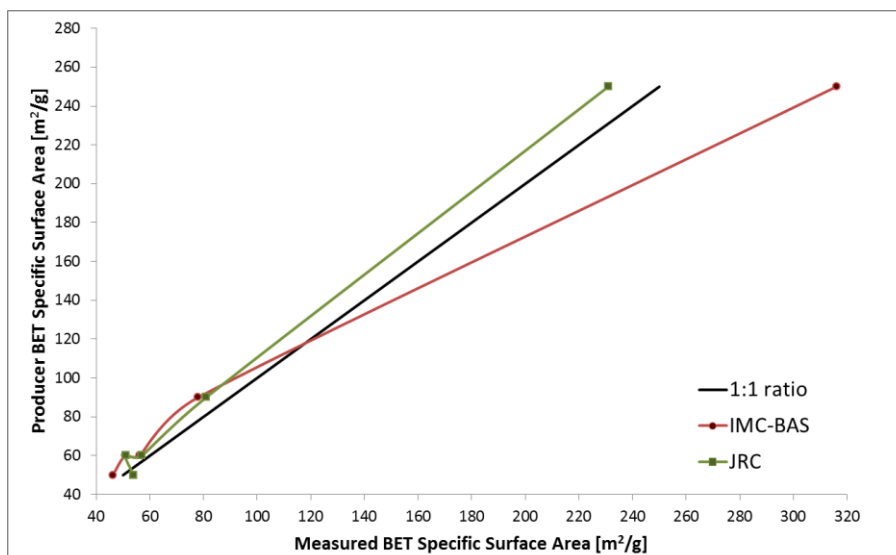


Figure 39a. SAXS specific surface area data plotted against the BET specific surface area data.



**Figure 39b. Producer BET specific surface area data plotted against the measured BET specific surface area data.**

It should also be mentioned that the SAXS Porod plateau is determined in a  $q$  range up to  $0.3 \text{ \AA}^{-1}$ , which corresponds in the direct space to dimensions down to 2 nm. This means that it is very difficult to estimate a roughness smaller than 2 nm under these conditions (leading to an additional surface area). This could explain why, in BET measurements,  $N_2$  molecules, smaller than 2 nm, might in general “see” more surface; therefore the determination of surface area for very small and bigger (>200 nm) particles needs more attention. Both of these issues could be of great importance for the SSA measurements of high-surface area nanomaterials.

## 11. XRD measurements

### 11.1. XRD analysis

X-Ray Diffraction (XRD) analysis is based on the principle that crystalline materials diffract X-rays in a characteristic pattern unique for each material. In this technique, a beam of X-rays is diffracted into many specific directions on regular atomic lattice, which allows determining the atomic and molecular structure of a crystal. XRD can therefore be used to identify different polymorphs, such as typical  $\text{TiO}_2$  polymorphs rutile, brookite and anatase. The width of the reflections can also give information about the size of the diffracting domains (crystallites), which for nanoparticles may often (but not always) correspond to particle size.

An important factor in the determination of the particle size by means of XRD is the instrument contribution to the width of the XRD profile. Each instrument has a unique contribution to the X-ray diffraction profile, which should be documented for detailed data comparisons using e.g. a large crystallite standard. For the analysis, IMC-BAS used quartz ( $\text{SiO}_2$ ) (NIST SRM1878, median particle size of 1.4  $\mu\text{m}$  after grinding) and NRCWE used a  $\text{CeO}_2$  (NIST SRM674a) standard. To assess the contribution from the two instruments, the full width at half maximum, FWHM, was measured on the standards and plotted as a radian angle. It is seen that the contribution from the instrument is greater and with some variability for the instrument at IMC-BAS than the instrument used by NRCWE.

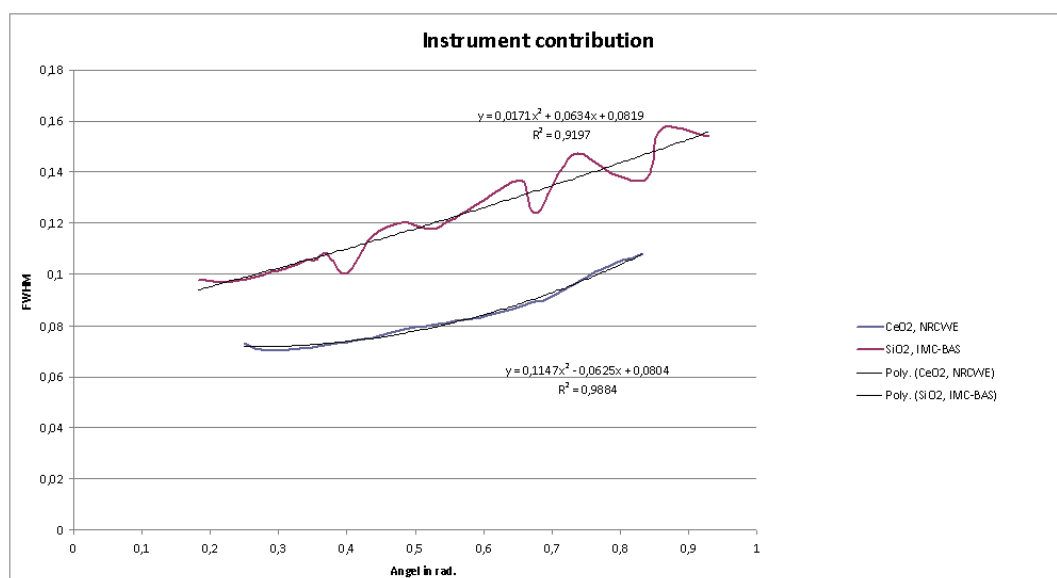


**Figure 40.** Graph of instrument contribution to the width of the reflections for data collected by NRCWE and IMC-BAS. The x-axis is the angle in radians and the y-axis is FWHM.

Table 33 and Figure 40 show the theoretical contribution from the instruments at IMC-BAS and at NRCWE. The instrument contribution is found as the FWHM of the reflections in the



dataset of standards.  $2\theta$  is expressed in radians. For each instrument the best fit for FWHM (standard) as a function of  $2\theta$  (radians) is found. The difference between the two instruments is calculated for four specific points.

**Table 33. Summary of the theoretical contributions for the instrument at IMC-BAS and NRCWE.**

$2\theta$	Rad	Contribution from instrument at IMC-BAS (Rad)	Contribution from instrument at NRCWE (Rad)	Difference (Rad)	Comment
<b>25.31</b>	0.220871	0.096737	0.072191	0.0245464	Anatase, highest reflection
<b>27.434</b>	0.239407	0.098058	0.072011	0.0260473	Rutile, highest reflection
<b>50</b>	0.436332	0.112819	0.074966	0.0378526	
<b>75</b>	0.654498	0.13072	0.088628	0.0420926	

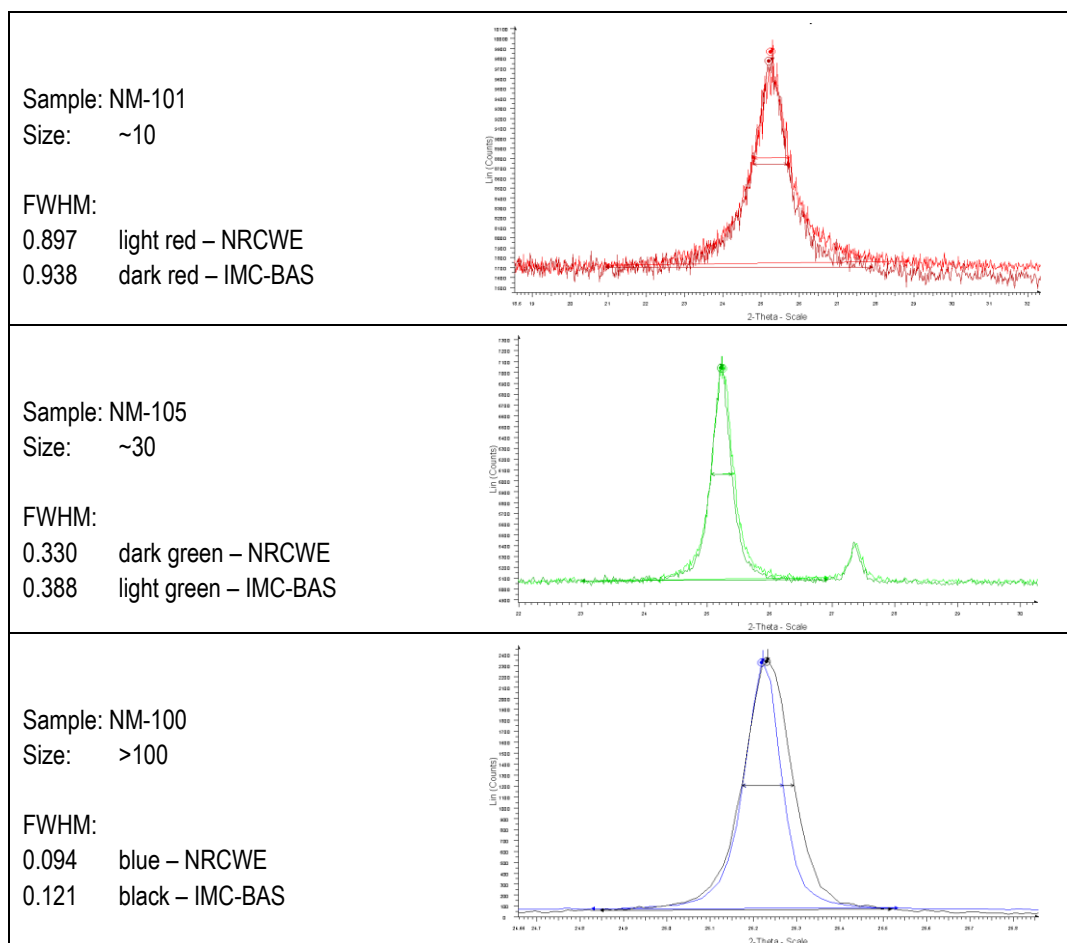


**Figure 41. The first reflection of anatase NMs of 3 different particle sizes. Note that the larger the particles are, the narrower the reflections are, and the more the instrument contribution matters. Direct visual comparison was enabled by scaling the NRCWE diffractograms to the height of the IMC-BAS data shift the position so reflections start at the same angle.**

It is evident that the instrumental contribution matters most when the reflections are narrow, i.e. for large crystals, and the effect is clearly seen e.g. when comparing the first reflection for the samples containing anatase: NM-101, NM-102, NM-105 and NM-100, see Figure 41. For data measured by ICM-BAS compared to data from NRCWE both a visual and a quantitative relative “left shift” are observed. The listed FWHM values are found by calculations using the Bruker EVA software.

XRD was carried out on the samples by several laboratories: IMC-BAS, NRCWE, LNE and JRC, and Table 34 gives an overview of the results of the XRD measurements on the NMs.

## 11.2. XRD results

XRD can be measured in different setups and the use of different wavelengths is possible, but for standard measurements this is less important, as long as it is taken into account. Most databases are based on irradiation using Cu K $\alpha$  X-rays.

All data presented in this report were recorded in reflection mode (either in  $\theta$ - $2\theta$  or glancing angle geometries) using Cu K $\alpha$  radiation. Reflection mode analysis has the advantage that very small samples can be used (though more material is recommended) and as the scatter is usually detectable until high values of  $2\theta$ , unit cells can be determined with high accuracy. Ideally, internal standards are used to control for differences between instruments, but this was not done here.

AT NRCWE the TiO<sub>2</sub> NMs were measured in a standard sample holder, 2.5 cm in diameter and approximately 1 mm deep, made of PMMA. The samples were filled in the sample holders and a glass plate was used to press the material into the holder and level the sample surface with the sample holder. IMC-BAS measured the TiO<sub>2</sub> NMs in a standard plastic sample holder, 2.5 cm in diameter and 1 mm deep. The NMs were filled in the sample holder and a glass plate was used to press the material into the holder, to ensure a flat sample with the correct height, i.e. the same as height of the sample holder. At LNE the TiO<sub>2</sub> NMs powders were prepared and placed in sample holders for Spinner. For the JRC measurements, the NM powder was ‘glued’ to a Si wafer using PMMA and samples were mounted vertically in a sample holder.

The TiO<sub>2</sub> samples are crystalline and contain anatase, rutile or a mixture of both. XRD can be used to determine which polymorph is in the sample, and for crystals smaller than 100 nm, XRD can be used to calculate the size of the crystals.

**Table 34. Phase identification by XRD measurements of the TiO<sub>2</sub> NMs.**

Material	Laboratory	Vial no.		Phase Identified
NM-100	NRCWE	0006	0007	Anatase
		0211	0213	
		0214	0406	
		0408		
	IMC-BAS	0079	0081	Anatase
		0083		
JRC	04877 (RT)	01275 (-80 °C)	Anatase	
NM-101	NRCWE	0239	0415	Anatase
		0510	0729	
	IMC-BAS	1266	1268	Anatase
		1270		
	JRC	0150 (RT)	1596 (-80 °C)	Anatase
	NM-102	NRCWE	0121	0477
1000				
IMC-BAS		0092	0094	Anatase
		0095		
JRC		1050 (RT)	3282 (-80 °C)	Anatase
NM-103		NRCWE	0223	0541
	2097			
	IMC-BAS	0615	0617	Rutile
		0618		
	JRC	0040	2901	Rutile
	LNE	0280	0281	Rutile
NM-104	NRCWE	0228	0416	Rutile
		0440		
	IMC-BAS	0529	0530	Rutile
		0533		
	JRC	4259 (RT)	0715 (-80 °C)	Rutile
	LNE	0287	0289	Rutile
NM-105	NRCWE	0051	0058	Anatase and Rutile 88.2 : 11.8
		0078		
	IMC-BAS	2242	2244	Anatase and Rutile 86.36 : 13.64
		2247		
	JRC	2616 (RT)	02706 (-80 °C)	Anatase and Rutile
	LNE	0431	0438	Anatase and Rutile 81.5 : 18.5

RT = room temperature, i.e. the sample was stored at room temperature

Figure 43 and Figure 44 show the X-ray diffractograms of the TiO<sub>2</sub> NMs and the results from the various crystallite size analyses from NRCWE, IMC-BAS, LNE and JRC are summarized in Table 35. The X-ray diffractograms show good agreement between the laboratories.

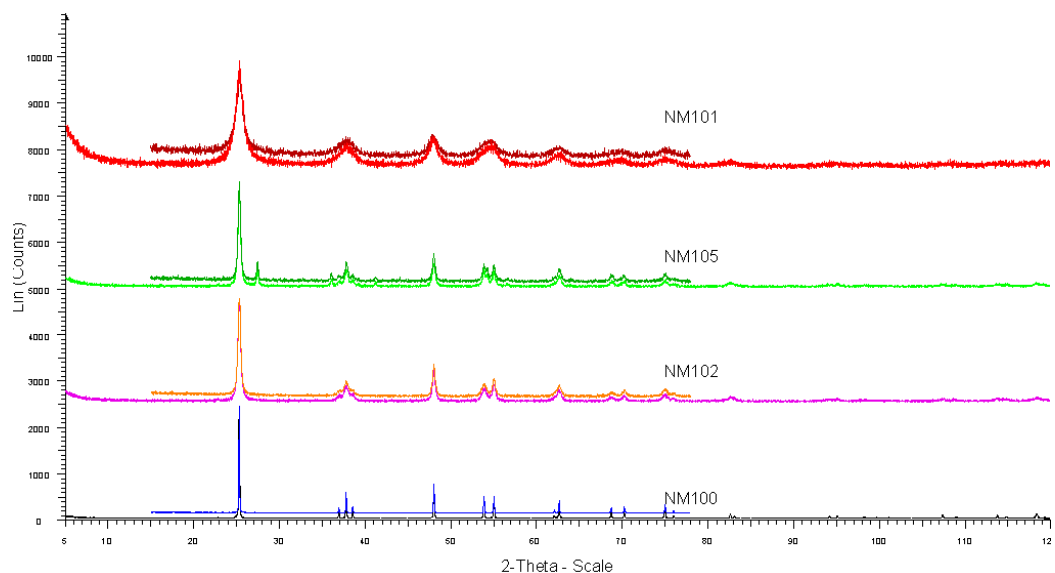


**Figure 42.** The diffraction data from NRCWE and IMC-BAS for NM-100, NM-101, NM-102 and NM-105. The lower (long) curves are measured at IMC-BAS and the upper (short) curves at NRCWE.

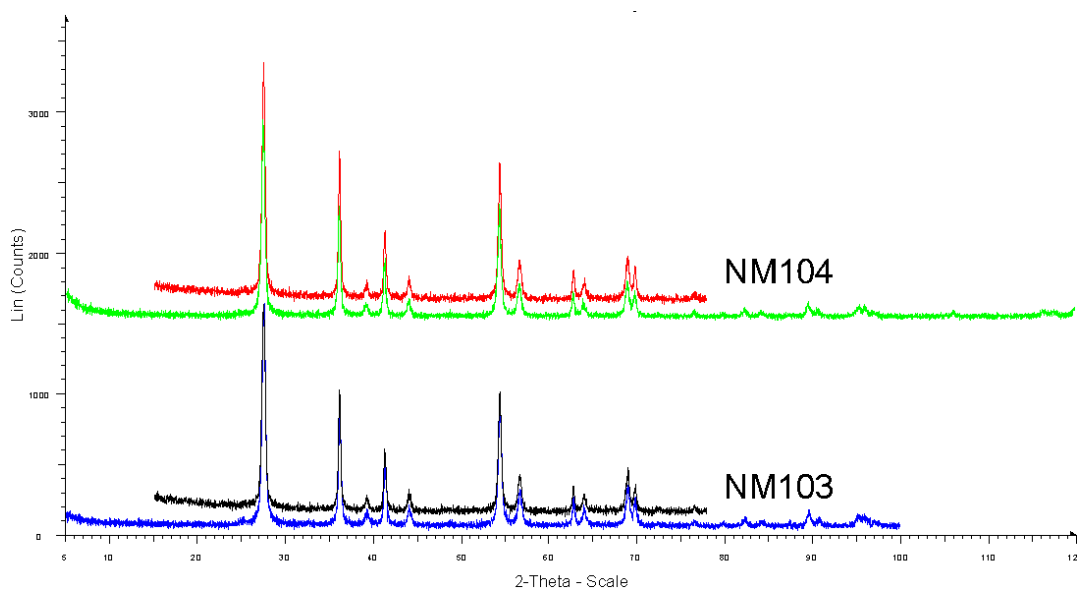


**Figure 43.** Diffraction data from NRCWE and IMC-BAS for NM-103 and NM-104. The lower (long) curves are measured at IMC-BAS and the upper (short) curves at NRCWE.

The JRC also performed the XRD analysis of TiO<sub>2</sub> NMs and the resulting diffractograms are shown in Figure 44.

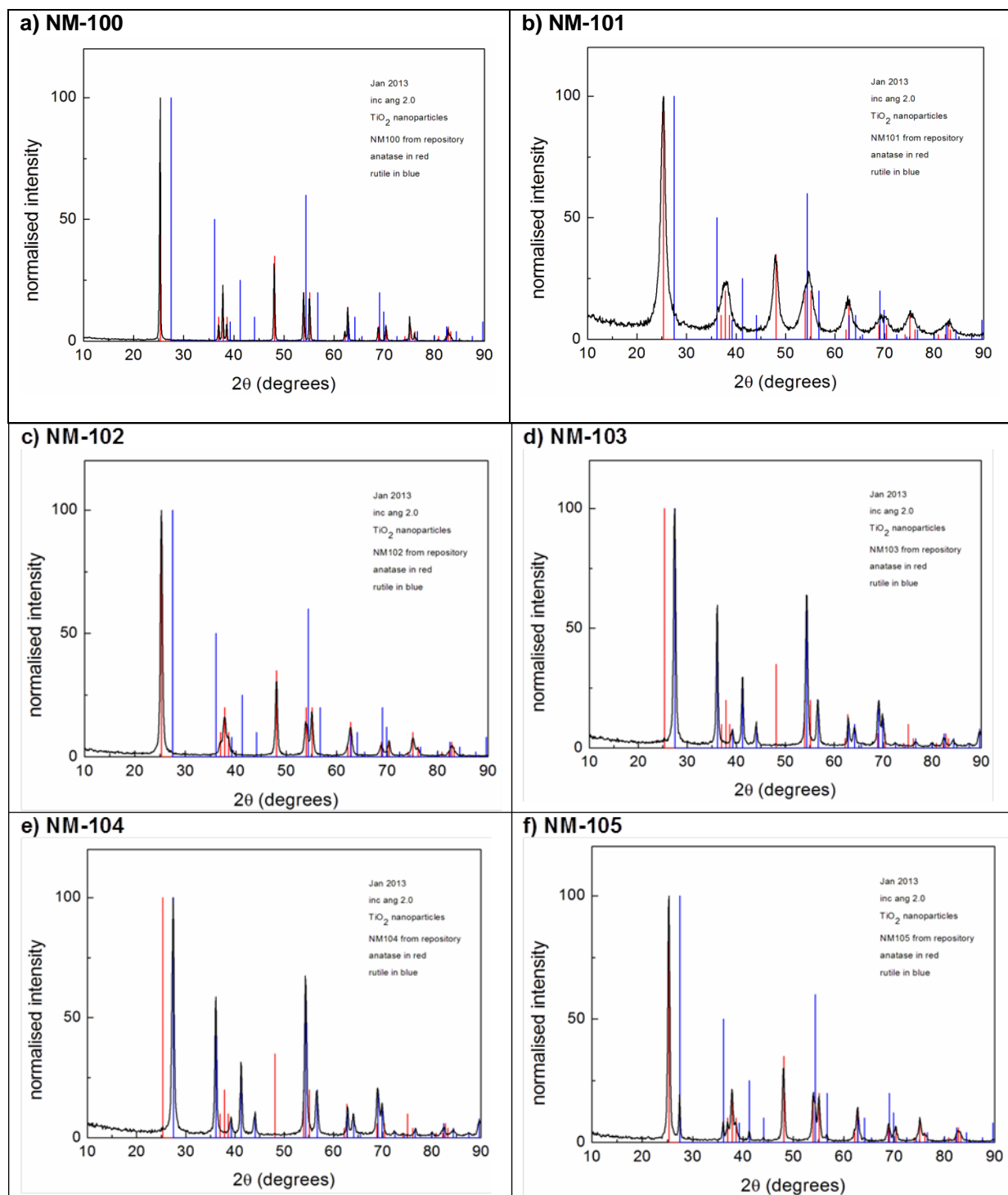
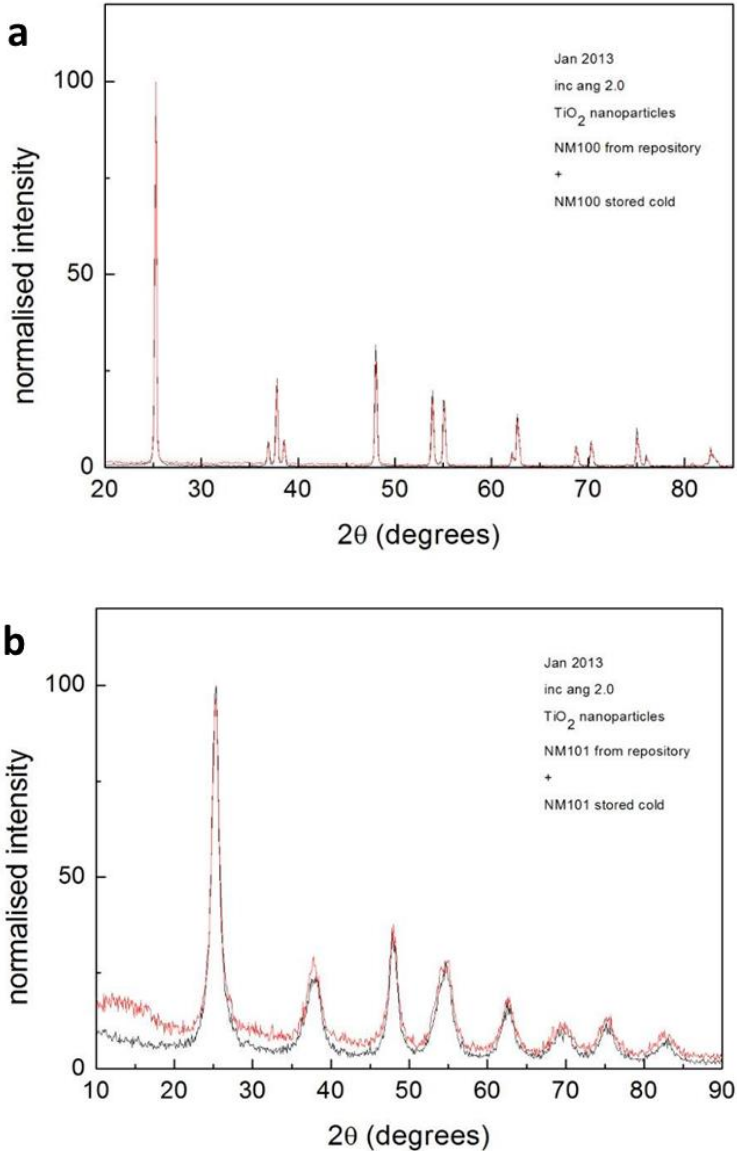
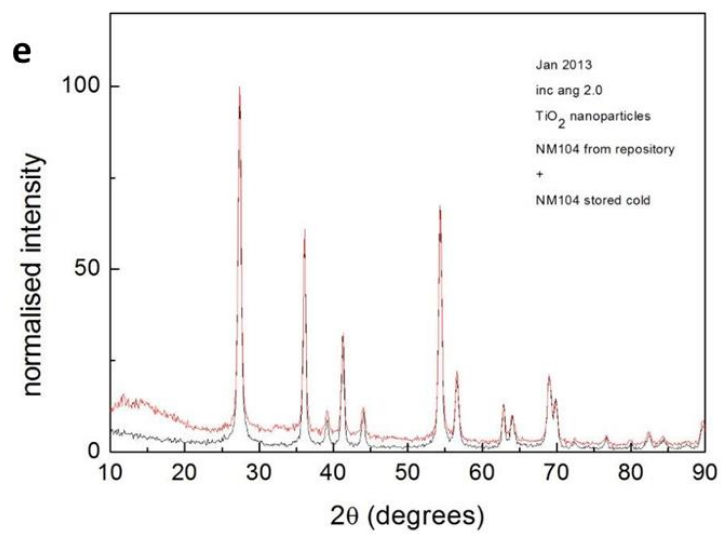
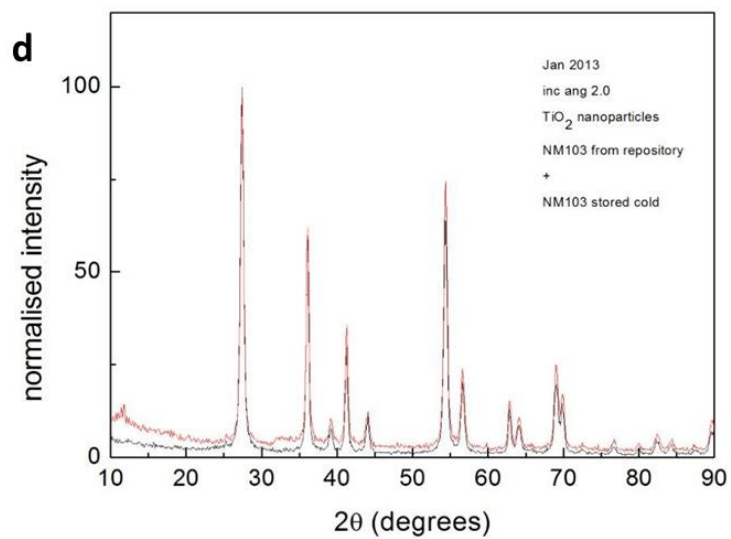
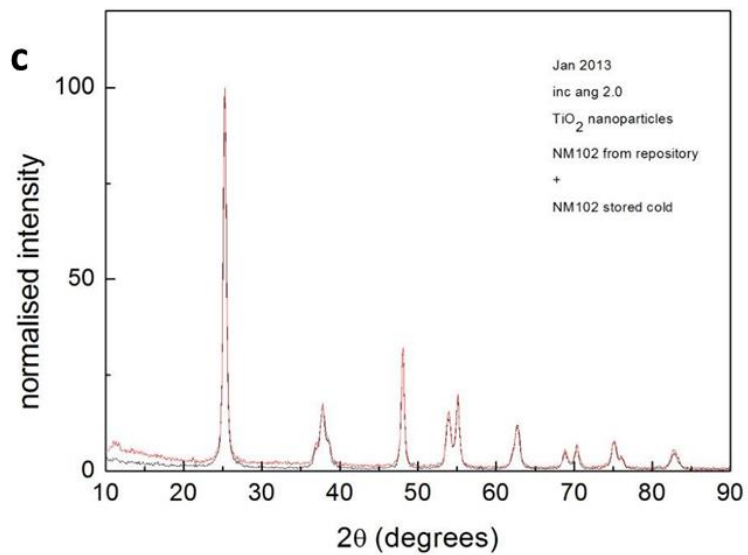
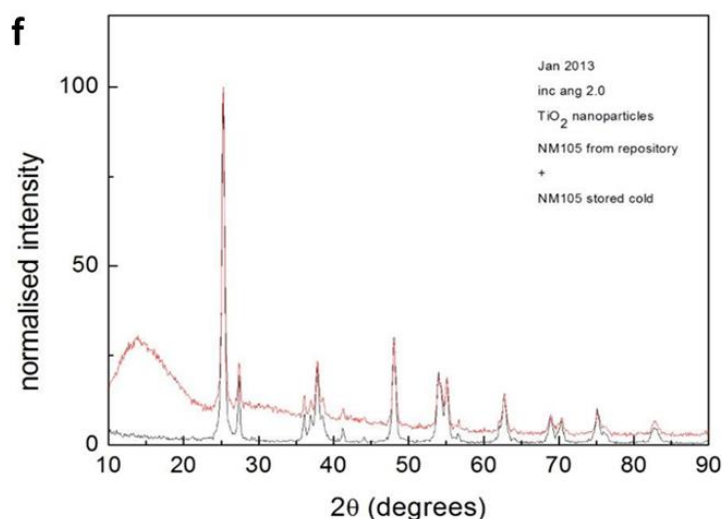


Figure 44. XRD diffraction data from JRC for TiO<sub>2</sub> NMs (black). The theoretical position of reflexes associated to rutile (blue) and anatase (red) phases are also shown.

Additional XRD analysis was performed for the NMs stored at room temperature and at minus 80°C and results are presented in Figure 45. The JRC study confirms that NM-100, NM-101 and NM-102 are in anatase phase, NM-103 and NM-104 are in rutile phase, and for NM-105 both phases are present. As expected for TiO<sub>2</sub> NMs, there were no observed differences in the crystal structures of samples stored at the two different temperatures. For the materials stored at high temperatures, a higher background contribution is observed due to the sample method mounting used and small amount of material available.







**Figure 45. XRD diffraction data from JRC for a) NM-100, b) NM-101, c) NM-102, d) NM-103 e) NM-104 and f) NM-105 stored at two different temperatures: room temperature (black line) and minus 80°C (red line).**

The crystallite size estimation data for the  $\text{TiO}_2$  NMs are summarized in Table 35. For clarity, the results have been rounded to the nearest integer number and, based on the general consideration that the true standard deviation (SD) is in the order of  $\pm 5$  nm, SD is not listed. Most programs for calculations on powder diffraction data underestimate the error.

The results for NM-100 (the bulk NM) stand out. According to the supplier the crystal size is between 200 nm and 220 nm. The data from NRCWE and the Fullprof data from IMC-BAS conclude that the crystals are large, but XRD size data should not be used if the calculated sizes exceed 100 nm. The Peak fit and TOPAS from IMC-BAS find a crystal size around 60 nm, which is much smaller than expected. As the same measured data is used for the different calculations at IMC-BAS, there is no obvious explanation for this difference. In the JRC measurement, the peak width indicates a minimum crystal size of 80 nm but this result does not consider any additional broadening (e.g. instrumental or strain), which would increase the measured value of the crystal size minimum value. Additionally, any twinning or polycrystallinity in the larger particles (as seen in the TEM) would also lead to a smaller crystal size determined by XRD, compared to actual particle size of the material.

For the other NMs the difference between the largest and smallest calculated sizes is less than 10 nm. The calculated sizes from NRCWE are in all cases larger than those from IMC-BAS. This is ascribed to differences in instrumental performance and the calculation procedures used. However, almost all the differences can be covered by the estimated 5 nm real standard deviation in the analysis.



**Table 35. Summary of XRD crystallite sizes calculated for TiO<sub>2</sub> using various instruments and principles.**

Laboratory	Method	NM-100 <sup>§</sup> (nm)	NM-101 (nm)	NM-102 (nm)	NM-103 (nm)	NM-104 (nm)	NM-105 (Anatase) (nm)	NM-105 <sup>&amp;</sup> (Rutile) (nm)
Supplier Information		200-220	<10	-	20	20	21	?
IMC-BAS							Anatase:Rutile 86.36:13.64	
	Scherrer eq.	57	5	18	-	19	18	23
	TOPAS	62	5	16	19	20	18	27
	Fullprof	168	5	18	20	19	19	36
NRCWE							Anatase:Rutile 88.2 : 11.8	
	Scherrer eq.	>100	7	23	26	27	27	62
	TOPAS, IB	>100	7	26	25	25	27	88
	TOPAS,FWHM	>100	7	28	28	29	31	123
JRC	Scherrer eq.	>80	8	21	20	21	22	40
LNE							Anatase:Rutile 81.5: 18.5	
	Scherrer eq.	-	-	-	-	-	32	-

<sup>§</sup>Size-data not reliable due to the large crystallite size.

<sup>&</sup>Size data not reliable due to high error in determining the background and height of reflection (rutile is a minor fraction).  
Additionally, a large deviation from reflex to reflex was observed.

## **12. Transmission Electron Microscopy (TEM)**

The TEM experiments were performed by CODA-CERVA and IMC-BAS. Given that a sub-1-nm-resolution is the aim for NM characterisation, TEM is one of the few techniques, in addition to SEM and in specific cases AFM, with sufficient resolution. TEM yields number-based results, allows size measurements but also specific shape measurements and characterization of surface topologies on a number basis (per particle). It allows distinguishing between characterization of primary particles and aggregates/agglomerates as well as phase identification and was successfully applied to the TiO<sub>2</sub> NMs.

The TEM results give both a qualitative and a quantitative description.

A qualitative description of the NM is provided based on representative and selected micrographs taken by conventional Bright Field (BF) electron microscopy. This method is described in detail in section 12.1.2.

To measure the characteristics of primary particles of the TiO<sub>2</sub> NMs, the Feret Min and Feret Max were measured in CODA-CERVA following a systematic selection procedure for unbiased random particle collection at appropriate magnifications. The method is described in more detail in section 12.1.3. An automated method in which single primary particles are separated from aggregates/agglomerates based on their morphology is discussed as well.

CODA-CERVA developed a standardised procedure for performing a quantitative analysis of the physical characteristics of aggregated and agglomerated NMs by TEM after applying systematic random sampling. The method is described in detail in section 12.1.4 and also in De Temmerman et al., 2012. The characteristics of aggregates/agglomerates were analysed after dispersion using the generic NANOGENOTOX dispersion protocol, where a low concentration of BSA is applied to stabilise the aggregates, and using a similar dispersion in double distilled water.

### **12.1. Sample preparation and analytical methods**

#### **12.1.1. Sample preparation**

The generic NANOGENOTOX dispersion protocol for toxicity testing (Jensen et al., 2011) was modified in order to optimize measurements of the NMs. These modifications include variations of the dispersion media, NM concentration and sonication energy.

Specifically, the NMs were brought in the selected dispersion medium that was water with BSA for the first series of experiments, and water only for the second series of experiments at a concentration optimized for TEM analysis: 2.56 mg/ml and sonicated for 16 minutes using a Vibracell™ 75041 ultrasonifier (750 W, 20 kHz, Fisher Bioblock Scientific, Aalst,

Belgium) equipped with a 13 mm horn (CV33) at 40 % amplitude. This setup resulted in an average horn power of about 26 W and a sample specific energy of approximately  $2530 \pm 20$  MJ/m<sup>3</sup>. During sonication, the samples were cooled in icy water to prevent excessive heating. After sonication, the samples were diluted to a concentration of 0.512 mg/ml.

In the presence of proteins, like BSA used to stabilise the dispersion, the dispersed NMs were brought on pioloform- and carbon-coated, 400 mesh copper grids (Agar Scientific, Essex, England) that were pretreated with 1 % Alcian blue (Fluka, Buchs, Switzerland) to increase hydrophilicity as described by Mast and Demeestere, 2009. For NMs dispersed in water, the charge of the grid was adapted to the charge of the NMs.

In IMC-BAS, the NMs were transferred onto carbon-coated copper grids without Alcian blue pretreatment using a special tool, a platinum wire loop (0.2 mm Pt wire, one end of which is bent as loop with external diameter of 2.5-3.0 mm). The following operations were carried out during the transferring a suspension onto EM grids:

- (i) catching a grid by tweezers with reverse action;
- (ii) disposing the tweezers on a table surface in a way ensuring direct contact of the grid and the filter paper;
- (iii) careful sinking and extracting the Pt loop in/from the vessel with suspension of nanoparticles in a liquid media (in this stage, a thin film of nanoparticles suspension is formed in the loop space due to the surface tension);
- (iv) careful touching the Cu grid placed on the filter paper by the Pt loop (in this operation, the whole surface of Cu grid in contact with the Pt loop is covered by nanoparticles while liquid media is absorbed by the filter paper);

NB: (iii-iv) operation can be performed 1 or 2 times (the covered by nanoparticles Cu grid is ready for observation immediately or after a few seconds of drying at ambient temperature).

For AFM measurements at CEA, stock dispersions of 3.41 g NM per L in 0.01 M HNO<sub>3</sub> were prepared by 20 min sonication at 40 % amplitude. The NMs were deposited on freshly cleaved mica, dipping it 30 s in a 100-fold diluted suspension followed by rinse in pure water.

### **12.1.2. Recording of the electron micrographs**

In IMC-BAS, well-contrasted BF images of NMs irrespective of their composition were obtained using:

- (i) a Philips TEM420 at 120 kV acceleration voltage;
- (ii) EM grids with holey carbon support film
- (iii) well calibrated regimes in EM for recording images on photo plates (Kodak electron image film SO-163);

- (iv) appropriate developing of EM films;
- (v) high-resolution scanner technique to transfer the image from EM film into digital file;
- (vi) image processing.

In CODA-CERVA, the samples were imaged in bright field (BF) mode using a Tecnai Spirit TEM (FEI, Eindhoven, The Netherlands) with Biotwin lens configuration operating at 120 kV at a spot-size considered suitable by CODA-CERVA.

The condenser lens current was chosen such that the beam was parallel and images were taken approximately 500 nm below minimal contrast conditions, where Fresnel fringes were minimal and contrast was judged to be optimal. Micrographs were recorded using a 4\*4 K CCD camera (Eagle, FEI). To achieve maximal traceability of information, each micrograph was stored together with its administrative and sample preparation information and with the information related to its imaging conditions in a dedicated database integrated in the iTEM software (Olympus, Münster, Germany). At several levels, modifications of the TIA image acquisition software (FEI) and of the iTEM software were made to transfer the micrographs and their associated microscope data efficiently in the iTEM database:

- (i) The TIA protocol for batch conversion of the software-specific SER- and EMI-formats was adjusted to avoid excessively long file names.
- (ii) (An imaging C- and libtiff library-based module, referred to as the TIA-TAG module, was developed in iTEM. This module reads the information relevant for image analysis and quality control in the private tags of the TIF image files and renders it accessible in a new information tab of the iTem software. In addition, the TIA TAG module facilitates calibration of images by automatically converting the pixel size from mm scale to nm scale.
- (iii) New fields were defined in the iTEM database specifying the sample and sample preparation characteristics. Where applicable, drop lists were foreseen to avoid typing errors.

### **12.1.3. Qualitative TEM characterisation and measurement of primary particles**

A qualitative description of the NMs was provided based on conventional BF electron microscopy. This description included:

- (i) representative and calibrated micrographs,
- (ii) agglomeration- and aggregation status,
- (iii) general morphology,
- (iv) surface topology,

- (v) structure (crystalline, amorphous, ...)
- (vi) description of the presence of contaminants and aberrant particles.
- (vii) an analysis of the homogeneity of the distribution of the particles on the EM-grid, required to do a representative quantitative analysis.

To measure the characteristics of primary particles of a NM manually, the Feret Min and Feret Max were measured in CODA-CERVA following a systematic random sampling based on stereology at an appropriate magnification. Briefly: Micrographs were taken at 10 fixed positions determined by the microscope stage. On these micrographs, a grid with a mesh of 100 nm by 100 nm was placed at random. The primary particle on each tenth intersection, counted from left to right was measured. When no particle was located at this intersection, the horizontal grid lines were followed until a primary particle was located on an intersection, see Figure 46.

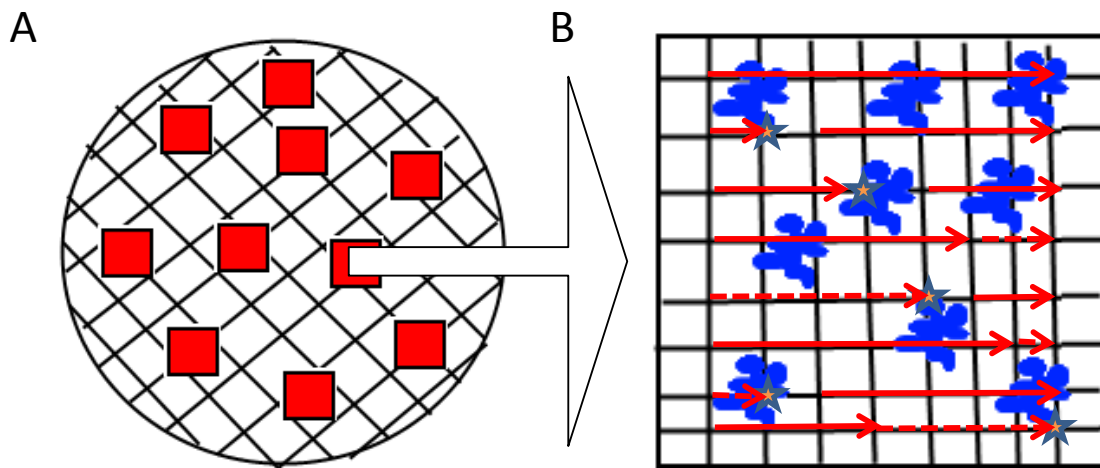


**Figure 46** Schematic overview of the systematic random sampling. (A) TEM grid with 10 fixed positions indicated by red squares. (B) TEM micrograph with a 100 nm by 100 nm mesh grid. Primary particles on the intersections of the grid were measured. The stars indicate the measured primary particles. Full red lines: Counting procedure from left to right until each 10<sup>th</sup> intersection. Dashed red line: the horizontal grid lines were followed until a primary particle was located on an intersection.

The Feret Max and Feret Min were measured manually as indicated in Figure 47. The Feret Mean of the particle was calculated as the mean of Feret Min and Feret Max. The aspect ratio was calculated as the ratio of Feret Max and Feret Min.

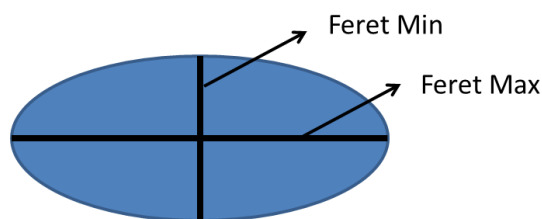


**Figure 47. Schematic view of the Feret Min and Feret Max measurements of a primary particle.**

**Table 36. Quantitative parameters and their description as described in the iTEM software.**

Measured parameter <sup>1</sup>	Description
Area <sup>4,3</sup> (nm <sup>2</sup> )	Projection area
Convex Area <sup>3</sup> (nm <sup>2</sup> )	The area of the convex hull (envelope) bounding the measured object.
Rectangle Max (nm <sup>2</sup> )	The area of the biggest rectangle whose sides consist of tangents to the measured object borders.
Rectangle Mean (nm <sup>2</sup> )	The area of the mean rectangle whose sides consist of tangents to the measured object borders.
Rectangle Min <sup>5</sup> (nm <sup>2</sup> )	The area of the smallest rectangle whose sides consist of tangents to the measured object borders.
ECD <sup>6</sup> (nm)	The equivalence refers to the area of the measured object. The ECD is the diameter of a circle that has an area equal to the area of the measured object.
Feret Max <sup>4</sup> (nm)	The maximum distance of parallel tangents at opposing measured object borders.
Feret Mean <sup>7</sup> (nm)	The mean distance of parallel tangents at opposing measured object borders.
Feret Min <sup>4</sup> (nm)	The minimum distance of parallel tangents at opposing measured object borders.
Radius of Inner Circle (nm)	Radius of the maximal circle inside the measured object.
Central Distance Max (nm)	The maximum distance between the centre and the border of a measured object.
Central Distance Mean (nm)	The mean distance between the centre and the border of a measured object.
Central Distance Min (nm)	The minimum distance between the centre and the border of a measured object.
Diameter Max (nm)	The maximum diameter of a measured object (for angles in the range 0° through 179° with step width 1°).
Diameter Mean (nm)	The mean diameter of a measured object (for angles in the range 0° through 179° with step width 1°).
Diameter Min (nm)	The minimum diameter of a measured object (for angles in the range 0° through 179° with step width 1°).
Convex Perimeter <sup>3</sup> (nm)	The length of the perimeter of the convex hull (envelope) bounding the particle.
Perimeter <sup>3</sup> (nm)	The sum of the pixel distances along the closed boundary.
Aspect Ratio <sup>8</sup>	The maximum ratio of width and height of a bounding rectangle for the measured object.
Convexity <sup>9</sup>	The fraction of the measured object's area and the area of its convex hull.
Elongation	The elongation of the measured object can be considered as lack of roundness. It results from the sphericity.
Shape Factor <sup>10</sup>	The shape factor provides information about the "roundness" of the measured object. For a spherical measured object the shape factor is 1; for all other measured objects it is smaller than 1.
Sphericity	Describes the sphericity or 'roundness' of the measured object by using central moments.

1 These parameters are used in the iTEM software and are described in the iTEM help files

2 The descriptor in brackets gives the synonym for the iTEM parameter as described in ISO

3 As described in ISO 9276-6:2008

4 As described in ISO 13322-1:2004

5 Feret box area<sup>3</sup>

6 Area equivalent diameter<sup>4</sup>

7 Angle-average Feret diameter

8 Shape factor<sup>4,3</sup>

9 Solidity<sup>3</sup>

10 Form Factor<sup>3</sup>

Semi-automatic measurement of primary particles could be performed on some NMs as well. Single primary particles could be automatically selected in the dataset based on their morphology (shape and surface properties). In 10 micrographs, all detected and measured particles were manually classified, either as single primary particles or as aggregates/agglomerates. In the generated subdataset, which contained only the classified single primary particles, a correlation matrix of 23 physical parameters, which describes the NM (Table 36) was set up.

Measurands that describe the morphology of the single primary particles and which show to have low correlation ( $< 0.5$ ) with the ECD were selected for an automated classification in the other micrographs, resulting in a large dataset consisting of separated populations of single primary particles and aggregates/agglomerates.

#### **12.1.4. Quantitative analysis of aggregated/agglomerated NM based on TEM micrographs**

To avoid subjectivity in the selection of particles by the microscopist, the positions on the EM grid where micrographs were taken, were selected randomly and systematically as shown in Figure 46. The grid was placed randomly into the holder, and positions distributed evenly over the entire area were predefined by the microscope stage. When the field of view was obscured, e.g. by a grid bar or an artifact, the stage was moved sideways to the nearest suitable field of view.

For the NM dispersed in water containing BSA using the generic NANOGENOTOX protocol, three independent samples were analyzed. Per sample, five micrographs were made with a 4\*4 k Eagle CCD camera (FEI) at a magnification of 18500 times. For the given microscope and camera configuration, this magnification corresponds with a pixel size of 0.60 nm and a field of view of 2.45  $\mu\text{m}$  by 2.45  $\mu\text{m}$ . This implies a lower particle size detection limit of approximately 6 nm, supporting on the criterion of Merkus, 2009, that large systematic size deviations can be avoided if the particle area is at least hundred pixels. The field of view limits the upper size detection limit to 245 nm, one tenth of the image size as recommended (Matsuda and Gotoh, 1999). To estimate the number of particles required for the estimation of the mean particle diameter with a confidence level, it is assumed that the particle size distribution follows a log-normal size distribution. The minimal number of particles can then be calculated according to Matsuda and Gotoh, 1999. Their equation allows calculating the sample size required for the estimation of mean particle diameter with an uncertainty of 5 percent.

For the NM dispersed in water only, ten micrographs of one sample of each NM were analyzed described above. The magnification was optimized for each NM.

The 'Detection module' of iTEM was used for threshold-based detection of the NM. Briefly, the contrast and brightness of the micrographs were optimized, the involved particles were enclosed in a pre-defined frame or region of interest and thresholds were set to separate particles from the background based on their electron density and size. Particles consisting of less than fifty pixels and particles on the border of the frame were omitted from analysis.

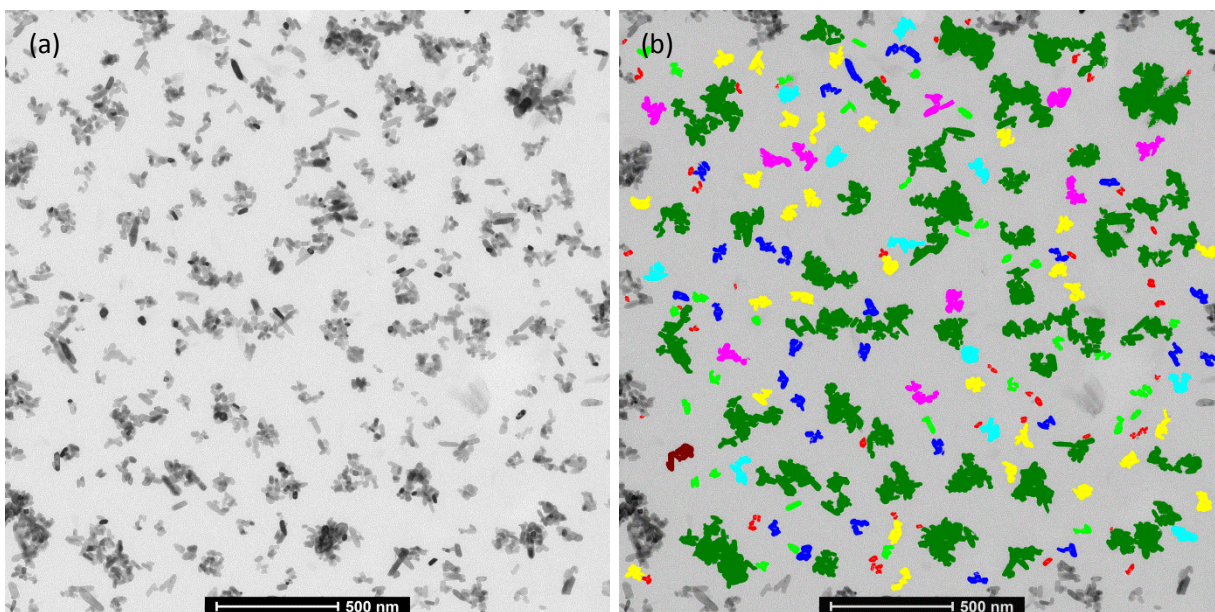
For each particle, 23 quantitative parameters, described in Table 36, are measured and considered relevant for its characterization. Each particle detected in a micrograph was identified by a unique number, written in the overlay of the image. This allowed the selection of data of individual particles and the post-analysis deletion of erroneously detected particles. In general, artifacts were characterized by their morphology and a grey value lower than the mean grey value of the background plus three times its standard deviation. Particles fulfilling this criterion were identified and deleted automatically and particles with an unusual morphology, judged to be artifacts based on visual inspection on the micrographs, were omitted manually from analysis.

Figure 48 illustrates the detection methodology using iTEM software. The NPs that are detected on the TEM image shown in Figure 48(a) are given in colour Figure 48(b). The different colours on the annotated micrograph are related to the size of the detected NPs.

In addition to the micrograph related information, the intermediate and annotated images obtained during image analysis and the results and reports of these analyses were stored in the database, linked to the original micrograph.

Sigmaplot (Systat, Cosinus Computing, Drunen, the Netherlands) was used to calculate statistics and histograms. The normality of the distributions of the measured parameters was tested with the Shapiro-Wilk and the Kolmogorov-Smirnov tests, while the homogeneity of variances was tested with the Spearman rank correlation test. Since these assumptions were not met, the non-parametric Kruskal-Wallis one-way ANOVA was performed and data were compared pairwise with the Dunn's Method to determine the micrograph and sample effects, and to determine the effect of sonication on the number of particles per grid area.





**Figure 48** An example of particle detection using iTEM software applied to NM-103. The TiO<sub>2</sub> particles that are detected on the TEM image (a) are *colour-coded* after analysis with iTEM software (b): *red: 0-1000 nm<sup>2</sup>, green: 1000-2000 nm<sup>2</sup>, blue: 2000-3000 nm<sup>2</sup>, yellow: 3000-4000 nm<sup>2</sup>, cyan: 4000-5000 nm<sup>2</sup>, pink: 5000-6000 nm<sup>2</sup>, brown: 6000-7000 nm<sup>2</sup> and dark green > 7000 nm<sup>2</sup>. Particles at the borders of detection region are black and are omitted from analysis. Bar 500 nm (CODA-CERVA).*

The normality of the distributions and the homogeneity of variances were met for the mean values of the median mean diameter, the median sphericity and the median shape factor of the different TiO<sub>2</sub> NM that were obtained in independent analyses.

Hence, a one-way analysis of variance (ANOVA) was performed and data were compared pairwise with the Tukey test. The measured parameters were classified by principle component analysis using the SAS statistical software (SAS Institute Inc., Cary, NC, USA).

## 12.2. Results for transmission electron microscopy

### 12.2.1. Sample preparation and image analysis

In a preliminary experiment, the effects of sonication were examined. The number of particles of representative titanium dioxide NM (NM-104), per grid area increased proportionally with sonication time (Figure 49). For 5 and 10 minutes of sonication of NM-104, the total number of detected aggregates was 814 and 927, respectively. This was higher than 795, the number of particles allowing an estimation of the geometric mean particle size with an error of maximum 5 % (Matsuda and Gotoh, 1999). The corresponding median mean particle diameters were 65 and 67 nm, respectively, and did not differ significantly. Only 17 aggregates were measured for unsonicated NM-104, such that the median mean diameter for this sample could not be evaluated reliably.

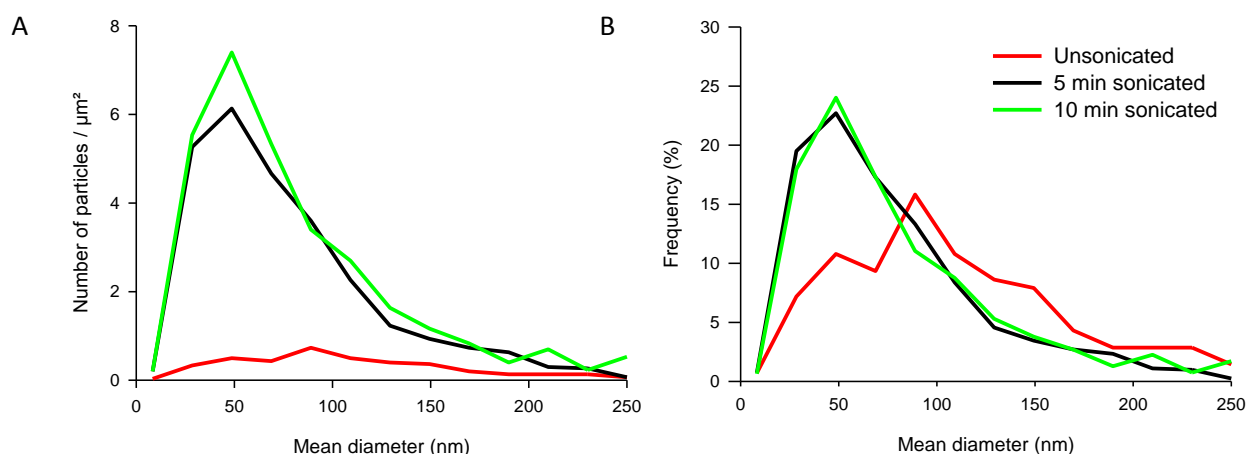


**Figure 49.** Effect of sonication on the size distribution of the TiO<sub>2</sub> NM-104. The number of particles per μm<sup>2</sup> of grid area for a concentration of 1 mg/ml (A) and the corresponding frequencies (B) are represented as a function of their mean diameter.

Using this methodology, a stable dispersion of NM could be obtained in CODA-CERVA in water and in water containing 0.05 % BSA for NM-103 and NM-104 but not for NM-102 and NM-105.

A representative micrograph of NM-103 was analyzed in CODA-CERVA using three image analysis softwares, namely iTEM, Visilog and ImageJ. Particles in the same micrograph were detected and analyzed semi-automatically (Figure 50). For a selected micrograph, 130 to 162 particles were detected depending on filters and the exclusion criteria of the particles available in the software.

To be able to compare results between programs, the ECD was selected because this was defined and calculated the same way in all programs. No significant differences in ECD were found between the Image analysis softwares (Table 37).

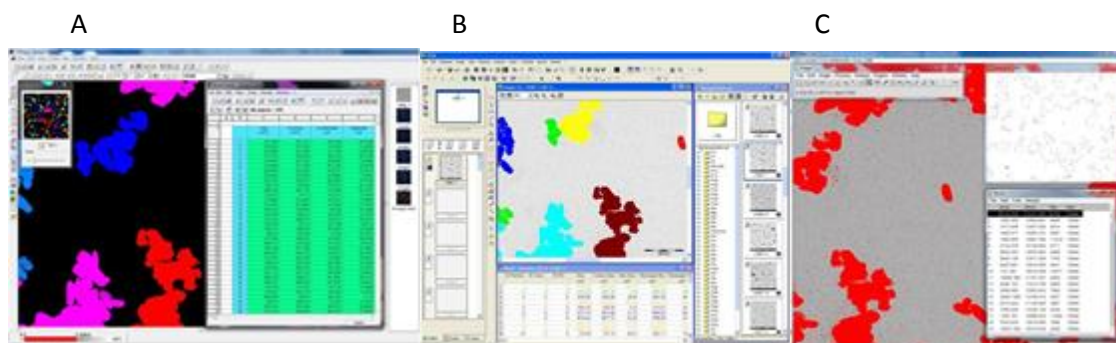


**Figure 50.** Illustration of the detection and analysis of aggregates with the TEM image analysis software used in NANOGENTOX project. A) Visilog (Noesis, Saint Aubin, France); B) iTEM (Olympus, Münster, Germany) and C) ImageJ (NIH, Bethesda, USA).

**Table 37 Qualitative TEM analysis with the iTEM, Visilog and ImageJ software of NM-103.**

Software	ECD (nm) (N)*
iTEM	64 <sup>a</sup> (133)
Visilog	70 <sup>a</sup> (130)
Image J	60 <sup>a</sup> (162)

\* Median Area equivalent circular diameter with the analysed number of particles (N).

<sup>a, b</sup> Different letters indicate significantly different mean values by Kruskal-Wallis One Way Analysis of Variance on Ranks ( $p < 0.05$ )

## 12.2.2. Results for NM-100

### Qualitative analysis of NM-100

NM-100 was evenly distributed over the complete grid surface, suggesting that the charge of the NM is compatible with the charge of the grid. As illustrated in Figure 51 and Figure 52, NM-100 consists of single particles and aggregates/agglomerates. A broad distribution in the size of primary particles of NM-100 is observed on all the TEM images. Primary particle sizes ranging from 20 nm up to 300 nm are detected. The micrograph in Figure 51 illustrates the occurrence of small aggregates/agglomerates. The aggregates have a size ranging from 30 nm up to 700 nm, measured directly on the TEM images. The general morphology of the primary subunits of the NM is equi-axed and rounded, or slightly elongated. Their suggested 3D structure is spherical or ellipsoidal. The aggregates and agglomerates tend to be more or less equi-axed, possibly due to steric preference, or have a more fractal-like structure.

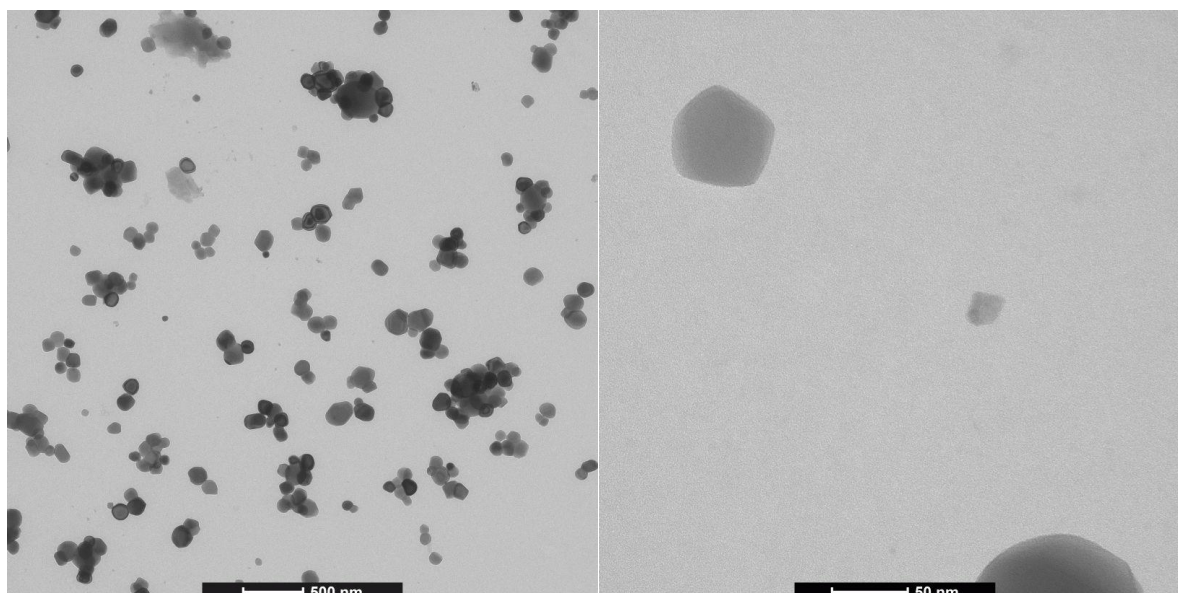


**Figure 51. Representative TEM-micrograph of NM-100 showing particles dispersed in double distilled water (CODA-CERVA).**

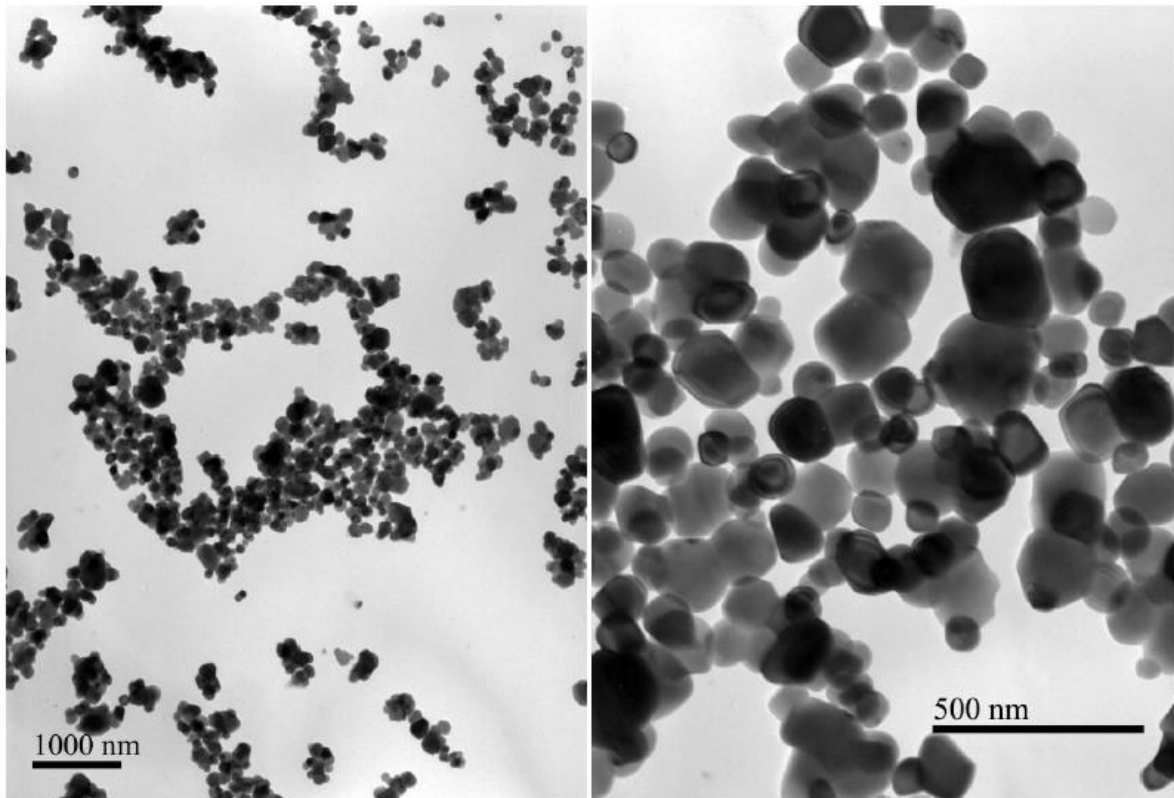


**Figure 52. NM-100 TEM-micrograph showing the range in agglomerate and aggregate sizes and typical euohedral morphology of the individual crystallites in the material (left). Selected TEM-micrograph taken at higher resolution illustrating the samples are composed mainly of aggregates sintered at crystal facets (right). (IMC-BAS).**

### **Quantitative analysis of dispersed aggregates and agglomerates of NM-100**

The semi-automatic detection and measurement of aggregates and agglomerates of TiO<sub>2</sub> nanoparticles based on mass thickness contrast is relatively straightforward. In 10 micrographs, 614 particles are detected for NM-100 dispersed into double distilled water. Figure 53 represents the obtained raw data as number-based histograms of “shape” parameters. The descriptive statistics are summarized in Table 38.

The average value (Mean), standard deviation (Std Dev), the standard error on the mean (Std Err), and the smallest (Min) and largest (Max) observation, are presented. However, since for all measured parameters of the examined NM, the Kolmogorov-Smirnov and the Shapiro-Wilk probabilities are smaller than 0.001 (not shown), none of these parameters can be assumed to be normally distributed. Hence, non-parametric estimates of these parameters describe the sample better. These include the median and the 25 and 75 percentiles.

The amount of aggregates and agglomerates smaller than 100 nm is 27.1 %. Table 39 summarizes the number of aggregates and agglomerates smaller than 100 nm, 50 nm and 10 nm for NM-100. The sphericity of the particles is larger than 0.33 for 76.3 % and larger

than 0.67 for 38.8 % of the particles. According to Krumbein and Sloss, 1963, a value larger than 0.33 corresponds with medium sphericity and a value larger than 0.67 corresponds with high sphericity. Two peaks can be distinguished in the sphericity-diagram. The shape factor distribution peaks at a value almost equal to 1.0.

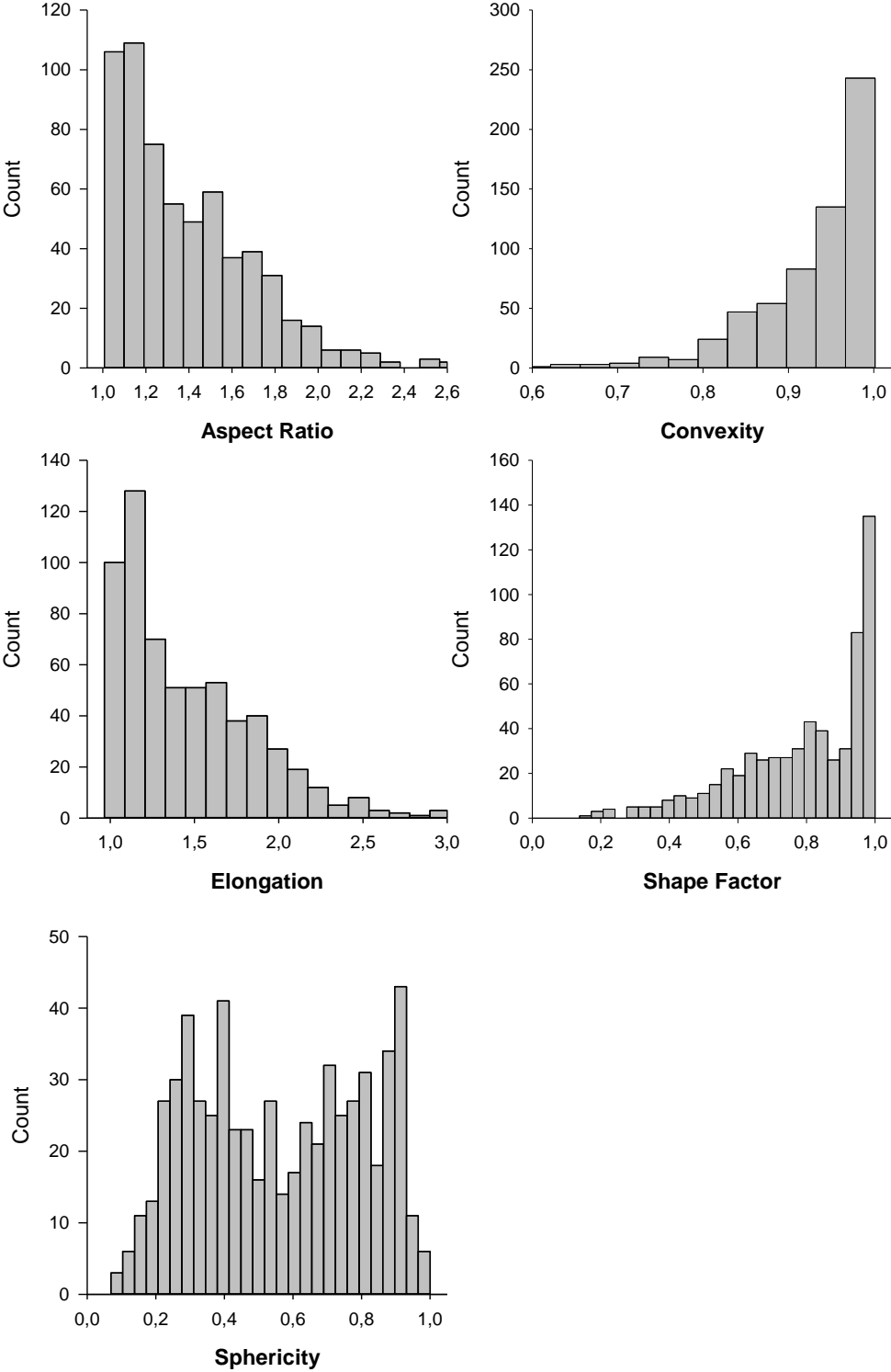


**Figure 53. Histograms showing the number-based ‘Shape’ distributions of dispersed aggregates and agglomerates of NM-100.**

**Table 38. Descriptive statistics of dispersed aggregates and agglomerates of NM-100 (based on measurement of 614 particles).**

Measured parameter	Mean	Std Dev	Std Err	Max	Min	Median	25%	75%
Diameter Mean (nm)	190.6	144.1	5.8	943.2	17.9	155.6	95.2	246.7
Diameter Max (nm)	210.6	163.2	6.6	1050.2	20.1	171.5	100.3	272.4
Diameter Min (nm)	148.7	102.9	4.2	802.4	13.0	125.5	86.7	190.3
ECD (nm)	162.4	106.0	4.3	661.6	16.4	143.1	93.3	211.8
Feret Mean (nm)	182.6	133.7	5.4	910.2	17.8	150.7	94.8	235.1
Feret Max (nm)	210.9	163.3	6.6	1051.9	20.4	171.4	100.2	272.8
Feret Min (nm)	145.4	97.8	3.9	733.4	13.0	124.8	86.9	184.8
Central Distance Mean (nm)	81.3	53.6	2.2	343.7	7.8	71.6	46.1	105.7
Central Distance Max (nm)	110.5	88.6	3.6	621.1	9.9	88.5	51.3	142.5
Central Distance Min (nm)	46.0	26.2	1.1	198.3	0.8	46.4	28.1	60.3
Radius of Inner Circle (nm)	59.9	31.2	1.3	203.5	6.4	58.9	42.6	75.5
Next Neighbor Distance (nm)	347.5	149.1	6.0	1239.6	87.6	317.3	244.1	425.9
Perimeter (nm)	642.0	585.5	23.6	4619.8	53.6	479.9	298.1	794.4
Area (nm <sup>2</sup> )	29514	41305	1667	343773	211	16088	6833	35241
Convex Area (nm <sup>2</sup> )	34623	55402	2236	505030	222	16496	6937	38717
Convex Perimeter (nm)	599.2	443.1	17.9	3043.4	54.4	492.4	309.3	775.3
Rectangle Mean (nm <sup>2</sup> )	50189	84212	3399	821431	312	22160	8985	54735
Rectangle Max (nm <sup>2</sup> )	54585	93351	3767	871588	326	23775	9364	58161
Rectangle Min (nm <sup>2</sup> )	44429	72427	2923	748527	294	20726	8593	49637
Aspect Ratio	1.391	0.307	0.012	2.640	1.011	1.300	1.143	1.570
Convexity	0.930	0.072	0.003	0.995	0.402	0.955	0.898	0.986
Elongation	1.467	0.414	0.017	3.479	1.003	1.355	1.132	1.707
Shape Factor	0.790	0.190	0.008	0.994	0.150	0.831	0.665	0.961
Sphericity	0.559	0.243	0.010	0.994	0.083	0.544	0.343	0.780

**Table 39. Number of dispersed aggregates and agglomerates (expressed in %) of NM-100 smaller than 100 nm, 50 nm and 10 nm.**

	< 100 nm (%)	< 50 nm (%)	< 10 nm (%)
<b>NM-100</b>	27.1	12.3	0

### 12.2.3. Results for NM-101

#### Qualitative analysis of NM-101

NM-101 was evenly distributed over the complete grid surface, suggesting that the charge of the NM is compatible with the charge of the grid. NM-101 mostly consists of aggregates and agglomerates, as illustrated in Figure 54. The primary particle size is approximately 5 nm and, as shown on the insert in Figure 54, NM-101 exhibits the electron diffraction pattern of

anatase. The aggregates have a size ranging from 10 nm up to 170 nm, measured manually on the TEM images and have a very irregular surface, as illustrated by Figure 55. The general morphology of the primary particles of NM-101 is equi-axed and rounded, or slightly elongated. Their suggested 3D structure is spherical or ellipsoidal. The aggregates and agglomerates also tend to be more or less equi-axed, possibly due to steric preference, or have a more fractal-like structure.

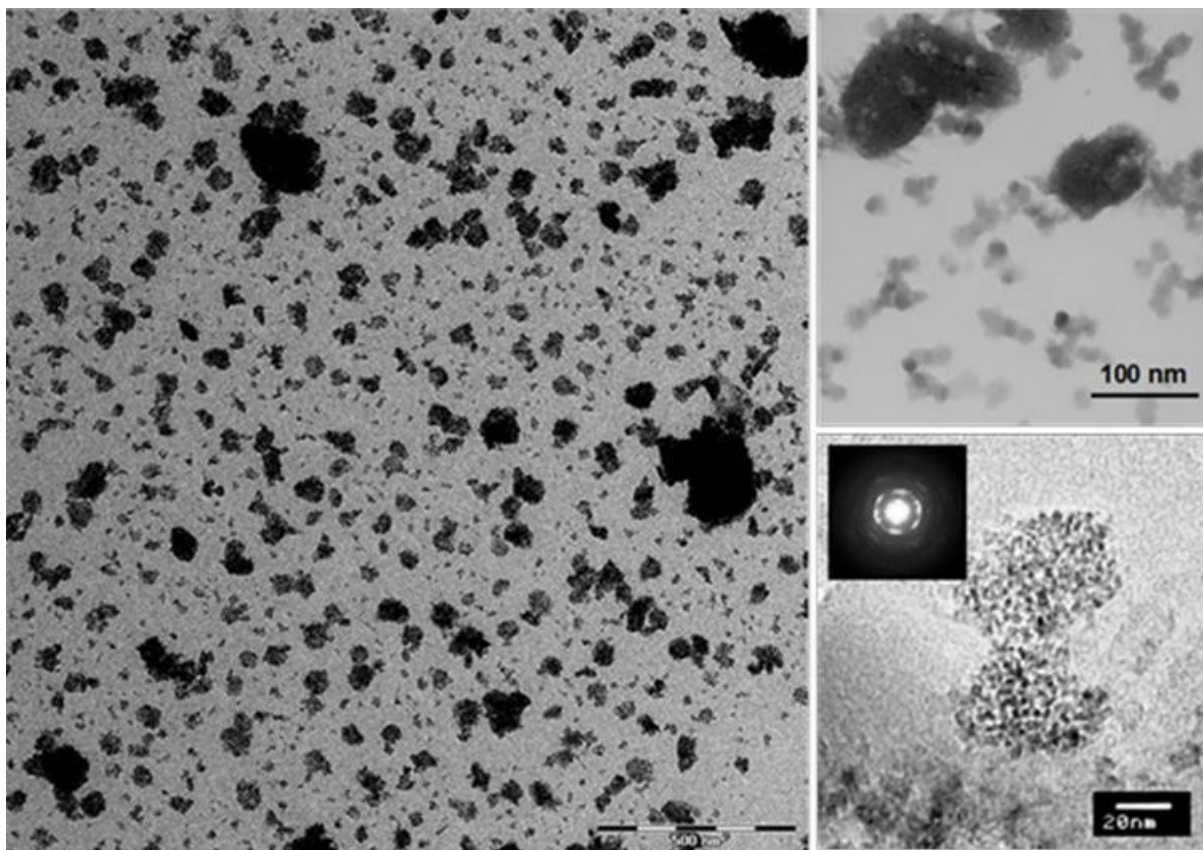


**Figure 54. NM-101: (Left) Representative TEM micrograph of well-dispersed sample taken for quantitative TEM-analysis; scale bar is 500nm. (Right) Selected TEM-micrograph showing the sample aggregates. (insert) Electron diffraction pattern of NM-101: anatase (IMC-BAS).**

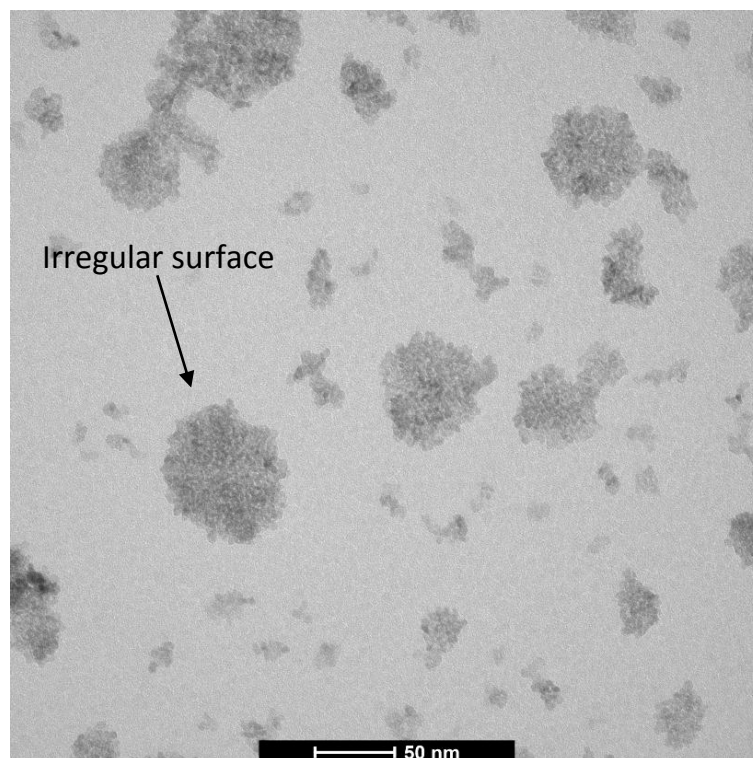


**Figure 55. Selected micrograph of NM-101, illustrating that the aggregates/agglomerates have a very irregular surface. (CODA-CERVA)**

### **Quantitative analysis of dispersed aggregates and agglomerates of NM-101**

The semi-automatic detection and measurement of TiO<sub>2</sub> nanoparticles dispersed in water based on mass thickness contrast was relatively straightforward. In 10 micrographs, 1802 particles were detected. Figure 56 represents the obtained raw data as number-based histograms of “shape” parameters. The descriptive statistics are summarized in Table 40.

The average value (Mean), the standard deviation (Std Dev), the standard error on the mean (Std Err), and the smallest (Min) and largest (Max) observation, are presented. However, since for all measured parameters of all examined NM, the Kolmogorov-Smirnov and the Shapiro-Wilk probabilities are smaller than 0.001 (not shown), none of these parameters can be assumed to be normally distributed. Hence, non-parametric estimates of these parameters describe the sample better. These include the median and the 25 and 75 percentiles.

The amount of aggregates/agglomerates smaller than 100 nm is 95.2 %. Table 41 summarizes the number of aggregates and agglomerates smaller than 100 nm, 50 nm and 10 nm for the specimen. The sphericity is larger than 0.33 for 65.0 % and larger than 0.67 for 15.7 % of the particles. According to Krumbein and Sloss, 1963, a value larger than 0.33 corresponds with medium sphericity and a value larger than 0.67 corresponds with high sphericity. The shape factor distribution of NM-101 peaks at a value almost equal to 0.3. 84.4



% of the particles have a shape factor smaller than 0.5, which is in line with observation of qualitative EM that the aggregates and agglomerates have a very irregular surface.

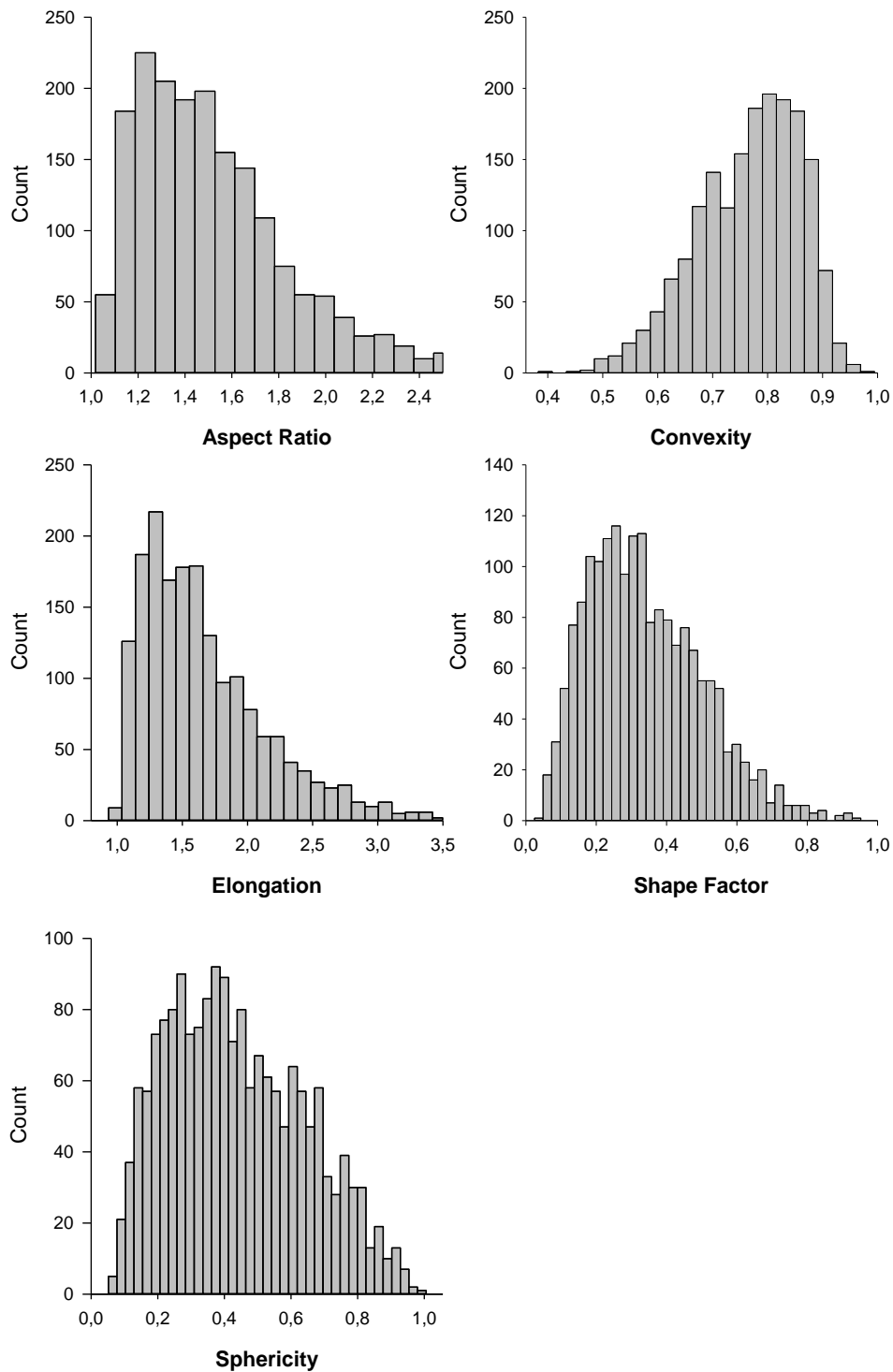


**Figure 56. Histograms showing the number-based 'Shape' distributions of dispersed aggregates and agglomerates of NM-101.**

**Table 40. Descriptive statistics of dispersed aggregates and agglomerates of NM-101 (based on measurement of 1802 particles)**

Measured parameter	Mean	Std Dev	Std Err	Max	Min	Median	25 %	75 %
Diameter Mean (nm)	34.7	30.3	0.7	201.0	3.3	22.6	14.1	45.8
Diameter Max (nm)	38.7	33.9	0.8	220.8	3.5	25.4	16.0	50.6
Diameter Min (nm)	26.4	23.1	0.5	137.6	2.2	16.8	10.8	35.7
ECD (nm)	26.6	22.8	0.5	128.2	3.1	17.2	10.9	35.6
Feret Mean (nm)	33.0	28.6	0.7	187.3	3.3	21.4	13.6	44.1
Feret Max (nm)	38.8	33.9	0.8	220.9	3.7	25.4	16.0	50.6
Feret Min (nm)	25.7	22.5	0.5	131.1	2.4	16.2	10.5	34.6
Central Distance Mean (nm)	13.6	11.7	0.3	69.5	1.5	8.8	5.7	18.4
Central Distance Max (nm)	20.8	18.4	0.4	130.3	1.8	13.5	8.4	27.1
Central Distance Min (nm)	6.0	6.4	0.2	40.9	0.0	3.7	1.6	7.8
Radius of Inner Circle (nm)	7.7	6.9	0.2	49.3	0.8	4.8	3.0	10.0
Next Neighbour Distance (nm)	38.4	17.7	0.4	113.1	4.9	36.9	25.2	50.4
Perimeter (nm)	175.2	195.6	4.6	1568.6	10.2	98.4	57.0	229.3
Area (nm <sup>2</sup> )	965	1695	40	12918	8	233	94	993
Convex Area (nm <sup>2</sup> )	1279	2333	55	22143	8	310	126	1310
Convex Perimeter (nm)	108.4	94.8	2.2	623.1	9.9	70.0	44.3	144.7
Rectangle Mean (nm <sup>2</sup> )	1872	3456	81	34291	11	448	184	1899
Rectangle Max (nm <sup>2</sup> )	2039	3774	89	38772	12	489	197	2107
Rectangle Min (nm <sup>2</sup> )	1663	3071	72	28635	10	389	164	1671
Aspect Ratio	1.524	0.333	0.008	3.243	1.044	1.461	1.268	1.693
Convexity	0.766	0.094	0.002	0.975	0.395	0.781	0.701	0.840
Elongation	1.676	0.492	0.012	3.960	1.007	1.561	1.298	1.926
Shape Factor	0.339	0.161	0.004	0.933	0.039	0.316	0.215	0.446
Sphericity	0.437	0.205	0.005	0.985	0.064	0.410	0.270	0.594

**Table 41. Number of dispersed aggregates and agglomerates (expressed in %) of NM-101 smaller than 100 nm, 50 nm and 10 nm.**

	< 100 nm (%)	< 50 nm (%)	< 10 nm (%)
<b>NM-101</b>	95.2	77.3	10.7

## 12.2.4. Results for NM-102

### Qualitative analysis of NM-102

NM-102 precipitated immediately after sonication both in double distilled water as well as in the solution BSA and water. As a consequence, the dispersed nanomaterial is not suitable for quantitative analysis.

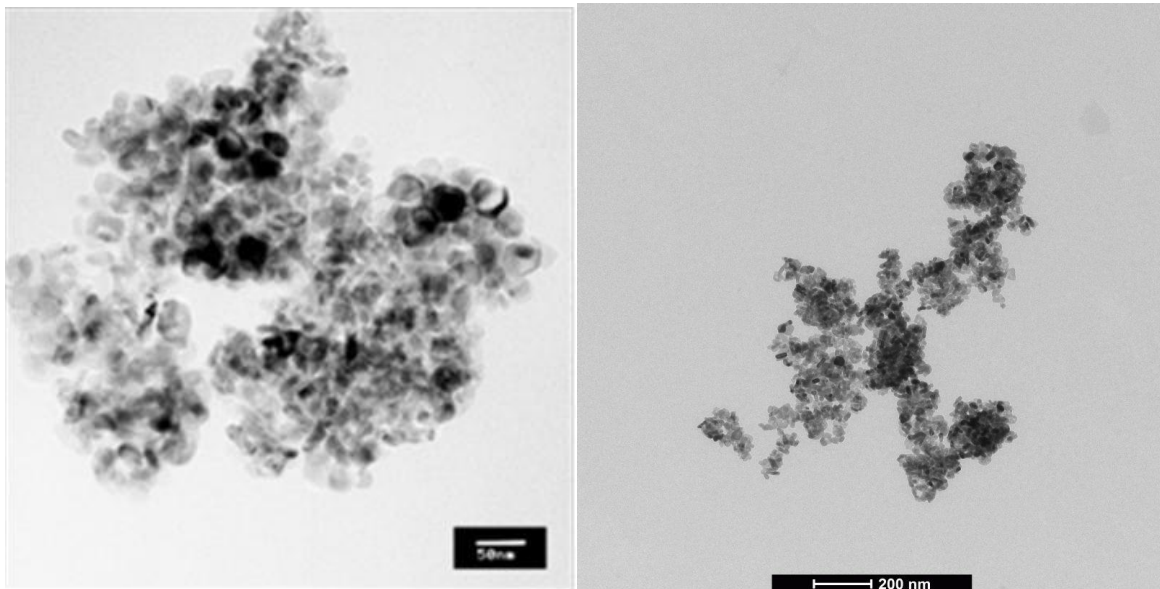


**Figure 57. Selected TEM image showing 100 to 500 nm-size aggregates/agglomerates in NM-102 dispersed in water (CODA-CERVA, left). Selected higher resolution TEM-image showing the nanocrystalline anatase aggregates with individual crystallite sizes typically smaller than 50 nm (IMC-BAS, right).**

TEM images demonstrate that for NM-102 only large aggregates were detected on the EM-grid. Such an aggregate is shown in the selected micrograph in Figure 57. The aggregates tend to have a more fractal-like structure. A range in primary particle morphologies is observed on the image as well, and in projection primary particles appear as circles, ellipses, rectangles or squares. It is important to note, however, that the apparent differences in primary particle shapes are the result of projection of similar particles with different orientations. The circles generally have a diameter of about 16 nm. The ellipses have a short axis of 16 nm and a long axis of 25 nm. The rectangles measure 16 nm by 40 nm. The side of the squares is approximately 30 nm.

### Quantitative analysis of dispersed aggregates and agglomerates of NM-102

NM-102 precipitated immediately after dispersion. Therefore the quantitative analysis could not be performed.

## 12.2.5. Results for NM-103

### Qualitative analysis and primary particle measurement of NM-103

NM-103 was evenly distributed over the complete grid surface, suggesting that the charge of the NM is compatible with the charge of the grid. NM-103 consists mainly of aggregates and agglomerates, as illustrated by Figure 59. Single particles are rarely detected. The variation in the size of the primary particles of the nanomaterial is limited. Primary particle sizes ranging from 20 nm up to 100 nm are detected. The aggregates have a size ranging from 40 nm up to 400 nm, measured manually.

The selected micrograph shown in Figure 60 illustrates the shape of the primary particles and aggregates. The general morphology of the primary particles of the NM is mainly elongated and rounded, suggesting an ellipsoidal, rod-like 3D structure. More circular and more angular particles are also detected. In most cases, the aggregates and agglomerates tend to have a more fractal-like structure. More equi-axed aggregates are sometimes detected, possibly due to steric preference. The presence of contaminating material with low mass-thickness contrast is observed in this specimen. Possibly this is a remnant of the coating of the particles.

The analysis of NM-103 dispersed with the NANOGENOTOX protocol revealed that NM-103 contains of small elongated prismatic primary particles with an aspect ratio of 1.7 - 1.8 measured in their projection in EM images and a short size (Feret Min) of 19 - 24 nm, depending on the used methodology. All analysed primary particles were smaller than 100 nm (Table 42). The Feret Mean and Feret Max of these particles were lognormal distributed, Feret min and Aspect ratio was lognormal distributed for semi-automatic measurements but not for manual measurements (Figure 58) (CODA-CERVA). Significant differences were found between manual and semi-automatic measurements ( $p = 0.02$ ). The Feret min, Feret Max, Feret Mean and Aspect ratio of these particles manually measured in IMC-BAS were found to be lognormal distributed.

**Table 42. Primary particle, Feret Min, Feret Max, Feret Mean, percentage of particles with a Feret Min lower than 100 nm and Aspect ratio of NM-103.**

Laboratory	Feret Min $\pm$ SD (nm)	Feret max $\pm$ SD (nm)	Feret mean $\pm$ SD (nm)	< 100 nm	Aspect ratio	n
CODA-CERVA (man)	21.9 $\pm$ 1.4 <sup>a</sup>	37.9 $\pm$ 1.6 <sup>a</sup>	30.1 $\pm$ 1.5 <sup>a</sup>	100 %	1.7 $\pm$ 1.3 <sup>a</sup>	40
CODA-CERVA (auto)	19.2 $\pm$ 1.4 <sup>b</sup>	32.5 $\pm$ 1.6 <sup>b</sup>	27.1 $\pm$ 1.5 <sup>a</sup>	100 %	1.7 $\pm$ 1.3 <sup>a</sup>	1317
IMC-BAS (man)	23.7 $\pm$ 5.9 <sup>c</sup>	42.8 $\pm$ 15.0 <sup>c</sup>	33.3 $\pm$ 9.4 <sup>c</sup>	100 %	1.82 $\pm$ 0.53 <sup>c</sup>	440

\* Geometric mean  $\pm$  the geometric standard deviation (SD) [15]

<sup>a, b</sup> Different letters indicate significantly different mean values by Kruskal-Wallis One Way Analysis of Variance on Ranks ( $p < 0.05$ )

<sup>c</sup> Arithmetic mean  $\pm$  the standard deviation

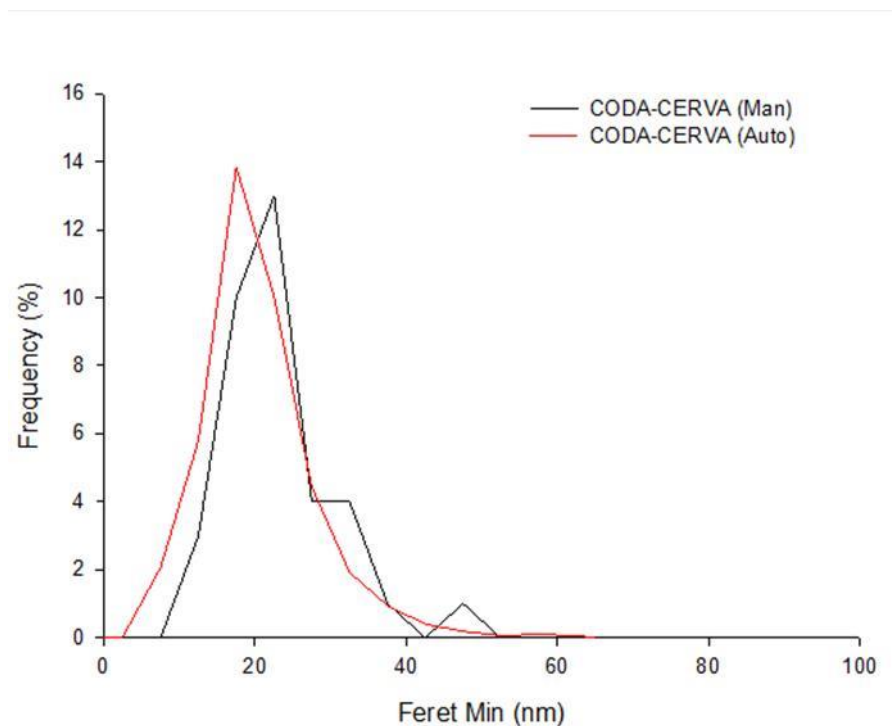


**Figure 58. Qualitative TEM image analysis of NM-103. The graph illustrates the primary particle Feret Min size distribution in function of the frequency. The manual measurement (CODA-CERVA (Man)) and the semi-automatic measurement (CODA-CERVA (Auto)) are given.**

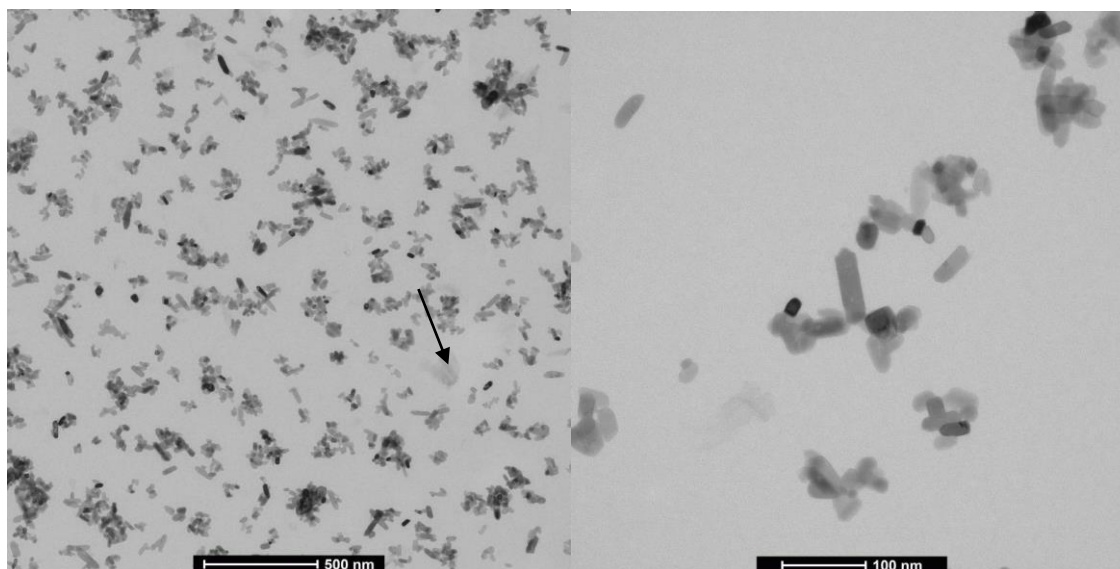


**Figure 59. Representative micrograph of aggregates and agglomerates of NM-103 dispersed in distilled water (left). TEM image at higher magnification of primary particles and small aggregates of NM-103 (right). The arrows indicate contaminant material.**

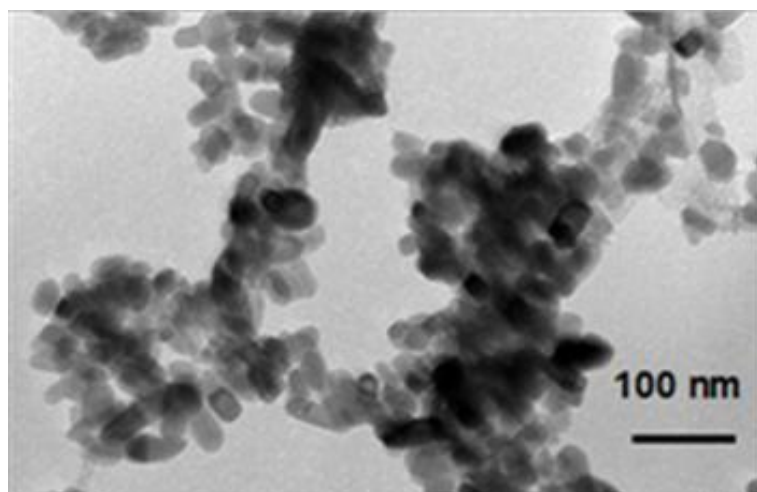


**Figure 60. NM-103: Selected TEM micrograph showing  $\mu\text{m}$ -sized aggregates of NM-103.**

### **Quantitative analysis of dispersed aggregates and agglomerates of NM-103**

Quantitative TEM analysis was performed for NM-103 dispersed in water and according to the NANOGENOTOX protocol.

The semi-automatic detection and measurement of dispersed aggregates and agglomerates of NM-103 was based on mass thickness contrast.

For NM-103 dispersed in water, 919 particles are detected in 10 micrographs. Figure 61 represents the obtained raw data as number-based histograms of “shape” parameters. The descriptive statistics are summarized in Table 43. For NM-103 dispersed with the NANOGENOTOX protocol in water containing BSA, 2641 particles are detected in 15 micrographs (3 independent experiments of 5 micrographs) by semi-automatic detection. Table 45 gives the descriptive statistics of the analysis of aggregates and agglomerates of NM-103 dispersed according to the NANOGENOTOX protocol.

The average value (Mean), the standard deviation (Std Dev), the standard error on the mean (Std Err), and the smallest (Min) and largest (Max) observation, are presented. However, since for all measured parameters of the examined NM, the Kolmogorov-Smirnov and the Shapiro-Wilk probabilities are smaller than 0.001 (not shown), none of these parameters can be assumed to be normally distributed. Hence, non-parametric estimates of these parameters describe the sample better. These include the median and the 25 and 75 percentiles.

For aggregates and agglomerates of NM-103 dispersed in water, the amount of particles smaller than 100 nm is 51.8 %. Table 44 summarizes the number of particles smaller than 100 nm, 50 nm and 10 nm for the specimens. The sphericity is larger than 0.33 for 53.0 % and larger than 0.67 for 11.0 % of the particles. According to Krumbein and Sloss, 1963, a value larger than 0.33 corresponds with medium sphericity and a value larger than 0.67

corresponds with high sphericity. The shape factor distribution has a maximum at a value of about 0.5. 56.5 % of the particles have a shape factor smaller than 0.5.

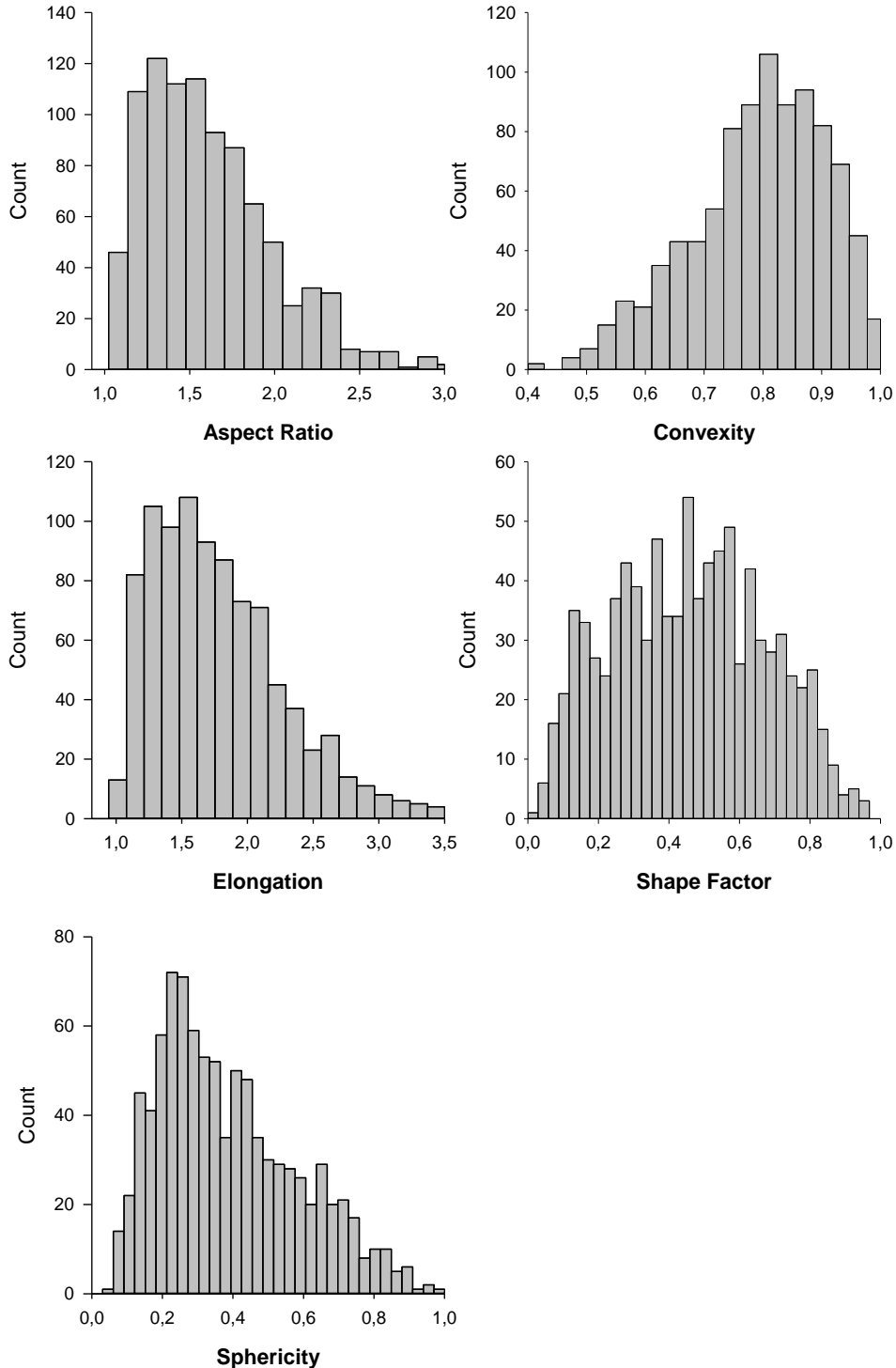


**Figure 61. Histograms showing the number-based 'Shape' distributions of aggregates and agglomerates of NM-103 dispersed in water.**

**Table 43. Descriptive statistics of aggregates and agglomerates of NM-103 dispersed in water (based on measurement of 919 particles).**

Measured parameter	Mean	Std Dev	Std Err	Max	Min	Median	25 %	75 %
Diameter Mean (nm)	126.4	96.5	3.2	705.3	9.0	97.0	65.2	156.6
Diameter Max (nm)	141.8	108.7	3.6	803.4	10.2	108.0	72.5	176.3
Diameter Min (nm)	91.3	69.8	2.3	554.7	5.6	71.3	48.9	107.9
ECD (nm)	91.3	59.7	2.0	478.1	8.3	73.9	52.3	110.8
Feret Mean (nm)	118.3	89.2	2.9	673.6	9.2	91.8	61.5	145.0
Feret Max (nm)	142.0	108.7	3.6	803.3	10.1	108.3	72.6	176.2
Feret Min (nm)	87.4	66.2	2.2	553.6	6.3	69.1	47.1	102.9
Central Distance Mean (nm)	47.1	32.1	1.1	256.2	3.9	38.0	26.4	57.3
Central Distance Max (nm)	76.2	59.1	2.0	435.0	4.8	58.7	38.7	95.4
Central Distance Min (nm)	14.8	10.9	0.4	128.6	0.1	13.0	8.2	19.3
Radius of Inner Circle (nm)	23.1	10.3	0.3	106.2	2.7	21.8	16.5	27.8
Next Neighbour Distance (nm)	149.5	66.5	2.2	481.5	28.8	136.1	105.2	176.9
Perimeter (nm)	581.6	718.3	23.7	7413.6	29.1	344.6	213.9	646.8
Area (nm <sup>2</sup> )	9347	15989	527	179515	54	4288	2149	9638
Convex Area (nm <sup>2</sup> )	14088	27957	922	302814	60	5334	2510	13338
Convex Perimeter (nm)	389.3	295.9	9.8	2257.1	27.9	299.5	200.9	475.6
Rectangle Mean (nm <sup>2</sup> )	21404	42441	1400	448958	84	8182	3684	20173
Rectangle Max (nm <sup>2</sup> )	23768	47449	1565	490306	86	8887	4059	22580
Rectangle Min (nm <sup>2</sup> )	18380	36310	1198	380163	80	7071	3236	17204
Aspect Ratio	1.622	0.388	0.013	3.659	1.038	1.554	1.333	1.830
Convexity	0.793	0.114	0.004	0.983	0.408	0.807	0.723	0.881
Elongation	1.792	0.527	0.017	4.339	1.013	1.703	1.390	2.075
Shape Factor	0.457	0.214	0.007	0.944	0.027	0.462	0.285	0.626
Sphericity	0.387	0.197	0.006	0.975	0.053	0.345	0.232	0.517

**Table 44. Number of dispersed aggregates and agglomerates (expressed in %) of NM-103 smaller. than 100 nm, 50 nm and 10 nm.**

	< 100 nm (%)	< 50 nm (%)	< 10 nm (%)
<b>NM-103</b>	51.8	12.7	0.1



**Table 45. Descriptive statistics of aggregates and agglomerates NM-103 dispersed following the NANOGENOTOX dispersion protocol (based on measurement of 2541 particles).**

Measured parameter	Mean	SD	SEM	Max	Min	Median	25 %	75 %
Diameter Mean (nm)	97.1	94.4	1.8	775.4	7.2	67.2	33.0	128.7
Diameter Max (nm)	110	107	2	894	8	76	37	145
Diameter Min (nm)	67	64	1	460	4	48	20	92
ECD (nm)	66.9	57.0	1.1	440.9	6.8	51.7	25.3	92.3
Feret Mean (nm)	89.9	85.8	1.7	663.1	7.2	63.7	30.6	120.7
Feret Max (nm)	109.9	107.3	2.1	895.0	8.0	75.9	37.3	145.6
Feret Min (nm)	64.0	60.3	1.2	451.7	3.6	46.5	19.8	87.0
Central Distance Mean (nm)	35.3	31.6	0.6	253.6	3.1	26.6	13.1	47.4
Central Distance Max (nm)	59.0	58.4	1.1	463.9	3.8	40.5	19.2	78.6
Central Distance Min (nm)	10	9	0	111	0	8	3	14
Radius of Inner Circle (nm)	22.5	14.4	0.3	129.0	2.1	20.7	12.3	30.9
Next Neighbour Distance (nm)	99.9	56.2	1.1	479.0	5.4	96.5	57.9	134.5
Perimeter (nm)	469	637	12	6728	21	233	103	560
Area (nm <sup>2</sup> )	6071	10848	211	152667	36	2101	502	6685
Convex Area (nm <sup>2</sup> )	9535	19529	380	259709	37	2591	588	9413
Convex Perimeter (nm)	295	284	6	2185	21	208	99	397
Rectangle Mean (nm <sup>2</sup> )	14918	31447	612	412611	52	3942	900	14289
Rectangle Max (nm <sup>2</sup> )	16665	35586	692	479884	58	4340	1020	15754
Rectangle Min (nm <sup>2</sup> )	12660	26442	515	383118	43	3427	731	12244
Aspect Ratio	1.794	0.584	0.011	6.280	1.055	1.660	1.389	2.015
Convexity	0.772	0.128	0.002	0.988	0.362	0.780	0.683	0.874
Elongation	2.013	0.796	0.016	8.829	1.008	1.823	1.464	2.321
Shape Factor	0.431	0.233	0.005	0.980	0.030	0.401	0.237	0.620

## 12.2.6. Results for NM-104

### Qualitative analysis of NM-104

NM-104 was evenly distributed over the complete grid surface, suggesting that the charge of the NM and the grid were compatible. NM-104 dispersed into double distilled water consisted of aggregates and agglomerates see Figure 62 and Figure 63; single particles were more rarely detected. A variation in size and shape of the NM-104 primary particles is observed in the TEM images. Primary particle sizes ranging from 8 nm up to 200 nm are detected. The general morphology of the primary particles of the NM is mainly elongated and rounded, suggesting an ellipsoidal, rod-like 3D structure. More angular particles are frequently detected as well. It is important to note, however, that the apparent differences in primary particle shape are the result of projection of similar particles with different orientations.

The representative TEM image of NM-104 prepared according to the NANOGENOTOX protocol is shown in Figure 62(A). The primary particles of NM-104 are about 25 nm along the smaller dimension and they occur mainly in branched aggregates/agglomerates of ca. 100-200 nm. Particle morphology varies from equi-dimensional euhedral to elongated.

The aggregates and agglomerates have sizes ranging from 20 nm up to 500 nm, measured

directly on the TEM images. In most cases, the aggregates and agglomerates tend to have a more fractal-like structure. More equi-axed aggregates are often detected as well, possibly due to steric preference. The presence of contaminant material, appearing as relatively electron-lucent structures, is observed in NM-104 in Figure 62(A). Diffraction contrast, which indicates that the material is crystalline, can be observed in the primary particles. Figure 63(B) shows a particle that exhibits the Moiré effect showing an interference pattern due to the polycrystallinity of the NM.

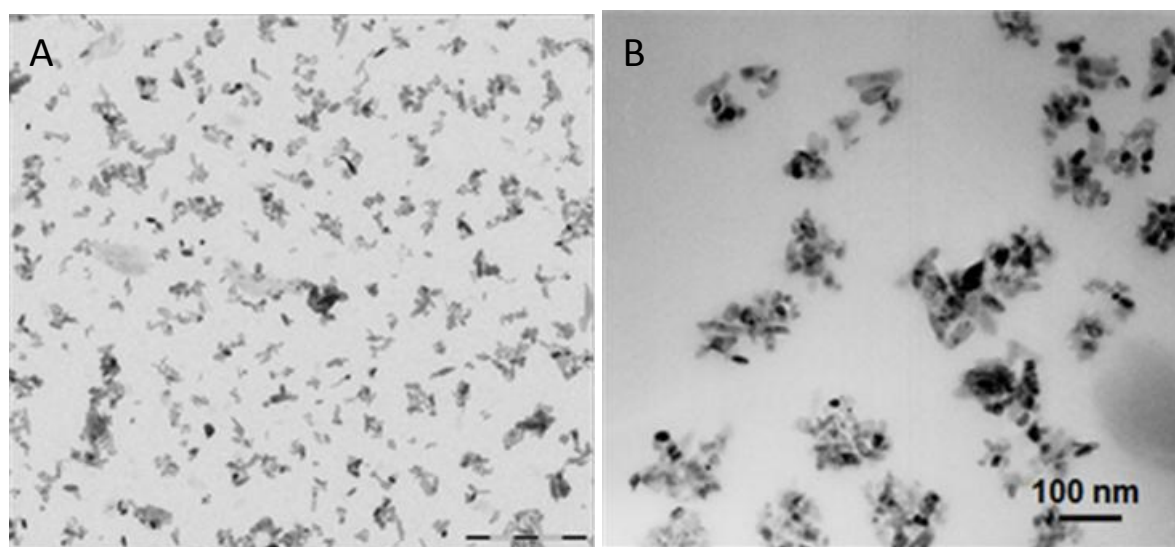


**Figure 62.** Micrographs of dispersed aggregates and agglomerates of NM-104. (left) A representative TEM micrograph that shows the typical aggregate/agglomerate size in the material (Bar is 500nm). (right) TEM micrograph showing a close-up of the aggregates showing the presence of equidimensional euhedral and some elongated crystals of rutile (IMC-BAS).

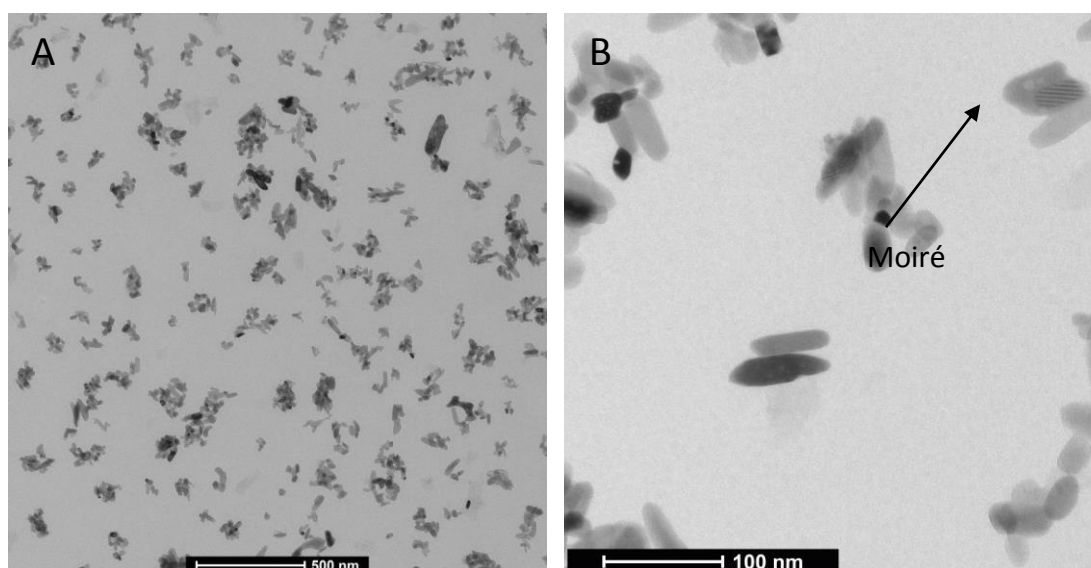


**Figure 63.** (left) Representative micrograph of aggregates and agglomerates of NM-104 dispersed in water. (right) Selected micrograph of NM-104, illustrating the size and shape of the primary particles, aggregates and agglomerates of NM-104.

### **Quantitative analysis of dispersed aggregates and agglomerates of NM-104**

The semi-automatic detection and measurement of NM-104 TiO<sub>2</sub> nanoparticles dispersed in water was based on mass thickness contrast. In 10 micrographs, 1265 aggregates and agglomerates are detected in the samples of NM-104. Figure 64 represents the obtained raw data as number-based histograms of “shape” parameters. The descriptive statistics are summarized in Table 46. For CODA-CERVA, 3739 aggregates and agglomerates are detected in 15 micrographs (3 independent experiments of 5 micrographs) by semi-automatic detection. Table 48 gives the descriptive statistics of the analysis of aggregates and agglomerates of NM-104 dispersed according to the NANOGENOTOX dispersion protocol.

The average value (Mean), the standard deviation (Std Dev), the standard error on the mean (Std Err), and the smallest (Min) and largest (Max) observation, are presented. However, since for all measured parameters of the examined NMs, the Kolmogorov-Smirnov and the Shapiro-Wilk probabilities are smaller than 0.001 (not shown), none of these parameters can be assumed to be normally distributed. Hence, non-parametric estimates of these parameters describe the sample better. These include the median and the 25 and 75 percentiles.

The amount of aggregates and agglomerates smaller than 100 nm is 53.3 %. Table 47 summarizes the number of particles smaller than 100 nm, 50 nm and 10 nm for NM-104.

The shape factor distribution has a maximum at a value of about 0.2. 77.7 % of the particles have a shape factor smaller than 0.5.

The sphericity is larger than 0.33 for 49.3 % and larger than 0.67 for 8.0 % of the particles. According to Krumbain and Sloss, 1963, a value larger than 0.33 corresponds with medium sphericity and a value larger than 0.67 corresponds with high sphericity.

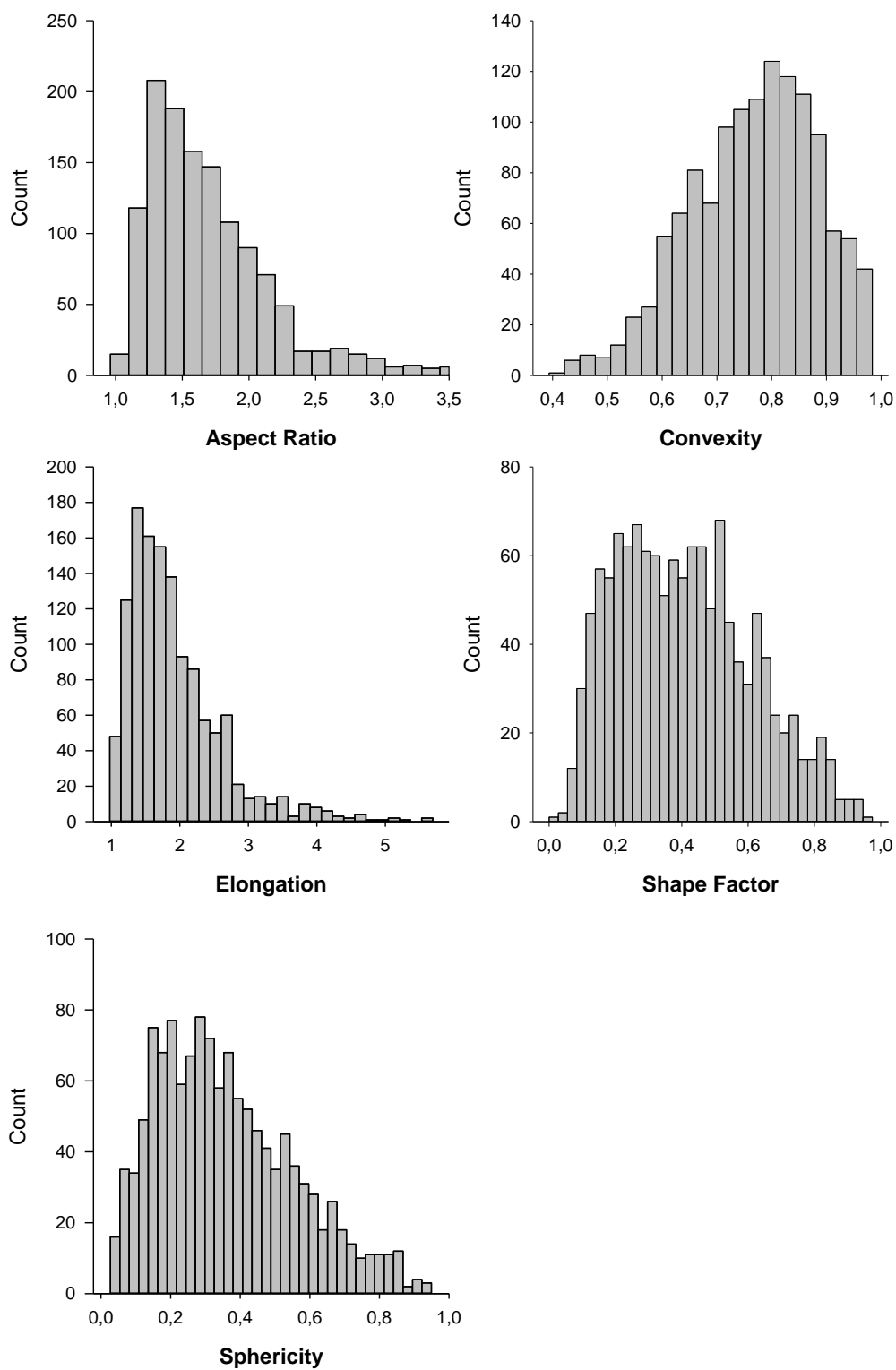


**Figure 64. Histograms showing the number-based 'Shape' distributions of dispersed aggregates and agglomerates of NM-104.**

**Table 46. Descriptive statistics of aggregates and agglomerates of NM-104 dispersed in water (based on measurement of 1265 particles).**

Measured parameter	Mean	Std Dev	Std Err	Max	Min	Median	25%	75%
Diameter Mean (nm)	117.8	76.4	2.1	648.6	9.3	95.4	65.5	147.8
Diameter Max (nm)	132.7	86.5	2.4	774.8	10.6	107.4	73.3	165.3
Diameter Min (nm)	81.9	52.4	1.5	433.7	7.8	67.0	46.7	102.6
ECD (nm)	82.7	45.5	1.3	334.6	8.3	70.9	51.0	103.5
Feret Mean (nm)	109.2	69.1	1.9	571.4	9.3	88.8	61.5	136.7
Feret Max (nm)	132.9	86.5	2.4	774.7	10.6	107.2	73.5	165.5
Feret Min (nm)	78.5	49.5	1.4	416.9	8.4	65.2	45.4	97.9
Central Distance Mean (nm)	43.3	25.2	0.7	208.6	3.9	36.7	26.3	54.3
Central Distance Max (nm)	71.5	47.8	1.3	418.4	5.3	57.5	39.5	88.4
Central Distance Min (nm)	13.2	9.3	0.3	70.8	0.0	11.8	7.0	17.7
Radius of Inner Circle (nm)	20.7	8.6	0.2	85.8	3.3	19.4	14.7	24.8
Next Neighbour Distance (nm)	131.5	48.2	1.4	376.2	18.8	127.2	98.7	161.9
Perimeter (nm)	520.8	500.5	14.1	6161.2	30.4	351.8	222.0	636.0
Area (nm <sup>2</sup> )	6998	8768	247	87942	54	3948	2041	8418
Convex Area (nm <sup>2</sup> )	10424	15363	432	188768	60	5162	2487	11601
Convex Perimeter (nm)	358.8	229.3	6.4	1898.4	28.2	291.0	201.3	450.0
Rectangle Mean (nm <sup>2</sup> )	16166	24425	687	304682	86	7678	3706	18297
Rectangle Max (nm <sup>2</sup> )	18061	27632	777	337512	90	8626	4026	20255
Rectangle Min (nm <sup>2</sup> )	13738	20622	580	269883	80	6664	3230	15199
Aspect Ratio	1.711	0.497	0.014	4.802	1.044	1.602	1.359	1.930
Convexity	0.768	0.114	0.003	0.983	0.414	0.778	0.686	0.853
Elongation	1.919	0.691	0.019	5.688	1.027	1.749	1.432	2.219
Shape Factor	0.408	0.201	0.006	0.974	0.027	0.392	0.243	0.544
Sphericity	0.359	0.196	0.006	0.948	0.031	0.327	0.203	0.488

**Table 47. Number of aggregates and agglomerates of NM-104 dispersed in water (expressed in %) smaller than 100 nm, 50 nm and 10 nm.**

	< 100 nm (%)	< 50 nm (%)	< 10 nm (%)
<b>NM-104</b>	53.3	12.1	0.1

**Table 48. Descriptive statistics of aggregates and agglomerates of NM-104 dispersed following the NANOGENOTOX dispersion protocol (based on measurement of 3739 particles).**

Measured parameter	Mean	SD	SEM	Max	Min	Median	25%	75%
Area (nm <sup>2</sup> )	4368	7741	127	149999	36	1667	530	5072
Convex Area (nm <sup>2</sup> )	6699	14019	229	274061	37	2045	593	6889
Rectangle Max (nm <sup>2</sup> )	11602	24948	408	454934	58	3424	1004	11898
Rectangle Mean (nm <sup>2</sup> )	10421	22173	363	425922	54	3100	908	10649
Rectangle Min (nm <sup>2</sup> )	8909	18572	304	370845	43	2706	761	9107
ECD (nm)	58.5	46.3	0.8	437.0	6.8	46.1	26.0	80.4
Feret Max (nm)	94.4	85.1	1.4	863.9	7.7	68.7	37.7	125.9
Feret Mean (nm)	77.6	68.8	1.1	667.4	7.3	56.2	30.6	104.6
Feret Min (nm)	56.0	49.9	0.8	465.9	4.2	41.2	20.3	76.0
Next Neighbour Distance (nm)	89.2	44.6	0.7	574.5	8.5	86.5	58.3	117.6
Radius of Inner Circle (nm)	20.8	12.4	0.2	103.6	2.1	19.0	12.3	28.3
Central Distance Max (nm)	50.8	46.8	0.8	483.8	3.8	36.3	19.4	68.1
Central Distance Mean (nm)	30.7	25.4	0.4	241.1	3.1	23.5	13.3	41.3
Central Distance Min (nm)	9	8	0	79	0	8	3	12
Diameter Max (nm)	94	85	1	864	8	69	38	126
Diameter Mean (nm)	83.5	75.1	1.2	739.4	7.3	60.5	33.0	111.6
Diameter Min (nm)	58	53	1	506	4	43	21	80
Convex Perimeter (nm)	254	228	4	2227	22	184	99	344
Perimeter (nm)	376	493	8	8553	22	207	103	457
Aspect Ratio	1.741	0.496	0.008	4.630	1.034	1.627	1.384	1.966
Convexity	0.783	0.125	0.002	1.000	0.388	0.793	0.695	0.884
Elongation	1.934	0.668	0.011	6.280	1.011	1.777	1.456	2.233
Shape Factor	0.457	0.229	0.004	0.984	0.020	0.439	0.265	0.636

### Grouping parameters by principle component analysis

Principal component analysis (PCA) of the dataset consisting of the twenty-three parameters obtained by quantitative TEM analysis was performed on NM-103 and NM-104, see Figure 65, and allowed classifying the parameters in three uncorrelated principle components (PC) explaining approximately 93 % of the variability in the samples (Table 49). Examination of the component pattern profiles of this PCA showed that PC 1 mainly consists of direct size measures and 2D size measurements. The direct size measures include the Feret max, Feret mean, Feret min, central distance max, central distance mean, diameter max, diameter mean and diameter min. The 2D size measurements include area, convex area, rectangle max, rectangle mean, rectangle min, ECD, convex perimeter and perimeter. The convexity and the shape factor of the aggregates are inversely correlated with their size: as size increases, the surface becomes more complex. PC 2 is importantly determined by the aspect ratio, elongation and sphericity, which reflect the shape of the particles. PC 3 is mostly determined by the convexity and shape factor, parameters reflecting the surface topology of the particles.

One representative parameter was selected from each of the classifications based on PCA to describe and compare the TiO<sub>2</sub> NMs. The mean diameter was chosen as a size measure, the sphericity was chosen as a shape measure and the shape factor was chosen as a measurand for surface topology, see Figure 66 and Table 50.

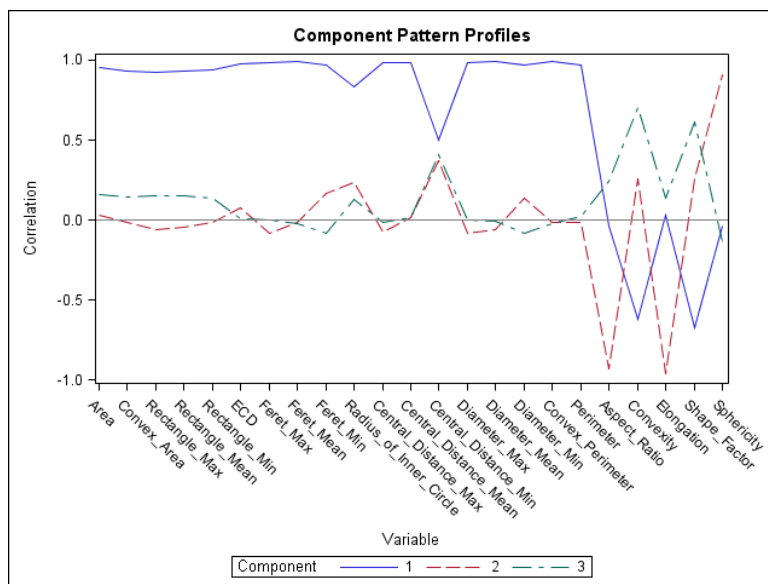


**Figure 65.** Representative examples of component pattern profiles of quantitative TEM analysis of NM-104 categorized into three principle components (blue line, red dashed line and green dashed line).

**Table 49.** Representation of the proportion of the eigenvalues of the correlation matrix in each principle component.

	PC1 <sup>x</sup>	PC2 <sup>x</sup>	PC3 <sup>x</sup>	Cumulative <sup>x</sup>
<b>NM-103</b>	73.5 ± 0.5 %	13.3 ± 0.3 %	5.1 ± 0.3 %	91.9 ± 0.2 %
<b>NM-104</b>	73.1 ± 0.8 %	13.2 ± 0.1 %	5.6 ± 0.4 %	91.9 ± 0.5 %

<sup>x</sup>Mean values of medians ± SD are represented for 3 independent analyses

The curves of NM-103 and NM-104 (Figure 66) show that the number-based mean diameter, sphericity and shape factor distributions of NM-103 and NM-104 are very similar. TEM analysis showed that the general morphology of the TiO<sub>2</sub> nanomaterials, described based on the guidelines of Jensen, 2011, was quite comparable, see Table 51. All samples consist of high porosity nanostructured materials, which may be considered aggregates of primary euohedral TiO<sub>2</sub> particles.

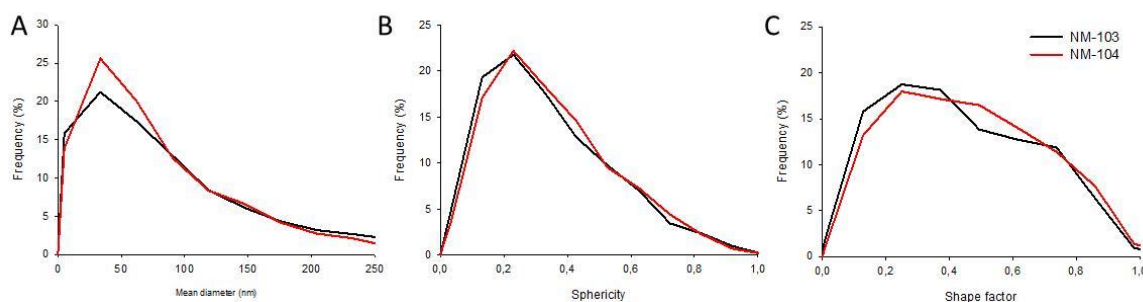


**Figure 66.** Number-based distributions of the mean diameter (A), sphericity (B) and shape factor (C) of agglomerates and aggregates of TiO<sub>2</sub> NMs dispersed following the protocol. The frequency of the agglomerates and aggregates of TiO<sub>2</sub> NM are represented as NANOGENOTOX a function of mean diameter, sphericity and shape factor.

**Table 50.** Characterization by quantitative TEM of aggregated TiO<sub>2</sub> NMs dispersed following the NANOGENOTOX dispersion protocol.

	Mean diameter (nm) <sup>x</sup>	Sphericity <sup>x</sup>	Shape factor <sup>x</sup>	% < 100 nm <sup>x,y</sup>
<b>NM-103</b>	67 ± 1 <sup>a</sup>	0.40 ± 0.01 <sup>a</sup>	0.29 ± 0.02 <sup>a</sup>	66.0 ± 2.0 <sup>a</sup>
<b>NM-104</b>	60 ± 2 <sup>b</sup>	0.44 ± 0.02 <sup>a</sup>	0.32 ± 0.01 <sup>a</sup>	70.7 ± 0.4 <sup>b</sup>

<sup>x</sup> Mean values of medians ± SD are represented for 3 independent analyses

<sup>y</sup> The percentage of aggregates with a minimal Feret diameter smaller than 100 nm is represented.

<sup>a, b</sup> Different letters indicate significantly different mean values by One Way Analysis of Variance and pairwise compared with Tukey test.

**Table 51.** Tabular summary describing the morphology of aggregates/agglomerates of NM-103 and NM-104 dispersed following the NANOGENOTOX protocol according to Jensen, 2011.

Sample	Sphericity	Shape factor	General morphology
<b>NM-103</b>	Low sphericity	Very angular to sub-angular	Angular, low sphericity
<b>NM-104</b>	Low sphericity	Angular to sub-rounded	Sub-angular, low sphericity

## 12.2.7. Results for NM-105

### Qualitative analysis and measurement of primary particles of NM-105

NM-105 dispersed in double distilled water precipitated immediately after sonication, and as a consequence, the specimen is not suitable for quantitative analysis.

TEM micrographs show that only large agglomerates of TiO<sub>2</sub> particles are detected on the EM-grid. Such an aggregate is shown in the selected TEM image in Figure 67. The aggregates tend to have a more fractal-like structure. A range in primary particle morphology and size is observed, as illustrated in Figure 67. Primary particles with a circular or slightly



elongated and a more angular 2D shape are detected in the image, suggesting a spherical, ellipsoidal or cuboidal 3D structure. The primary particles have a diameter ranging from about 10 nm to 45 nm. Diffraction contrast, which indicates that the NM is crystalline, is clearly observed on the TEM images.

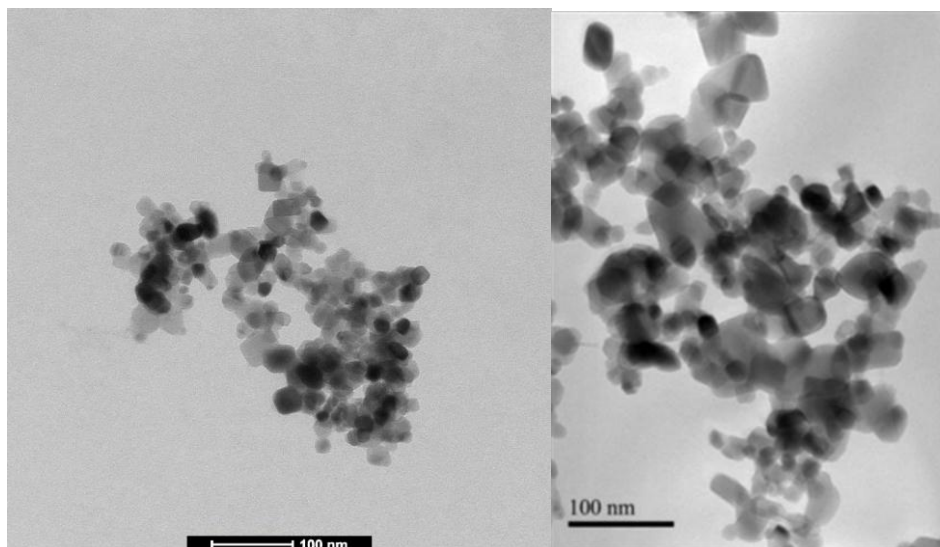


**Figure 67. (left) Selected micrograph of an aggregate of NM-105 dispersed in water. (right) Selected micrograph of an aggregate showing that it mainly consists of equidimensional to weakly elongated euhedral of rutile (IMC-BAS).**

Neither IMC-BAS nor CODA-CERVA could obtain a stable dispersion suitable for quantitative TEM analysis using the generic NANOGENOTOX protocol. As can be seen from Figure 67 and Table 52, NM-105 contains small ellipsoidal primary particles with an aspect ratio of 1.3 and a size of 17 - 19 nm, depending on the used methodology. All analysed primary particles were smaller than 100 nm (Table 52). The Feret Min (Figure 68), Feret Mean and Feret Max of these particles were lognormal distributed; the Aspect ratio was lognormal distributed for semi-automatic measurements but not for manual measurements. No significant ( $p < 0.05$ ) differences were found between manual and semi-automatic measurements.

**Table 52. Comparison of manual and semi-automatic measurements of the primary particles of NM-105.**

Laboratory	Feret Min $\pm$ SD (nm)	Feret max $\pm$ SD (nm)	Feret mean $\pm$ SD (nm)	<100 nm	Aspect ratio	n
CODA-CERVA (man)	19.0 $\pm$ 1.5 <sup>a</sup>	25.8 $\pm$ 1.4 <sup>a</sup>	22.6 $\pm$ 1.4 <sup>a</sup>	100 %	1.36 $\pm$ 1.3 <sup>a</sup>	47
CODA-CERVA (auto)	17.3 $\pm$ 1.5 <sup>a</sup>	24.2 $\pm$ 1.4 <sup>a</sup>	21.6 $\pm$ 1.5 <sup>a</sup>	100 %	1.36 $\pm$ 1.2 <sup>a</sup>	1421

\* Geometric mean  $\pm$  the geometric standard deviation (SD) [15]

a, b Different letters indicate significantly different mean values by Kruskal-Wallis One Way Analysis of Variance on Ranks ( $p < 0.05$ )

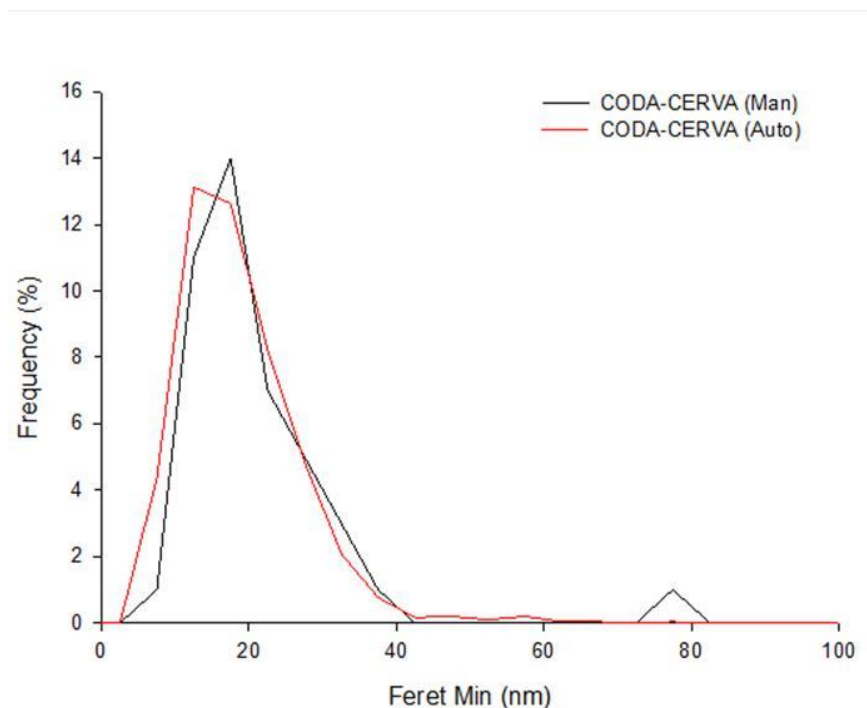


**Figure 68. Comparison of manual and semi-automatic measurement of primary particles of NM-105. The curves show primary particle Feret Min size distribution as a function of frequency.**

#### **Quantitative analysis of dispersed aggregates and agglomerates of NM-105**

NM-105, dispersed in double distilled water as well as dispersed following the NANOGENOTOX dispersion protocol, precipitates immediately after sonication, and thus quantitative analysis could not be performed.

#### **Comparison of primary particle measurements between laboratories**

The primary particle sizes for the TiO<sub>2</sub> NMs as resulting from the analyses performed by different institutions are given in Table 53. As seen from the data, some variations are observed, but the different results are within the standard variation.

**Table 53. Primary particle size of the TiO<sub>2</sub> NMs analysed by different laboratories.**

<b>Material</b>	<b>ECD (nm) ± SD (N<sup>&amp;</sup>); CODA-CERVA</b>	<b>ECD (nm) ± SD (N<sup>&amp;</sup>); INRS</b>	<b>Diameter (nm); IMC-BAS</b>
<b>NM-100</b>	50-90*	-	150
<b>NM-101</b>	6*	-	5
<b>NM-102</b>	21 ± 10 (1395)	22 ± 6 (100)	22
<b>NM-103</b>	26 ± 10 (1317)	26 ± 6 (101)	22
<b>NM-104</b>	26 ± 10 (1099)	26 ± 7 (100)	23
<b>NM-105</b>	21 ± 9 (1421)	24 ± 5 (105)	Rutile: 15*; Anatase: 20.5± 58.6**

\* Manual measurement. \*\* Manual Measurements using ImageJ software. &N= number of particles observed

### 12.3. Combination of the results of quantitative AFM and TEM analyses

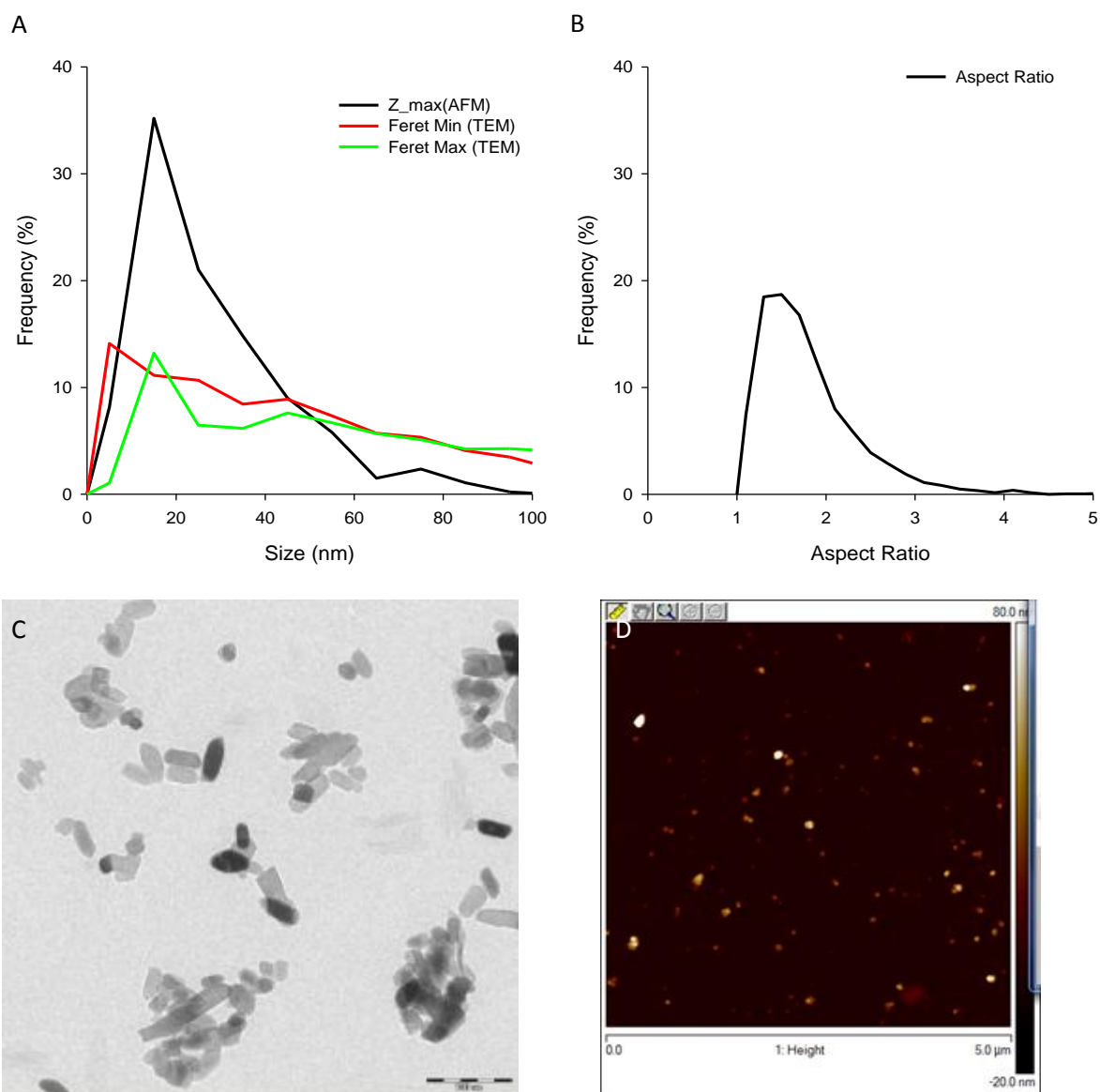
Results of quantitative AFM and TEM analyses are highly complementary. Quantitative TEM allows determining the minimal and maximal size of aggregates in the X-Y plane, measured as Feret min and Feret Max. AFM estimates the third dimension of a NM, measured as Z-max (Figure 69, Figure 70, Table 54, Table 55). The combination of the results of both techniques gives an insight in the 3D properties of the NM. A direct link can be made between the Feret Min and Feret Max on a per particle level. Their ratio, as the aspect ratio, is a measure for aggregate morphology. Regrettably, no direct link can be made between AFM and TEM results at the per-particle-level because different particles are analyzed. Therefore, results can only be compared at the population level, matching (statistical) characteristics of size distributions. The visualization of NM in TEM micrographs can assist in the interpretation of the values measured by AFM.

Figure 69C and Figure 70C show that the aggregates of the titanium dioxide NM-103 and NM-104 are fractal-like. Combining the AFM result with primary particle dimensions (Figure 69A and Figure 70A) tends to confirm the observation (Figure 69C and Figure 70C) that most aggregates are approximately 1.5 primary particles thick. The aggregates of NM-103 and NM-104 are wider (Feret min) than high (Z-max) and longer (Feret max) than wide (Feret min) (Table 54, Table 55, Figure 69B and Figure 70B).

It must be stressed however that for the TiO<sub>2</sub> NM, the preparation protocols are different from AFM to TEM samples. Indeed, the sonication in acidic medium performed for AFM samples is likely to lead to better dispersed and more stable suspensions, and therefore smaller aggregates. This, and possible preferential orientation towards the grid, explains why the AFM distributions in Figure 69 and Figure 70 are less polydisperse than the corresponding TEM distributions.

**Table 54. Characterization of NM-103 in three dimensions.**

Laboratory	Technique	Parameter	Median (N)
CEA	AFM	Z max	22.3 (466)
CODA-CERVA	TEM	Feret Min	46.5 (2641)
CODA-CERVA	TEM	Feret Max	75.9 (2641)



**Figure 69.** Characterization of the aggregates of TiO<sub>2</sub> NM-103 in three-dimensions by combination of TEM and AFM. A) Number based size distributions of Feret Min, Feret max and Z\_max. B) Number based distribution of the aspect ratio. Representative TEM (C) and AFM (D) micrographs visualizing the morphology of the aggregates.

**Table 55.** Characterization of Titanium dioxide NM-104 in three dimensions.

Laboratory	Technique	Parameter	Median (N)
CEA	AFM	Z max	21.8 (458)
CODA-CERVA	TEM	Feret Min	41.2 (3739)
CODA-CERVA	TEM	Feret Max	68.7 (3739)

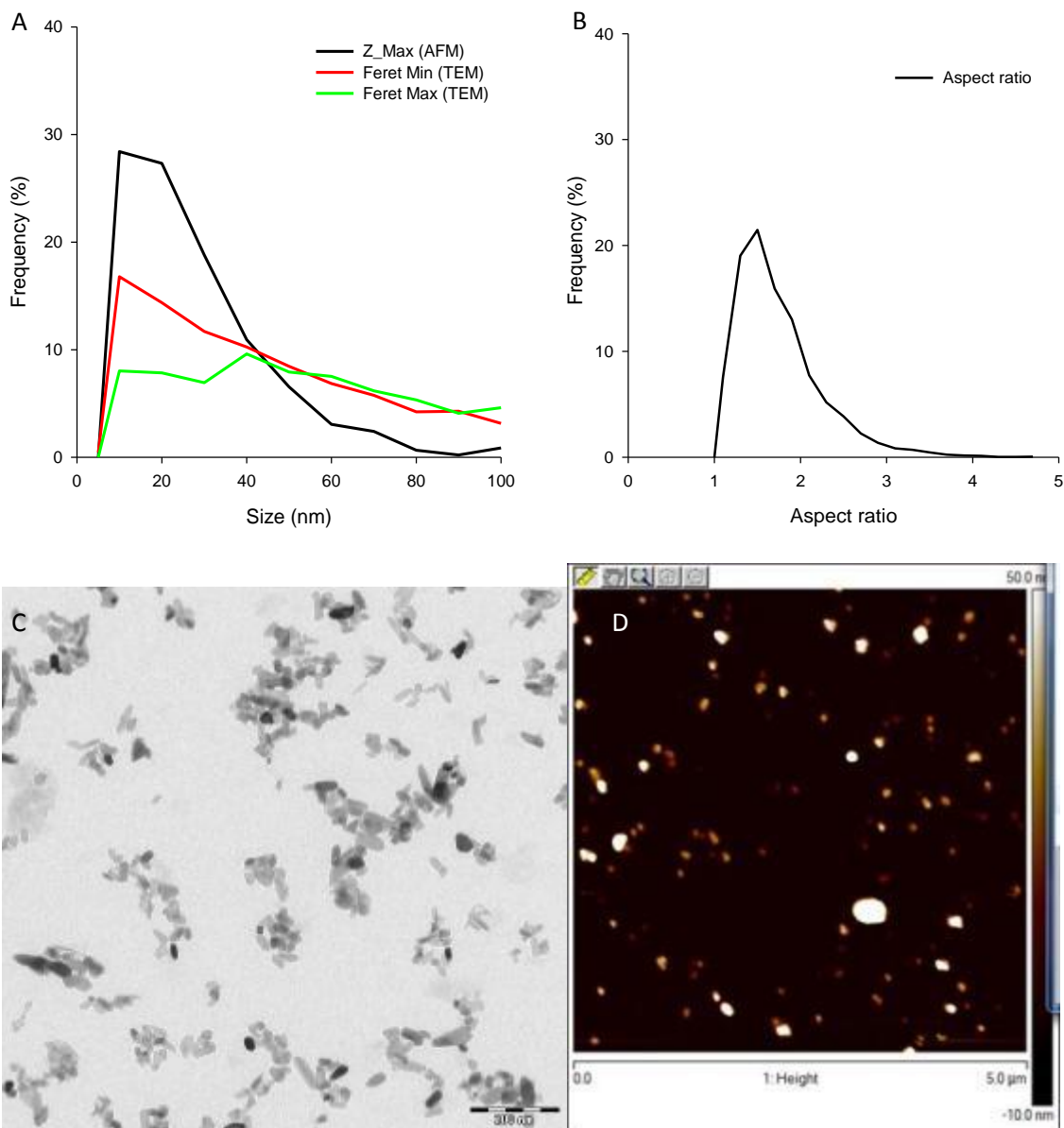


**Figure 70.** Characterization of the aggregates of TiO<sub>2</sub> NM-104 in three-dimensions by combination of TEM and AFM. A) Number based size distributions of Feret Min, Feret max and Z\_max. B) Number based distribution of the aspect ratio. Representative TEM (C) and AFM (D) micrographs visualizing the morphology of the aggregates.

## 12.4. Discussion of TEM results

### Sample preparation

To characterize a NM, sonication is applied as a standard preparatory step to disperse large aggregates and agglomerates as recommended in OECD guidelines (2012). The sonication energy required to prepare a TiO<sub>2</sub> NM sample in its most disperse state was determined as suggested by Powers et al. (2006).

## Qualitative and quantitative analyses based on TEM micrographs

The general guidelines for image acquisition and analysis proposed by Pyrz and Buttrey (2008) were adapted to the analysis of NMs. TEM imaging conditions were chosen such that a compromise is reached that combines a sufficient number of particles per image with a resolution providing an acceptable number of pixels per image, while the useful range contained the large majority of the particles.

Since this method contains no material specific steps, it can readily be adapted to characterize aggregates and agglomerates of a variety of NMs, provided that they can be coated quantitatively to the EM-grid and distinguished from the background. For most metal oxides and for metallic NMs, the latter poses no problem.

The pre-processing of images remains limited, only  $N \times N$  averaging was essential, and is appropriate for the examined  $\text{TiO}_2$  NMs. This avoids loss of information and addition of artefacts associated with significant processing reducing errors into the analysis. Automation allows measuring multiple and arithmetically complex parameters, described in Table 36, on a high number of detected particles. It reduces operator-induced bias and assures a statistically relevant number of measurements avoiding the tedious repetitive task of manual measurement. Manual primary particle measurements remained labour intensive and only 3 parameters were measured.

Access to multiple parameters allows selecting the optimal parameter in function of a specific material or purpose as exemplified hereafter. The mean diameter, and Feret mean (Riley et al., 2003, Podczeczek and Mia, 1996) are the result of multiple diameters measured under different angles. Therefore, they can be used to estimate the size of particles with complex surface topology more precisely than simple parameters, such as Feret min, Feret max, diameter min and diameter max. The measurement of the equivalent circle diameter (ECD), calculated from the projected surface area, assumes a spheroidal particle morphology like most separation and light scattering based techniques. Hence, ECD suits comparison of results obtained by techniques such as disc centrifugation and dynamic light scattering. To define a material as a NM, the percentage of aggregates smaller than 100 nm can be calculated from the number-based distribution of Feret min, an estimate for minimal size in one dimension. In the examined sonicated  $\text{TiO}_2$ , these percentages were much higher than 50 %, defining them as NM according to (EC, 2011). Since *stricto sensu*, not the aggregate size, but the size of the primary particles complies with this condition, the actual percentage can be assumed much higher. The standard deviation of this measure ranging from 0.4 to 2 % for  $\text{TiO}_2$  NMs suggests that this method can also be useful in specific cases where, warranted by concerns for environment, health, safety or competitiveness, the number size

distribution of 50 % may be replaced by a threshold between 1 and 50 % (EC, 2011). Size measurements like the aggregate projected area (Area) and the aggregated maximum projected length (Feret Max) are suitable to assess fractal like NM (Boldridge, 2009; Bau et al. 2010). Combined with the size and overlap coefficient of primary particles, the fractal dimensions can be inferred from these specific aggregate size measures according to Brasil et al., 1999. These fractal dimensions are used to explain different phenomena in physics, chemistry, biology and medicine (Nel et al., 2009).

Principle component analysis demonstrated that the measured twenty-three parameters measured by quantitative TEM analysis could be subdivided objectively for both TiO<sub>2</sub> NMs (NM-103 and NM-104) into three orthogonal classes representing size, shape and surface topology, as reported earlier for synthetic amorphous silica NM (De Temmerman, 2011). Barrett (1980) proposed a fourth parameter for NM characterization, namely the surface texture. According to ISO (2008), this parameter could be estimated from fractal dimension of the particles.

The characterization of a NM by at least one parameter of each of the three classes based on PCA is in line with the guidelines in (SCENIHR, 2010; EFSA 2011; OECD, 2010) that parameters of these classes are essential for the characterization and identification of a NM, e.g. in the context of the risk assessment of the application of NMs in the food and feed chain. The findings of Chu et al. (2011) corroborate this, showing that the size, physical form and morphology parameters determine the access of NM to human cells and cell organelles. In this context, the properties of individual particles measured in two dimensions can be more meaningful than one-dimensional parameters. Certain subpopulations cannot be distinguished based on one parameter but can be distinguished based on combinations of parameters for size, shape and surface topology, as described earlier by Barrett (1980).

## 13. Dustiness

### 13.1. Description and measurement

Dustiness is defined as the propensity of a material to emit dust during agitation. A European standard (EN15051) has been established containing two methods (the rotating drum and continuous drop methods). However, EN15051 is not fully suitable for nanomaterials, as also stated in EN 15051. Other procedures are therefore currently under investigation. In this study dustiness was tested using two different agitation methods: a downscaled EN15051 rotating drum (the small rotating drum (SD)) method and the Vortex shaker (VS) method.

It is important to note that dustiness is not an intrinsic physical or chemical defined property of a powder. Its level depends on e.g. characteristic properties of the powders and the activation energy in the simulated handling, and thus different values may be obtained by different test methods.

Among others, the reasons for EN 15051 not applying to nanomaterials are the following:

- it uses relatively bulky experimental setups, which limit their use in collective protection equipment such as fume cupboards.
- it requires a large amount of material, typically above 500 g.
- it is associated with mass-based protocols that give no indication of:
  - \* the determinants of expected potential toxicity such as the number of particles, their size distribution, their shape.
  - \* the presence or absence of particles smaller than 100 nm, or submicron particles.

The SD method is a miniaturised version of the EN15051 drum developed by NRCWE (Schneider and Jensen. 2008). Test comparisons of respirable dustiness have shown strong agreement between the SD and the EN15051 standard drum (Jensen et al., 2012).

The Vortex shaker method, or VS method, consists of a centrifuge tube continuously agitated by vibration in which the test material is placed. Originally proposed by Baron et al. (2002), this method was also used later by Isamu et al. (2009). More recently, INRS has developed this approach, particularly in the context of a collaborative project within the network PEROSH (Witschger et al. 2011).

Among the useful features of the SD and the VS methods are that only little material (between less than 0.1 and 6 grams) is needed for a test, as compared to the traditional methods described in the EN15051 standard (several hundred grams). In addition, the smaller size equipment is easier to place in an approved fume cupboard or safety cabinet, greatly improving the safety of the experimenters.



The SD and VS methods determination of dustiness in respirable size-fractions were combined with number concentration and size-distribution analysis of the dust particles for both SD and VS methods. In addition, as possible in the existing SD method protocol, the inhalable fraction was systematically measured. For few of the tests conducted with the VS method, electron microscopy (EM) observations were performed.

Finally, particle-size distributions data are reported from measurements using Electrical Low-Pressure Impactor (ELPI™ Classic) for the VS method, and Fast Mobility Particle Sizer (FMPS) and Aerodynamic Particle Sizer (APS) for the SD method. This difference arose, as the two institutions did not have the same equipment for testing the NMs.

The objective of this study is to analyse the propensity of the TiO<sub>2</sub> NMs to generate fine dust during simulated agitation of raw powder. The nanomaterial powders were compared with each other according to their index of dustiness. Two indexes have been defined, one based on the number of particles emitted, and the other according to the mass of particles emitted. In addition, we were able to compare the results between the two fundamentally different methods. SD and VS, since TiO<sub>2</sub> NM powders were tested with both methods.

## **13.2. Experimental Setup and Results**

### **13.2.1. Small rotating drum method**

The small rotating drum, Figure 71 was designed by NRCWE as a downscaled version of the EN 15051 rotating drum while maintaining important test parameters. Reduction in size was made to reduce sample size ( $\leq 6$  g per run) and to improve safety in handling by enabling placement in a regular-size fume hood. The drum consists of a cylindrical part [internal diameter 16.3 cm. length 23.0 cm. volume 4.80 l] with a truncated cone at each end (half angle 45°. length 6.3 cm. volume of two cones 1.13 l). The total volume of the drum is 5.93 l. The drum was made of stainless steel and all inside surfaces were polished to  $450 \pm 50$  gloss units to minimise surface adhesion and to facilitate cleaning. The drum was electrically grounded as prescribed by EN 15051. The drum contains three lifter vanes (2 x 22.5 cm). Experiments were conducted at 11 rpm to obtain the same number of powder parcels falling per minute as in the EN 15051 test (Schneider and Jensen. 2008). The 11 lpm inlet air to the drum was controlled at 50 % relative humidity (RH) and HEPA-filtered to ensure no particle background.



**Figure 71. Photograph showing the high-gloss polished inside of the dustiness drum. Also note the three lifter vanes marked a. b. and c at each 120° in the drum.**

In the applied set-up, respirable dust is collected by a GK2.69 respirable dust sampler at 4.2 lpm (BGI. UK) and dust particle size-distributions are measured using the Fast Mobility Particle Sizer (FMPS 3091. TSI), with a range of 5.6 to 560 nm and providing a size distribution expressed in electric mobility equivalent diameter, and the Aerodynamic Particle Sizer (APS 3321. TSI) with a range of 0.5 to 20  $\mu\text{m}$  and providing a size distribution expressed as the equivalent aerodynamic diameter, see Figure 72. A GRIMM CPC may be connected for simultaneous number-concentration measurements, but not used in this study.

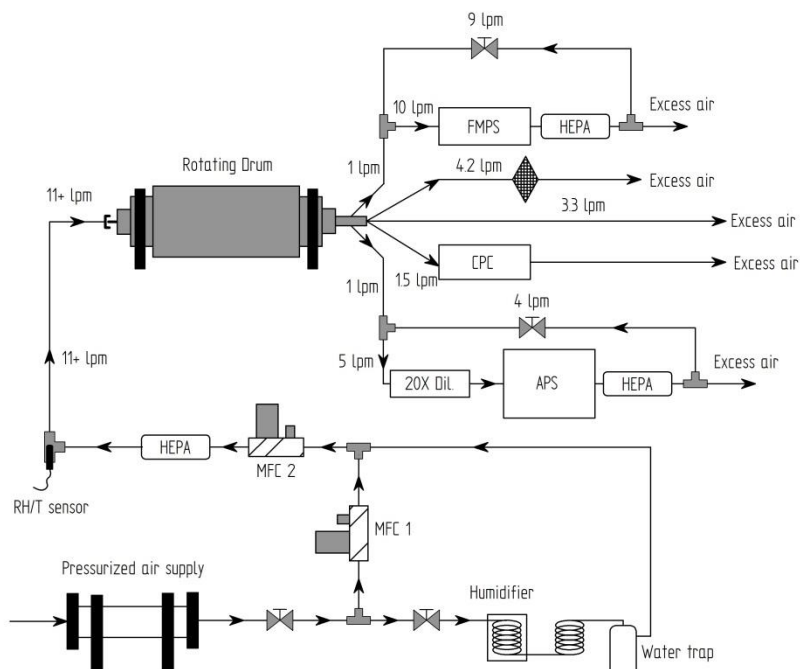


**Figure 72. Small rotating drum setup at NRCWE in the standard set-up for sampling respirable dust simultaneously with online size distribution analyses by FMPS. APS and number concentration by CPC.**

The dustiness test was conducted in triplicates for each NM after a so-called saturation run completed to coat all inner surfaces of the system with dust. The saturation test was performed using 2 grams of powder and rotation for 60 s. Then the actual triplicate tests were completed using 6 grams of test material per run. After each run, the drum was emptied by pouring out the residual powder and gently tapping the drum three times with a rubber hammer. When loading the powder was carefully placed centrally in the drum on the upwards moving side of a lifter vane placed vertical at bottom position. Then the drum was sealed, followed by 60 s of background measurements to ensure a particle free test atmosphere and perform zero-measurements for the online instruments. The experiment was then initiated by rotating the drum for 60 s during which particles were emitted and led through the airflow to the sampling train. After the drum was stopped, measurements and sampling was continued for additional 120 s to catch the remaining airborne particles in the dust cloud. Thus, the total time during for measurement is 180 s. The drum and sampling lines were thoroughly cleaned between each powder type using a HEPA-filter vacuum cleaner designed for asbestos cleaning and wet wiping. Then the drum was left to dry in air before testing the next powder.

The mass of collected respirable dust was determined after conditioning the filters and controls in a weighing room (22°C; 50 %RH) using a Sartorius microbalance (Type R162 P; Sartorius GmbH. Göttingen. Germany). The mass is used to categorise the dustiness levels of the powders according to EN15051. Calculations of Dustiness Indexes,  $DI_{mass}$ , were done according to:

$$DI_{mass} = \frac{Q_{drum} \cdot m_{filter}}{Q_{cyclone} \cdot m_{drum}}$$

$Q_{drum}$  and  $Q_{cyclone}$  are the flows through the drum and cyclone respectively.  $m_{filter}$  is the blind-filter corrected filter mass in mg and  $m_{drum}$  is the powder mass loaded into the drum in kg.

In addition to the mass-based dustiness index,  $DI_{number}$ , an index for the total number of particles generated per mg of material during the 60 s of rotation and the following 120 s were calculated as:

$$DI_{Number} = \frac{Q_{drum}}{m_{drum}} \cdot \sum_{t=0}^{180s} N_t^{cpc}$$

where  $m_{drum}$  is the used mass of powder in mg and  $N_{cpc}$  is the CPC count in particles/cm<sup>3</sup>.

Number size distributions were calculated as the summed up numbers over the 180 s as measured by FMPS and APS.

**Table 56. Number of dust particles and mass-based dustiness indexes of TiO<sub>2</sub> NMs. As explained in the text experimental data with the SD method are obtained over a test time of 180 s.**

NM	Test mass (g)	Dustiness index		
		Number (1/mg) CPC	Inhalable	Mass (mg/kg) Respirable
NM-101	6	1.10E+06	728 (±10)	24 (±9)
NM-102	2	2.96 E+05	268 (±39)	15 (±2)
NM-103	6	1.80E+07	9185 (±234)	323 (±166)
NM-104	6	4.13E+05	3911 (±235)	38 (±166)
NM-105	6	3.16E+05	1020 (±20)	28 (±10)

Figure 73 shows the particle number size distributions of aerosols generated during rotating drum dustiness testing of the TiO<sub>2</sub> NMs. The TiO<sub>2</sub> powders generate fine aerosol with an electrical mobility equivalent peak diameter typically between 200 and 250 nm. Larger μm-size-modes are present in all samples. One material, NM-103, was very dusty and generated slightly higher concentration of μm-size dust particles than sub-μm-size particles. This is an unusual particle size-distribution profile.

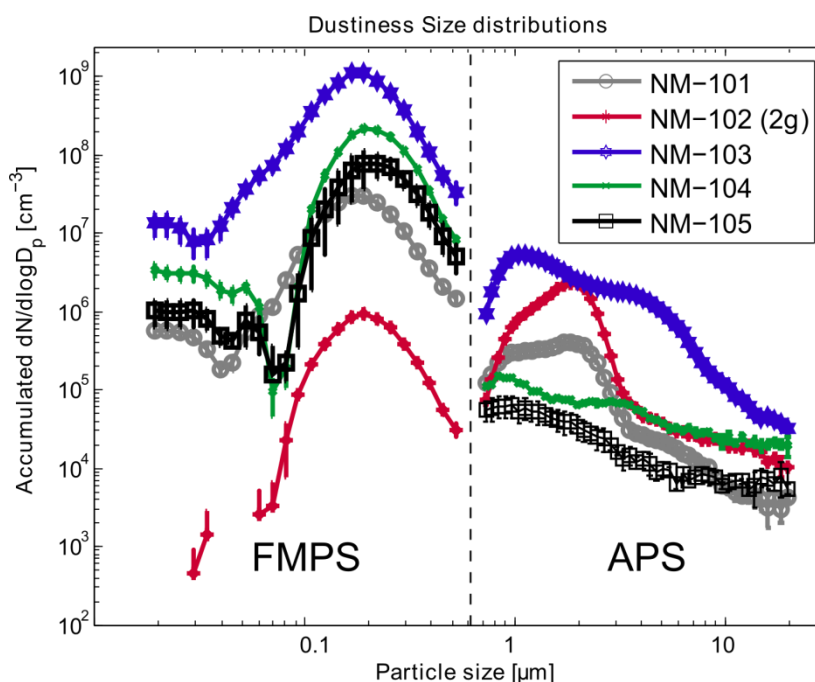


**Figure 73. Particle number size distributions for TiO<sub>2</sub> NMs. All distributions are presented as given by the FMPS (electrical mobility equivalent diameter) and APS (aerodynamic equivalent diameter).**

Figure 74 and Figure 75 show respectively the dustiness ranking of inhalable and respirable dust for TiO<sub>2</sub> NMs. Compared to conventional mass-based dustiness indexing of the EN

15051 standard, the TiO<sub>2</sub> NMs vary from low to high dustiness in both size fractions. There also seems to be good agreement between inhalable and respirable indexing.

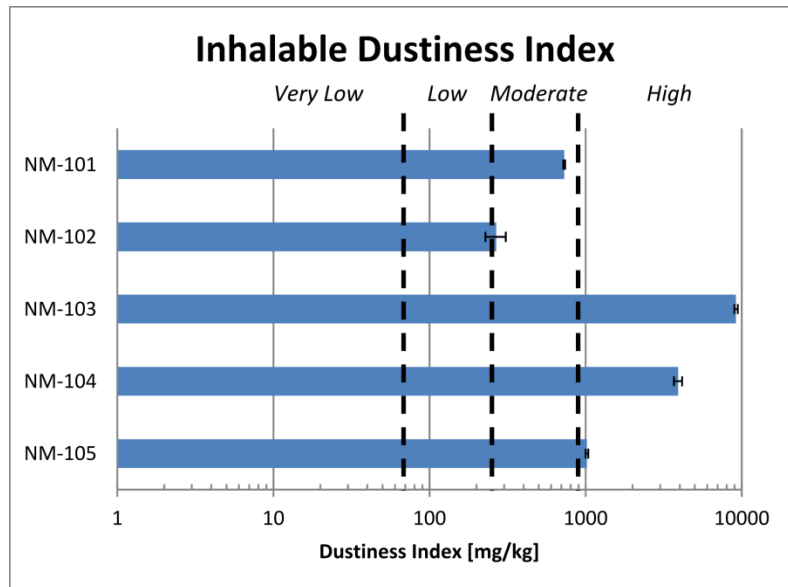


Figure 74. Dustiness ranking of inhalable dust for and TiO<sub>2</sub> NMs as obtained with the small rotating drum method at NRCWE.

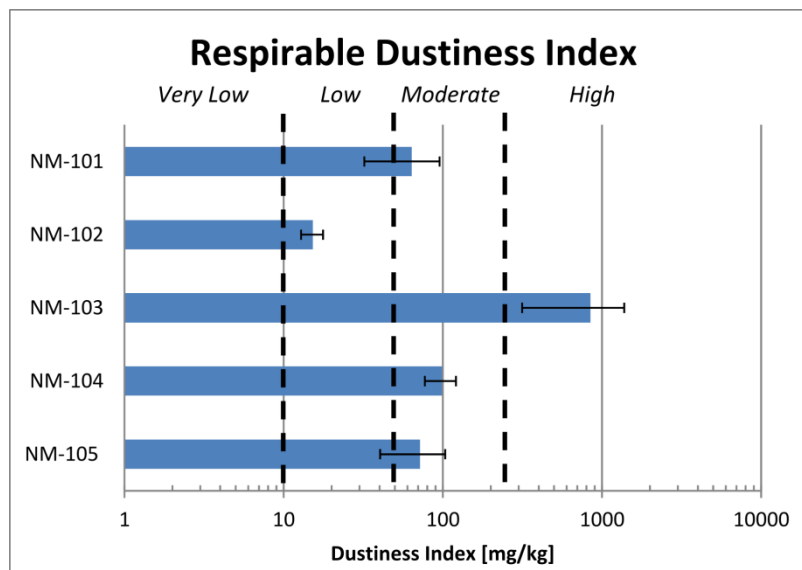


Figure 75. Dustiness ranking of respirable dust for TiO<sub>2</sub> NMs as obtained with the small rotating drum method at NRCWE.

### 13.2.2. Vortex shaker method

The vortex shaker method consists of a centrifuge stainless tube agitated by a vortex in which the test powdered material is placed together with 100 µm diameter bronze beads. These are used to help the de-agglomeration of powders. HEPA filtered air, controlled at 50

% RH, pass through the tube in order to transfer the released aerosol to the sampling and measurement section. The protocol developed for the experiments performed at INRS used two different versions of the sampling and measurement section.

All tests conducted with VS method used approximately 0.5 mL powder, which was placed in the sample vial together with 5 g bronze beads (100  $\mu\text{m}$ ), used to agitate and de-agglomerate the powder. The sample is allowed conditioning in the 50 % RH before the shaker for a powder agitation period of 3600 s (60 min).

The first version of the sampling and measurement was devoted for real-time measurement using ELPI™ Classic (Electrical Low Pressure Impactor) (10 lpm, Dekati) for size distributions according to the equivalent aerodynamic diameter and Condensation Particle Counter (CPC, Model 3786 UWCPC, TSI) for number concentrations. This version was also devoted for collecting airborne particles for subsequent electron microscopy observations. Tests were completed in triplicates for each NM.

The CPC used was the Model 3785 Water-based CPC (TSI, USA). This CPC detects particles from 5 to >3000 nm. It provides a wide, dynamic, particle-concentration range, an essential characteristic for the tests considered. Featuring a single-particle-counting mode with continuous, live-time coincidence correction and a photometric mode, the CPC measures particle number concentrations at  $<10^7$  particles/cm<sup>3</sup>.

ELPI™ is an instrument to measure airborne particle size distribution and concentration in real-time. It operates in the size range of 7 nm – 10  $\mu\text{m}$  in its standard configuration. Because of its wide particle size range and rapid response (< 5 s), the ELPI™ has been considered an ideal measurement instrument for the analysis of the unstable concentrations and size distributions, or the evolution of size distributions that could be observed in these tests. To prevent particle bounce and charge transfer during the tests, all collection substrates (PVC GELMAN GLA-5000 5  $\mu\text{m}$  / 25 mm) were greased.

The results of the tests performed with this first version of the VS method leads to the determination of:

- Dustiness indices expressed as the total number of particles emitted (based on data from CPC).
- Particle size-distribution of the aerosol (based on data from ELPI™ Classic in its standard configuration).

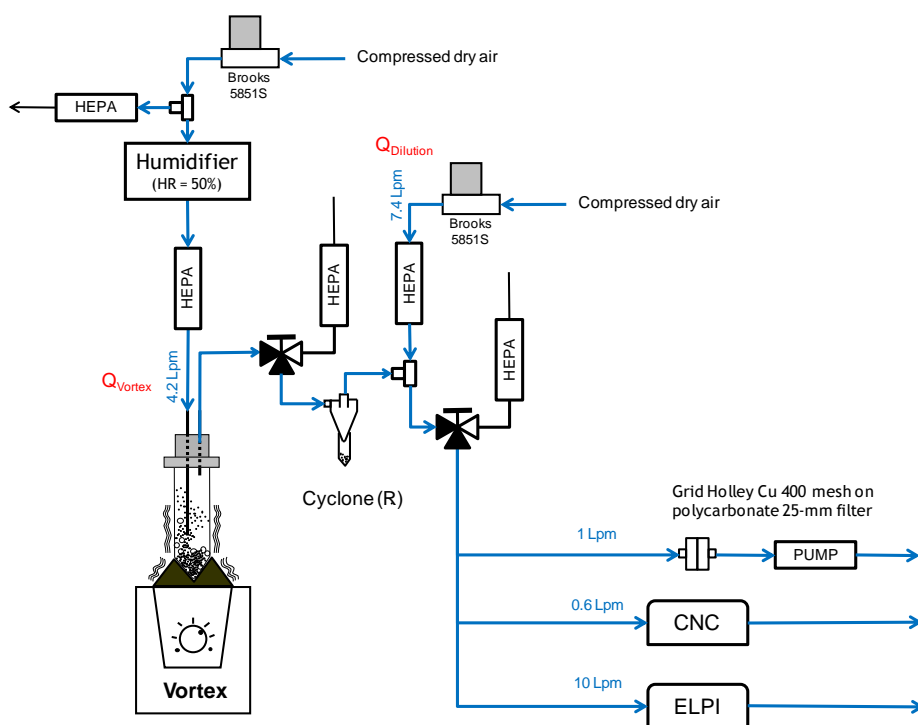


**Figure 76. Experimental set-up of the vortex shaker method for measuring number concentrations and particle-size distributions and for collecting airborne particles for subsequent EM observations.**

In the ELPI, the measured current signals are converted to (aerodynamic) size distribution using particle size dependent relations describing the properties of the charger, the impactor stages, and the effective density of the particles. The particle effective density provides a relationship between mobility and aerodynamics sizes. Effective density is a parameter that is complex to measure (Olferta et al., 2007), and values for samples used in the project are not available in the literature. Therefore, the following assumption has been made for the data from the ELPI: spherical particle with a density equal to the density of the condensed phase of the material constituting the NM. Densities used were  $3.84 \text{ g/cm}^3$  for NM-100, NM-101, NM-102 and  $4.26 \text{ g/cm}^3$  for NM-103, NM-104, NM-105 based on Teleki et al. (2008). If this assumption is questionable, there is no robust method that can be applied to polydispersed aerosols over a wide size range, such as those used here. However, to assess the effect of this parameter on the results, the number size distributions were also calculated for a density of  $1 \text{ g/cm}^3$ .

$S_{Vortex}^{Number(CNC)}$  is the total number of generated particles from the Vortex tube and it was calculated as:

$$S_{Vortex}^{Number(CNC)} = [Q_{Vortex} + Q_{Dilution}] \cdot \Delta t \cdot \sum_{i=0}^T C_{CNC}(t_0 + i \cdot \Delta t)$$

Where:

- $T$  is the time over which the total number of particles is calculated. This time is between 5 and 3600s, the latter being the test duration in the original protocol of the VS method.
- $\Delta t$  is the step time of the CNC (for all tests it was set as 5 s)
- $C_{CNC}(t_0+i\cdot\Delta t)$  is the number concentration measured during the time interval
- $Q_{Vortex}$  is the total airflow rate passing through the vortex tube (4.2 lpm)
- $Q_{Dilution}$  is the flow rate of dilution air (7.4 lpm).

$DI_{Number(CNC)}$  is the dustiness index in number of particles per gram, and it was calculated as the total number of generated particles divided by the total mass of the test NM sample in milligrams (unit 1/mg):

$$DI_{Number(CNC)} = \frac{S_{Vortex}^{Number(CNC)}}{m_{NM}}$$

To get information on particle morphology of the emitted aerosol, a simple but specific sampling set-up has been designed (not shown here). Transmission electron microscope (TEM) copper grids were taped onto 25 mm diameter polycarbonate membrane filters (0.4 or 0.8 $\mu$ m). Fibre backing filters were used to support the polycarbonate filters. Airflow was driven by a pump at a flow rate of 1 L/min. The duration of the sampling was set to 1 hour. The sampling period was set equal to the duration of a test (1 hour). For some tests, the sample was accumulated over two trials in order to have enough particles to observe. Different TEM copper grids having different carbon films have been used (Carbon film, Quantifoil Holey Carbon Films or Holey Carbon Support Film).

It is important to note that the duration of the test is a relevant test parameter as the process is dynamic. In the original INRS protocol developed, the duration of a test was set equal to 3600 s. But in the first version of the set-up (Figure 76), as the instruments measure in real time, it is possible to perform the calculation for different durations between 0 and 3600 s. In this report, the calculations based on the condensation nuclei counter CNC data were performed for two durations: 180 s and 3600 s. The first duration (180 s) was chosen to be consistent with the SD method. For the second version of the setup, the duration of the test was set to 3600 s, which corresponds to the original protocol of the VS method.

The second version of the setup (Figure 77) is used for collecting respirable mass fraction of the emitted aerosol. The respirable mass fraction is obtained by sampling with a GK2.69 cyclone (BGI. UK). The filters have been pre-weighed and post-weighed following the recommendations of the ISO 15767:2009 on the same analytical balance. Only one test was performed with this setup due to time constraints. Therefore the results are not presented



with a confidence interval based on reproducibility. However, measurement uncertainty has been calculated for each measurement performed.

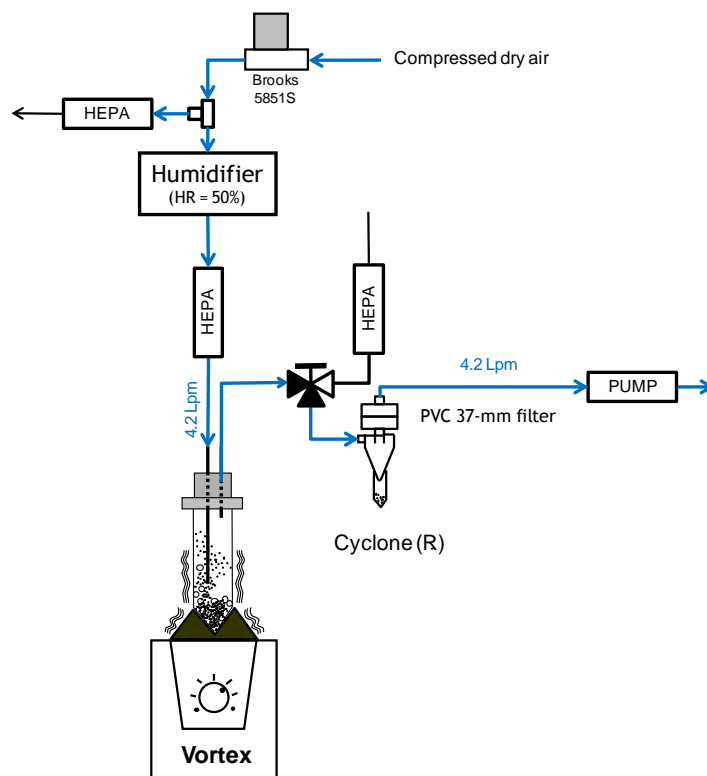


**Figure 77. Experimental set-up of the vortex shaker method for collecting respirable mass fraction of the emitted aerosol.**

$DI_{Mass(GK2.69)}$  is the dustiness index in respirable mass (mg) of particles per kilogram and it was calculated as the respirable mass of generated particles in milligrams divided by the total mass of the test NM sample in kilograms:

$$DI_{Mass(GK2.69)} = \frac{S_{Vortex}^{NumMass(GK2.69)ber(CNC)}}{m_{NM}}$$

The recommendations of the standard ISO 15767:2009 were followed to determine the LOD of the weighing procedure for the filters used for sampling respirable mass of particles during this project. The LOD for the PVC GELMAN GLA-5000 (5  $\mu\text{m}/37\text{ mm}$ ) filters was equal to 20ng. This value is used to determine the LOD expressed in dustiness index.

The preparation of NM samples for VS testing included: 1) taking a series of 7 samples of 0.5  $\text{cm}^3$  from the vial containing the nanomaterial, 2) accurately weighing the samples. Three samples are devoted for testing with the first version of the set-up, one for the second version (respirable mass fraction measurement) and three for the gravimetric water content measurement. The gravimetric water content was performed using a HR83 Halogen Moisture

Analyzer (Mettler Toledo) and following a drying program defined specifically for small quantities of used NM (Temperature = 160°C; duration = 170 s).

The weighing of the NM samples was performed with a XP205 analytical balance (10 µg readability, Mettler Toledo) while the weighing of the 37-mm filters from the respirable sampler was performed with a MX5 microbalance (1 µg readability, Mettler Toledo).

Particular attention was given to cleaning the experimental device between successive tests. All pipes and other connections were systematically cleaned with water and/or ethanol and dried in an oven, or eventually changed. The checking of the airflows was performed using a primary flow bubble calibrator (Gillian® Gillibrator 2). Prior to each test, the cleanliness of the air was assessed on the basis of measurements made using the condensation nuclei counter. In the case of a non-compliant result, the cleaning was performed again or pipes and other connections changed. The validation of a test depends on several factors such as: 1) the stability of the parameters during the test, 2) a good reproducibility of measured number concentrations, 3) the sequence of steps for the respirable aerosol sampling, among others.

The entire set-up was located inside a variable volume fume hood to prevent exposure of the operator. Similarly, all operations like weighing, water content measurement and sample preparation were carried out in a specific containment system that has a unique turbulent-free, low flow design which allows our sensitive balance to operate without fluctuation and protects the operator from exposure to airborne particles that could be released when handling and weighing NM samples.

### 13.2.3. Results for the Vortex Shaker Method

Table 57 lists the gravimetric water content (expressed in weight percent) and bulk density of the nanomaterials in powders. The results were obtained in tests conducted by INRS.

**Table 57. Gravimetric water content and bulk density of the TiO<sub>2</sub> NMs.**

<b>Material</b>	<b>Sample mass (mg)</b>	<b>Water content (wt % dry)</b>	<b>Bulk density (g/cm<sup>3</sup>)</b>
<b>NM-100</b>	135	1 %	0.69
<b>NM-101</b>	110	10 %	0.41
<b>NM-102</b>	120	3 %	0.31
<b>NM-103</b>	126	2 %	0.44
<b>NM-104</b>	108	3 %	0.33
<b>NM-105</b>	112	1 %	0.10

Experimental data obtained with the VS method are summarised in Table 58. Number-based data with the VS method are calculated from the time profiles with two test durations of 180 s

and 3600 s. The first duration (180 s) was chosen to correspond to the test duration of the SD method. The mass-based data, obtained with test duration of 3600 s. correspond to the respirable fraction only as the inhalable fraction was not part of the VS original protocol.

**Table 58. Number-based and mass-based dustiness indexes of TiO<sub>2</sub> NMs.**

NM-10X	Test mass (mg)	Dustiness Index			
		Number (1/g)			Mass (mg/kg)
		T = 180 s		T = 3600 s	
		CPC (s.D) <sup>b</sup>	ELPI <sup>a</sup> (s.D) <sup>b</sup>	CPC (s.D) <sup>b</sup>	Respirable (s.D) <sup>c</sup>
NM-100	341.7	1.2.10 <sup>5</sup> (± 2.7.10 <sup>4</sup> )	1.0.10 <sup>5</sup> (± 2.2.10 <sup>4</sup> )	8.3.10 <sup>5</sup> (± 3.4.10 <sup>5</sup> )	1.5.10 <sup>3</sup> (± 1.33.10 <sup>-3</sup> )
NM-101	206.6	1.6.10 <sup>5</sup> (± 7.04.10 <sup>4</sup> )	3.2.10 <sup>5</sup> (± 7.0.10 <sup>4</sup> )	3.1.10 <sup>6</sup> (± 3.5.10 <sup>5</sup> )	5.6.10 <sup>3</sup> (± 5.00.10 <sup>-3</sup> )
NM-102	153.7	9.6.10 <sup>4</sup> (± 9.3.10 <sup>3</sup> )	9.6.10 <sup>4</sup> (± 8.5.10 <sup>4</sup> )	7.0.10 <sup>5</sup> (± 2.8.10 <sup>4</sup> )	9.2.10 <sup>3</sup> (± 8.25.10 <sup>-3</sup> )
NM-103	216.8	5.4.10 <sup>4</sup> (± 8.0.10 <sup>4</sup> )	2.0.10 <sup>6</sup> (± 2.7.10 <sup>5</sup> )	1.9.10 <sup>6</sup> (± 1.7.10 <sup>5</sup> )	1.9.10 <sup>4</sup> (± 1.70E-02)
NM-104	165.6	4.3.10 <sup>4</sup> (± 3.6.10 <sup>3</sup> )	2.5.10 <sup>5</sup> (± 2.8.10 <sup>5</sup> )	2.1.10 <sup>5</sup> (± 2.8.10 <sup>4</sup> )	6.4.10 <sup>3</sup> (± 5.67.10 <sup>-3</sup> )
NM-105	50.3	3.5.10 <sup>4</sup> (± 1.3.10 <sup>4</sup> )	9.9.10 <sup>5</sup> (± 1.1.10 <sup>6</sup> )	2.3.10 <sup>5</sup> (± 2.7.10 <sup>5</sup> )	1.1.10 <sup>4</sup> (± 9.66.10 <sup>-3</sup> )

<sup>a</sup> The assumption for calculating the number of particles emitted from the data from the ELPI is: spherical particle with a density equal to the density of the condensed phase of the material constituting the NM. Densities used were 3.84 g/cm<sup>3</sup> for NM-100, NM-101, NM-102 and 4.26 g/cm<sup>3</sup> for NM-103, NM-104, NM-105 based on Teleki et al. (2008).

<sup>b</sup> standard deviation calculated over 3 repeats

<sup>c</sup> measurement uncertainty as there was no repeat for this tests

### 13.2.4. Comparison of the SD and VS methods

Figure 78 shows the respirable mass dustiness indices obtained by the SD and VS methods.

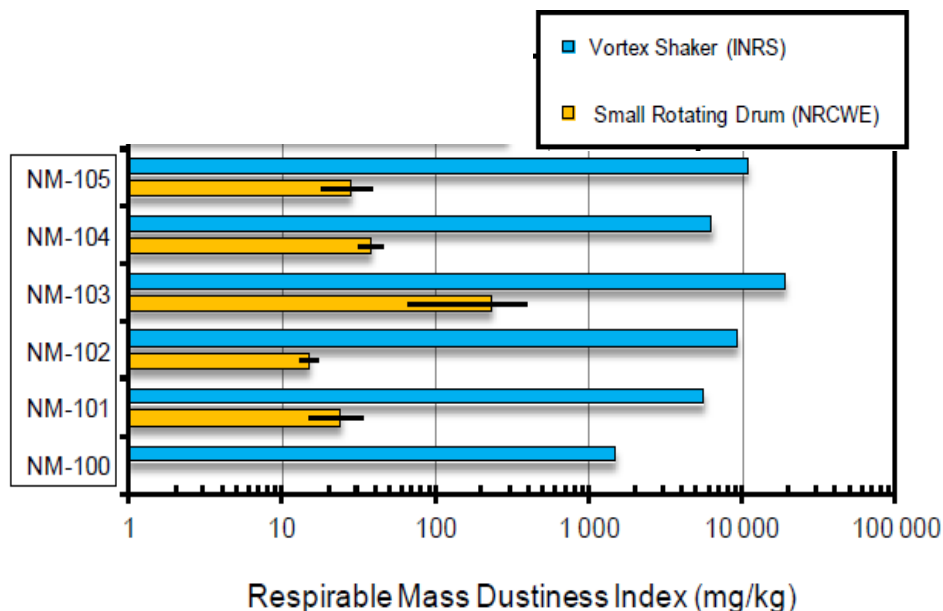


**Figure 78. Comparison between respirable mass dustiness indices obtained with the small rotating drum and vortex shaker method. Errors bars on the SD values correspond to the reproducibility over 3 repeats.**

The comparison between the small drum and Vortex shaker results shows that no significant correlation between these two methods can be found. Further evaluation of the VS method is needed in order to link it to the standardised Rotating Drum method. As already stated, dustiness is not an intrinsic physical or chemical defined property of a powder, but its level depends on both characteristic properties of the powders and the activation energy in the simulated handling. Therefore different values may be obtained by different test methods (test apparatus, operation procedure, sampling and measurement strategy, etc.). Hence, direct comparability is not expected between the SD and the VS. Moreover, the absence of a harmonised approach for the measurement strategies and techniques, metrics and size ranges and the procedures for data analysis and reporting may additionally limits the comparison of the results obtained by the two dustiness methods.

## 14. Discussion and Conclusions

### 14.1. Materials and Dispersion

The JRC launched the repository for representative nanomaterials in February 2011 with the preparatory work starting in 2008, and it hosts more than 20 different types of nanomaterials at the JRC Ispra (Italy) site. The nanomaterials in the repository had the following code: NM-XXX, where XXX is a material unique digital identifier. In 2014 the code format was changed to JRCNM<5digit number><letter><six digit number>. The <5digit number> is a digital identifier unique to one material, the <letter> refers to the batch, and the <six digit number> is the vial number for a specific material and batch.

The representative nanomaterials were introduced by the JRC to support the OECD Working Party on Manufactured Nanomaterials' programme "Safety Testing of a Set of Representative Manufactured Nanomaterials", established in November 2007, as well as national and international research projects within and outside the EU. The OECD WPMN recommended testing selected nanomaterials for a series of agreed end-points and the titanium dioxides, NM-100, NM-101, NM-102, NM-103, NM-104 and NM-105 are some of the key materials of the OECD WPMN programme.

Also outside the OECD WPMN programme, characterisation of nanomaterials and applicable methods are studied intensively to understand nanomaterials both in a regulatory and a scientific context. Recently, the JRC published a report regarding "Requirements on measurements for the implementation of the European Commission definition of the term "nanomaterial" (see Linsinger et al. 2012) that evaluates the limits and advantages of the existing methods for characterisation of nanomaterials, and the reader is referred to it for additional information on the areas of applicability of methods.

Information on physico-chemical characterisation of the TiO<sub>2</sub> NMs as well as stability and homogeneity information for NM-102, NM-103, NM-104 and NM-105 are presented in the current report with special regard to its use and appropriateness as representative nanomaterial. The physico-chemical characterisation of the TiO<sub>2</sub> NMs was performed within the NANOGENOTOX project, and by the JRC. An overview of the characterisation performed for each of the six TiO<sub>2</sub> NMs and the measurement methods applied is given in chapter 3.

In the NANOGENOTOX project a dispersion protocol was developed which was used for the in vitro and in vivo experiments with the 3 types of materials investigated, TiO<sub>2</sub>, SiO<sub>2</sub> and MWCNT and such a protocol is obviously not optimised for the single material type, let alone the individual experiments. The NANOGENOTOX batch dispersion medium is sterile filtered

0.05 % w/v BSA water with 0.5% v/v ethanol prewetting. According to the dispersion protocol the NMs are dispersed into the media using sonication and the sonicator seems to have an important influence on the degree of dispersion and final particle size distribution in the medium. A part of the physico-chemical characterisation was done using the NANOGENOTOX protocol, but for investigating the inherent properties also other dispersion protocols were tested.

After preparation of the dispersion of the test item, analysis should always be performed to ensure dispersion stability, as successful (liquid) sample splitting can only be conducted if a homogeneous dispersion has been achieved, otherwise a much higher sampling error will be introduced. Dispersion can be assessed using for example light scattering techniques such as Dynamic Light Scattering (DLS) or optical microscopy. Each characterisation method has limitations, which operators must be aware of. For example, DLS is not suitable to resolve a broad particle size distribution, as potentially larger particles can mask the signal of the smaller nanoparticles. In order to resolve multi-modal particle distribution, techniques that have a separation mechanism element integrated in the analytical tool will be more suitable, such as a Field Flow Fractionation. In addition to errors incurred from sub-sampling steps, stability of the dispersion is important for nanoparticle characterisation, as only stable dispersions give reliable characterisation data.

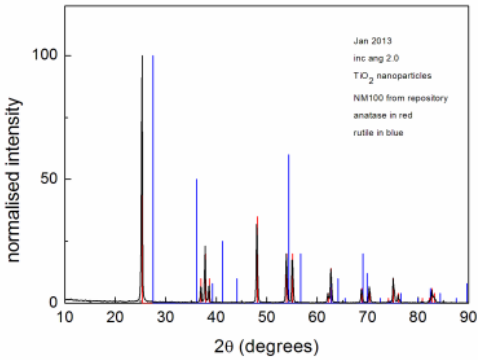
## **14.2. Characterisation**

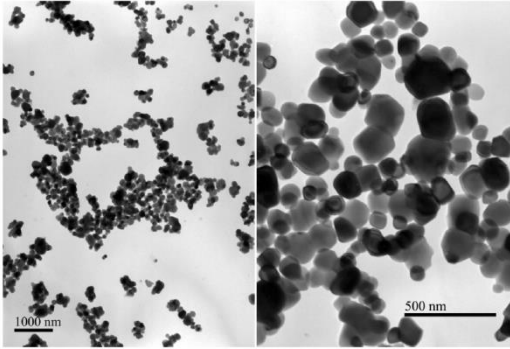
Almost all of the OECD endpoints on physico-chemical testing have been completed for the principal OECD WPMN material, NM-105. Also the alternate materials, NM-100, NM-101, NM-102, NM-103 and NM-104 have been extensively characterised. The determination of the octanol water coefficient is not feasible for nanomaterials (OECD 2013), and was considered to be irrelevant for sparingly soluble and insoluble nanomaterials (in the sense of nanomaterials that can be solubilised). Although the photocatalytic activity is considered to be very relevant for TiO<sub>2</sub> nanomaterials, this was outside the scope of the NANOGENOTOX project, and thus no data is available for this report. Analysis of intrinsic hydroxyl radical formation capacity, using the Benzoic acid probe for quantification, gave no detectable radical after 24 and 48-hour incubation (limit of detection 1.1 nmol OH/mg).

### 14.2.1. Overview tables of characterisation data

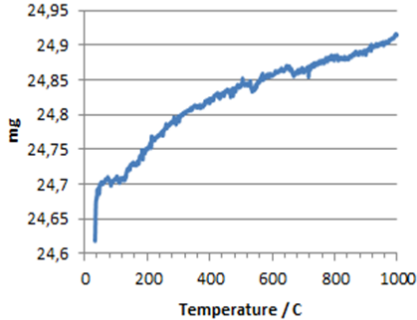
Table 4 gives an overview of the physico-chemical characterisation performed, the methods used and the institutions involved in the testing. Table 59 to Table 64 summarise the results obtained in for the 6 different titanium dioxides. Appendix E gives an overview of the overview.

**Table 59. Overview of results from the physico-chemical characterisation of NM-100.**

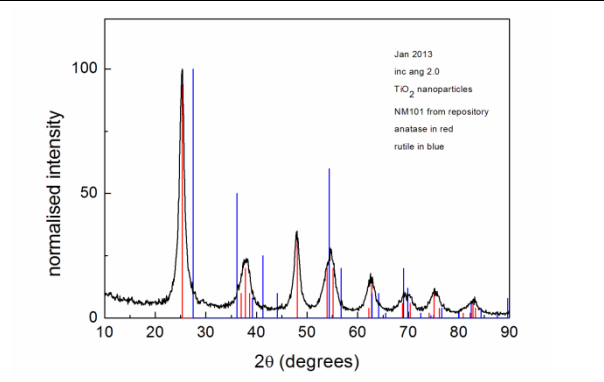
Method	Institution	Results, NM-100
<b>Homogeneity</b>		End-point not tested
<b>Agglomeration / aggregation</b>		
DLS	JRC	Ultra-pure water dispersion Z-average (nm): 228.6, Pdl: 0.145
TEM	IMC-BAS, CODA-CERVA	Aggregates : size from 30 to 700 nm
<b>Water Solubility</b>		
24-hour acellular <i>in vitro</i> incubation test	NRCWE	The 24-hour dissolution ratio of NM-100 was measured in three different media: 0.05 % BSA in water, Gambles solution and Caco2 media. NM-100 is soluble in 0.05 % BSA in water and in Caco2 medium. All impurities were detected in Caco2 media only, suggesting that the solubility behaviour of the impurities and NM-100 depends on the medium.
<b>Crystalline phase</b>		
XRD	JRC	 Anatase
	NRCWE	Anatase
	IMC-BAS	Anatase
<b>Dustiness</b>		
Vortex Shaker Method	INRS	Respirable mass (mg/kg): 1500 ± 0.00133

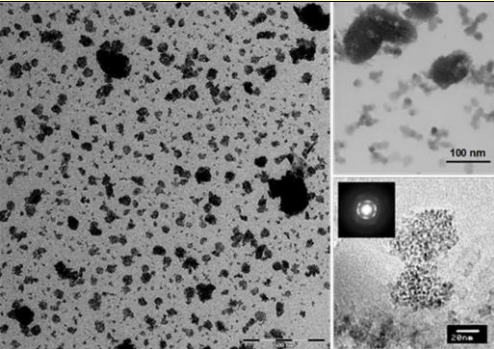
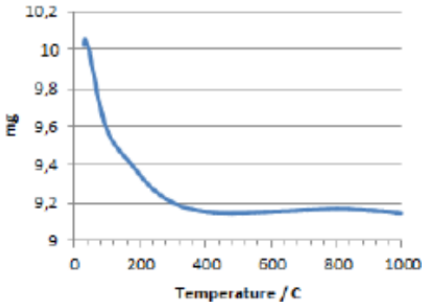
Method	Institution	Results, NM-100
<b>Crystallite size</b>		
XRD	JRC	> 80 nm (Scherrer eq.)
	NRCWE	57 nm (Scherrer eq.) 62 nm (TOPAS) 168 nm (Fullprof)
	IMC-BAS	<100 nm (Scherrer eq.) <100 nm (TOPAS, IB) <100 nm (TOPAS, FWHM)
<b>Representative TEM picture(s)</b>		
TEM	CODA-CERVA, IMC-BAS	 <p>Aggregates with dense, complex structure</p>
<b>Particle size distribution</b>		
TEM	CODA-CERVA	Primary particles: size from 50 to 90 nm
	IMC-BAS	Primary particle size: 150 nm
TEM	IMC-BAS, CODA-CERVA	Number in % of particles smaller than 100 nm, 50 nm and 10 nm <100 nm – 27.1 %, <50 nm – 12.3 % <10 nm – 1.7 %
DLS	JRC	<ul style="list-style-type: none"> <li>Ultra-pure water dispersion</li> </ul> Z-average (nm): 228.6, Pdl: 0.145
<b>Specific Surface Area</b>		
BET	IMC-BAS	9.230 (m <sup>2</sup> /g)
	JRC	Material stored at 40 °C : 10.03 m <sup>2</sup> /g Material stored at -80 °C : 10.35 m <sup>2</sup> /g
<b>Zeta Potential (surface charge)</b> End-point not tested		



Method	Institution	Results, NM-100
<b>Surface Chemistry</b>		
XPS	JRC	<ul style="list-style-type: none"> <li>Elements identified in the surface O (<math>53.8 \pm 0.7</math> at%), C (<math>27.7 \pm 0.7</math> at%), Ti (<math>17.3 \pm 0.5</math> at%), K (<math>1.2 \pm 0.3</math> at%)</li> <li>Elements identified in the surface after Ar ion etching (2 min, 3 keV) O (67.42 at%), C (4.73 at%), Ti (25.96 at%), K (1.9 at%)</li> </ul>
TGA	NRCWE	<p style="text-align: center;"><b>TGA of NM100</b></p>  <p style="text-align: right;">The change in weight is due to buoyancy.</p>
<b>Photo-catalytic activity</b>		End-point not tested
<b>Pour-density</b>		End-point not tested
<b>Porosity</b>		
BET	IMC-BAS	Micropore volume (mL/g): 0.0
<b>Octanol-water partition coefficient</b>		End-point not relevant
<b>Redox potential</b>		
OxoDish fluorescent sensor plate for O <sub>2</sub> detection	NRCWE	The evolution of O <sub>2</sub> level during 24-hour incubation was measured in three different media. Different dO <sub>2</sub> values were observed for all applied media. In the 0.05 % BSA-water NM-100 showed negligible reactivity. In Gambles solution and Caco2 medium decrease of O <sub>2</sub> level is observed. The results suggest that NM-100 is inactive or reductive in the different incubation media. Particle reactivity may easily exceed 1 μmol O <sub>2</sub> /mg.
<b>Radical formation</b>		End-point not tested
<b>Composition</b>		
ICP-OES	IMC-BAS	> 0.01 %: K(>0.1 %) : P 0.05-0.01 % : Zr 0.001-0.005 % : Ca Na
EDS	IMC-BAS	Si - 2800 ppm, P - 2100 ppm, Al - 900 ppm, K - 2500 ppm, Cr - 300 ppm, Fe - 4900 ppm, Ti - 58.57 (wt %), O (wt%) calculated - 40.08

**Table 60. Overview of results from the physico-chemical characterisation of NM-101.**

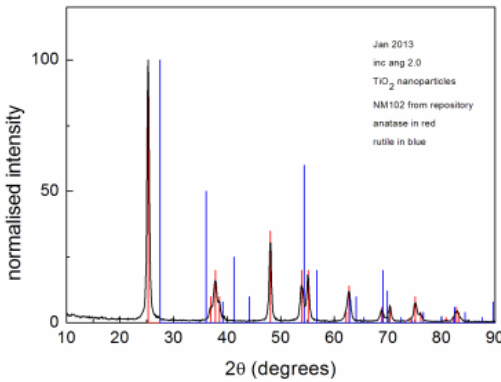
Method	Institution	Results, NM-101	
<b>Homogeneity</b> End-point not tested			
<b>Agglomeration / aggregation</b>			
SAXS	CEA	Primary particle size: Equivalent diameter for spheres: 8 nm	
TEM	IMC-BAS, CODA-CERVA	Aggregates: size from 10 to 170 nm.	
<b>Water Solubility</b>			
24-hour acellular <i>in vitro</i> incubation test	NRCWE	The 24-hour dissolution ratio was measured in three different media: 0.05 % BSA in water, Gambles solution and Caco2 media. NM-101 is slightly soluble in Caco2 media and the Al impurity is soluble in all media. The dissolved amounts vary considerably with medium, as does the relative amounts of dissolved Al impurities compared with dissolved Ti, suggesting that the solubility behaviour of the impurities and NM-101 depends on the medium.	
<b>Crystalline phase</b>			
XRD	JRC		Anatase
	NRCWE	Anatase	
	IMC-BAS	Anatase	
<b>Dustiness</b>			
Small Rotating Drum	NRCWE	Inhalable dustiness index: $728 \pm 10$ Mass respirable (mg/kg): $24 \pm 9$	
Vortex Shaker Method	INRS	Mass respirable (mg/kg): $5600 \pm 0.005$	
<b>Crystallite size</b>			
SAXS	CEA	Primary particle size: Equivalent diameter for spheres: 8 nm	
XRD	JRC	8 nm (Scherrer eq.)	
	NRCWE	7 nm (Scherrer eq.) 7 nm (TOPAS, IB) 7 nm (TOPAS, FWHM)	
	IMC-BAS	5 nm (Scherrer eq.) 5 nm (TOPAS) 5 nm (Fullprof)	

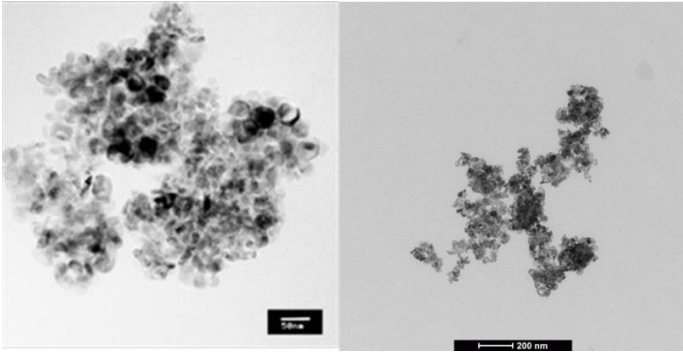
Method	Institution	Results, NM-101
<b>Representative TEM picture(s)</b>		
TEM	CODA-CERVA, IMC-BAS	Aggregates with complex, fractal-like structure 
<b>Particle size distribution</b>		
SAXS	CEA	Primary particle size: Equivalent diameter for spheres: 8 nm
TEM	CODA-CERVA	Primary particle size: 6 nm
	IMC-BAS	Primary particle size: 5 nm
TEM	IMC-BAS, CODA-CERVA	Number in % of particles smaller than 100 nm, 50 nm and 10 nm <100 nm – 95.2 %, <50 nm – 77.3 % <10 nm - 10.7 %
<b>Specific Surface Area</b>		
BET	IMC-BAS	316.07 m <sup>2</sup> /g
	JRC	Material stored at 40 °C : 234.47 m <sup>2</sup> /g Material stored at -80 °C : 229.00 m <sup>2</sup> /g
SAXS	CEA	169.5 ± 8.5 m <sup>2</sup> /g
<b>Zeta Potential (surface charge)</b> End-point not tested		
<b>Surface Chemistry</b>		
XPS	JRC	<ul style="list-style-type: none"> <li>Elements identified in the surface [results in at%]  O (55.9 ± 0.7), C (23.4 ± 0.5), Ti (20.5 ± 0.1), Fe/Ca (1.2 ± 0.3)</li> <li>Elements identified in the surface after Ar ion etching (2 min, 3 keV)  O (62 at%), C (12.69 at%), Ti (25.28 at%)</li> </ul>
GC-MS	NRCWE	GC-MS analysis results (retention time in min.): Sllane?: 31.6 and 32.9; Hexadecanoic acid methyl ester: 33.4; Hexadecanoic acid: 33.9; Octadecanoic acid: 35.8
TGA	NRCWE	<p><b>TGA of NM101</b></p>  <p>A significant mass loss is observed below and above 100°C. The first and largest, below 100 °C, is most likely water. The second is around 200 °C and is most likely a coating.</p>

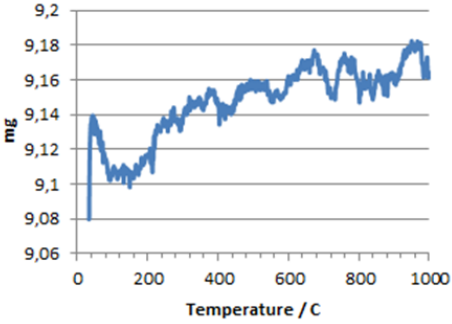
Method	Institution	Results, NM-101
<b>Photo-catalytic activity</b>		
End-point not tested		
<b>Pour-density</b>		
End-point not tested		
<b>Porosity</b>		
BET	IMC-BAS	Micropore volume (mL/g): 0.00179
<b>Octanol-water partition coefficient</b>		
End-point not relevant		
<b>Redox potential</b>		
OxoDish fluorescent sensor plate for O <sub>2</sub> detection	NRCWE	The evolution of O <sub>2</sub> level during 24-hour incubation was measured in three different media. Different dO <sub>2</sub> values were observed for all applied media. In the 0.05 % BSA-water and Gambles solution NM-101 showed negligible reactivity. In Caco2 medium increase of O <sub>2</sub> level is observed. The results suggest that NM-101 is inactive or oxidative in the different incubation media. Particle reactivity may easily exceed 1 µmol O <sub>2</sub> /mg.
<b>Radical formation</b>		
End-point not tested		
<b>Composition</b>		
ICP-OES	CODA-CERVA	>0.01 % : Na(> 0.1 %), Al, P, S, Zr 0.001-0.005 % : K, Ca
EDS	IMC-BAS	Si - 2900 ppm, P - 2700 ppm, Al - 900 ppm, S - 2200 ppm, Ti - 58.79 (wt %), O (wt%) calculated - 40.35

**Table 61. Overview of results from the physico-chemical characterisation of NM-102.**

Method	Institution	Results, NM-102
<b>Homogeneity</b>		
DLS	CEA	Repeated DLS studies were performed between vials and within vials. NM-102 tends to sediment quickly and no stable dispersion could be obtained; the results are thus not conclusive.
<b>Agglomeration / aggregation</b>		
SAXS	CEA	Structure and size parameters extracted from SAXS data. Gyration radius of primary particles and aggregates 2xRg <sub>1</sub> : 12.8 nm and 2xRg <sub>2</sub> : 560 nm, fractal dimension D <sub>f</sub> : 3 and number N <sub>part/agg</sub> of particles per aggregate: 20000
DLS	CEA	<ul style="list-style-type: none"> <li>Ultra-pure water dispersion (intra vial study) Z-average (nm): 442.6. ± 76.6, Pdl: 0.428 ± 0.058</li> <li>Ultra-pure water dispersion (inter vial study) Z-average (nm): 408.9 ± 23.2, Pdl: 0.427 ± 0.012</li> </ul>
TEM	IMC-BAS, CODA-CERVA	Individual crystallite sizes typically smaller than 50 nm Aggregates with size in the range of 100-500 nm.

Method	Institution	Results, NM-102
<b>Water Solubility</b>		
24-hour acellular <i>in vitro</i> incubation test	NRCWE	The 24-hour dissolution ratio of NM-102 was measured in three different media: 0.05 % BSA in water, Gambles solution and Caco2 media. NM-102 is slightly soluble in Gambles solution and Caco2 medium. The solubility behaviour of the impurities and NM-102 varies and depends on the medium.
<b>Crystalline phase</b>		
XRD	JRC	 <p>Anatase</p>
	NRCWE	Anatase
	IMC-BAS	Anatase
<b>Dustiness</b>		
Small Rotating Drum	NRCWE	Inhalable dustiness index: $268 \pm 39$ Mass respirable (mg/kg): $15 \pm 2$
Vortex Shaker Method	INRS	Mass respirable (mg/kg): $9200 \pm 0.00825$
<b>Crystallite size</b>		
SAXS	CEA	Primary particle size: Equivalent diameter for spheres: 22 nm. $2xRg_1$ is 12.8nm
XRD	JRC	21 nm (Scherrer eq.)
	NRCWE	23 nm (Scherrer eq.) 26 nm (TOPAS, IB) 28 nm (TOPAS, FWHM)
	IMC-BAS	18 nm (Scherrer eq.) 16 nm (TOPAS) 18 nm (Fullprof)

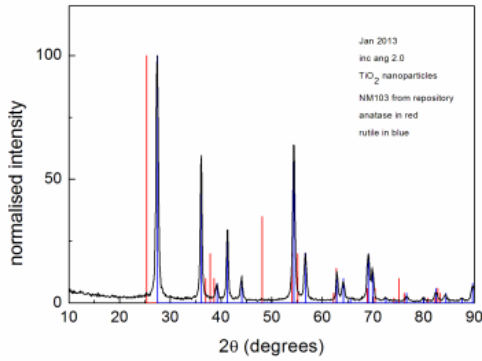
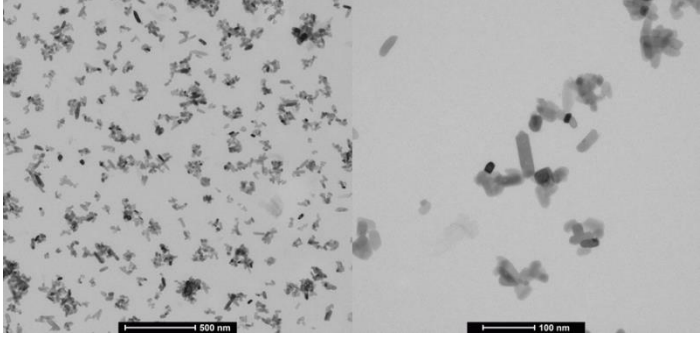
Method	Institution	Results, NM-102
<b>Representative TEM picture(s)</b>		
TEM	CODA-CERVA, IMC-BAS	 <p>Nanocrystalline anatase aggregates with individual particles typically smaller than 50 nm.</p>
<b>Particle size distribution</b>		
SAXS	CEA	Primary particle size: Equivalent diameter for spheres: 22 nm, $2xRg_1$ is 12.8nm
TEM	CODA-CERVA	Primary particle size: $21 \pm 10$ nm (median of 1395)
	IMC-BAS	Primary particle size: 22 nm
	INRS	Primary particle size: $22 \pm 6$ nm (median of 1317)
TEM	IMC-BAS, CODA-CERVA	Aggregates with fractal structure can be observed. Aggregates have a size in range of 20-500 nm.
DLS	CEA	<ul style="list-style-type: none"> <li>Ultra-pure water dispersion (intra vial study) [results in nm] Z-average: <math>442.6 \pm 76.6</math>, Pdl: <math>0.428 \pm 0.058</math>, FWHM peak width: <math>460.3 \pm 232.7</math></li> <li>Ultra-pure water dispersion (inter vial study) [results in nm] Z-average: <math>423.3 \pm 59.4</math>, Pdl: <math>0.427 \pm 0.042</math>, FWHM peak width: <math>414.1 \pm 107.6</math></li> </ul>
<b>Specific Surface Area</b>		
BET	IMC-BAS	$77.992 \text{ m}^2/\text{g}$
	JRC	Material stored at $40 \text{ }^\circ\text{C}$ : $78.97 \text{ m}^2/\text{g}$ Material stored at $-80 \text{ }^\circ\text{C}$ : $82.88 \text{ m}^2/\text{g}$
SAXS	CEA	$65.6 \pm 3.3 \text{ m}^2/\text{g}$
<b>Zeta Potential (surface charge)</b>		
Zetametry	CEA	NM-102 forms a stable suspension at pH lower than 4, with positively charged nanoparticles (exceeding 30 mV). The zeta potential varied significantly as function of pH from 40 mV at pH 2 to -45 mV around pH 12. IEP: 6.

Method	Institution	Results, NM-102
<b>Surface Chemistry</b>		
XPS	JRC	<ul style="list-style-type: none"> <li>Elements identified in the surface O (<math>50.7 \pm 1.5</math> at%), C (<math>23.4 \pm 2.4</math> at%), Ti (<math>18.6 \pm 0.9</math> at%)</li> <li>Elements identified in the surface after Ar ion etching (2 min, 3 keV) O (47.12 at%), C (34.71 at%), Ti (18.27 at%)</li> </ul>
TGA	NRCWE	<p style="text-align: center;"><b>TGA of NM102</b></p>  <p style="text-align: right;">No significant mass loss is observed below and above 100 °C</p>
<b>Photo-catalytic activity</b>		End-point not tested
<b>Pour-density</b>		End-point not tested
<b>Porosity</b>		
BET	IMC-BAS	Micropore volume (mL/g): 0.00034
<b>Octanol-water partition coefficient</b>		End-point not relevant
<b>Redox potential</b>		
OxoDish fluorescent sensor plate for O <sub>2</sub> detection	NRCWE	The evolution of O <sub>2</sub> level during 24-hour incubation was measured in three different media. Different dO <sub>2</sub> values were observed for all applied media. In the 0.05% BSA-water NM-102 showed negligible reactivity. In Gambles solution and Caco2 medium increase of O <sub>2</sub> level is observed. The results suggest that NM-102 is inactive or oxidative in the different incubation media. Particle reactivity may easily exceed 1 μmol O <sub>2</sub> /mg.
<b>Radical formation</b>		End-point not tested
<b>Composition</b>		
ICP-OES	CODA-CERVA	> 0.01% : S 0.005-0.01 % :Ca, Zr 0.001-0.005 % : K, Na, P, W
EDS	IMC-BAS	Si - 800 ppm, Al - 500 ppm, Fe - 700 ppm, Ti - 59.73 (wt %), O (wt%) calculated - 40.07

**Table 62. Overview of results from the physico-chemical characterisation of NM-103.**

Method	Institution	Results, NM-103
<b>Homogeneity</b>		
DLS	CEA, INRS	Repeated DLS studies were performed between vials and within vials. The reproducibility within vials (tested on two vials) is of a few percent. The systemic variation between the results from different laboratories for different vials is higher than 15%.
<b>Agglomeration / aggregation</b>		
SAXS	CEA	Structure and size parameters extracted from SAXS data. Gyration radius of primary particles and aggregates $2xRg_1$ : 26 nm and $2xRg_2$ : 140 nm, fractal dimension $D_f$ : 2.2 and number $N_{part/agg}$ of particles per aggregate: 113
DLS	CEA	<ul style="list-style-type: none"> <li>Ultra-pure water dispersion (intra vial study) Z-average (nm): <math>113.8 \pm 1.8</math>, Pdl: <math>0.252 \pm 0.007</math> Z-average (nm): <math>112.6 \pm 4.7</math>, Pdl: <math>0.222 \pm 0.022</math></li> <li>Ultra-pure water dispersion (inter vial study) Z-average (nm): <math>113.2 \pm 3.25</math>, Pdl: <math>0.242 \pm 0.018</math></li> </ul>
	INRS	<ul style="list-style-type: none"> <li>Ultra-pure water dispersion (intra vial study) Z-average (nm): <math>132.3 \pm 7.3</math>, Pdl: <math>0.187 \pm 0.066</math></li> <li>Ultra-pure water dispersion (inter vial study) Z-average (nm): <math>119.6 \pm 11.0</math>, Pdl: <math>0.224 \pm 0.033</math></li> </ul>
TEM	CODA- CERVA, IMC-BAS	Primary particles: size from 20 to 100 nm Aggregates : size from 40 to 400 nm Low sphericity and angular aggregates Ferret min: 46.5 (2641) nm Ferret max: 75.9 (2641) nm
AFM	CEA	Z max: 22.3 (466) nm
<b>Water Solubility</b>		
24-hour acellular <i>in vitro</i> incubation test	NRCWE	The 24-hour dissolution ratio of NM-103 was measured in three different media: 0.05% BSA in water, Gambles solution and Caco2 media. NM-103 is slightly soluble in Caco2 media and Al and Si impurities are soluble in all media. The amounts vary considerably with medium, as does the relative amounts of dissolved Al and Si impurities compared with dissolved Ti, suggesting that the solubility behaviour of the impurities and NM-103 depends on the medium.



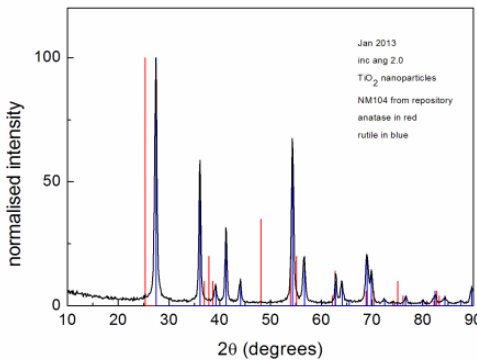
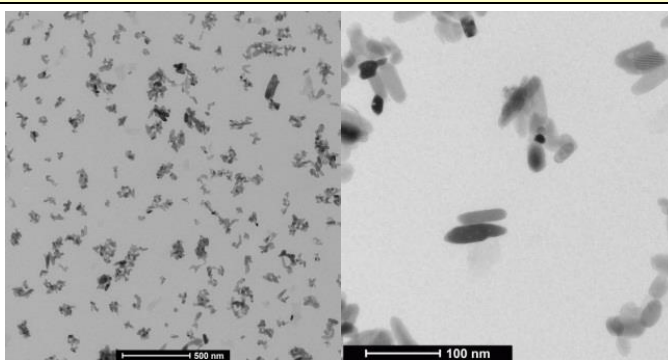
Method	Institution	Results, NM-103
<b>Crystalline phase</b>		
XRD	NRCWE	Rutile
	IMC-BAS	Rutile
	LNE	Rutile
	JRC	 <p>Jan 2013 inc ang 2.0 TiO<sub>2</sub> nanoparticles NM103 from repository anatase in red rutile in blue</p> <p style="text-align: right;">Rutile</p>
<b>Dustiness</b>		
Small Rotating Drum	NRCWE	Inhalable dustiness index: 9185 ± 234 Mass respirable (mg/kg): 323 ± 166
Vortex Shaker Method	INRS	Mass respirable (mg/kg): 19000 ± 0.017
<b>Crystallite size</b>		
SAXS	CEA	Primary particle size: Equivalent diameter for spheres: 28 nm 2xRg <sub>1</sub> is 26 nm
XRD	JRC	20 nm (Scherrer eq.)
	NRCWE	26 nm (Scherrer eq.) 25 nm (TOPAS, IB) 28 nm (TOPAS, FWHM)
	IMC-BAS	19 nm (TOPAS) 20 nm (Fullprof)
<b>Representative TEM picture(s)</b>		
TEM	IMC-BAS CODA-CERVA	 <p>NM-103 consists mainly of small aggregates. Single particles are rarely detected.</p>

Method	Institution	Results, NM-103
<b>Particle size distribution</b>		
SAXS	CEA	Primary particle size: Equivalent diameter for spheres: 28 nm. $2xRg_1$ is 26nm
TEM	CODA-CERVA	Primary particle size: 26 ±10 nm (median of 1317) Feret min: 19.2 nm (median of 1317) Feret max: 32.5 nm (median of 1317) Feret mean: 27.1 ± 1.5 nm (median of 1317) Small, elongated, prismatic primary particles with an aspect ratio 1.7
	IMC-BAS	Primary particle size: 22 nm Feret min: 23.7 nm (median of 440) Feret max: 42.7 nm (median of 440) Feret mean: 33.3 ± 9.4 nm (median of 440) Small, elongated, prismatic primary particles with an aspect ratio 1.82
	INRS	Primary particle size: 26 ± 6 nm (median of 101)
TEM	IMC-BAS, CODA-CERVA	Number in % of TiO <sub>2</sub> NM particles smaller than 100 nm, 50 nm and 10 nm <100 nm – 51.8 %, <50 nm – 12.7 % <10 nm – 0.1 %
DLS	CEA	<ul style="list-style-type: none"> <li>Ultra-pure water dispersion (intra vial study) [results in nm] Z-average: 113.8 ± 1.8, Pdl: 0.252 ± 0.007, FWHM peak width: 74.0 ± 5.7 Z-average: 112.6 ± 4.7, Pdl: 0.232 ± 0.022, FWHM peak width: 73.1 ± 16.4</li> <li>Ultra-pure water dispersion (inter vial study) [results in nm] Z-average: 113.2 ± 3.2, Pdl: 0.242 ± 0.018, FWHM peak width: 73.6 ± 11.1</li> </ul>
	INRS	<ul style="list-style-type: none"> <li>Ultra-pure water dispersion (intra vial study) Z-average (nm): 132.3 ± 7.3, Pdl: 0.187 ± 0.066</li> <li>Ultra-pure water dispersion (inter vial study) [results in nm] Z-average: 119.6 ± 11.0, Pdl: 0.224 ± 0.033, FWHM peak width: 73.6 ± 0.6</li> </ul>
<b>Specific Surface Area</b>		
BET	IMC-BAS	50.835 ± 1.8 m <sup>2</sup> /g
	JRC	Material stored at 40 °C : 51.69 m <sup>2</sup> /g Material stored at -80 °C : 50.86 m <sup>2</sup> /g
SAXS	CEA	51.1 ± 1.8 m <sup>2</sup> /g
<b>Zeta Potential (surface charge)</b>		
Zetametry	CEA	NM-103 forms a stable suspension at pH lower than 4, with positively charged nanoparticles (exceeding 30 mV). The zeta potential, however, varied greatly as function of pH from 45 mV at pH 2 to -45 mV around pH 12. NM-103 is unstable at pH around 6 (with zeta pot. +40 mV on the supernatant) which may be associated with the surface heterogeneities of this coated material. The high value of IEP (8.2) is most likely due to the presence of Al coating on the surface.

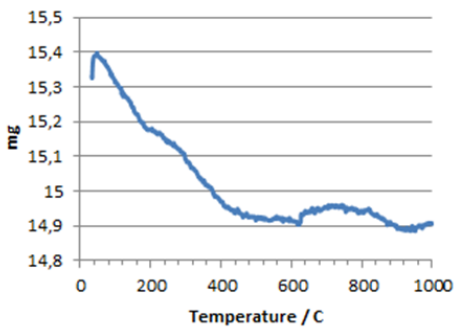
Method	Institution	Results, NM-103																
<b>Surface Chemistry</b>																		
XPS	JRC	<ul style="list-style-type: none"> <li>Elements identified in the surface [results in at%] O (<math>56.0 \pm 1.2</math>), C (<math>25.9 \pm 1.4</math>), Ti (<math>10.7 \pm 0.4</math>), Al (<math>4.9 \pm 0.4</math>), Fe/Ca (<math>2.5 \pm 1.0</math>)</li> <li>Elements identified in the surface after Ar ion etching (2 min, 3 keV) O (66.6 at%), C (7.1 at%), Ti (20.6 at%), Al (4.0 at%), %, Fe/Ca (1.5 at%)</li> </ul>																
GC-MS	NRCWE	GC-MS analysis results (retention time in min.): Dimetoxymethylsilane: 2.4; Silane?: 3.3; Silane: 7																
TGA	NRCWE	<div style="display: flex; align-items: center;"> <div style="flex: 1;"> <p style="text-align: center;"><b>TGA of NM103</b></p> <table border="1"> <caption>Approximate TGA Data Points</caption> <thead> <tr> <th>Temperature (°C)</th> <th>Weight (mg)</th> </tr> </thead> <tbody> <tr><td>0</td><td>22.75</td></tr> <tr><td>100</td><td>22.45</td></tr> <tr><td>200</td><td>22.40</td></tr> <tr><td>400</td><td>22.25</td></tr> <tr><td>600</td><td>22.18</td></tr> <tr><td>800</td><td>22.12</td></tr> <tr><td>1000</td><td>22.10</td></tr> </tbody> </table> </div> <div style="flex: 1; padding-left: 20px;"> <p>A small but gradual weight loss is observed, which may in fact be due to evaporation / combustion in several steps. There appears to be a change in the slope around 200 °C and weight loss is observed above 100 °C and is most likely due to a coating</p> </div> </div>	Temperature (°C)	Weight (mg)	0	22.75	100	22.45	200	22.40	400	22.25	600	22.18	800	22.12	1000	22.10
Temperature (°C)	Weight (mg)																	
0	22.75																	
100	22.45																	
200	22.40																	
400	22.25																	
600	22.18																	
800	22.12																	
1000	22.10																	
<b>Photo-catalytic activity</b>		End-point not tested																
<b>Pour-density</b>		End-point not tested																
<b>Porosity</b>																		
BET	IMC-BAS	Micropore volume (mL/g): 0.0																
<b>Octanol-water partition coefficient</b>		End-point not relevant																
<b>Redox potential</b>																		
OxoDish fluorescent sensor plate for O <sub>2</sub> detection	NRCWE	The evolution of O <sub>2</sub> level during 24-hour incubation was measured in three different media. Different dO <sub>2</sub> values were observed for all applied media. In the 0.05 % BSA-water NM-103 showed negligible reactivity. In Gambles solution and Caco2 medium decrease of O <sub>2</sub> level is observed. The results suggest that NM-103 is inactive or reductive in the different incubation media. Particle reactivity may easily exceed 1 μmol O <sub>2</sub> /mg.																
<b>Radical formation</b>		End-point not tested																
<b>Composition</b>																		
ICP-OES	CODA-CERVA	> 0.01 % : Al(> 0.1%), Na, S 0.005-0.01 % : Ca 0.001-0.005 % : Fe, K, Mg, Zr																
EDS	IMC-BAS	Si - 6800 ppm, S - 2600 ppm, Al - 34300 ppm, Fe - 600 ppm, Ti - 54.74 (wt %), O (wt%) calculated - 40.82																

**Table 63. Overview of results from the physico-chemical characterisation of NM-104.**

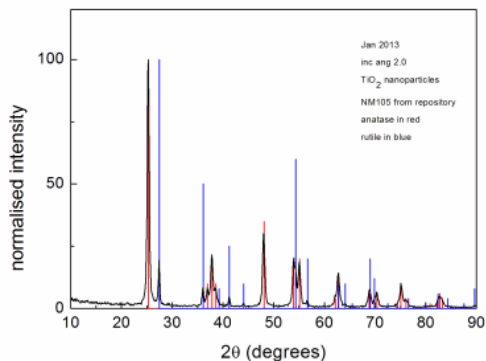
Method	Institution	Results, NM-104
<b>Homogeneity</b>		
DLS	CEA, NRCWE	Repeated DLS studies were performed between vials and within vials. The observed variability between and within the vials is very low (2-3%), which demonstrates very good homogeneity of the material.
<b>Agglomeration / aggregation</b>		
SAXS	CEA	Structure and size parameters extracted from SAXS data. Gyration radius of primary particles and aggregates $2xRg_1$ : 26 nm and $2xRg_2$ : 160 nm, fractal dimension $D_f$ : 2.3 and number $N_{part/agg}$ of particles per aggregate: 171
DLS	CEA	<ul style="list-style-type: none"> <li>Ultra-pure water dispersion (intra vial study) Z-average (nm): <math>128.3 \pm 0.8</math>, Pdl: <math>0.222 \pm 0.003</math> Z-average (nm): <math>128.9 \pm 1.8</math>, Pdl: <math>0.220 \pm 0.005</math></li> <li>Ultra-pure water dispersion (inter vial study) Z-average (nm): <math>128.6 \pm 1.3</math>, Pdl: <math>0.221 \pm 0.004</math></li> </ul>
	NRCWE	<ul style="list-style-type: none"> <li>Ultra-pure water dispersion (intra vial study) Z-average (nm): <math>125.3 \pm 1.7</math>, Pdl: <math>0.210 \pm 0.011</math></li> <li>Ultra-pure water dispersion (inter vial study) Z-average (nm): <math>126.5 \pm 2.7</math>, Pdl: <math>0.214 \pm 0.013</math></li> </ul>
TEM	CODA-CERVA	Primary particles: size from 8 to 200 nm Aggregates : size from 20 to 500 nm Low sphericity and sub-angular aggregates
	IMC-BAS	Feret min: 41.2 (3739) nm Feret max: 68.7 (3739) nm
AFM	CEA	Z max: 21.8 (458) nm
<b>Water Solubility</b>		
24-hour acellular <i>in vitro</i> incubation test	NRCWE	The 24-hour dissolution ratio of NM-104 was measured in three different media: 0.05 % BSA in water, Gambles solution and Caco2 media. NM-104 is slightly soluble in Caco2 media. The amounts vary considerably with medium, as does the relative amounts of dissolved Al impurities compared with dissolved Ti, suggesting that the solubility behaviour of the impurities and NM-104 depends on the medium.

Method	Institution	Results, NM-104
<b>Crystalline phase</b>		
XRD	JRC	 <p>Rutile</p>
	NRCWE	Rutile
	IMC-BAS	Rutile
	LNE	Rutile
<b>Dustiness</b>		
Small Rotating Drum	NRCWE	Inhalable dustiness index: $3911 \pm 235$ Mass respirable (mg/kg): $38 \pm 166$
Vortex Shaker Method	INRS	Mass respirable (mg/kg): $6400 \pm 0.00567$
<b>Crystallite size</b>		
SAXS	CEA	Primary particle size: Equivalent diameter for spheres: 27 nm $2xRg_1$ is 26 nm
XRD	JRC	21 nm (Scherrer eq.)
	NRCWE	27 nm (Scherrer eq.) 25 nm (TOPAS, IB) 29 nm (TOPAS, FWHM)
	IMC-BAS	19 nm (Scherrer eq.) 20 nm (TOPAS) 19 nm (Fullprof)
<b>Representative TEM picture(s)</b>		
TEM	CODA-CERVA, IMC-BAS	 <p>Aggregates with fractal structure. Single primary particles with elongated and rounded shape often detected</p>

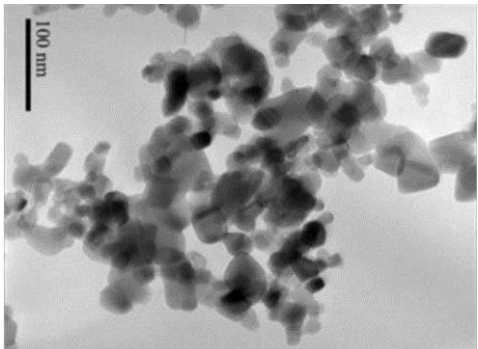
Method	Institution	Results, NM-104
<b>Particle size distribution</b>		
SAXS	CEA	Primary particle size: Equivalent diameter for spheres: 27 nm. $2xRg_1$ is 26nm
TEM	CODA-CERVA	Primary particle size: $26 \pm 10$ nm (median of 1099)
	IMC-BAS	Primary particle size: 23 nm
	INRS	Primary particle size: $26 \pm 7$ nm (median of 100)
TEM	IMC-BAS, CODA-CERVA	Number in % of TiO <sub>2</sub> NM particles smaller than 100 nm, 50 nm and 10 nm <100 nm – 53.3%, <50 nm – 12.1% <10 nm – 0.1%
DLS	CEA	<ul style="list-style-type: none"> <li>Ultra-pure water dispersion (intra vial study) [results in nm] Z-average: <math>128.3 \pm 0.8</math>, Pdl: <math>0.222 \pm 0.003</math>, FWHM peak width: <math>95.9 \pm 10.9</math> Z-average: <math>128.9 \pm 1.8</math>, Pdl: <math>0.222 \pm 0.005</math>, FWHM peak width: <math>84.4 \pm 8.6</math></li> <li>Ultra-pure water dispersion (inter vial study) [results in nm] Z-average: <math>128.6 \pm 1.6</math>, Pdl: <math>0.221 \pm 0.004</math>, FWHM peak width: <math>89.0 \pm 10.3</math></li> </ul>
	NRCWE	<ul style="list-style-type: none"> <li>Ultra-pure water dispersion (intra vial study) [results in nm] Z-average: <math>125.3 \pm 1.7</math>, Pdl: <math>0.210 \pm 0.011</math>, FWHM peak width: <math>82.7 \pm 5.5</math></li> <li>Ultra-pure water dispersion (inter vial study) [results in nm] Z-average: <math>126.5 \pm 2.7</math>, Pdl: <math>0.214 \pm 0.013</math>, FWHM peak width: <math>84.7 \pm 5.8</math></li> </ul>
<b>Specific Surface Area</b>		
BET	IMC-BAS	$56.261 \text{ m}^2/\text{g}$
	JRC	Material stored at 40 °C : $57.07 \text{ m}^2/\text{g}$ Material stored at -80 °C : $57.18 \text{ m}^2/\text{g}$
SAXS	CEA	$52.4 \pm 2.1 \text{ m}^2/\text{g}$
<b>Zeta Potential (surface charge)</b>		
Zetametry	CEA	NM-104 forms a stable suspension at pH lower than 4, with positively charged nanoparticles (exceeding 30 mV). The zeta potential varied significantly as function of pH, from 45 mV at pH 2 to -45 mV around pH 12. NM-104 is unstable at pH around 6 (with zeta pot. +40 mV on the supernatant) which may be assisted with the surface heterogeneities of this coated material. The high value of IEP (8.2) is most likely due to the presence of Al coating on the surface.

Method	Institution	Results, NM-104
<b>Surface Chemistry</b>		
XPS	JRC	<ul style="list-style-type: none"> <li>Elements identified in the surface O (<math>63.5 \pm 0.8</math> at%), C (<math>16.3 \pm 0.3</math> at%), Ti (<math>13.1 \pm 0.3</math> at%), Al (<math>7.1 \pm 1.0</math> at%)</li> <li>Elements identified in the surface after Ar ion etching (2 min, 3 keV) O (19.63 at%), C (7.32 at%), Ti (19.63 at%), Al (9.22 at%)</li> </ul>
TGA	NRCWE	<p style="text-align: center;"><b>TGA of NM104</b></p>  <p>A small gradual weight loss is observed. It most likely occurs in two steps, as there appears to be a change in the slope around 200 °C. The second weight loss is above 100 °C and is most likely due to a coating. For the last weight loss around 320 °C a peak is seen at the DTA curve indicating a phase transformation.</p>
GC-MS	NRCWE	GC-MS analysis results (retention time in min.): Tetramethyl silicate: 4.9; Glycerol: 13; Silane: 31.6, Silane: 32.9; Hexadecanoic acid methyl ester: 33.4; Hexadecanoic acid: 33.9; Octadecanoic acid: 35.8
<b>Photo-catalytic activity</b>		End-point not tested
<b>Pour-density</b>		End-point not tested
<b>Porosity</b>		
BET	IMC-BAS	Micropore volume (mL/g): 0.0
<b>Octanol-water partition coefficient</b>		End-point not relevant
<b>Redox potential</b>		
OxoDish fluorescent sensor plate for O <sub>2</sub> detection	NRCWE	The evolution of O <sub>2</sub> level during 24-hour incubation was measured in three different media. Different dO <sub>2</sub> values were observed for all applied media. In the 0.05 % BSA-water NM-104 showed negligible reactivity. In Gambles solution and Caco2 medium increase of O <sub>2</sub> level is observed. The results suggest that NM-104 is inactive or oxidative in the different incubation media. Particle reactivity may easily exceed 1 μmol O <sub>2</sub> /mg.
<b>Radical formation</b>		End-point not tested
<b>Composition</b>		
ICP-OES	CODA-CERVA	> 0.01 % : Al(> 0.1 %), Ca, Na, S 0.001-0.005 % : K, Mg, Zr
EDS	IMC-BAS	Si -1800 ppm, S - 3200 ppm, Al - 32200 ppm, Ti - 55.60 (wt %), O (wt%) calculated - 40.68

**Table 64. Overview of results from the physico-chemical characterisation of NM-105.**

Method	Institution	Results, NM-105
<b>Homogeneity</b>		
DLS	CEA, INRS, NRCWE	Repeated DLS studies were performed between vials and within vials. The observed variability within and between vials is very low, only a few percent.
<b>Agglomeration / aggregation</b>		
SAXS	CEA	Structure and size parameters extracted from SAXS data. Gyration radius of primary particles and aggregates $2xRg_1$ : 26 nm and $2xRg_2$ : 130 nm, fractal dimension $D_f$ : 2.45 and number $N_{part/agg}$ of particles per aggregate: 117
DLS	CEA	<ul style="list-style-type: none"> <li>Ultra-pure water dispersion (intra vial study)</li> </ul> Z-average (nm): $124.5 \pm 3.9$ , Pdl: $0.172 \pm 0.020$
	INRS	<ul style="list-style-type: none"> <li>Ultra-pure water dispersion (intra vial study)</li> </ul> Z-average (nm): $132.9 \pm 1.6$ , Pdl: $0.057 \pm 0.006$
	NRCWE	<ul style="list-style-type: none"> <li>Ultra-pure water dispersion (inter vial study)</li> </ul> Z-average (nm): $130.4 \pm 4.5$ , Pdl: $0.141 \pm 0.006$
	JRC	<ul style="list-style-type: none"> <li>Ultra-pure water dispersion (ultrasonic bath)</li> </ul> Z-average (nm): 554.9, Pdl: 0.679 <ul style="list-style-type: none"> <li>Ultra-pure water dispersion (ultrasonic tweeter)</li> </ul> Z-average (nm): 155.6 Pdl: 0.163
TEM	IMC-BAS, CODA-CERVA	Agglomerates and aggregates tend to have a fractal-like structure. Primary particles have a spherical, ellipsoidal or cuboidal structure. Primary particles sizes: 10-45 nm.
<b>Water Solubility</b>		
24-hour acellular <i>in vitro</i> incubation test	NRCWE	The 24-hour dissolution ratio of NM-105 was measured in three different media: 0.05 % BSA in water, Gambles solution and Caco2 media. NM-105 is slightly soluble in Caco2 media. No impurities were detected in any medium.
<b>Crystalline phase</b>		
XRD	JRC	 <p>Anatase and rutile</p>
	NRCWE	Anatase and rutile 88.2 : 11.8
	IMC-BAS	Anatase and rutile 86.36 : 13.64
	LNE	Anatase and rutile 81.5 : 18.5



Method	Institution	Results, NM-105
<b>Dustiness</b>		
Small Rotating Drum	NRCWE	Inhalable dustiness index: $1020 \pm 20$ Mass respirable (mg/kg): $28 \pm 10$
Vortex Shaker Method	INRS	Mass respirable (mg/kg): $11000 \pm 0.00966$
<b>Crystallite size</b>		
SAXS	CEA	Primary particle size: Equivalent diameter for spheres: 30 nm $2xRg_1$ is 26 nm
XRD	JRC	Anatase: 22 nm; rutile 40 nm (Scherrer eq.)
	NRCWE	Anatase 27 nm Rutile 62 nm (Scherrer eq.) Anatase 27 nm Rutile 88 nm (TOPAS, IB) Anatase 31 nm Rutile 123 nm (TOPAS, FWHM)
	IMC-BAS	Anatase 18 nm Rutile 23 nm (Scherrer eq.) Anatase 18 nm Rutile 27 nm (TOPAS) Anatase 19 nm Rutile 36 nm (Fullprof)
	LNE	Anatase 32 nm (Scherrer eq.)
<b>Representative TEM picture(s)</b>		
TEM	CODA-CERVA, IMC-BAS	 <p>Primary particles with a circular or slightly elongated shape. Aggregates with complex structure.</p>
<b>Particle size distribution</b>		
SAXS	CEA	Primary particle size: Equivalent diameter for spheres: 30 nm, $2xRg_1$ is 26nm
TEM	CODA-CERVA	Primary particle size: $21 \pm 9$ nm (median of 1421)
	IMC-BAS	Primary particle size: Rutile: 15 nm; anatase: $20.5 \pm 58.6$
	INRS	$24 \pm 5$ nm (median of 105)
TEM	CODA-CERVA	Feret min: 17.3.0 nm (median of 1421) Feret max: 24.2 nm (median of 1421) Feret mean: $21.6 \pm 1.5$ nm (median of 1421) Small, elongated, prismatic primary particles with an aspect ratio 1.36

Method	Institution	Results, NM-105
<b>Particle size distribution, cont.</b>		
DLS	CEA	<ul style="list-style-type: none"> <li>Ultra-pure water dispersion (intra vial study) [results in nm] Z-average: <math>124.5 \pm 3.9</math>, Pdl: <math>0.172 \pm 0.020</math>, FWHM peak width: <math>69.2 \pm 6.5</math></li> </ul>
	INRS	<ul style="list-style-type: none"> <li>Ultra-pure water dispersion (intra vial study) Z-average (nm): <math>132.9 \pm 1.6</math>, Pdl: <math>0.057 \pm 0.006</math></li> </ul>
	NRCWE	<ul style="list-style-type: none"> <li>Ultra-pure water dispersion (inter vial study) [results in nm] Z-average: <math>130.4 \pm 4.5</math>, Pdl: <math>0.141 \pm 0.006</math>, FWHM peak width: <math>62.5 \pm 1.2</math></li> </ul>
	JRC	<ul style="list-style-type: none"> <li>Ultra-pure water dispersion (ultrasonic bath) Z-average (nm): 554.9, Pdl: 0.679</li> <li>Ultra-pure water dispersion (ultrasonic tweeter) Z-average (nm): 155, Pdl: 0.163</li> </ul>
<b>Specific Surface Area</b>		
BET	IMC-BAS	46.175 m <sup>2</sup> /g
	JRC	Material stored at 40 °C (two samples): 52.81m <sup>2</sup> /g and 53.37 m <sup>2</sup> /g Material stored at -80 °C (two samples): 55.49 m <sup>2</sup> /g and 53.66 m <sup>2</sup> /g
SAXS	CEA	$47.0 \pm 2.3$ m <sup>2</sup> /g
<b>Zeta Potential (surface charge)</b>		
Zetametry	CEA	NM-105 forms a stable suspension at pH lower than 4 with positively charged nanoparticles (exceeding 30 mV). The zeta potential, however, varied greatly as function of pH from 45 mV at pH 2 to -45 mV around pH 12. IEP: 6.6
<b>Surface Chemistry</b>		
XPS	JRC	<ul style="list-style-type: none"> <li>Elements identified in the surface O (<math>54.0 \pm 0.3</math> at%), C (<math>24.5 \pm 0.6</math> at%), Ti (<math>21.5 \pm 0.4</math> at%)</li> <li>Elements identified in the surface after Ar ion etching (2 min, 3 keV) O (62.98 at%), C (11.93 at%), Ti (25.1 at%),</li> </ul>
TGA	NRCWE	<div style="display: flex; align-items: center;"> <div style="flex: 1;"> <p style="text-align: center;"><b>TGA of NM105</b></p> <p style="text-align: center;">Temperature / C</p> </div> <div style="flex: 1; padding-left: 20px;"> <p>No mass loss is observed. On the DTA curve a phase transition is seen at 322 °C.</p> </div> </div>
<b>Photo-catalytic activity</b>		End-point not tested
<b>Pour-density</b>		End-point not tested
<b>Porosity</b>		
BET	IMC-BAS	Micropore volume (mL/g): 0.0
<b>Octanol-water partition coefficient</b>		End-point not relevant

Method	Institution	Results, NM-105
<b>Redox potential</b>		
OxoDish fluorescent sensor plate for O <sub>2</sub> detection	NRCWE	The evolution of O <sub>2</sub> level during 24-hour incubation was measured in three different media. Different dO <sub>2</sub> values were observed for all applied media. In the 0.05 % BSA-water and Caco2 medium NM-105 showed negligible reactivity. In Gambles solution an increase of O <sub>2</sub> level is observed. The results suggest that NM-105 is inactive or oxidative in the different incubation media. Particle reactivity may easily exceed 1 µmol O <sub>2</sub> /mg.
<b>Radical formation</b>		End-point not tested
<b>Composition</b>		
ICP-OES	CODA-CERVA	0.001-0.005 %: Na
EDS	IMC-BAS	Si -700 ppm, Al - 400 ppm, Ti - 59.81 (wt %), O (wt%) calculated - 40.07

#### 14.2.2. Characterisation data, description and conclusion

The **homogeneity** within and between vials was investigated by DLS for NM-102, NM-103, NM-104 and NM-105, as was the reproducibility of results between laboratories. For NM-102 a very poor reproducibility was found (about 20 %) which most likely is due to inappropriate data treatment method than issues concerning the homogeneity of sub-sampling. For NM-103 and NM-104 the intra-vial reproducibility seemed to depend on both the mesurand and the laboratory. At INRS, the variability of data from the cumulant analysis (Z-average and Pdl) is only a few percent, whereas it is much higher for the position of the peak obtained from Padé-Laplace analysis. At CEA, the variability intra-vial observed is about 6 to 10 percent. However, a systematic variation of 15 % from one laboratory to the other was observed, which is greater than the intravial reproducibility. Given the consistency of the results obtained from each laboratory, the content of the vials is believed to be rather homogeneous and the variations are considered to originate from a systematic difference in sample preparation caused e.g. by different types of sonicators. However, the homogeneity study was performed using DLS to investigate and, as the results from the DLS method do not always reflect the underlying size distribution of the dispersed particles (Calzolari et al., 2011), a validation of the results would be beneficial.

In general, results indicate high zeta-potential values for TiO<sub>2</sub> NMs that are dispersed in acidic solution and thus confer stability in such media. Only NM-103 and NM-104 exhibit higher stability in non-acidic media possibly due to heterogeneities of these coated NMs.

The elemental analysis showed that NM-100, NM-101, NM-102 and NM-105 are rather pure, consisting of between 91.3 to 99.8 %wt titanium dioxide. For NM-103 and NM-104 a high percentage of Al and Si was found, due to the presence of inorganic and organic coatings. The TiO<sub>2</sub> NMs were analysed using several techniques: EDS, ICP-OES, TGA and DTA.

Material	Calculated indicative content of TiO <sub>2</sub> * (%wt)	Major impurities identified by EDS	Major impurities identified by XPS
NM-100	97.7	Al, Si, P, K, Fe,	C, K
NM-101	98.1	Al, Si, S, P	C
NM-102	99.6	Al, Si, Fe	C
NM-103	91.3	Al, Si S, Fe	C, Al
NM-104	92.7	Al, Si, S	C, Al
NM-105	99.8	Al, Si	C

\*The calculation is based on the titanium content given in Table 13 and the ratio of the molar weight of one Ti atom (47.9 g/mol) to two oxygen atoms (32.0 g/mol).

The two coated TiO<sub>2</sub> materials, NM-103 and NM-104, contain significant impurities directly related to the presence of the coating. All the TiO<sub>2</sub> NMs appear to contain some aluminium and silica (see Table 13) and in addition traces of other elements were identified for all NMs except NM-105 (see Table 14). The TGA analysis indicated that the three NMs, NM-101, NM-103 and NM-104 has a significant mass loss above 100°C which may be ascribed to the presence of coating or associated organic compounds. The TGA for NM-100, NM-102 and NM-105 had a weight change due to buoyancy, and in addition a phase transition was identified for NM-104 and NM-105 at 320°C and 322°C. Thus, the elemental analyses performed were indicative, and the outcomes reflect also that the materials have an industrial origin, as within one NM not all samples contain the same impurities, and sub-samples of one vial may be of slightly different composition. More information regarding the nature of the impurities should be generated for the future.

The TiO<sub>2</sub> NMs were analysed by XPS, a technique that gives information on the elemental surface composition of the materials down to a depth of about 10 nm. The analysis indicated presence of carbon in all materials and this was largely attributed to carbon contamination on the surface of the particles. In addition, presence of aluminium was identified in NM-103 and NM-104, and for NM-100 potassium was detected. The XPS results are confirmed by elemental analysis that suggests presence of aluminium and potassium for these NMs.

The XRD measurements reveal that all NM materials are crystalline. NM-100, NM-101 and NM-102 contain TiO<sub>2</sub> only in the anatase phase; in NM-103 and NM-104 contain only the rutile phase, and in NM-105 both anatase and rutile phases are present in the ratio 81.5: 18.5. No crystalline impurities were identified by the XRD method.

The combined results of homogeneity analysis, elemental analysis and XRD analysis indicate that these materials may work well as representative nanomaterials, but the volume at which repeatability can be reached needs to be established; possibly involving additional sub-sample homogenisation, or other treatments to enable use as reference materials

The TEM analysis showed the TiO<sub>2</sub> NMs consist of highly agglomerated and aggregated primary particles. The TEM micrographs indicate that the TiO<sub>2</sub> NMs have a polydisperse particle size distribution; the average value of the primary particle size was estimated to be below 26 nm for NM-103, NM-104 and NM-105, below 10 nm for NM-102, and above 100 nm for NM-100; for NM-100 primary particle sizes ranging from 20 nm up to 300 nm were detected. The shape of the particles was statistically analysed for two NMs: NM-103 and NM-104 and the results are given in the table below that summarises the morphology of aggregates/agglomerates of TiO<sub>2</sub> NMs according to Krumbain and Schloss (1963).

Material	Sphericity	Shape factor	General morphology
NM-103	Low sphericity	Very angular to sub-angular	Angular, low sphericity
NM-104	Low sphericity	Angular to sub-rounded	Sub-angular, low sphericity

Analysis of TEM micrographs showed that the general morphology of the NMs was quite comparable. All NMs consist of highly aggregated nanoparticles with fractal like morphology.

TEM micrographs also allowed an analysis of the primary particle size of the TiO<sub>2</sub> NMs, see the table below. The primary particle size is in good agreement both between laboratories using the same technique.

Material	ECD (nm) ± SD (N <sup>&amp;</sup> ); CODA-CERVA	ECD (nm) ± SD (N <sup>&amp;</sup> ); INRS	Diameter (nm); IMC-BAS
NM-100	50-90*	-	150
NM-101	6*	-	5
NM-102	21 ± 10 (1395)	22 ± 6 (100)	22
NM-103	26 ± 10 (1317)	26 ± 6 (101)	22
NM-104	26 ± 10 (1099)	26 ± 7 (100)	23
NM-105	21 ± 9 (1421)	24 ± 5 (105)	Rutile: 15*; Anatase: 20.5± 58.6**

\* Manual measurement. \*\* Manual Measurements using ImageJ software. &N= number of particles observed

The solubility of the TiO<sub>2</sub> NMs in BSA/water (i.e. the NANOGENOTOX batch dispersion medium), Gambles solution and Caco2 medium was investigated. TiO<sub>2</sub> as a substance is rather insoluble in all three media; however a more pronounced presence of Ti was detected in the Caco2 cell media. It should be noted that the impurities containing the elements Al and Si have a different dissolution pattern from TiO<sub>2</sub> and they dissolve better in all media in the 24-hour incubation experiment.

The pH and O<sub>2</sub> reactivity of the TiO<sub>2</sub> dispersed in BSA/water, Gambles solution and Caco2 medium were assessed using a commercial Sensor Dish Reader system that enables in situ measurement of pH and O<sub>2</sub> concentration at 1 s resolution. In all experiments the pH and O<sub>2</sub>

evolution was investigated over 24 hours as compared with the evolution in the pure media. All experiments were conducted in a cell incubator and all dispersions were prepared following the generic BSA/water NANOGENOTOX dispersion protocol. The experiments showed limited pH reactivity, but a burst in O<sub>2</sub> was observed. Interestingly, the reactivity may not be exerted to similar degree in the different media. It appears as though the reactivity for the TiO<sub>2</sub> NMs often is less pronounced in BSA water medium than in Gambles solution and Caco2 media. Additionally, different NM materials behaved differently in Gambles solution and Caco2 media. NM-100 and NM-103 acted reductively and NM-102 exhibits oxidative properties. The maximum O<sub>2</sub> change was in the order of 40 µmol/mL corresponding to more than 1 µmol O<sub>2</sub>/mg. The use of the SDR system is still at experimental level and clear data interpretation is not yet possible. It is, however, very evident that the NMs do react and have influence on the O<sub>2</sub> concentrations in the dispersions. It is currently assumed that the O<sub>2</sub> variability indicates that the TiO<sub>2</sub> NMs are redox-active due to direct electron transfer processes or due to dissolution-related reactions.

Specific surface area measurements using BET show specific surface area values of the same order of magnitude for the TiO<sub>2</sub> NMs, from 46.2 (NM-105) to 77.9 (NM-102) m<sup>2</sup>/g apart from NM-101 which exhibits very high SSA of 316 m<sup>2</sup>/g and NM-100 which exhibits very low SSA of 9.2 m<sup>2</sup>/g. NM-101 and NM-102 have some microporosity, as well as some micro surface area, i.e. in addition to particle size and shape also internal porosity contributes to the specific surface area.

For dustiness the small rotating drum (SD) and the Vortex shaker (VS) methods were applied and are currently proposed as standardised test methods for nanomaterials as the dustiness methods in EN15051 do not directly apply to nanomaterials. Both methods are based on agitation, and for both the determination of dustiness in respirable size-fractions were combined with number concentration and size-distribution analysis of the dust particles. In addition, as it was possible in the SD method protocol, the inhalable fraction was systematically measured. For a few of the tests conducted with the VS method, electron microscopy (EM) observations were performed. Finally, particle-size distributions data were reported from measurements using Electrical Low-Pressure Impactor (ELPI™ Classic) for the VS method, and Fast Mobility Particle Sizer (FMPS) and Aerodynamic Particle Sizer (APS) for the SD method. The comparison between the small drum and Vortex shaker results shows that no significant correlation between these two methods can be found. Further evaluation of the VS method is needed in order to understand the most appropriate test conditions and metrics and potential link the results to results using the SD.

## 15. References

- Baron P.A., Maynard A.D. and Foley M. (2002) Evaluation of Aerosol Release During the Handling of Unrefined Single Walled Carbon Nanotube Material. NIOSH DART-02-191 December 2002
- Barrett P.J. (1980) The shape of rock particles, a critical review. *Sedimentology*, 27(3):291-303.
- Batenburg K.J., Bals S., Sijbers J., Kubel C., Midgley P.A., Hernandez J.C., Kaiser U., Encina E.R., Coronado E.A. and Van Tendeloo G. (2009) 3D imaging of nanomaterials by discrete tomography. *Ultramicroscopy*, 109(6):730-740.
- Bau S., Witschger O., Gensdarmes F., Rastoix O. and Thomas D. (2010) A TEM-based method as an alternative to the BET method for measuring off-line the specific surface area of nanoaerosols. *Powder Technology*, 200(3):190-201.
- Boldridge D. (2010) Morphological Characterization of Fumed Silica Aggregates. *Aerosol Science and Technology*, 44(3):182-186.
- Brasil A.M., Farias T.L. and Carvalho M.G. (1999) A recipe for image characterization of fractal-like aggregates. *Journal of Aerosol Science*, 30(10):1379-1389.
- Briggs D. and Seah M.P. (1983) *Practical surface analysis*, 2<sup>nd</sup> ed, vol1, Wiley, New York.
- Brunauer S., Emmett P. H. & Teller E. (1938) Adsorption of gases in multimolecular layers. *J. Am. Chem. Soc.* 60, pp. 309-319
- Calzolari L., Gilliland D., Garcia C.P. and Rossi F. (2011) Separation and characterization of gold nanoparticle mixtures by flow-field-flow fractionation. *Journal of Chromatography A*, 1218 (27), pp. 4234-4239.
- Cedervall T., Lynch I., Lindman S., Berggård T., Thulin E., Nilsson H., Dawson K.A. and Linse S. (2007) Understanding the nanoparticle–protein corona using methods to quantify exchange rates and affinities of proteins for nanoparticles. *The National Academy of Sciences of the USA, PNAS* vol. 104 no.7 pp. 2050-2055.
- Chen, S.-Z., Zhang, P.-Y., Zhu, W.-P., Chen, L., Xu, S.-M. (2006) Deactivation of TiO<sub>2</sub> photocatalytic films loaded on aluminium: XPS and AFM analyses. *Appl. Surface. Sci.* 252; 7532-7538
- Christensen V.R., Jensen S.L., Guldberg M. and Kamstrup O. (1995) Effects of chemical composition of man-made vitreous fibers on the rate of dissolution in vitro at different pHs. *Environmental Health Perspectives* 102/5, 83-86.
- Cho W.-S., Duffin R., Howie S.E.M., Scotton C.J., Wallace W.A.H., MacNee W., Bradley M., Megson I.L. and Donaldson K. (2011) Progressive severe lung injury by zinc oxide nanoparticles; the role of Zn<sup>2+</sup> dissolution inside lysosomes. *Particle and Fibre Toxicology* 2011, 8:27
- Chu Z., Huang Y., Tao Q. and Li Q. (2011) Cellular uptake, evolution, and excretion of silica nanoparticles in human cells. *Nanoscale*, 3(8):3291-3299.
- De Temmerman, P.-J., van Doren E., Verleysen E., van der Stede Y., Francisco M.A.D. and Mast J. (2012) Quantitative characterization of agglomerates and aggregates of pyrogenic and precipitated amorphous silica nanomaterials by transmission electron microscopy. *Journal of Nanobiotechnology* 2012, 10:24
- Dick C.A.J., Brown D.M., Donaldson K. and Stone V. (2003) The role of free radicals in the toxic and inflammatory effects of four different ultrafine particle types. *Inhalation toxicology* 15/1, 39-52
- EC (European Commission) (2011) Commission Recommendation of 18 October 2011 on the definition of nanomaterial (2011/696/EU). OJ L 275, 20.10.2011, 38-40

- EFSA (2011) Guidance on the risk assessment of the application of nanoscience and nanotechnologies in the food and feed chain [<http://www.efsa.europa.eu/en/efsajournal/doc/2140.pdf>]
- Friedrich H., de Jongh P.E., Verkleij A.J., de Jong K.P. (2009) Electron tomography for heterogeneous catalysts and related nanostructured materials. *Chem Rev*, 109(5):1613-1629
- Förster H. and Tiesler H. (1993) Contribution to comparability of in vitro and in vivo man-made mineral fibre (MMMMF) durability experiments. *Glastechnology Bereitung* 66/10, 255-266.
- Hill R.J. and Madsen I.C. (1986) The effect of profile step width on the determination of crystal structure parameters and estimated standard deviations by X-ray Rietveld analysis. *Journal of Applied Crystallography* 19, 10-18. DOI: 10.1107/S0021889886090076
- ISO (2004) ISO 13322-1: Particle size analysis -Image analysis methods-. In: Part 1: Static image analysis methods.
- ISO (2008) ISO 9276-6: Part 6: Descriptive and quantitative representation of particle shape and morphology. In: Representation of results of particle size analysis. Geneva.
- Isamu O, Hiromu S, Masashi G (2009) Dustiness testing of engineered nanomaterials. *Journal of Physics: Conference Series* 012003
- Jensen K.A et al. (2012). Presentation. "Nanomaterial dustiness. A comparison between three different methods" [http://www.nanosafe.org/home/liblocal/docs/Nanosafe2012/presentations%20orales/Session%205/O5c1%20Jensen%20et%20al\\_Dustiness%203%20Methods%20Comparison\\_NANOSAFE2012%20vs%20\[Mode%20de%20compatibilit%C3%A9\].pdf](http://www.nanosafe.org/home/liblocal/docs/Nanosafe2012/presentations%20orales/Session%205/O5c1%20Jensen%20et%20al_Dustiness%203%20Methods%20Comparison_NANOSAFE2012%20vs%20[Mode%20de%20compatibilit%C3%A9].pdf)
- Jiang J., Oberdörster G. and Biswas P. (2009) Characterization of size, surface charge, and agglomeration state of nanoparticle dispersions for toxicological studies. *Journal of Nanoparticle Research*, 11(1):77-89.
- Kim S.H., Mulholland G.W. and Zachariah M.R. (2009) Density measurement of size selected multiwalled carbon nanotubes by mobility-mass characterization. *Carbon*, 47, 1297-1302.
- Krumbein W.C. and Sloss L.L. (1963) *Stratigraphy and Sedimentation*. San Francisco
- Lengyel J.S., Milne J.L. and Subramaniam S. (2008) Electron tomography in nanoparticle imaging and analysis. *Nanomedicine (London)*, 3(1):125-131.
- Linsinger T, Roebben G., Gilliland D., Calzolari L., Rossi F., Gibson N. and Klein C. (2012) Requirements on measurements for the implementation of the European Commission definition of the term 'nanomaterial'. 52 pp. EUR 25404 EN
- Marek, K.( 2009) Compilation of PZC and IEP of sparingly soluble metal oxides and hydroxides from literature. *Adv. Colloid Interface Sci.*, 152 (1-2): 14-25.
- Mast J. and Demeestere L. (2009) Electron tomography of negatively stained viruses: application in their diagnosis. *Diagnostic Pathology*, 4:5.
- Mastrorarde D.N. (1997) Dual-axis tomography: an approach with alignment methods that preserve resolution. *J Struct Biol*, 120(3): 343-352.
- Matsuda H. and Gotoh K. (1999) Study on the sample size required for the estimation of mean particle diameter. *Advanced Powder Technology*, 10(2):159-173.
- Merkus H.G. (2009) *Particle Size Measurements*. 1 edn. Pijnacker: Springer.
- Morris J., Willis J., Di Martinis D., Hansen B., Laursen H., Riego Sintes, J., Kearns P., Gonzalez, M. (2011) Science policy considerations for responsible nanotechnology decisions. *Nature Nanotechnology*, 6:73-77.



- Nel A.E., Madler L., Velegol D., Xia T., Hoek E.M., Somasundaran P., Klaessig F., Castranova V. and Thompson M. (2009) Understanding biophysicochemical interactions at the nano-bio interface. *Nature Materials*, 8(7):543-557.
- Nobbmann U., Connah M., Fish B., Varley P., Gee C., Mulot S., Chen J., Zhou L., Lu Y., Sheng F., Yi J. and Harding S.E. (2007) Dynamic light scattering as a relative tool for assessing the molecular integrity and stability of monoclonal antibodies. *Biotechnology and Genetic Engineering Reviews* 24: 117-128
- Nordstöm, D.K. and Munoz, J.L. (1994) *Geochemical Thermodynamics*. Second edition. Blackwell Scientific Publications. 493 pp.
- OECD (2010). ENV/JM/MONO(2009)20-REV-ENG. Guidance Manual for Sponsors, OECD, Paris.
- OECD (2012). ENV/JM/MONO(2012)40. Guidance on sample preparation and dosimetry for the safety testing of manufactured nanomaterials, OECD, Paris.
- OECD (2013) ENV/CHEM/NANO(2013)22. Report of the OECD expert meeting on the physical chemical properties of manufactured nanomaterials and test guidelines, OECD, Paris.
- Olferta J.S., Symonds J.P.R. and Collings N. (2007) The effective density and fractal dimension of particles emitted from a light-duty diesel vehicle with a diesel oxidation catalyst. *Journal of Aerosol Science*, 38, 69-82.
- Oosthuizen L., Swart H. C., Viljoen P. E., Holloway P. H. and Berning G. L. P. (1997) *Applied Surface Science*, 120, 9.
- Osmond-McLeod M.J., Poland C.A., Murphy F., Waddington L., Morris H., Hawkins S.C., Clark S., Aitken R., McCall M.J., Donaldson K. (2011) Durability and inflammogenic impact of carbon nanotubes compared with asbestos fibres. *Part Fibre Toxicol*, vol. 8, no. 15.
- Penczek P., Marko M., Buttle K. and Frank J. (1995) Double-tilt electron tomography. *Ultramicroscopy* 60(3):393-410.
- Podczek F. and Mia Y. (1996) The influence of particle size and shape on the angle of internal friction and the flow factor of unlubricated and lubricated powders. *International Journal of Pharmaceutics*, 144(2):187-194.
- Powers K.W., Brown S.C., Krishna V.B., Wasdo S.C., Moudgil B.M. and Roberts S.M. (2006) Research Strategies for Safety Evaluation of Nanomaterials. Part VI. Characterization of Nanoscale Particles for Toxicological Evaluation. *Toxicol Sci*, 90(2):296-303.
- Pyrz W.D. and Buttrey D.J. (2008) Particle Size Determination Using TEM: A Discussion of Image Acquisition and Analysis for the Novice Microscopist. *Langmuir*, 24(20):11350-11360.
- Riley C.M., Rose W.I. and Bluth G.J.S. (2003) Quantitative shape measurements of distal volcanic ash. *Journal of Geophysical Research*, 108(B10):2504.
- Roebben, G., Rasmussen, K., Kestens, V., Linsinger, T. P. J., Rauscher, H., Emons, H., Stamm, H. (2013) Reference materials and representative test materials: the nanotechnology case. *Journal of Nanoparticle Research*, Vol. 15, pp. 1455-1468.
- SCENIHR (2009). Scientific Committee on Emerging and Newly Identified Health Risks (SCENIHR), Opinion on "Risk Assessment of Products of Nanotechnologies", Brussels.
- SCENIHR (2010) Scientific Basis for the Definition of the Term "Nanomaterial" [[http://ec.europa.eu/health/scientific\\_committees/emerging/docs/scenih\\_r\\_o\\_030.pdf](http://ec.europa.eu/health/scientific_committees/emerging/docs/scenih_r_o_030.pdf)]
- Schneider T. and Jensen K.A. (2008) Combined single drop and rotating drum dustiness test of fine to nanosized powders using a small drum. *Annals of Occupational Hygiene* 52/1: 23-34.

- Schneider T. and Jensen K.A. (2009) Relevance of aerosol dynamics and dustiness for personal exposure to manufactured nanoparticles. *J Nanopart Res* 11:1637–1650
- Sebastian K., Fellman J., Potter R., Bauer J., Searl A., de Meringo A., Maquin B., de Reydellet A., Jubb G., Moore M., Preininger R., Zaitos B., Boymel P., Steenberg T., Madsen AL., Guldborg M. (2002) EURIMA test guideline: In vitro acellular dissolution of man-made vitreous silicate fibres. *Glass Science Technology* 75/5, 263-270.
- Singh, B. P.; Menchavez, R.; Takai, C.; Fujii, M.; Takahashi, M. (2005) Stability of dispersions of colloidal alumina particles in aqueous suspensions. *J. Colloid Interface Sci.*, 291 (1): 181- 186.
- Teleki A, Wengeler R, Wengeler L, Nirschl H, Pratsinis SE (2008) Distinguishing between aggregates and agglomerates of flame-made TiO<sub>2</sub> by high pressure dispersion, *Powder Technology* 181:292-300
- Tong J., Arslan I. and Midgley P. (2006) A novel dual-axis iterative algorithm for electron tomography. *J Struct Biol* 2006, 153(1):55-63.
- Van Doren E., De Temmerman P.-J., Francisco M and Mast J. (2011) Determination of the volume-specific surface area by using transmission electron tomography for characterization and definition of nanomaterials. *Journal of Nanobiotechnology*, 9(1):17.
- Wiecinski, P.N., Metz K.M., Mangham, A.N., Jacobson, K.H., Hamers, R.J., Pedersen, J.A (2009) Gastrointestinal biodurability of engineered nanoparticles: Development of an in vitro assay *Nanotoxicology* Volume: 3 Issue: 3 Pages: 202-U66
- Witschger O., Brouwer D., Jensen K.A., Koponen I.K., Berges M., Jankowska E., Dahman D., Burdett G. and Bard D. (2011) DUSTINANO: A PEROSH initiative towards a harmonized approach for evaluating the dustiness of nanopowders. 5th International Symposium on Nanotechnology, Occupational and Environmental Health August 9 - August 12, 2011 — Boston, MA, USA, in abstract book, p.178
- Xia T., Kovochich M., Brant J., Hotze M., Sempf J., Oberley T., Sioutas C., Yeh J.I., Wiesner M.R., Nel, A.E. (2006) Comparison of the abilities of ambient and manufactured nanoparticles to induce cellular toxicity according to an oxidative stress paradigm, *Nano Letters* 6/8, 1794-1807
- Yang, J., Bai, H., Tan, X., Lian, J. (2006), IR and XPS investigation of visible-light photocatalysis-Nitrogen-carbon-doped TiO<sub>2</sub> film. *Appl. Surface.Sci.*, 253; 1988-1994

## A. Appendix. SOP: Dynamic Light Scattering Measurements and Data Treatment

### General description of scientific background

Dynamic Light Scattering (DLS), also called Photon Correlation Spectroscopy (PCS) or Quasi-Elastic Light Scattering (QELS), is a technique of characterisation of colloidal systems based on the scattering of visible light resulting from the difference in refractive index between the dispersed colloids and the dispersion medium. The method may be applied for sizing particles suspended in a liquid in the range from about 0.6 nm to about 6  $\mu\text{m}$  depending on the optical properties of the material and medium.

The principle in DLS is measurement of fluctuations in laser light scattered by vibrating particles suspended in a liquid as function of time. The vibration is due to Brownian motion caused by collision with solvent molecules of the liquid. The Brownian motion varies as a function of particle size and causes variation in the intensity of scattered light as function of time. A correlator compares the signal measured at a time  $t_0$  with different very short time delays  $dt$  (autocorrelation). As the particles move, the correlation between  $t_0$  and subsequent  $dt$  signals decreases with time, from a perfect correlation (1) at  $t_0$ , to a complete decorrelation (0) at infinite time (order of milliseconds). In the case of big particles, the signal changes slowly and the correlation persists for a long time, whereas small particles have high Brownian movement causing rapid decorrelation.

A DLS instrument measures the velocity of Brownian motion, defined by the translational diffusion coefficient  $D$  of the particles. The particle size, or more precisely its hydrodynamic diameter  $d_h$ , is then estimated using the Stokes-Einstein equation assuming spherical shape:

$$d_h = \frac{kT}{3\pi\eta D}$$

$k$ : Boltzmann's constant

$D$ : translational diffusion coefficient

$T$ : absolute temperature

$\eta$ : viscosity

It should be noted that even if a particle is really spherical, the spherical DLS size is fundamentally different from the physical spherical size. The hydrodynamic size includes the double-layer of highly polarized water molecules around the physical particle. When the particle morphology is highly non-spherical, the hydrodynamic size should be understood as the equivalent hydrodynamic spherical size. Establishment of mean hydrodynamic size and size distributions (intensity, number, volume) is reached by DTS software algorithms, by fitting the correlation function in the data treatment.

## Chemicals and equipment

- Test material or chemical
- Dispersion medium
- Ultrasonic probe equipped with a standard 13 mm disruptor horn
- Dynamic Light Scattering apparatus
- Viscosimeter (e.g, Malvern Inc., SV-10 Vibro Viscometer) *Optional for measurement of true viscosities*
- Pipette and pipette tips
- Syringes and syringe filters or filter paper

## Specificities for Zetasizer NanoZS from Malvern Instruments

DLS measurements rely on non-invasive back scatter (NIBS<sup>®</sup>) technology developed by Malvern Instruments, in which the signal is detected at 173°. The signal is treated by a digital correlator, and transmitted to the computer. DTS software enables the fitting of correlation data either by a monomodal mode, called the cumulant analysis (as defined by ISO 13321 Part 8) to obtain a mean size (Z-average diameter) and a polydispersity index (Pdl), or by a multiple exponential known as the **CONTIN method** to obtain a distribution of particle sizes.

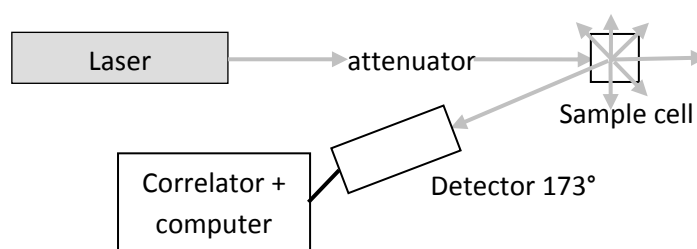
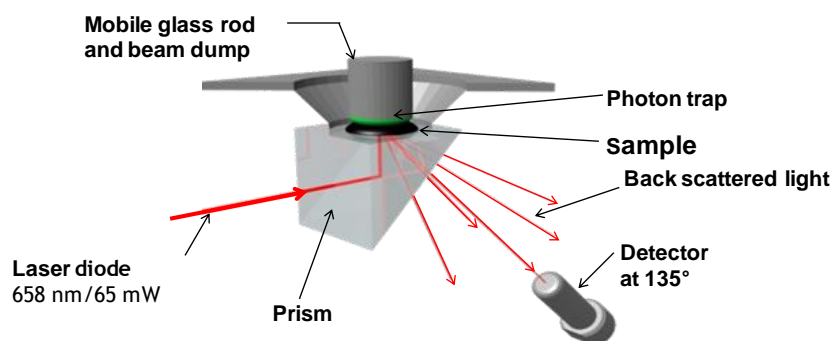


Figure A1. Simplified sketch of the optical configuration for DLS measurement by Zetasizer Nano ZS.

## Specificities for Vasco Cordouan

The VASCO<sup>™</sup> has an original design of the sample cell (thin layer technology) and optics arrangement. The configuration allows also the photo-detector to collect the back-scattered light signal at an angle of 135° (Figure A2 below). In addition, the cell is hermetically closed by a mechanical system that includes a mobile glass rod with a photon trap. This rod can both absorb the excess of transmitted light and control the sample thickness, down to few tens of microns. Decreasing the thickness of the sample (and then volume of analysis) reduces significantly the probability for a photon to be scattered several times. Thus, the multiple-scattering artifact is well reduced using this unique design. Also the thin layer technology prevents the sample from local heating.



**Figure A2. Configuration for DLS measurements by VASCO™.**

The NanoQ™ software proposes two acquisition modes:

- **Continuous mode** where the data acquisition is stopped by the user.
- **Statistical mode** where successive data acquisitions are performed automatically following a pattern set by the user (e. g. 15 successive acquisitions of 60 s each).

The NanoQ™ software supports two different algorithms for data analysis:

- **Cumulant method** (according to ISO 13321) for mono-disperse samples. The monomodal analysis of the autocorrelation function provides only a mean size value (light scattering intensity-averaged diameter also named as Z-averaged diameter) and a measure of the broadness of the distribution through the polydispersity index.
- **Padé-Laplace** method for polydisperse samples, which does not make any hypothesis for the number of components for multi-exponential analysis. The method gives as a result a discrete density of intensities (histogram), each of them corresponding to a given hydrodynamic diameter. Volume and number histograms are also available based on the Padé-Laplace analysis combined with a Mie algorithm. The NanoQ™ does not provide results expressed as continuous distribution curves for polydisperse samples.

## Sample preparation

Dispersions for analysis are prepared by mixing particulate material into a dispersion medium. A sub-sample of a suitable concentration is added to suitable measurement cuvettes. Dispersions are typically produced by sonication in a dispersion medium; SOPs were developed for dispersing the NMs, see e.g. <http://www.nanogenotox.eu>. The dispersion medium must be filtrated before use to avoid any dust contamination. This can be done by using syringe filters or filter paper with high efficiency. Usually filters with a 0.2 to 0.45  $\mu\text{m}$  pore-size are sufficient for filtration of dispersion media.

The concentration required for analysis depends e.g. on the relative refractive index between particles and dispersion medium, the particle size and polydispersity and the sample absorption. The Malvern apparatus is designed to measure samples over a large range of concentration and size of particles. Specifications of sample properties (concentration range, size of nanoparticles, medium) is found in the documentation from Malvern Instrument on their website. The dispersion must be stable during the measurement.

## Measurements

### Summary

Measurements are performed at ambient temperature according to the procedure appropriate for each type of apparatus. Sample properties such as material and dispersant refractive indices and viscosity are entered in the software for analysis. Number and duration of run and optical configuration are automatically optimised by the software for Malvern apparatus. For Cordouan apparatus, 15 runs of 60 s are performed.

### About ZetaSizer NanoZS from Malvern Instrument

DLS measurements can be performed in disposable polystyrene cuvettes (optical path 1 cm, volume 1 mL) or alternatively glass cuvettes (at NRCWE) or in semi micro polystyrene disposable cuvettes (optical path 1 cm, volume 500  $\mu$ L) or in clear disposable zeta cells DTS1061 just before zeta potential measurements (at CEA). The measurements are repeated 3 (CEA) or 6 (NRCWE) times with automatic determination of duration and number of runs, and averaged. The repeated analyses are conducted to enable omission of measurements with poor correlation data or abnormal solutions to the correlation function (must be carefully considered).

The following standard procedure is recommended as the general approach for DLS measurement of NM dispersions:

- Turn on the computer and DLS instrument
- Allow the instrument to warm up according to the manufacturer's recommendation (30 min).
- *Optional: Complete viscosity measurement using the SV-10 Vibro Viscometer mounted with the 10 mL flow-reactor placed in a thermostated water jacket. The measured dynamic viscosity is used as input data for the specific dispersion measured in the DTS software.*
- Upload the DTS software and the "Measurement" window for entering material specific data on dispersion medium, test material and specific analytical settings:
  - Refractive index and absorption values for dispersant and NM.
  - Temperature conditions (25°C) and equilibration time for measurement.

- The General purpose model is selected for initial evaluation of data and is the most generic model for calculation of size.
- Select a sample cuvette, ensure that it is dustfree and has no defects or scratches in the measurement area of the cuvette. Some producers have been found to deliver cuvettes with scratches or folding structure in the measurement area at one side of the cuvette. Dust may be cleaned out by rinsing the cuvette in dispersion medium.
- Fill in a suitable volume of dispersion into a measurement cuvette using a pipette.
- Place the sample cuvette in the sample holder in the DLS instrument.
- Run analysis (click “play” on the measurement window).
- The size analysis may be immediately accepted if the DTS Expert advice denotes the result quality as “Good”. If the result is not of good quality, the sample should be further analyzed for presence of dust, cuvette errors, large particles, sedimentation, wall-deposition etc.
- If the sample contains particles with large spread in size distribution, one may consider filtering the sample through different syringe filters to investigate presence of small nm-size particles. Small nm-size particles may not be fully resolved when larger particles are present due to the large drop ( $10^6$  per factor of ten in size ratio) in scattered light intensity with size.
- If parameters such as refractive indexes, absorption coefficient or viscosity were wrong or unknown at the measurement time, the correction can be made afterwards using the command Edit (right click on the measurement) in the DTS software.

The measurement conditions generally used at CEA and NRCWE are listed in Tables A1 and A2, respectively. The viscosity considered for measurement is generally the one of pure water, 0.8872 cP, but the data can be corrected afterwards for the values measured.

At CEA, the viscosity of water is considered for all samples prepared without addition of BSA or in the pH-adjusted protocol. For suspensions prepared according to the validated NANOGENOTOX protocol, all data were corrected considering the real viscosities measured by NRCWE (usually around 0.99 cP – 1 cP).

**Table A1. Conditions used at CEA, refractive index ( $R_i$ ), absorption or imaginary part ( $R_{abs}$ ) and dynamic viscosity.**

	Water (STP)	SiO <sub>2(amorphous)</sub>
$R_i$	1.33	1.50
$R_{abs}$		0.01
Viscosity [cP]	0.8872	-

**Table A2. Conditions used at NRCWE, refractive index ( $R_i$ ), absorption or imaginary part ( $R_{abs}$ ) and dynamic viscosity.**

	Water (STP)	SiO <sub>2(amorphous)</sub>
$R_i$	1.33	1.544
$R_{abs}$		0.20
Viscosity [cP]	0.8872	water

## DLS measurements for stability over time

DLS measurements for stability over time were performed on 500  $\mu\text{L}$  suspension in semi micro polystyrene cuvette (CEA) or 1 mL in standard disposable cuvette (NRCWE). The first measurement at  $t_0$  is performed as usual DLS measurements (described above) with automatic determination of parameters. The number of the run, duration, position and choice of attenuator are then recorded and used for the following measurements, which are scheduled over a period of approximately 16 h, usually every 30 min.

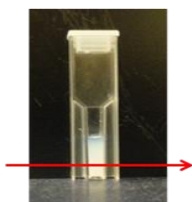


**Figure A3. Semi micro cuvette used at CEA for DLS measurements over time. The arrow represents the position of the laser beam probing the suspension.**

## On Vasco™ from Cordouan Technologies

The following procedure was used and is recommended:

- Turn on the Vasco™ 30 minutes before starting a measurement.
- Run the NanoQ™ software, enter the material specific data on dispersion medium and test nanomaterial as well as specific analytical settings (see table below). Temperature is set to 21 °C.
- Prior to any measurement, it is strongly recommended to carefully clean the cell to avoid pollution from previous measurements. The cleaning operation has to be made gently according to the manufacturer's recommendations.
- Once the cell is perfectly clean, introduce the sample to analyse. For that, use a plastic pipette to extract a sample from the suspension to analyse and drop off a small volume ( $\approx 2 \mu\text{l}$ ) in the centre of the cell as shown on the picture below. In order to perform measurements under good conditions, the suspension to be analysed should cover entirely the bottom of the cell, as this correspond to the upper surface of the glass prism guiding the laser beam. For the suspensions analysed in NANOGENOTOX, the thickness of the liquid was set to about 1.5 mm (position "up" of the dual thickness controller). After closing the mechanical system, measurements can begin.
- Run the analysis.
- Process the data.



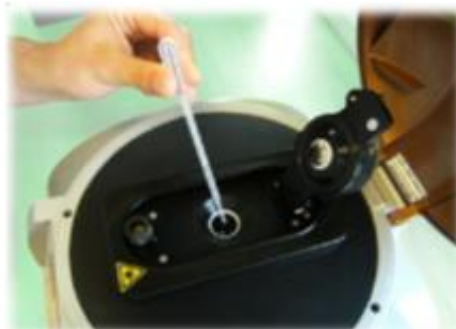


**Figure A4. Illustration of sample deposition on Vasco™ apparatus.**

The conditions used at INRS for the analysis with the Vasco™ are reported in Table A3.

**Table A3. Conditions used at INRS, refractive index ( $R_i$ ), absorption or imaginary part ( $R_{abs}$ ) and dynamic viscosity.**

	<b>Water</b>	<b>SiO<sub>2</sub>(amorphous)</b>
<b><math>R_i</math></b>	1.33	1.54
<b><math>R_{abs}</math></b>		0.2
<b>Viscosity [cP]</b>	0.97	0.97

For all measurements performed with the Vasco™ in the NANOGENOTOX project, the "statistical mode" was used, i.e. 15 successive measurements, each with a duration of 60 seconds.

## Data treatment

### Summary

A monomodal model, the cumulant analysis is used to treat the raw data correlograms (decaying as exponential). It determines a Z-average (diameter of particles scattering with higher intensity) and a polydispersity. Since these samples are quite polydisperse, more sophisticated models, such as the CONTIN method, are applied as multimodal analysis to reveal size distributions.

### About ZetaSizer NanoZS from Malvern Instrument

The actual raw data obtained from a dynamic light scattering experiment is the autocorrelation function, which is an exponential decay with a characteristic time related to the size of the diffusing object. An example of correlation data is shown in Figure A5 for two NM-104 samples (0.5 g/L TiO<sub>2</sub>, 0.036 mol/L of monovalent salt), one stable suspension at pH 2.8 (red curves) and the supernatant of an aggregated sample at pH 10.1 (green curves). The data used are the averaged data for 3 consecutive measurements.

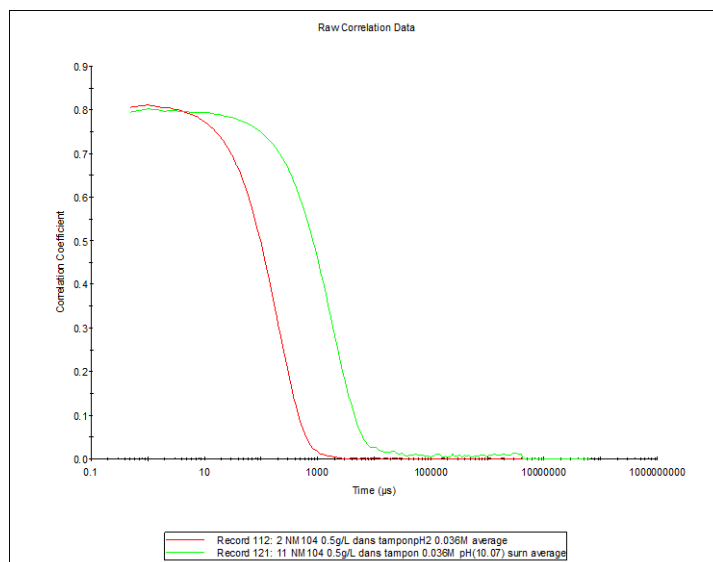


**Figure A5.** Example of raw correlation data for two NM-104 samples (0.5 g/L TiO<sub>2</sub> in 0.036 mol/L ionic buffer), one stable suspension of relatively dispersed particles at pH2.8 (red curve), and one unstable sample of big aggregates at pH 10.1 (green curve, measure on supernatant).

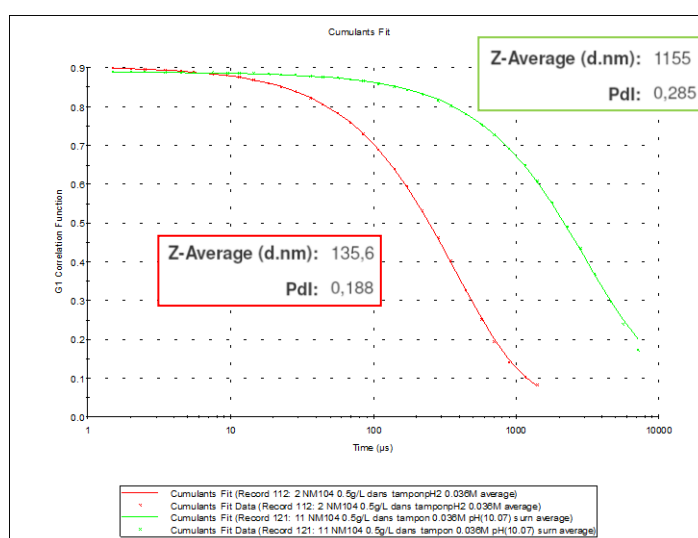


**Figure A6.** Example of data and fits by the Cumulant method, together with calculated values of Z average and polydispersity, for two NM-104 (TiO<sub>2</sub>) samples (0.5 g/L TiO<sub>2</sub> in 0.036 mol/L ionic buffer, stable suspension at pH 2.8 in red and unstable sample of big aggregates at pH 10.1 in green).

The raw correlation data are analysed to extract information on size and distribution. Various algorithms can be used and the simplest is the *Cumulants analysis*, which fits the data by approximating the single exponential decay by a degree 2 Taylor development function. This provides a Z-average mean value, which corresponds to the particle size diffusing with the highest intensity, and a polydispersity index (Pdl) for this monomodal distribution. In the DTS software, the corresponding graph is entitled “Cumulants fit”. The method applies to

monomodal distributions with polydispersity lower than 0.25, and is in agreement with ISO 13321 standard. For higher polydispersity, the two parameters Z-average and Pdl alone do not accurately describe the sample size distribution and a multimodal analysis is necessary. Some examples of Cumulant fits analysis applied to NM-104 are shown in Figure A6. The high Pdl obtained for the sample at pH 10 indicates that this model is not advanced enough to determine an accurate size distribution for this sample.

For polydispersity indices between 0.08 and 0.5, the correlation data can be better analyzed by the *CONTIN method*. It fits the correlation data to the best combination of a set of 24 exponential functions, giving rise to a size distribution over 24 granulometric classes. In DTS software, this fit is denominated as “distribution fit”, “data fit” or “size fit” (Figure A7).

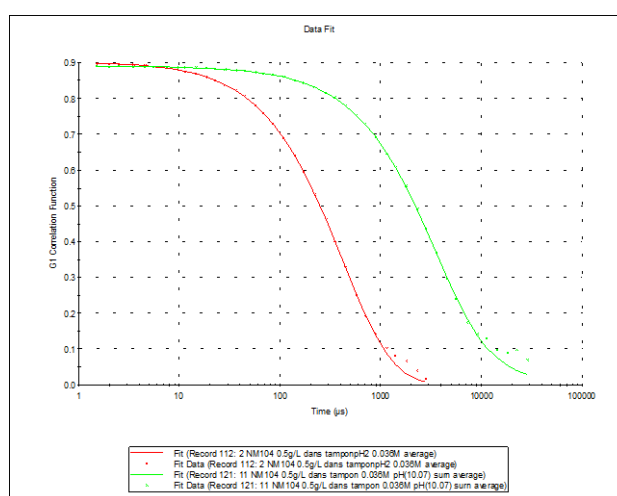


**Figure A7. Example of data and fits by the CONTIN method, for two NM-104 (TiO<sub>2</sub>) samples (0.5 g/L TiO<sub>2</sub> in 0.036 mol/L ionic buffer, stable suspension at pH 2.8 in red and unstable sample of big aggregates at pH 10.1 in green).**

Taking into account the refractive indices of material and dispersant, Mie Theory can be applied to represent size distribution in volume. The number size distribution can then be calculated from simple geometrical considerations (Figure A8). Distribution data can be retrieved from DTS software in the form of tables of diameter, percentage and width for the three main peaks.

It should be noted that for 2 particles with a size ratio of 10, the bigger particle contributes 10<sup>3</sup> times more than the smaller one to the volume distribution, and 10<sup>6</sup> times more to the distribution by intensity. Since DLS measurements are based on intensity, this means that the light scattered by a few large particles may totally cover the signal from the smaller ones.

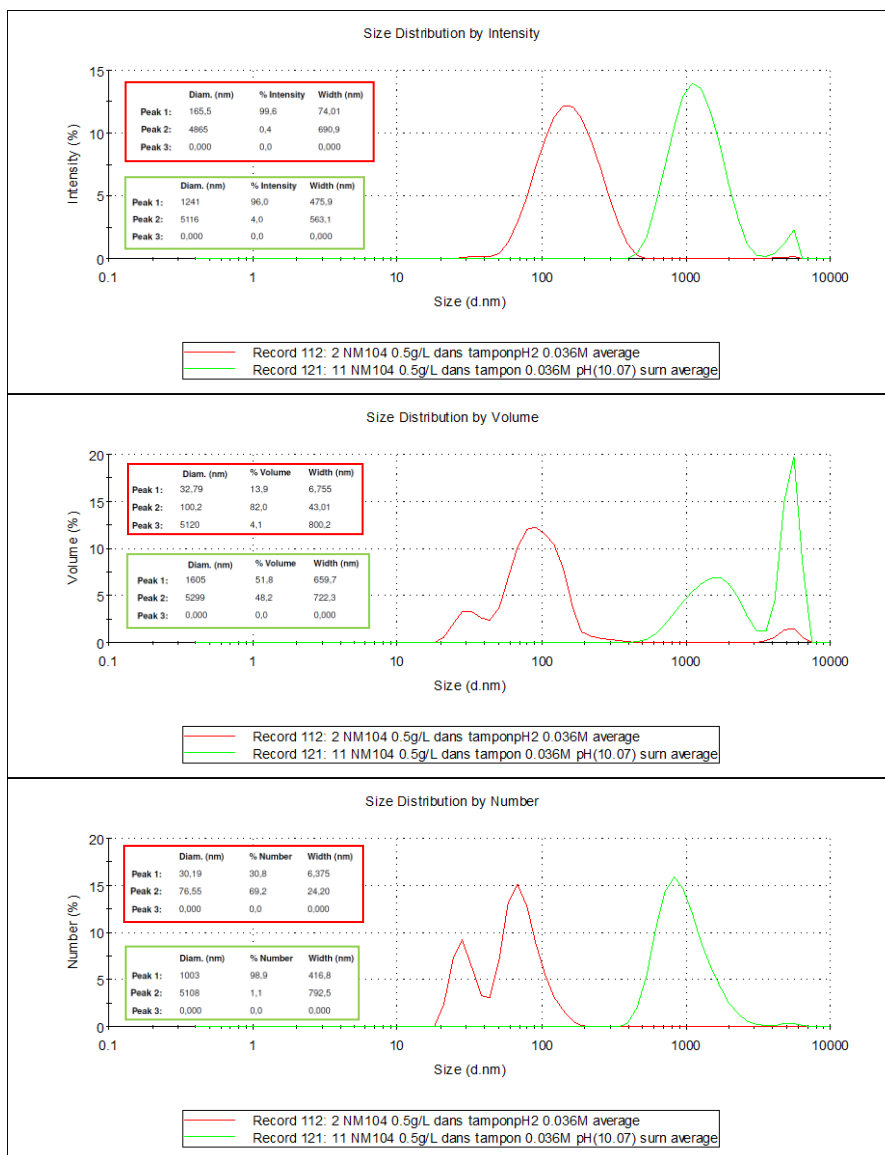


**Figure A8.** Example of size distributions by intensity, by volume and by number, together with tables of numerical values for the three main peaks of each distribution, for two NM-104 (TiO<sub>2</sub>) samples (0.5 g/L TiO<sub>2</sub> in 0.036 mol/L ionic buffer, stable suspension at pH 2.8 in red and unstable sample of big aggregates at pH 10.1 in green).

After controlling correlation data and fits, an average measurement is calculated with the software. As an example, the main graphs observed for the 3 initial measurements of a sample of NM-104 at pH 2.8 (0.5 g/L TiO<sub>2</sub>, 0.036 mol/L of monovalent salt) are displayed in Figure A9. Since the correlation data are good, the 3 measurements are all taken into consideration for the averaged data.

The main parameter reported in the results section is “Z-average”, which represents the mean size contributing to the major part of the signal **in intensity**. For polydisperse samples, this value mostly gives a hint about the aggregation state of the particles but does not reflect the hydrodynamic size of most of the dispersed particles (in number), which of course is

much lower. When Z-average is higher than approximately 500 nm, it can only be deduced that there are big aggregates in suspension but the numerical value is usually meaningless.

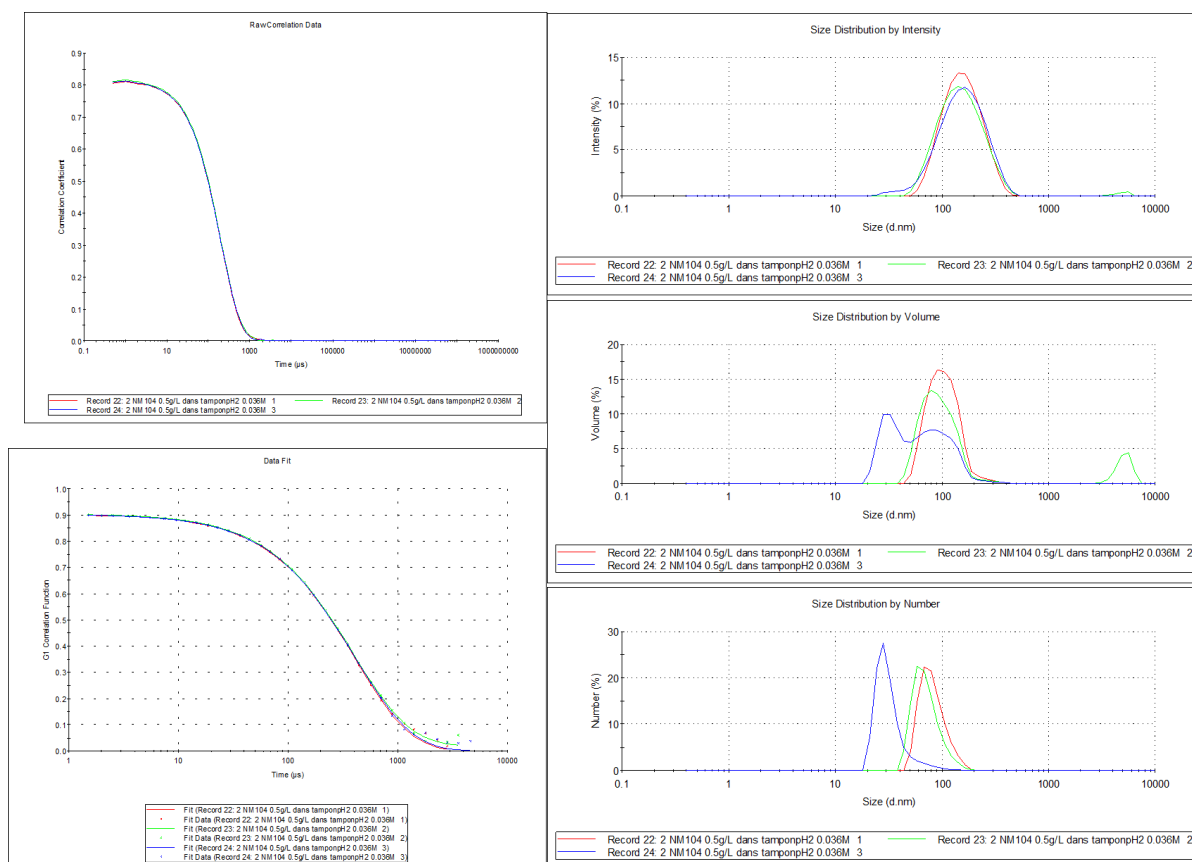


**Figure A9. Main graphs reported by DTS software for 3 consecutive measurements of a NM-104 (TiO<sub>2</sub>) sample (pH 2.8, 0.5 g/L TiO<sub>2</sub> in 0.036 mol/L aqueous ionic medium).**

## On Vasco™ from Cordouan Technologies

As for the Zetasizer NanoZS, the raw data obtained from Vasco™ is the autocorrelation function, which is an exponential decaying function with a characteristic time related to the size of the diffusing object.

## Comments on use and applicability

DLS is very suitable for size and stability analysis of particles in liquid dispersions. However, great care should be taken in interpretation of data; especially when the sample contains both μm- and small nm-size particles. For better accuracy of size-determination, it is important to obtain true values of the optical properties and viscosity of the dispersion liquid.

## References

Support documents can be downloaded from <http://www.malvern.com>, application library section.

## B. Appendix. The Sensor Dish Reader System

The hydrochemical reactivity was assessed regarding acid-base reactivity and influence on the oxygen balance using a recently developed 24-well SDR (SensorDish Reader) system (PreSens Precision Sensing GmbH, Germany) intended for use for in vitro assays (Figure B1). Determination of the acid-base reactivity is particularly important in cell media, where a buffer usually is applied to ensure pH stability in the bioassay. However, if a NM is particularly reactive, this pH buffer may be insufficient at sufficiently high NM doses. The O<sub>2</sub> reactivity may be another important parameter and relates to hydrochemical reactions that consume or liberate oxygen. Deviations in the O<sub>2</sub>-balance can be caused by different reactions including redox-reactions, protonation and deprotonation in the dispersion. These phenomena may be caused by catalytic reactions, but also dissolution, transformation of molecular speciation and precipitation in the medium under investigation.



**Figure B1. Sensor Dish Reader, examples of sensor products and illustration of the SDR measurement principle. In this study we used the 24-well Oxy- and HydroDish for O<sub>2</sub> and pH monitoring. Source: PreSens Precision Sensing GmbH, Germany.**

The pH variation was measured using the HydroDish® fluorescent sensor plate for pH detection with up to ± 0.05 pH resolution for pH 5 to 9. Measurement is not possible outside of this range.

The O<sub>2</sub> variation was measured using the OxoDish® fluorescent sensor plate for O<sub>2</sub> detection with ± 2 % air saturation resolution. The OxoDish® sensor can measure O<sub>2</sub> concentrations between 0 and 250 % saturation, corresponding to 0 to 707.6 µmol/l.

In brief, the fluorescent sensor spots are placed at the bottom of each well in the dishes. For our study, we used 24 well plates. The sensor spot contains a luminescent dye. It is excited by the SensorDish® Reader using a laser diode, placed below the multidish, which is only active when analyses are done, and the sensor luminescence lifetime is detected through the transparent bottom. The luminescence lifetime of the dye varies with the oxygen partial pressure (OxoDish®) and the pH of the sample (HydroDish®), respectively. This signal is converted to oxygen and pH values by the instrument software. The sensor plates are pre-calibrated and the calibration data are uploaded and used for the specific plates used.

## Experimental Procedure

Samples were prepared by prewetting the NMs with 0.5 % v/v ethanol and dispersion in 0.05 % w/v BSA water by probe-sonication following the generic NANOGENOTOX dispersion protocol. Chemically pre-analysed and approved Nanopure filtered water was used for the batch dispersion to ensure minimum background contamination in the test.

The incubation media included 0.5 % BSA-water, low-Ca Gambles solution and Caco2 medium. BSA water was included in the study to assess the behaviour of the NMs in the batch dispersion medium, which is the first stage in all the biological tests in NANOGENOTOX. The reactivity was tested at doses 0.32, 0.16, 0.08 and 0 mg/mL and a total volume of 2 mL was entered into each well of the SDR plates. Figure B2 illustrates the general procedure.

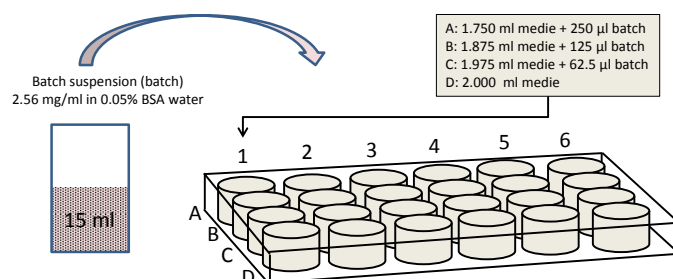


**Figure B2. Principal sketch of the dosing into the SDR plates resulting in 2 mL test medium in each well. In this way six dose-response measurements can be made in one test round.**

After 24-hours incubation, the maximum dose and control media from the pH and O<sub>2</sub> wells were retrieved by pipette, filtered through a 0.2 µm CAMECA syringe filter and centrifuged in Eppendorf tubes for 60 minutes at 20,000xG RCF using a Ole Dich table top centrifuge. NM samples were placed in the outer ring and pure reference media in the inner ring. Then the upper 1.25 mL of each filtrate from the pH and O<sub>2</sub> wells were sampled, pooled (2.5 mL) in Eppendorf tubes and stabilised with 1 mL 2 % HNO<sub>3</sub> water (sample diluted 5/7). The liquids

were then stored in darkness until sent for analyses. All vials were washed and rinsed in acid before use.

## **Data Treatment and Evaluation**

The reactivity of each NM was evaluated qualitatively from the evolution of the pH and O<sub>2</sub> over time for each NM at the four dose levels, including the blank control. The SDR pH-values were plotted directly as function of time. The data were then evaluated visually comparing the SDR values of exposed wells with that of the un-exposed control media as well the readings from the initial medium readings in each of the wells to assess if there would be any systematic offset in some of the sensors. This sensor evaluation was always done using the blank control as the assumed correct internal reference value.

For the O<sub>2</sub> analyses, the difference between time-resolved readings from "exposure doses" and the medium control ( $dO_2 = (O_{2,dose} - O_{2,medium\ control})$ ) were plotted as function of time.

For both pH and O<sub>2</sub>, if the SDR readings from the dosed media showed no difference or followed the same trend as the reference media, the NM was assumed to have negligible pH reactivity or influence on the oxygen balance through redox reactivity or dissolution.



## C. Appendix. SOP for surface charge and isoelectrical point by zetametry

### General description

Dispersion state and stability of suspensions are governed by an equilibrium between attractive (mainly van der Waals) and repulsive (electrostatic or steric) interactions. A stable suspension is obtained if repulsive interactions overcome the attractive ones, which are responsible for aggregation and subsequent sedimentation. Zeta potential is a good indicator of the magnitude of repulsive interactions between charged particles. The charge at the very surface of the particles is

not accessible and Zeta potential corresponds to the potential at the shear plane. This is the boundary between the bulk dispersant and the double layer of solvent and ions moving together with the particles, see Figure C1. The

reciprocal Debye length,  $\kappa^{-1}$ , represents the thickness of this double layer. The zeta-potential varies with pH due to protonation-deprotonation of the material surface. From colloid science, a suspension of small particles is considered stable if the zeta-potential exceed  $|30|$  mV.

For low pH (acidic medium), the surface of metal oxide (MO) materials is protonated ( $\text{MOH}_2^+$ ), i.e. positively charged. For high pH the deprotonation results in negatively charged particles ( $\text{MO}^-$ ). The pH-value at which the charge is reversed determines the so-called isoelectric point (IEP) where the dispersion is unstable. IEP can be determined by titration, but can also be measured from manually prepared different dispersions displaying the same ionic strength for various pH. The zeta potential can be highly influenced by the properties of the medium, such as ionic strength (by compression of the double layer), or adsorbing molecules or ions (especially multivalent ions).

The zeta potential ( $\zeta$ ) is not directly measurable and is calculated from the measurement of electrophoretic mobility  $U_E$  using Henry's equation:

$$U_E = \frac{2 \varepsilon \zeta f(\kappa a)}{3 \eta}$$

$\varepsilon$ : dielectric constant of medium

$\eta$ : viscosity

$\kappa$ : inverse of the Debye length, a: radius of a particle

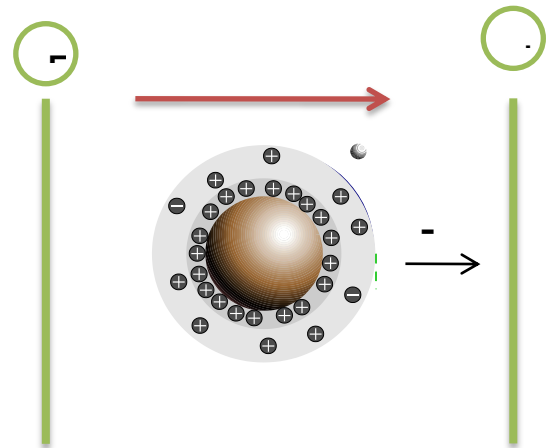


**Figure C1. scheme of charged particle in electric field applied between electrodes of zeta cell.**

$f(\kappa a) = 1.5$  for aqueous suspensions in the Smoluchowski approximation

In practice, the sample is exposed to an electric field which induces the movement of charged particles towards the opposite electrode.

## Chemicals and equipment

- HNO<sub>3</sub> (analytical grade)
- NaOH (analytical grade)
- NaNO<sub>3</sub> (analytical grade)
- Purified water (MilliQ or Nanopure water)
- Ultrasonic probe Sonics & Materials, VCX500-220V, 500 W, 20 kHz equipped with a standard 13 mm disruptor horn, or equivalent
- pH-meter with standard pH probe
- Zetasizer Nano ZS (e.g. Malvern Instruments), equipped with laser 633 nm
- Autotitrator (Malvern MPT-2) –*optional for automatic determination of IEP*
- Malvern computer software (DTS 5.03 or higher) to control the Zetasizer
- Clear, disposable zeta cells (DTS1061 - DTS1060C)

## Sample preparation

### Summary

Samples for zeta potential measurements are prepared as aqueous suspensions of 0.5 g/L for TiO<sub>2</sub> nanomaterials with constant ionic strength of 0.036 mol/L (monovalent salt) and controlled pH. They are prepared by dilution of concentrated sonicated stock suspensions of 10 g/L into pH and ionic strength controlled “buffers” prepared by addition of HNO<sub>3</sub>, NaOH and NaNO<sub>3</sub> in various proportions.

## Stock suspension preparation

20 mL of stock suspensions of 10 g/L NM in pure water are prepared as follows:

200 mg of NM is weighed and introduced in a 20 mL gauged vial (with protective gloves, mask and glasses, and damp paper towel around the weigh-scale).

- The 20 mL gauged vial is completed with ultrapure water (MilliQ®)
- The suspension is transferred into a flask suitable for sonication (a 40 mL large-neck glass flask of internal diameter 38 mm was used, height of 20 mL liquid 20 mm), making sure that all the settling material is recovered.
- The suspension is dispersed by ultrasonication for 20 min at 40 % amplitude in an ice-water bath. Probe, sample and bath are placed in a sound abating enclosure, and in a fume hood.

## Preparation of “buffer” solution

Denominated “buffer” solutions are aqueous ionic solutions of  $\text{Na}^+$ ,  $\text{H}^+$ ,  $\text{NO}_3^-$  and  $\text{OH}^-$ , designed to display the same ionic strength with a modulated pH.

- A first set of concentrated buffer solutions (0.1 mol/L of salt, various pH) are prepared by addition of  $\text{HNO}_3$ ,  $\text{NaOH}$  and  $\text{NaNO}_3$  in various proportions in ultrapure water.
- Then 20 mL of these concentrated buffers are poured into 50 mL gauged vials completed with ultrapure water, giving a new set of buffers with a salt concentration of 0.04 mol/L and a pH ranging from 1.5 to 12.5. The combination of the two buffers gives access to the necessary intermediate pH.
- By this procedure, acidic buffers contain 0.04 mol/L of  $\text{NO}_3^-$  and various ratios of  $\text{Na}^+/\text{H}^+$  as counter ions; likewise, basic buffers contain 0.04 mol/L of  $\text{Na}^+$  and various ratios of  $\text{NO}_3^-/\text{OH}^-$ .

## Preparation of suspensions for zeta potential measurements and determination of isoelectric point

In this SOP Zeta potential measurements are performed on 0.5 g/L suspensions for  $\text{TiO}_2$  samples. 5 g/L suspensions of the  $\text{TiO}_2$  samples are used right after sonication. Series of samples are prepared by addition of 400  $\mu\text{L}$  of concentrated NM suspension and 3.6 mL of 0.04 mol/L buffer solutions in a 5 mL glass flask. This leads to samples of 0.5 g/L  $\text{TiO}_2$  and a constant ionic concentration of 0.036 mol/L in monovalent salt.

For each NM, an additional sample is prepared in MilliQ or Nanopure water with the same NM concentrations, i.e. 400  $\mu\text{L}$  of concentrated NM suspension and 3.6 mL of water.

## Measurements and data treatment

### Summary

For each suspension of known pH, fixed ionic strength and fixed NM concentration, the measurements for determining the zeta potential are performed on a general purpose mode with automatic determination of measurement parameters. Three measurements are performed and averaged for reporting. For unstable samples, measurements are performed on supernatants. Zeta potentials are then plotted against pH to determine the stability domains and isoelectric points (IEP).

Equilibrium pH of the suspensions are measured and considered as pH values for the reported results. The suspension to be characterised by zetametry are inserted in Malvern patented folded capillary cells with gold electrodes (volume 0.75 to 1 mL), DTS1061. Zeta measurements (electrophoretic mobility) are performed on the “*general purpose*” mode at

25°C with automatic optimisation of laser power, voltage settings, the number of runs (10 - 100) and run duration, and repeated 3 times with no equilibration time as the sample is already at ambient temperature.

The Smoluchowski model ( $F(ka)=1.5$ ) was used, considering the high polarity of aqueous solvent, and hence a thin double layer around the particles. For the dispersant, the refractive index  $R_i$ , absorption  $R_{abs}$ , viscosity and di-electric properties considered are the ones of pure water and the table below lists the parameters used for dispersant and material properties.

**Table C1. Properties of dispersant and material used for zeta potential measurements.**

	Water (STP)	TiO <sub>2</sub>
$R_i$	1.33	2.49
$R_{abs}$		0.01
Viscosity [cP]	0.8872	-

## Data treatment

Electrophoretic mobility is measured by a combination of laser Doppler velocimetry, a technique based on the phase shift of the laser beam induced by the movement of particles under an electric field, and phase analysis light scattering (patented M3-PALS technique). In this “mixed mode measurement” (M3), the measurement consists of the application of an alternative electric field in two modes, a fast field reversal mode, and a slow field reversal mode. The light scattered at an angle 17° is combined with the reference beam and the resulting signal is treated by the computer (Figure C2). During the fast field reversal mode, the electro-osmose effect is negligible, allowing to determine an accurate mean zeta potential, whereas the slow field reversal mode helps modelling the distribution of potentials.

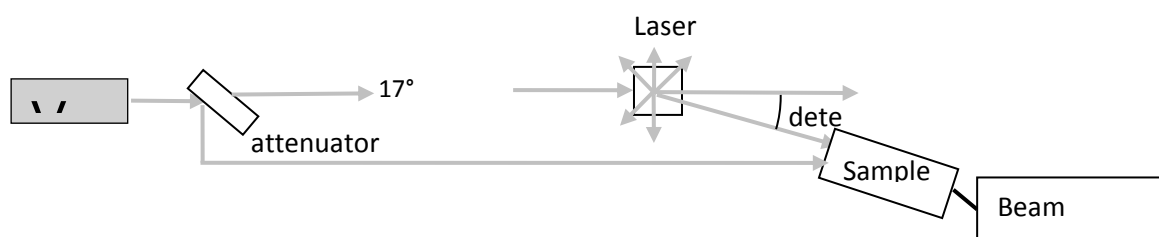


**Figure C2. Simplified scheme of optical configuration for zeta potential measurement by Zetasizer NanoZS.**

An example of the main data plots returned by DTS software from zeta potential measurements is shown in figure C3 (phase plot and corresponding electric field applied, mean zeta potential and zeta potential distribution).

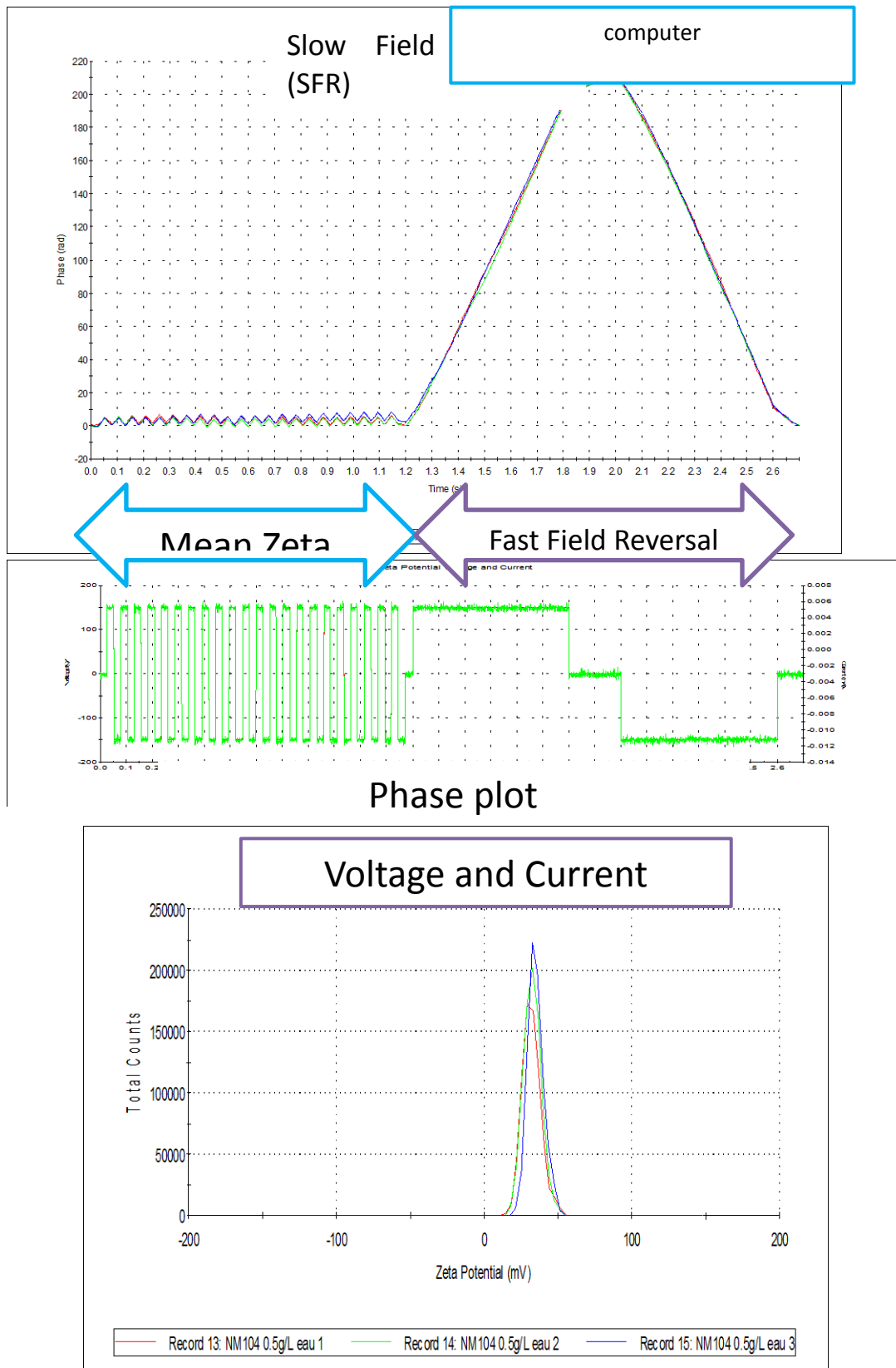


**Figure C3.** Data plots retrieved from zeta potential measurements by Nanosizer ZS, example of 3 consecutive measurements of a suspension of NM-104 (TiO<sub>2</sub>) at 0.5 g/L in pure water.

More details regarding the results of zeta potential measurements with the M3-PALS technique are available in the documentation from Malvern Instruments and can be downloaded from <http://www.malvern.com>, application library section. The reported value is the average of zeta potential values from the 3 measurements (determined during the fast field reversal step), with possible exclusion of diverging data.

## D. Appendix. SOP for Small Angle X-ray Scattering.

This appendix describes the general procedure applied at CEA/LIONS (Laboratoire Interdisciplinaire sur l'Organisation Nanométrique et Supramoléculaire) to perform Small Angle X-ray Scattering measurements and the data treatment to extract physico-chemical properties of materials. This procedure was applied to characterise the TiO<sub>2</sub> NMs as powders and in aqueous suspension.

### General description

Small-Angle X-ray Scattering is a technique based on the interaction between X-rays and electrons to probe the structure of materials. The processed data is the number of X-rays scattered by a sample as a function of angular position of a detector, see Figure D1.

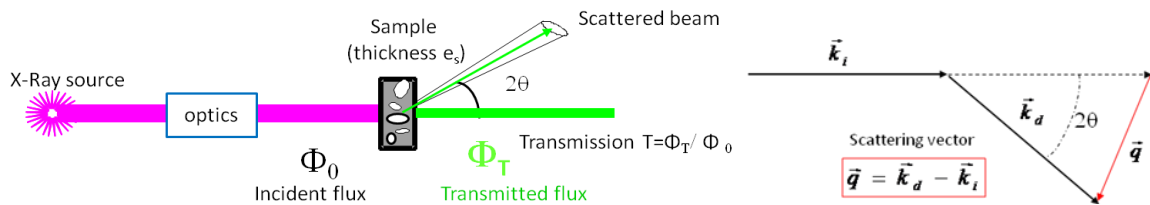


**Figure D1. Schematic set up for SAXS and physical quantities**

2D raw data images are converted into diffractograms displaying the **scattered intensity  $I$**  as a function of scattering vector  $q$  defined by:

$$q = \frac{4\pi \sin \theta}{\lambda}$$

$\lambda$  : X-ray wavelength

The experimental scattering intensity is defined as the differential scattering cross-section per unit volume of sample and can be expressed as follows:

$$I(q) = \frac{1}{V} \frac{d\sigma}{d\Omega} = \frac{n_1 C_{ij}}{\eta_2 (\varphi_0 ST) dt} \frac{1}{\Delta\Omega} \frac{1}{e}$$

$\sigma$  : scattering cross-section

$V$  : volume of sample

$C_{ij}$ : number of counts detected on a pixel  $ij$  during  $dt$

$\eta_1$ : detector quantum efficiency when measuring the direct beam

$\eta_2$ : detector quantum efficiency for the count  $C_{ij}$

$(\varphi_0 ST)$ : flux (in detector unit counts/s) integrated over the whole beam transmitted by the sample

T: transmission of the sample

$\Delta\Omega$ : solid angle covered by one pixel seen from the center of the sample ( $\Delta\Omega = p^2/D^2$  with  $p$  the pixel size and  $D$  the sample to detector distance)

The intensity is then expressed in **absolute scale** (in  $cm^{-1}$ ) to be independent of the experimental set up parameters (X-ray wavelength, experimental background, time for acquisition, sample thickness, etc.).

General theorems of experimental physics have been developed to extract different properties of nanostructured material from the diffractograms, such as shape of nanoparticles, surface area, interactions occurring, etc.  $I(q)$  curves can also be theoretically calculated from assumed nanostructures to fit the experimental curves.

In the simple case of binary samples, the scattering intensity is proportional to:

- the electronic contrast, more precisely the square of scattering length density difference between the two materials  $(\Delta\rho)^2$ ,
- the concentration of the scattering object (in volume fraction), in case of suspensions for example.

Ultra Small Angle X-ray Scattering (USAXS) measurements give access to X-ray scattering data for a range of smaller  $q$  and then complement the SAXS diffractograms. It requires a specific and very precise set-up, different from the one used for SAXS.

## Equipment

The experimental set up (X-ray source, optical elements, detectors, etc.) and the procedure for absolute scaling of data has been thoroughly described by Zemb (Zemb et al., 2003) and Né (Né et al., 2000).

## Apparatus

The main set up components used for SAXS and USAXS experiments at CEA/LIONS are listed below:

- X-ray generator: Rigaku generator RUH3000 with copper rotating anode ( $\lambda = 1.54 \text{ \AA}$ ), 3kW
- Homemade optic pathways and sample holders (with two channel-cut Ge (111) crystals in Bonse/Hart geometry for USAXS set up (Lambard et al., 1992)
- Flux measurement for SAXS set up: pico amperemeter Keithley 615
- Flux measurement for USAXS set up: DonPhysik ionisation chamber
- Detector for SAXS set up: 2D image plate detector MAR300
- Detector for USAXS set up: 1D high count rate CyberStar X200 associated to a scintillator/ photomultiplier detector.



All experimental parameters are monitored by computer by a centralised control-command system based on TANGO, and interfaced by Python programming. 2D images are treated using the software *ImageJ* supplemented with some specific plugging developed at CEA/LIONS by Olivier Taché (Taché, 2006).

## Calibration

A sample of 3 mm of Lupolen® (semi crystalline polymer) is used for the calibration of the intensity in absolute scale, the maximum intensity being adjusted to  $6 \text{ cm}^{-1}$ .

A sample of 1 mm of octadecanol is used for the calibration of the  $q$  range (calculation of sample-to-detector distance), the position of the first peak standing at  $0.1525 \text{ \AA}^{-1}$ .

Calibrations in intensity and in  $q$  range are performed before each series of measurements.

## Sample preparation

Almost any kind of material can be analysed by SAXS, whether as a powder, a colloidal suspension, a gel, or even self-supported hybrid materials, as long as the sample prepared meets some requirements of transmission and scattering properties.

Depending on the X-ray absorption coefficient of the material and its scattering properties, the sample thickness has to be adjusted to get a transmission as close as possible to the target transmission of 0.3 (optimal absorption/transmission ratio).

The sample thickness  $e$  is directly linked to the transmission  $T$  by the following equation:

$$e = -\frac{1}{\mu} \ln(T)$$

$\mu$ : X-ray absorption coefficient of the material,

$T$ : transmission,  $T = \text{transmitted flux} / \text{incident flux of the direct beam}$

If not self-supported (liquids, powders or gel), the material to be analysed is inserted in a cell, which can be made of glass (capillary), or X-ray transparent material such as Kapton® (polyimide). A measurement of the empty cell is performed and subtracted as a background for the sample measurement. See Figure D2 for examples of cells used at CEA/LIONS.

## Powders

The coefficient of absorption depends on the material and on the energy. For the Cu K $\alpha$  emission (8 keV) that is used on our setup, the coefficient for TiO<sub>2</sub> is  $\mu_{\text{TiO}_2} = 470 \text{ cm}^{-1}$ . The optimal sample thickness (equivalent thickness of dense material) to get a transmission of 0.3 is  $25 \text{ \mu m}$  for TiO<sub>2</sub>.

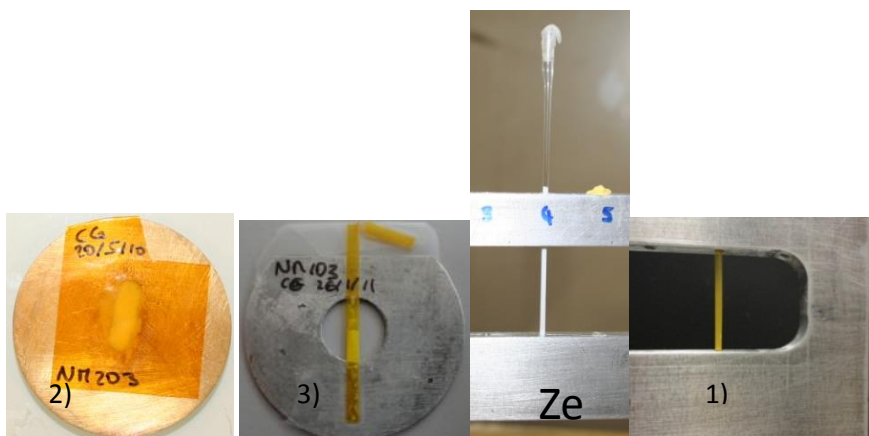


**Figure D2. Examples of different type of cells used for SAXS measurements, 1) double sticky kapton® cell for powders, 2) 1.5 mm flattened polyimide capillary for powders, 3) 1.5 mm glass capillary for powder or liquid samples, 4) 1.5 mm polyimide capillary for powder or liquid samples.**

The TiO<sub>2</sub> powder samples were prepared between two sticky kapton® films pressed on a 0.4 mm brass cell (typical thickness of dense material around 30 µm). However, it was inferred that the presence of glue may affect the calculation of specific surface area of powders. Therefore, in a subsequent step, the TiO<sub>2</sub> powder samples were measured in a flattened polyimide capillary, mounted on a circular sample holder. The typical equivalent thickness of dense material obtained is 30 µm.

### **Aqueous suspensions**

The usual thickness of aqueous samples for SAXS measurement is 1mm with an acquisition time of 1 hour. Dispersions for analysis are typically produced by sonication in a dispersion medium. The concentration required for analysis depends on the relative scattering length densities between particles and dispersion medium, and the density of materials. The sample must be stable within the time-frame of the measurement.

Typical concentration in oxide for NANOGENOTOX suspensions is 3 g/L. Since the scattering length density of silicon dioxide is relatively low, higher concentrations were used when possible.

### **Measurements**

In order to calculate the sample transmission, the flux of incident and transmitted beam are measured and averaged over 200 s before running the SAXS measurement. The time of acquisition necessary for SAXS experiment depends on the sample properties. For TiO<sub>2</sub> powders, two measurements were performed: one with a short time of 200 s or 150 s to get unsaturated data for small angles (low q), and one for a long time of 1800 s to get data in the high q region with low signal/noise ratio.

For aqueous suspensions prepared for NANOGENOTOX, SAXS measurements were performed in kapton capillaries of internal thickness 1.425 mm and run for 3600 s, leading to transmissions of about 0.25. USAXS measurements were performed in 1 mm or 1.5 mm non-sticky double kapton cells, cell types are shown in Figure D2.

## Data treatment

Raw data, translated into intensity as a function of the scattering vector  $q$ , are first normalised by parameters of the experiments such as acquisition time, sample thickness and calibration constants determined using reference samples, thus expressing data in absolute scale ( $\text{cm}^{-1}$ ). Backgrounds are then subtracted. To get continuous diffractograms for the whole  $q$  range SAXS data obtained for short and long times are combined with USAXS data.

For powder samples, the Porod law is applied to extract specific surface areas of raw materials. Data from suspensions are fitted with a model describing fractal aggregates of primary particles. In this model, the whole  $q$  range is divided into sections reflecting different structural levels in the sample, and fitted by local Porod and Guinier scattering regimes. Intensity average parameters are then determined such as radius of gyration for the primaries and for the aggregates, and a fractal dimension for the aggregates. Invariants are calculated, which give a correlation between the sample concentration and the specific surface area obtained in suspension.

## Raw data treatment

### SAXS data

#### *Radial averaging of 2D image (ImageJ)*

2D images from the detector are converted into Intensity =  $f(\text{scattering vector } q)$  graphs by the software ImageJ together with SAXS plugging. The process follows mainly these steps:

- Determination of the centre coordinates (direct beam position)
- Application of a mask to remove pixels corresponding to the beam stop and around the photodiode
- Radial averaging of the intensity, knowing pixel size, sample-detector distance and wavelength (example of parameters in Figure D3), conversion of pixel position into scattering vector  $q$ , and creation of a .rgr file containing  $I(q)$  data.

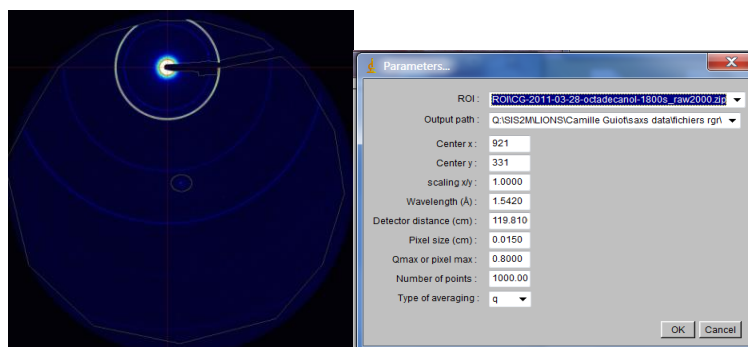


Figure D3. Example of raw 2D image (octadecanol) and parameters used for radial averaging with ImageJ

### ***Absolute scaling of $I(q)$ (pySAXS)***

In order to scale the data to the absolute scale in  $\text{cm}^{-1}$ ,  $I(q)$  data generated by *ImageJ* as .rgf files are treated by an in-house program called *pySAXS* and based on python programming.

The scaling involves a subtraction of the detector background and normalisation by exposition time, sample transmission, sample thickness and K constant. The K constant is calibrated with Lupolen® sample and allows conversion of intensity in photons into absolute intensity in  $\text{cm}^{-1}$ . An example of parameters used for the scaling is shown in Figure D4.

The subtraction of the empty cell signal and normalisation by the sample thickness can be done in a subsequent step.

### **USAXS data**

Raw USAXS data are generated as intensity vs angle data in .txt files. Data treatment is achieved using *pySAXS* and involves the following steps:

- Subtraction of the “rocking curve” (signal with empty cell) normalised by the intensities at  $0^\circ$  (transmission).
- Desmearing, taking into account the effective size of the “punctual” detector (cf reference 0)
- Conversion of angle into  $q$  range
- Normalisation by the sample thickness.

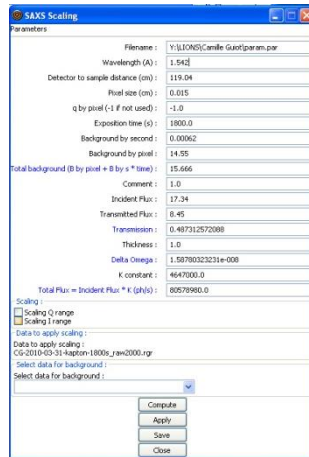


Figure D4. Example of SAXS scaling parameter file from PySAXS software

## Data analysis

General theorems of X-ray scattering have been developed to analyze SAXS data. Here are presented some simple laws for **binary systems** (two phase samples) that may be of use in NANOGENTOX framework.

### Porod's Law

In the high  $q$  range, sample diffractograms display an intensity decreases in a  $q^{-4}$  trend, called the "Porod region". This region corresponds in the "real space" to the scale of the interfaces (for smooth interfaces).

Therefore, for a binary sample, the asymptotic limit of the so-called "Porod's plateau", when data are represented in  $Iq^4$ , is related to the total quantity of interface  $\Sigma$  (in  $m^2/m^3$ ) between the two phases, as follows:

$$\Sigma [m^{-1}] = \frac{\lim_{plateau} (I \cdot q^4)}{2\pi(\Delta\rho)^2}$$

where  $\Delta\rho$  is the difference in scattering length density between the two phases. For a binary sample of **known thickness**, the volume fraction of a material  $\varphi_A$ , its specific surface area  $S_A/V_A$  (surface developed/ volume of A in the binary sample) and  $\Sigma$  are linked by the following relation:

$$\Sigma [m^{-1}] = \frac{S_A}{V_A} \varphi_A$$

For example, for a suspension of oxide in water, the determination of Porod plateau gives access to the concentration of the sample if the specific surface area of particles suspended is known (and vice versa).

## Specific surface area determination from SAXS on powders

To treat raw SAXS data and get absolute intensities, the intensity by the thickness of the scattering material need to be normalised. However, for powder samples, the sample thickness is not well defined and cannot be precisely controlled as it depends on the powder compaction and the different scales of porosity, see Figure D5. To elude this problem, a model system is used, considering the effective thickness of material crossed by X-rays, called  $e_B$ , corresponding to an equivalent thickness if all the material would be arranged in a fully dense (no inner or outer porosity) and uniform layer.

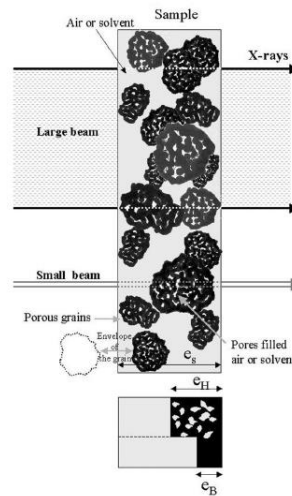


**Figure D5. Schematic representation of a powder sample for SAXS measurement, and definitions of equivalent thick-nesses  $e_H$  and  $e_B$ .**

The sample transmission is related to this equivalent thickness by the following equation:

$$e_B = -\frac{1}{\mu} \ln(T_{\text{exp}})$$

where  $\mu$  is the material absorption coefficient for X-Ray ( $\mu_{\text{TiO}_2} = 470 \text{ cm}^{-1}$ ) and  $T_{\text{exp}}$  is the **experimental transmission** (transmitted flux  $\Phi_T$ / incident flux  $\Phi_0$ ), i.e. transmission of the sample with regard to the transmission of the empty cell (kapton® alone, empty capillary, etc). The intensity scaled by this thickness  $e_B$  is called  $I_1$ . The Porod's law can then be applied for  $I_1$  to access the specific surface area of the powder.

Specific surface areas of powders are determined on the Porod plateau from the equation. The values in  $\text{m}^{-1}$  are then converted into  $\text{m}^2/\text{g}$  taking into account the material density  $\rho_m$ :

$$\sum \left[ \frac{\text{m}^2}{\text{g}} \right] = \frac{\sum [\text{m}^{-1}]}{\rho_m \left[ \frac{\text{g}}{\text{m}^3} \right]}$$

If no uncertainty is considered for the material density, the relative uncertainty of the specific surface area calculated is directly linked to the determination of the Porod plateau:

$$\frac{\Delta \Sigma[\frac{m^2}{g}]}{\Sigma[\frac{m^2}{g}]} = \frac{\Delta \Sigma[m^{-1}]}{\Sigma[m^{-1}]} = \frac{\Delta \lim(I)_1 q^4}{\lim(I)_1 q^4}$$

However, if we consider a quantifiable uncertainty on the material density, it is passed on to the calculated sample thickness  $e_B$  and the theoretical scattering length density of the material. Finally, the relative uncertainty on the specific surface area is increased by the uncertainty on the material density:

$$\frac{\Delta \Sigma[m^{-1}]}{\Sigma[m^{-1}]} = \frac{\Delta \lim(I)_1 q^4}{\lim(I)_1 q^4} + \frac{\Delta \rho_m}{\rho_m}$$

The uncertainty on the material density even contributes twice when the specific surface area is expressed in  $m^2/g$ :

$$\frac{\Delta \Sigma[\frac{m^2}{g}]}{\Sigma[\frac{m^2}{g}]} = \frac{\Delta \lim(I)_1 q^4}{\lim(I)_1 q^4} + 2 \frac{\Delta \rho_m}{\rho_m}$$

All specific surface area results, together with their uncertainty calculations are presented below. Errors on the Porod's plateaus have been determined manually for each diffractogram, and the uncertainty on the material density is considered to be about 5 %.

### Invariant theorem

When  $I(q)$  can be extrapolated to zero values of  $q$  (no interaction at a large scale, i.e. a flat signal for low  $q$ ) and at infinite  $q$  (usually with the Porod law), the following invariant theorem can be applied:

$$e = -\int_0^{\infty} I_{Abs} q^2 dq = 2\pi^2 \varphi(1-\varphi)(\Delta\rho)^2$$

This implies that the invariant  $Q$  is a constant for a defined composition, which gives access to the volume fraction  $\varphi$ , or to the evolution of interactions for a fixed composition.

### Guinier regime

For dilute samples of monodisperse objects (negligible position correlation between scattering objects, i.e. structure factor 1), the intensity in the low  $q$  region ( $qR_G \ll 1$ ) can be approximated to:

$$I(q) \approx A \left( 1 - \frac{(qR_G)^2}{3} + Bq^3 \right)$$

which gives access to the radius of gyration of the particles  $R_G$  with the slope of  $\ln(I)=f(q^2)$ .

## Data fits

Assuming values of parameters such as volume fraction, size, shape and polydispersity of scattering objects for a model sample, it is possible to calculate theoretical curves of  $I(q)$ . Therefore, the adjustment of such parameters to fit experimental curves allows for the modelisation of the sample properties.

## Unified model of aggregates in suspension for SAXS data treatment

A unified fitting approach, developed by Beaucage et al. (Beaucage et al., 1996; Kammler et al., 2004; Kammler et al., 2005) was used to treat X-ray scattering data from  $\text{SiO}_2$  suspensions composed of aggregates of primary particles. In this model, the whole  $q$  range is divided into sections reflecting different structural levels in the sample, and fitted by local Guinier, fractal and Porod scattering regimes, see Figure D6.

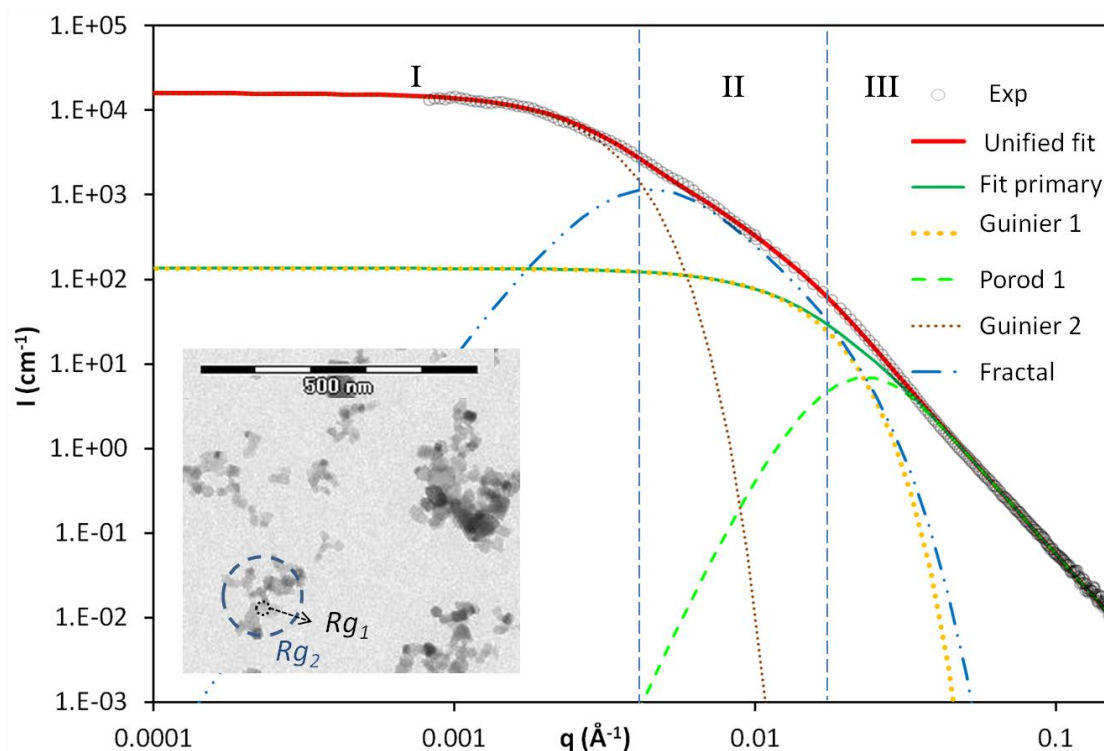


**Figure D6.** Example of SAXS diffractogram (NM-105, a  $\text{TiO}_2$ , suspension sonicated at pH 2 as circles) illustrating the unified fit (solid red line) and its components prevailing in each  $q$ -domain (dashed-dotted lines). Insert of TEM micrograph (by CODA-CERVA) illustrating the gyration radius of primary particles ( $R_{g1}$ ) and aggregates ( $R_{g2}$ ) used in the model. Exp = experimental data.



The scattering vector  $q$  is homogeneous to the reverse of a length, so large  $q$  values actually corresponds to small observation scale in the direct space.

For a smooth surface of primary particles, **at large  $q$**  (the scale of interfaces) the intensity decays as a power-law of  $q^{-4}$  defining the Porod regime:

$$I_{Porod1}(q) = B_1 q^{-4}$$

The coefficient  $B_1$  is directly linked to the specific surface area of the primary particles:

$$B_1 = 2\pi N(\Delta\rho)^2 S$$

with  $N$  and  $S$  respectively the number density and the average surface area of primary particles and  $\Delta\rho$  the difference of scattering length density between scattering object ( $\text{SiO}_2$ ) and medium (water).

This Porod regime is preceded **at lower  $q$**  by a Guinier regime, signature of the size of primary particles, and is described by:

$$I_{Guinier1}(q) = G_1 \exp\left(\frac{-q^2 Rg_1^2}{3}\right)$$

The sum of these two regimes (**Fit primary** in Figure D6) would describe scattering intensity resulting from individual uncorrelated primary particles, *i.e.* if they were perfectly dispersed and non-aggregated. It prevails in the large  $q$  range (domain III, Figure D6). The upturn of the intensity at small  $q$  is due to the association of primary particles into aggregates of finite size.

These aggregates also present a finite size and inner structure. Thus, a second Guinier regime is associated with the structural size of aggregates and prevails in the domain I defined in the Figure D6:

$$I_{Guinier2}(q) = G_2 \exp\left(\frac{-q^2 Rg_2^2}{3}\right)$$

The coefficients  $G_1$  and  $G_2$  are defined by:

$$G_i = N_i(\Delta\rho)^2 V_i^2$$

where  $N_i$  and  $V_i$  are respectively the number density and volume of object  $i$  (primary particle or aggregate).

These two Guinier regimes give access to the radii of gyration of the primary particles,  $Rg_1$  and of the aggregates,  $Rg_2$ .

The ratio of G1 to B1 is a measure of the anisotropy of the primary particles since

$$\frac{G_1}{B_1} \propto \frac{V^2}{2\pi S}$$

with  $V$  the volume of the particles and  $S$  their surface.

**For intermediate  $q$  range** between the scale of aggregates and the scale of primary particles (domain II in Figure D6), the intensity decays with a slope typical for the fractal regime of an aggregate and described by a power-law linked to the mass-fractal dimension  $D_f$ :

$$I_{Fractal}(q) = B_2 q^{-D_f}$$

The coefficient  $B_2$  is linked to  $D_f$ ,  $G_2$  and  $Rg_2$  by:

$$B_2 = \frac{G_2}{Rg_2^{D_f}} D_f \Gamma\left(\frac{D_f}{2}\right)$$

$\Gamma$  is the gamma function.

The fractal dimension  $D_f$  is a measure of the degree of ramification and density of aggregates (value between 1 and 3), see Hyeon-Lee et al., 1998.

An average number of primary particles per aggregate can be derived from the Guinier coefficients:

$$N_{part/agg} = \frac{G_2}{G_1}$$

The global unified fit is obtained by addition of the different terms (see Bushell et al., 2002).

To fit the experimental diffractograms, the total model curve

$$I(q) = I_{Porod1}(q) + I_{Guinier1}(q) + I_{Fractal}(q) + I_{Guinier2}(q)$$

is plotted and parameters ( $B_1$ ,  $G_1$ ,  $G_2$ ,  $D_f$ ,  $Rg_1$  and  $Rg_2$ ) are adjusted manually so that the model fits the best the experimental data. Three parameters are there to describe the primary particles, and three are also necessary to describe the aggregates structures of primary particles. Also in TEM three independent parameters were required to describe the aggregates.

Some geometrical restrictions have to be respected ( $D_f < 3$  ; volume of  $N$  primaries < volume of aggregate, total surface area of primaries cannot be smaller than the corresponding surface area for ideal spheres).

All SAXS data are treated to be represented in the absolute scale (intensity in  $\text{cm}^{-1}$ ). Therefore quantitative measurements are accessible and through the use of the invariant theorem and it is possible to calculate the exact concentration of samples, and then correlate the specific surface area developed in the suspension to the specific surface area of raw materials obtained from powder samples.

### Data and parameters determined by unified fit model for SAXS on $\text{TiO}_2$ suspensions

**Table D1.  $\text{TiO}_2$  suspensions in acidic medium.**

$\text{TiO}_2$ NM	NM-102	NM-103	NM-104	NM-105
$Rg_1$ (Angstrom)	64	130	130	130
$G_1$	33	140	122.5	135
$B_1$	7.20E-06	7.00E-06	7.00E-06	5.63E-06
$Rg_2$ (Angstrom)	2800	700	800	650
$G_2$	660000	15750	21000	350000
$D_f$	3	2.2	2.3	2.45
$B_2$	0.001	0.519	0.271	0.100
$N_{\text{part/agg}}$	20000.0	112.5	171.4	116.7
$V N_{\text{part}}/V_{\text{agg}}$	0.24	0.72	0.74	0.93
Invariant from fit ( $\text{cm}^{-4}$ )	7.59E+20	1.04E+21	9.44E+20	8.77E+20
Volumic fraction of NM in suspension	6.28E-04	8.58E-04	7.81E-04	7.26E-04
Suspension concentration from invariant (g/L)	2.66	3.63	3.31	3.07
Specific surface in suspension from Porod ( $\text{m}^{-1}$ ) (Sparticles/Vsuspension)	1.87E+05	1.82E+05	1.82E+05	1.46E+05
Specific surface of NM from invariant and Porod ( $\text{m}^2/\text{g}$ )	70.41	50.08	55.01	47.60
Theoretical concentration from weighing (g/L)	3.39	3.49	3.42	3.39
Specific surface area of NM determined by SAXS on powder	65.6	51.1	52.4	47

## References

1. T. Zemb, O. Taché, F. Né, and O. Spalla; "A high-sensitivity pinhole camera for soft condensed matter"; J. Appl. Crystal., 36, 800-805, **2003**.
2. F. Né, I. Grillo, O. Taché, and T. Zemb.; "From raw image to absolute intensity: Calibration of a guinier-mering camera with linear collimation"; J. de Physique IV, 10(P10), 403-413, **2000**.
3. O. Spalla, S. Lyonnard, and F. Testard; "Analysis of the small-angle intensity scattered by a porous and granular medium"; J. Appl. Crystal., 36, 338-347, **2003**.
4. J. Lambard, P. Lessieur and Th. Zemb; "A triple axis double crystal multiple reflection camera for ultra small angle X-ray scattering"; J. de Physique I France, 2 , 1191-1213, **1992**. Lambard, J.; Lesieur, P.; Zemb, T., A triple axis double crystal multiple reflection camera for ultra small angle X-ray scattering. J. Phys. I France 1992, 2 (6), 1191-1213.
5. O. Taché; « Une architecture pour un système évolutif de contrôle commande d'expériences de physique », Engineer thesis, **2006**, available at <http://iramis.cea.fr/sis2m/lions/tango/tango-ds/memoire.pdf>
6. Beaucage, G., Small-Angle Scattering from Polymeric Mass Fractals of Arbitrary Mass-Fractal Dimension. J. Appl. Crystal. **1996**, 29 (2), 134-146.
7. Kammler, H. K.; Beaucage, G.; Mueller, R.; Pratsinis, S. E., Structure of Flame-Made Silica Nanoparticles by Ultra-Small-Angle X-ray Scattering. Langmuir **2004**, 20 (5), 1915-1921.
8. Kammler, H. K.; Beaucage, G.; Kohls, D. J.; Agashe, N.; Ilavsky, J., Monitoring simultaneously the growth of nanoparticles and aggregates by in situ ultra-small-angle x-ray scattering. J. Appl. Physics **2005**, 97 (5), 054309-11.
9. Hyeon-Lee, J.; Beaucage, G.; Pratsinis, S. E.; Vemury, S., Fractal Analysis of Flame-Synthesized Nanostructured Silica and Titania Powders Using Small-Angle X-ray Scattering. Langmuir **1998**, 14 (20), 5751-5756.
10. Bushell, G. C.; Yan, Y. D.; Woodfield, D.; Raper, J.; Amal, R., On techniques for the measurement of the mass fractal dimension of aggregates. Advances in Colloid and Interface Science **2002**, 95 (1), 1-50.
11. Porod, G.; Glatter, O.; Kratky, O., General theory: Small-angle X-ray scattering. Academic Press ed.; Academic Press: New York, **1982**.

## E. Comparative overview of the TiO<sub>2</sub> NMs

The table below is a summary of the data given as an over in tables 59 to 64 in the main report and it allows a comparison of the TiO<sub>2</sub> NMs at a glance

Physico-chemical Properties and Material Characterization (from OECD list) method	NM characterised					
	NM-100	NM-101	NM-102	NM-103	NM-104	NM-105
Homogeneity DLS	-	-	Repeated DLS studies were performed between vials and within vials			
			NM-102 tends to sediment quickly and no stable dispersion could be obtained; the results are thus not conclusive	The reproducibility within vials (tested on 2 vials) is of a few percent. The systemic variation of the results from different laboratories for different vials is higher than 15%.	The observed variability between and within the vials is very low (2-3%), which demonstrates very good homogeneity of the material.	The observed variability within and between vials is very low, only a few percent.
Agglomeration / aggregation DLS	Ultra-pure water dispersion Z-average (nm): 228.6, Pdl: 0.145	-	Ultra-pure water dispersion (intra vial study)			
			Z-average (nm): 442.6. ± 76.6, Pdl: 0.428 ± 0.058	Z-average (nm): 113.8 ± 1.8, Pdl: 0.252 ± 0.007 Z-average (nm): 132.3 ± 7.3, Pdl: 0.187 ± 0.066	Z-average (nm): 128.3 ± 0.8, Pdl: 0.222 ± 0.003 Z-average (nm): 125.3 ± 1.7, Pdl: 0.210 ± 0.011	Z-average (nm): 124.5 ± 3.9, Pdl: 0.172 ± 0.020
			Ultra-pure water dispersion (inter vial study)			
			Z-average (nm): 408.9 ± 23.2, Pdl: 0.427 ± 0.012	Z-average (nm): 113.2 ± 3.25, Pdl: 0.242 ± 0.018 Z-average (nm): 119.6 ± 11.0, Pdl: 0.224 ± 0.033	Z-average (nm): 128.6 ± 1.3, Pdl: 0.221 ± 0.004 Z-average (nm): 126.5 ± 2.7, Pdl: 0.214 ± 0.013	Z-average (nm): 130.4 ± 4.5, Pdl: 0.141 ± 0.006
SAXS/USAXS	-	Primary particle size: Equivalent diameter for spheres: 8 nm	Gyration radius of primary particles and aggregates 2xRg <sub>1</sub> :			
			12.8 nm	26 nm	26 nm	26 nm
			2xRg <sub>2</sub> : 560 nm, fractal dimension D <sub>f</sub> : 3, number N <sub>part/agg</sub> of particles per aggregate: 20000	2xRg <sub>2</sub> : 140 nm, fractal dimension D <sub>f</sub> : 2.2, number N <sub>part/agg</sub> of particles per aggregate: 113	2xRg <sub>2</sub> : 160 nm, fractal dimension D <sub>f</sub> : 2.3, number N <sub>part/agg</sub> of particles per aggregate: 171	2xRg <sub>2</sub> : 130 nm, fractal dimension D <sub>f</sub> : 2.45, number N <sub>part/agg</sub> of particles per aggregate: 117
TEM	Aggregates : size from 30 to 700 nm	Aggregates: size from 10 to 170 nm.	Individual crystallite sizes typically smaller than 50 nm Aggregates with size in the	Primary particles: size from 20 to 100 nm Aggregates : size from 40 to 400	Primary particles: size from 8 to 200 nm	Agglomerates and aggregates tend to have a fractal-like structure. Primary particles have a spherical,

			range of 100-500 nm.	nm Low sphericity and angular aggregates Ferret min: 46.5 (2641) nm Ferret max: 75.9 (2641) nm	Aggregates : size from 20 to 500 nm Low sphericity and sub-angular aggregates Ferret min: 41.2 (3739) nm Ferret max: 68.7 (3739) nm	ellipsoidal or cuboidal structure. Primary particles sizes: 10-45 nm.
<b>Water solubility</b>  SDR (24-hour acellular <i>in vitro</i> incubation test) The 24-hour dissolution ratio was measured in three different media: 0.05 % BSA in water, Gambles solution and Caco2 media.	NM-100 is soluble in 0.05 % BSA in water and in Caco2 medium. Al impurities were detected in Caco2 media only, suggesting that the solubility behaviour of the impurities and NM-100 depends on the medium.	NM-101 is slightly soluble in Caco2 media and the Al impurity is soluble in all media. The dissolved amounts vary considerably with medium, as does the relative quantity of dissolved Al impurities compared with dissolved Ti, suggesting that the solubility behaviour of the impurities and NM-101 depends on the medium.	NM-102 is slightly soluble in Gambles solution and Caco2 medium. The solubility behaviour of the impurities and NM-102 varies and depends on the medium.	NM-103 is slightly soluble in Caco2 media and Al and Si impurities are soluble in all media. The amounts vary considerably with medium, as does the relative amounts of dissolved Al and Si impurities compared with dissolved Ti, suggesting that the solubility behaviour of the impurities and NM-103 depends on the medium.	NM-104 is slightly soluble in Caco2 media. The amounts vary considerably with medium, as does the relative amounts of dissolved Al impurities compared with dissolved Ti, suggesting that the solubility behaviour of the impurities and NM-104 depends on the medium.	NM-105 is slightly soluble in Caco2 media. No impurities were detected in any medium.
<b>Crystalline phase</b> XRD	Anatase	Anatase	Anatase	Rutile	Rutile	Anatase and rutile 88.2 : 11.8 86.36 : 13.64 81.5 : 18.5
<b>Dustiness</b>  Small rotating drum  Vortex shaker method	-	Inhalable dustiness index: 728 ± 10 mg/kg Mass respirable (mg/kg): 24 ± 9	Inhalable dustiness index: 268 ± 39 mg/kg Mass respirable (mg/kg): 15 ± 2	Inhalable dustiness index: 9185 ± 234 mg/kg Mass respirable (mg/kg): 323 ± 166	Inhalable dustiness index: 3911 ± 235 Mass respirable (mg/kg): 38 ± 166	Inhalable dustiness index: 1020 ± 20 Mass respirable (mg/kg): 28 ± 10
	Mass respirable (mg/kg): 1500 ± 0.00133	Mass respirable (mg/kg): 5600 ± 0.005	Mass respirable (mg/kg): 9200 ± 0.00825	Mass respirable (mg/kg): 19000 ± 0.017	Mass respirable (mg/kg): 6400 ± 0.00567	Mass respirable (mg/kg): 11000 ± 0.00966
<b>Crystallite size</b> SAXS/USAXS  XRD	-	Primary particle size: Equivalent diameter for spheres: 8 nm	Primary particle size: Equivalent diameter for spheres: 22 nm. 2xRg <sub>1</sub> is 12.8nm	Primary particle size: Equivalent diameter for spheres: 28 nm 2xRg <sub>1</sub> is 26 nm	Primary particle size: Equivalent diameter for spheres: 27 nm 2xRg <sub>1</sub> is 26 nm	Primary particle size: Equivalent diameter for spheres: 30 nm 2xRg <sub>1</sub> is 26 nm
	57 nm (Scherrer eq.) > 80 nm (Scherrer eq.) <100 nm (Scherrer eq.) 62 nm (TOPAS) <100 nm (TOPAS, IB) <100 nm (TOPAS, FWHM) 168 nm (Fullprof)	5, 7, 8 nm (Scherrer eq.) 7 nm (TOPAS, IB) 7 nm (TOPAS, FWHM) 5 nm (TOPAS) 5 nm (FULLPROOF)	18, 21, 23 nm (Scherrer eq.) 26 nm (TOPAS, IB) 28 nm (TOPAS, FWHM) 16 nm (TOPAS) 18 nm (Fullprof)	20, 26 nm (Scherrer eq.) 25 nm (TOPAS, IB) 28 nm (TOPAS, FWHM) 19 nm (TOPAS) 20 nm (Fullprof)	21, 27 nm (Scherrer eq.) 25 nm (TOPAS, IB) 29 nm (TOPAS, FWHM) 19 nm (Scherrer eq.) 20 nm (TOPAS) 19 nm (Fullprof)	Anatase 32, 22, 27 nm Rutile 40, 62 nm (Scherrer eq.) Anatase 27 nm Rutile 88 nm (TOPAS, IB) Anatase 31 nm Rutile 123 nm (TOPAS, FWHM)
<b>Representative TEM picture(s)</b> TEM	Aggregates with dense, complex structure	Aggregates with complex, fractal-like structure	Nanocrystalline anatase aggregates with individual particles typically smaller than 50 nm.	NM-103 consists mainly of small aggregates. Single particles are rarely detected.	Aggregates with fractal structure. Single primary particles with elongated and rounded shape often detected	Primary particles with a circular or slightly elongated shape. Aggregates with complex structure.
<b>Particle size distribution</b>	Primary particles: size from 50 to 90 nm Primary particle size: 150	Primary particle size: 6 nm	Primary particle size: 21 ± 10 nm (median of 1395)	Primary particle size: 26 ± 10 nm (median of 1317)	Primary particle size: 26 ± 10 nm (median of 1099)	Primary particle size: 21 ± 9 nm (median of 1421) / Rutile: 15 nm; anatase: 20.5 ± 58.6 / 24 ± 5 nm

TEM	nm	Primary particle size: 5 nm	Aggregates with fractal structure can be observed. Aggregates have a size in range of 20-500 nm.	Small, elongated, prismatic primary particles with an aspect ratio 1.7 / 1.82		(median of 105) Small, elongated, prismatic primary particles with an aspect ratio 1.36
	Number in % of particles smaller than 100 nm, 50 nm and 10 nm:					
	<100 nm – 27.1 %, <50 nm – 12.3 % <10 nm – 1.7 %	<100 nm – 95.2 %, <50 nm – 77.3 % <10 nm – 10.7 %	-	<100 nm – 51.8 %, <50 nm – 12.7 % <10 nm – 0.1 %	<100 nm – 53.3%, <50 nm – 12.1 % <10 nm – 0.1%	-
DLS	Ultra-pure water dispersion: Z-average (nm): 228.6, Pdl: 0.145	-	Ultra-pure water dispersion (intra vial study) [results in nm]			
			Z-average: 442.6 ± 76.6, Pdl: 0.428 ± 0.058, FWHM peak width: 460.3 ± 232.7	Z-average: 113.8 ± 1.8, Pdl: 0.252 ± 0.007, FWHM peak width: 74.0 ± 5.7 Z-average: 112.6 ± 4.7, Pdl: 0.232 ± 0.022, FWHM peak width: 73.1 ± 16.4 Z-average (nm): 132.3 ± 7.3, Pdl: 0.187 ± 0.066	Z-average: 128.3 ± 0.8, Pdl: 0.222 ± 0.003, FWHM peak width: 95.9 ± 10.9 Z-average: 128.9 ± 1.8, Pdl: 0.222 ± 0.005, FWHM peak width: 84.4 ± 8.6 Z-average: 125.3 ± 1.7, Pdl: 0.210 ± 0.011, FWHM peak width: 82.7 ± 5.5	Z-average: 124.5 ± 3.9, Pdl: 0.172 ± 0.020, FWHM peak width: 69.2 ± 6.5
			Ultra-pure water dispersion (inter vial study) [results in nm]			
			Z-average: 423.3 ± 59.4, Pdl: 0.427 ± 0.042, FWHM peak width: 414.1 ± 107.6	Z-average: 113.2 ± 3.2, Pdl: 0.242 ± 0.018, FWHM peak width: 73.6 ± 11.1 Z-average: 119.6 ± 11.0, Pdl: 0.224 ± 0.033, FWHM peak width: 73.6 ± 0.6	Z-average: 128.6 ± 1.6, Pdl: 0.221 ± 0.004, FWHM peak width: 89.0 ± 10.3 Z-average: 126.5 ± 2.7, Pdl: 0.214 ± 0.013, FWHM peak width: 84.7 ± 5.8	Z-average (nm): 132.9 ± 1.6, Pdl: 0.057 ± 0.006 Z-average: 130.4 ± 4.5, Pdl: 0.141 ± 0.006, FWHM peak width: 62.5 ± 1.2
						Ultra-pure water dispersion (ultrasonic bath) Z-average (nm): 554.9, Pdl: 0.679 Ultra-pure water dispersion (ultrasonic tweeter) Z-average (nm): 155, Pdl: 0.163
AFM	-	-	-	Z max: 22.3 (466) nm	Z max: 21.8 (458) nm	-
SAXS	Primary particle size: Equivalent diameter for spheres:					
	-	8 nm	22 nm, 2xRg <sub>1</sub> is 12.8nm	28 nm. 2xRg <sub>1</sub> is 26nm	27 nm. 2xRg <sub>1</sub> is 26nm	30 nm, 2xRg <sub>1</sub> is 26nm
<b>Specific surface area (SSA)</b> BET	9.230 (m <sup>2</sup> /g) Material stored at 40 °C : 10.03 m <sup>2</sup> /g Material stored at -80 °C: 10.35 m <sup>2</sup> /g	316.07 m <sup>2</sup> /g Material stored at 40 °C : 234.47 m <sup>2</sup> /g Material stored at -80 °C: 229.00 m <sup>2</sup> /g	77.992 m <sup>2</sup> /g Material stored at 40 °C : 78.97 m <sup>2</sup> /g Material stored at -80 °C: 82.88 m <sup>2</sup> /g	50.835 ± 1.8 m <sup>2</sup> /g Material stored at 40 °C: 51.69 m <sup>2</sup> /g Material stored at -80 °C: 50.86 m <sup>2</sup> /g	56.261 m <sup>2</sup> /g Material stored at 40 °C: 57.07 m <sup>2</sup> /g Material stored at -80 °C: 57.18 m <sup>2</sup> /g	46.175 m <sup>2</sup> /g Material stored at 40 °C (two samples): 52.81m <sup>2</sup> /g and 53.37 m <sup>2</sup> /g Material stored at -80 °C (two samples): 55.49 m <sup>2</sup> /g and 53.66 m <sup>2</sup> /g
SAXS	-	169.5 ± 8.5 m <sup>2</sup> /g	65.6 ± 3.3 m <sup>2</sup> /g	51.1 ± 1.8 m <sup>2</sup> /g	52.4 ± 2.1 m <sup>2</sup> /g	47.0 ± 2.3 m <sup>2</sup> /g
<b>Zeta potential (surface charge)</b>	-	-	NM-102 forms a stable suspension at pH lower than 4, with positively charged	NM-103 forms a stable suspension at pH lower than 4, with positively charged	NM-104 forms a stable suspension at pH lower than 4, with positively charged nanoparticles (exceeding 30	NM-105 forms a stable suspension at pH lower than 4 with positively charged nanoparticles (exceeding

Zeta-metry			nanoparticles (exceeding 30 mV). The zeta potential varied significantly as function of pH from 40 mV at pH 2 to -45 mV around pH 12. IEP: 6.	nanoparticles (exceeding 30 mV). The zeta potential varied greatly as function of pH from 45 mV at pH 2 to -45 mV around pH 12. NM-103 is unstable at pH around 6 (with zeta pot. +40 mV on the supernatant) which may be associated with the surface heterogeneities of this coated material. The high value of IEP (8.2) is most likely due to the presence of Al coating on the surface.	mV). The zeta potential varied significantly as function of pH, from 45 mV at pH 2 to -45 mV around pH 12. NM-104 is unstable at pH around 6 (with zeta pot. +40 mV on the supernatant) which may be assisted with the surface heterogeneities of this coated material. The high value of IEP (8.2) is most likely due to the presence of Al coating on the surface.	30 mV). The zeta potential, however, varied greatly as function of pH from 45 mV at pH 2 to -45 mV around pH 12. IEP: 6.6
<b>Surface chemistry (where appropriate). Presence of organic coating XPS</b>	Elements identified in the surface [results in at%]					
	O (53.8 ± 0.7 at%), C (27.7 ± 0.7 at%), Ti (17.3 ± 0.5 at%), K (1.2 ± 0.3 at%)	O (55.9 ± 0.7), C (23.4 ± 0.5), Ti (20.5 ± 0.1), Fe/Ca (1.2 ± 0.3)	O (50.7 ± 1.5 at%), C (23.4 ± 2.4 at%), Ti (18.6 ± 0.9 at%)	O (56.0 ± 1.2), C (25.9 ± 1.4), Ti (10.7 ± 0.4), Al (4.9 ± 0.4), Fe/Ca (2.5 ± 1.0)	O (63.5 ± 0.8 at%), C (16.3 ± 0.3 at%), Ti (13.1 ± 0.3 at%), Al (7.1 ± 1.0 at%)	O (54.0 ± 0.3 at%), C (24.5 ± 0.6 at%), Ti (21.5 ± 0.4 at%)
	Elements identified in the surface after Ar ion etching (2 min, 3 keV)					
	O (67.42 at%), C (4.73 at%), Ti (25.96 at%), K (1.9 at%)	O (62 at%), C (12.69 at%), Ti (25.28 at%)	O (47.12 at%), C (34.71 at%), Ti (18.27 at%)	O (66.6 at%), C (7.1 at%), Ti (20.6 at%), Al (4.0 at%), Fe/Ca (1.5 at%)	O (19.63 at%), C (7.32 at%), Ti (19.63 at%), Al (9.22 at%)	O (62.98 at%), C (11.93 at%), Ti (25.1 at%)
TGA and GC-MS on SOXHLET extracted compounds	No organic material identified	GC-MS analysis results (retention time in min.): Silane?: 31.6 and 32.9; Hexadecanoic acid methyl ester: 33.4; Hexadecanoic acid: 33.9; Octadecanoic acid: 35.8	No organic material identified	GC-MS analysis results (retention time in min.): Dimetoxymethylsilane: 2.4; Silane?: 3.3; Silane: 7	GC-MS analysis results (retention time in min.): Tetramethyl silicate: 4.9; Glycerol: 13; Silane: 31.6, Silane: 32.9; Hexadecanoic acid methyl ester: 33.4; Hexadecanoic acid: 33.9; Octadecanoic acid: 35.8	No organic material identified
<b>Porosity</b> BET	Micropore volume (mL/g): 0.0	Micropore volume (mL/g): 0.00179	Micropore volume (mL/g): 0.00034	Micropore volume (mL/g): 0.0	Micropore volume (mL/g): 0.0	Micropore volume (mL/g): 0.0
<b>Other relevant information (where available)</b> <b>Elemental analysis/impurities</b> Semi-quantitative ICP-OES <b>Elemental analysis/impurities</b> Semi-quantitative EDS	> 0.01 % : K(>0.1 %) : P 00.5-0.01 % : Zr 0.001-0.005 % : Ca Na  Si - 2800 ppm, P - 2100 ppm, Al - 900 ppm, K - 2500 ppm, Cr - 300 ppm, Fe - 4900 ppm, Ti - 58.57 (wt %), O (wt%) calculated - 40.08	>0.01 % : Na(> 0.1 %), Al, P, S, Zr 0.001-0.005 % : K, Ca  Si - 2900 ppm, P - 2700 ppm, Al - 900 ppm, S - 2200 ppm, Ti - 58.79 (wt %), O (wt%) calculated - 40.35	> 0.01% : S 0.005-0.01 % :Ca, Zr 0.001-0.005 % : K, Na, P, W  Si - 800 ppm, Al - 500 ppm, Fe - 700 ppm, Ti - 59.73 (wt %), O (wt%) calculated - 40.07	> 0.01 % : Al(> 0.1%), Na, S 0.005-0.01 % : Ca 0.001-0.005 % : Fe, K, Mg, Zr  Si - 6800 ppm, S - 2600 ppm, Al - 34300 ppm, Fe - 600 ppm, Ti - 54.74 (wt %), O (wt%) calculated - 40.82	> 0.01 % : Al(> 0.1 %), Ca, Na, S 0.001-0.005 % : K, Mg, Zr  Si -1800 ppm, S - 3200 ppm, Al - 32200 ppm, Ti - 55.60 (wt %), O (wt%) calculated - 40.68	0.001-0.005 % : Na  Si -700 ppm, Al - 400 ppm, Ti - 59.81 (wt %), O (wt%) calculated - 40.07



Europe Direct is a service to help you find answers to your questions about the European Union  
Freephone number (\*): 00 800 6 7 8 9 10 11

(\*) Certain mobile telephone operators do not allow access to 00 800 numbers or these calls may be billed.

A great deal of additional information on the European Union is available on the Internet.  
It can be accessed through the Europa server <http://europa.eu/>.

#### How to obtain EU publications

Our priced publications are available from EU Bookshop (<http://bookshop.europa.eu>),  
where you can place an order with the sales agent of your choice.

The Publications Office has a worldwide network of sales agents.  
You can obtain their contact details by sending a fax to (352) 29 29-42758.

European Commission

EUR 26637 EN – Joint Research Centre – Institute for Health and Consumer Protection

Title: Titanium Dioxide, NM-100, NM-101, NM-102, NM-103, NM-104, NM-105: Characterisation and Physico-Chemical Properties

Author(s) : Kirsten Rasmussen, Jan Mast, Pieter-Jan De Temmerman, Eveline Verleysen, Nadia Waegeneers, Frederic Van Steen, Jean Christophe Pizzolon, Ludwig De Temmerman, Elke Van Doren, Keld Alstrup Jensen, Renie Birkedal, Marcus Levin, Signe Hjortkjær Nielsen, Ismo Kalevi Koponen, Per Axel Clausen, Vivi Kofoed-Sørensen, Yahia Kembouche, Nathalie Thieriet, Olivier Spalla, Camille Guiot, Davy Rousset, Olivier Witschger, Sebastian Bau, Bernard Bianchi, Charles Motzkus, Boris Shivachev, Louiza Dimowa, Rositsa Nikolova, Diana Nihtianova, Mihail Tarassov, Ognyan Petrov, Snejana Bakardjieva, Douglas Gilliland, Francesca Pianella, Giacomo Ceccone, Valentina Spampinato, Giulio Cotogno, Neil Gibson, Claire Gaillard and Agnieszka Mech

Luxembourg: Publications Office of the European Union

2014 – 218 pp. – 21.0 x 29.7 cm

EUR – Scientific and Technical Research series – ISSN 1018-5593 (print), ISSN 1831-9424 (online)

ISBN 978-92-79-38188-1 (PDF)

ISBN 978-92-79-38189-8 (print)

doi: 10.2788/79554 (online)

#### Abstract

In 2011 the JRC launched a repository for Representative Nanomaterials to support both EU and international research projects, and especially the OECD Working Party on Manufactured Nanomaterials that leads an exploratory programme "Testing a Representative set of Manufactured Nanomaterials", aiming to generate and collect data on characterisation and (eco)toxicological properties to understand relevant end-points as well as the applicability of OECD Test Guidelines for testing nanomaterials.

The Repository responds to a need for nanosafety research purposes: availability of nanomaterial from a single production batch to enhance the comparability of results between different research laboratories and projects.

The present report presents the physico-chemical characterisation of the titanium dioxide (TiO<sub>2</sub>) from the JRC repository: NM-100, NM-101, NM-102, NM-103, NM-104 and NM-105. NM-105 was selected as principal material for the OECD test programme "Testing a representative set of manufactured nanomaterials". NM-100 is included as a bulk comparator.

The results for more than 15 endpoints are described in this report, including physico-chemical properties such as size and size distribution, crystallite size and electron microscopy images. Sample and test item preparation procedures are addressed. The results are based on studies by several European laboratories participating to the NANOGENOTOX Joint Action, and the JRC.

## JRC Mission

As the Commission's in-house science service, the Joint Research Centre's mission is to provide EU policies with independent, evidence-based scientific and technical support throughout the whole policy cycle.

Working in close cooperation with policy Directorates-General, the JRC addresses key societal challenges while stimulating innovation through developing new methods, tools and standards, and sharing its know-how with the Member States, the scientific community and international partners.

*Serving society*  
*Stimulating innovation*  
*Supporting legislation*

